

# **Thermochemical Storage and Lithium Ion Capacitors Efficiency of Manganese-Graphene Framework**



By

**Ntuthuko Wonderboy Hlongwa**

**(MSc Nanoscience)**

A thesis submitted in fulfilment of the requirements for the degree of

**Doctor of Philosophy**

UNIVERSITY of the  
Faculty of Science  
WESTERN CAPE

University of the Western Cape

Bellville, Cape Town, South Africa

**Supervisor: Prof Emmanuel Iwuoha**

**Co-supervisor: Dr Chinwe Ikpo**

**January 2018**

# KEYWORDS

Energy storage devices

Lithium-ion batteries

Supercapacitors

Lithium ion capacitors

$\text{LiMnPO}_4$

$\text{LiMn}_2\text{O}_4$

Activated carbon

Nanocomposite

Power density

Energy density

Nickel

Doping

Graphene

Coating

Capacitance



UNIVERSITY *of the*  
WESTERN CAPE

## ABSTRACT

Lithium ion capacitors are new and promising class of energy storage devices formed from a combination of lithium-ion battery electrode materials with those of supercapacitors. They exhibit better electrochemical properties in terms of energy and power densities than the above mentioned storage systems. In this work, lithium manganese oxide spinel ( $\text{LiMn}_2\text{O}_4$ ; LMO) and lithium manganese phosphate ( $\text{LiMnPO}_4$ ; LMP) as well as their respective nickel-doped graphenised derivatives (G-LMNO and G-LMNP) were synthesized and each cathode material used to fabricate lithium ion capacitors in an electrochemical assembly that utilised activated carbon (AC) as the negative electrode and lithium sulphate electrolyte in a two-electrode system. The synthetic protocol for the preparation of the materials followed a simple solvothermal route with subsequent calcination at 500 - 800 °C. The morphological, structural and electrochemical properties of the as prepared materials were thoroughly investigated through various characterisation techniques involving High resolution scanning electron microscopy (HRSEM), High resolution transmission electron microscopy (HRTEM), Fourier transform infrared spectroscopy (FTIR), Raman spectroscopy, X-ray diffraction (XRD), Small-angle X-ray scattering (SAXS), Electrochemical impedance spectroscopy (EIS), Cyclic voltammetry (CV) and Galvanostatic charge/discharge. The microscopic analysis for the G-LMNP revealed nanorods with diameters 20 – 100 nm and length of 100 nm - 3  $\mu\text{m}$ . The sizes of the nanorods were further confirmed by Small-angle X-ray scattering. Similarly, the morphological features of the G-LMNO represent nanorods which are however, interspersed with agglomerated nanoparticles due to higher temperature sintering that caused uncontrollable particle growth on the surface of the G-LMNO. The XRD patterns for the G-LMNP showed strong intensities of (011), (111), (200), (131) and (042) which are identified as orthorhombic structures with the  $Pnmb$  space group indexed to the olivine phase of  $\text{LiMnPO}_4$ . The diffraction

patterns for the G-LMNO showed all the crystallographic peaks at (111), (311), (400) which are indexed to the cubic spinel structure of  $\text{LiMn}_2\text{O}_4$ . Further results from FTIR showed that the spectrum of the G-LMNP is dominated by intramolecular vibration bands of the  $\text{PO}_4^{3-}$  anion at  $650 - 530 \text{ cm}^{-1}$  which confirm the presence of phospho-olivine phase in the material. Also the C-C vibrational frequency occurred at  $1630 \text{ cm}^{-1}$  thus confirming the presence of graphene in G-LMNP corroborated also by Raman results. Raman spectroscopy revealed bands at  $1463$  and  $1526 \text{ cm}^{-1}$  representing D and G bands of graphene along with the vibrational bands of  $\text{PO}_4^{3-}$  at  $980$  and  $1100 \text{ cm}^{-1}$ . The FTIR spectrum of G-LMNO is dominated by vibrational stretching mode of  $\text{MnO}_6$  octahedra at  $510 - 620 \text{ cm}^{-1}$  which are responsible for the formation of  $\text{LiMn}_2\text{O}_4$  with the C-C symmetric stretching band at  $1580 \text{ cm}^{-1}$  confirming the presence of graphene in the nanocomposite material as proven from Raman spectrum. The Raman results of the G-LMNO showed bands at  $1464$  and  $1529 \text{ cm}^{-1}$  representing D and G bands of graphene along with vibrational stretching bands of Mn-O at  $485 \text{ cm}^{-1}$ . The electrochemical characteristics of the G-LMNP || AC studied in  $1 \text{ M Li}_2\text{SO}_4$  showed that at a potential range of  $0 - 2 \text{ V}$  and  $0.1 \text{ A g}^{-1}$  current density, this lithium ion capacitor gave a specific capacitance of  $60 \text{ F g}^{-1}$  with capacitance retention of  $83 \%$  after  $750$  cycles. It rendered a maximum power density of  $18 \text{ kW kg}^{-1}$  and  $14.49 \text{ Wh kg}^{-1}$  energy density. It was discovered that the G-LMNP nanocomposite displayed better performance compared to LMP and LMNP under similar conditions. The LMP || AC exhibited specific capacitance, energy density and maximum power density of  $30 \text{ F g}^{-1}$ ,  $5.7 \text{ Wh kg}^{-1}$  and  $6.1 \text{ kW kg}^{-1}$ , respectively. LMNP || AC gave specific capacitance, energy density and maximum power density of  $54 \text{ F g}^{-1}$ ,  $9.4 \text{ Wh kg}^{-1}$  and  $16.7 \text{ kW kg}^{-1}$ , respectively. In a similar experiment, values obtained for the G-LMNO || AC lithium ion capacitor showed a specific capacitance of  $80 \text{ F g}^{-1}$  and  $70 \%$  capacitance retention recorded after  $1000$  charge–discharge cycles. This electrochemical assembly delivered a power and energy density at  $19.6 \text{ kW kg}^{-1}$  and  $12.32 \text{ Wh kg}^{-1}$ , respectively. It was found that the G-LMNO



nanocomposite showed enhanced electrochemical performance compared to LMO and LMNO under same condition. The LMO||AC exhibited specific capacitance, energy density and maximum power density of 21 F g<sup>-1</sup>, 3.1 Wh kg<sup>-1</sup> and 9.1 kW kg<sup>-1</sup>, respectively. The LMNO||AC revealed specific capacitance, energy density and maximum power density of 56 F g<sup>-1</sup>, 7.8 Wh kg<sup>-1</sup> and 10.6 kW kg<sup>-1</sup>, respectively. The results indicate that graphene coated on LMNP and LMNO improved the electrical conductivity enabling the devices to exhibit good electrochemical performance. These results show great potential in developing G-LMNO||AC and G-LMNP||AC lithium ion capacitors for practical applications. Additional studies conducted in this research involved thermochemical storage properties of LiMn<sub>2</sub>O<sub>4</sub> and CuMn<sub>2</sub>O<sub>4</sub> prepared through a modified Pechini method. Thermogravimetric redox tests in air established that both materials experienced fully reversible redox transformations when the temperature is varied between 900 and 1000 °C. These materials showed the stability of both Cu and Li mixed oxides after five consecutive redox cycles and, in accordance, the XRD confirmed that spinels retained their crystal structures after the treatment. Under the air tests conditions, reduction temperatures are higher than 940 °C for both oxides and the enthalpies of transformations are modest, with a maximum value of 36 kJ kg<sup>-1</sup> for LiMn<sub>2</sub>O<sub>4</sub>. However, when the reduction was performed in argon and the oxidation in air, there was an increase in the amount of oxygen exchanged in the gas-solids reactions and, subsequently, the heat storage capacity. Therefore, the heat recovered in the re-oxidation of CuMn<sub>2</sub>O<sub>4</sub> at 700 °C was 144 kJ kg<sup>-1</sup>, while LiMn<sub>2</sub>O<sub>4</sub> showed an enthalpy of 209 kJ kg<sup>-1</sup> (37 kJ mol<sup>-1</sup>). Thus, the stability and relatively high enthalpies of CuMn<sub>2</sub>O<sub>4</sub> and LiMn<sub>2</sub>O<sub>4</sub> are very good indicators of the applicability of these materials in thermochemical energy storage systems.

# DECLARATION

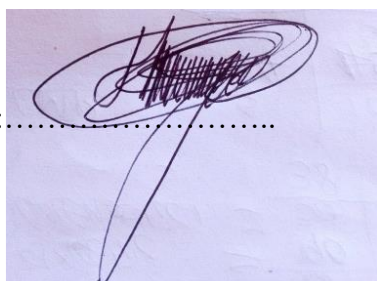
I declare that “*Thermochemical Storage and Lithium Ion Capacitors Efficiency of Manganese-Graphene Framework*” is my own work, that it has not been submitted before for any degree or examination in any other university, and that all the sources I have used or quoted have been indicated or acknowledged as complete references.



Ntuthuko Wonderboy Hlongwa

January 2018

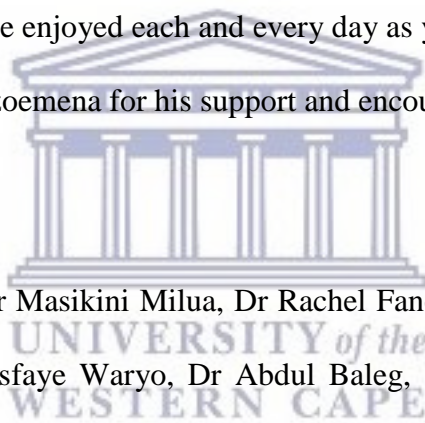
Signed:.....

A handwritten signature in black ink, consisting of several overlapping loops and a long, sweeping tail, positioned over a dotted line.

# ACKNOWLEDGEMENT

To the Almighty God that created and gave me mental, physical strength, dedication and courage to complete this project and the one behind all my successes, be the glory and honour.

**To my supervisor and mentors:** I would like to thank my supervisor, Professor Emmanuel Iwuoha, for the kindness, wisdom and generosity, encouragement and support that he has been giving throughout all my trials and tribulations during this research period. May God richly bless him. My co-supervisor, Dr Chinwe Ikpo, thank you for your enthusiasm, advice and guidance for this project, I have enjoyed each and every day as your student. I would also like to thank Professor Kenneth Ozoemena for his support and encouragement.

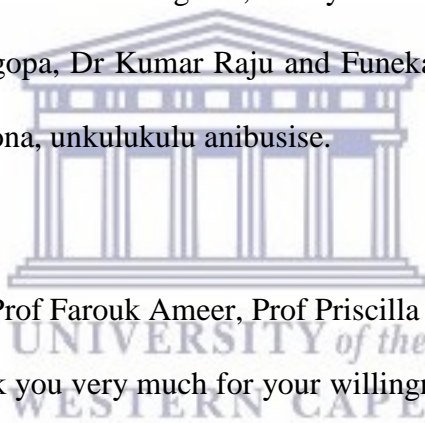


**To the SensorLab family:** Dr Masikini Milua, Dr Rachel Fanelwa Ajayi, Dr Natasha Ross, Dr Mawethu Bilibana, Dr Tesfaye Waryo, Dr Abdul Baleg, Siyabulela Hamnca, Olwethu Ngwanya, Zolani Myalo, Siyabonga Mdluli, Emmanuel Ramoroka Nomxolisi Dywili, Nomaphelo Ntshongontshi, Sinazo Qakala, Nolukholo Tyombo, Miranda Ndipingwi, Dr Keagen Pokpas, Dr Francis Ntumba Muya, Dr Meryck Ward, , Dr Lerato Phelane, Dr Lindsay Wilson, Candice Franke, thank you for sharing your opinions and experience through which I received the required information for my project, it has been fun working with you guys though frustrating at times, thanks to everyone who was ever able to help.

**To IMDEA Energy:** Dr Juan Coronado, Prof David Serrano, Dr Patricia Pizarro, Daniel Sastre, Hector Hernando, Jaime Sanchez, Dr Rebecca Marcilla, Dr Afshin Pendashteh, I would

like to express how I am grateful for the opportunity you provided me to visit your institute in Spain (Madrid), it was wonderful working with you guys.

**To my Family and Friends:** I am very grateful for the continued support and believing in me throughout my studies, My aunt and grandmother Phumlile Mbotho, Phanjiwe Mbotho, My brothers Xolani Mbotho, Msizi Hlongwa, Zithokozise Hlongwa, Lindokuhle Hlongwa, My sister Ntokozo Hlongwa, My Uncles Mkhonzeni Mbotho, Bheki Mbotho and Mthokozisi Mbotho, My cousins; Mxolisi (Smo) Mbotho, Sphamandla (B) Mbotho, Sfundu (Kati) Mbotho and my friends Mthuthuzeli Ngubo, Naledi Raleie, Philasande Ngcobo, Sihle Magubane, Sfiso Khanyile, Ayanda Masengemi and Xolani Ngema, To my CSIR friends who welcome me with warm hands Dr Katlego Makgopa, Dr Kumar Raju and Funeka Nkosi, Ngiyabonga kakhulu ngakho konke eningenzele khona, unkulukulu anibusise.



**To Chemistry Department:** Prof Farouk Ameer, Prof Priscilla Baker, Prof Martin Onani and Mrs Wilhemina Jackson, thank you very much for your willingness to assist in solving all the academic and technical problems.

**Sponsorship:** I would also like to thank the University of the Western Cape and the National Research Foundation (NRF) for funding my studies

# DEDICATION

This work is dedicated to

The memory of my late mother and father

Mrs Zandile Hlongwa and Mr Thembinkosi David Hlongwa.

And

My late aunt

Buyisile Mbotho.

May your wonderful souls rest in peace.



My grandmother

Phanjiwe Ntu Mbotho.

And my aunt

Phumlile Mbotho.

## LIST OF PUBLICATIONS

**Ntuthuko W. Hlongwa** Daniel Sastre, , Emmanuel Iwuoha, Alfonso Carrillo, Chinwe Ikpo, , David P. Serrano, Patricia Pizarro, Juan M. Coronado. *Exploring the Thermochemical Heat Storage Capacity of  $AMn_2O_4$  (A= Li or Cu) Spinels*. Solid State Ionics 2018 (320) 316-324 (published)

**Ntuthuko W. Hlongwa**, Natasha Ross, Chinwe Ikpo, Myra Nzaba, Miranda Ndipingwi , Priscilla Baker and Emmanuel Iwuoha. *Electrochemical Studies on Novel  $LiMnPO_4$  Coated with Magnesium-Gold Composite Thin Film in Aqueous Electrolytes*. Journal of Nano Research 2016 (44) 90-99(published)

Natasha Ross, **Ntuthuko W. Ntuthuko**, Miranda Ndipingwi, Chinwe Ikpo, Priscilla Baker, and Emmanuel Iwuoha. *Iron-Gold Coated- $LiMn_{2-x}O_4$  Nanowire High Power Cathode System Probed by Spectroscopic and Microstructural Analysis*. Journal of Nano Research 2016. (44):10-20 (published)

Nolubabalo Matinise, Noluthando Mayedwa, Chinwe O. Ikpo, **Ntuthuko W. Hlongwa**, Miranda M. Ndipingwi, Lerato Molefe, Nomxolisi Dywili, Anne Djoumessi Yonkeu, Tesfaye Waryo, Priscilla Baker and Emmanuel I. Iwuoha. *Bimetallic Nanocomposites of Palladium (100) and Ruthenium for Electrooxidation of Ammonia*. Journal of Nano Research 2016 (44) 100-13 (published)

Nomxolisi Dwyili, Njomo Njagi, Chinwe Ikpo, Anne Lutgarde Djoumessi Yonkeu, Suru Vivian John, **Ntuthuko W. Hlongwa**, Naledi Roleie and Emmanuel Iwuoha. *Anilino-Functionalized Graphene Oxide Intercalated with Pt Metal Nanoparticles for Application as Supercapacitor Electrode Material*. Journal of Nano Research 2016. (44):79-89 (published)

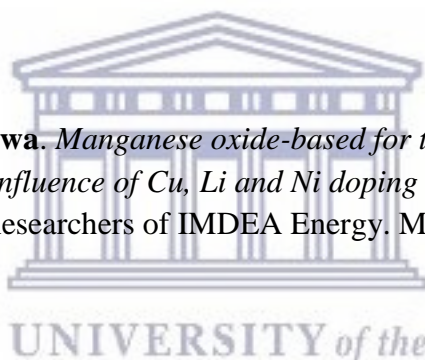
Natasha Ross, Myra Nzaba, **Ntuthuko W. Hlongwa**, Chinwe Ikpo, Priscilla Baker, and Emmanuel Iwuoha. *“Palladium-Gold Nanoalloy Surface Modified  $LiMn_2O_4$  Cathode for Enhanced Li-Ion Battery”* Hindawi Publishing Corporation Journal of Nanomaterials, Volume 2015.(8): 1-6 (published)

## LIST CONFERENCE PRESENTATION

**Ntuthuko W. Hlongwa**, Natasha. Ross, Chinwe Ikpo and Emmanuel. Iwuoha. *Nanoparticles –infused lithium manganese phosphate coated with magnesium –gold composite thin film- a possible novel material for lithium ion battery olivine cathode*. 7<sup>th</sup> international symposium on macro and supramolecular architecture and materials. Johannesburg, South Africa. 23-27 November 2014. **Poster presentation**

**Ntuthuko Wonderboy Hlongwa**, Chinwe Ikpo, Natasha. Ross, Miranda Ndipingwi and Emmanuel. Iwuoha. *Novel LiMnPO<sub>4</sub> Coated with Magnesium-Gold Composite Thin Film -A Possible Material for Lithium Ion Battery Olivine Cathode*. 3rd International symposium on electrochemistry: materials, analytical and physical electrochemistry today, University of the Western Cape, Bellville, South Africa. 26-28 May 2015. **Poster presentation**

**Ntuthuko Wonderboy Hlongwa**. *Manganese oxide-based for thermochemical energy storage: A comparison of the influence of Cu, Li and Ni doping on redox performance*. 5<sup>th</sup> Annual Workshop of Young Researchers of IMDEA Energy. Madrid, Spain, 16 December 2016. **Oral presentation**



**Ntuthuko W. Hlongwa**, Chinwe Ikpo and Emmanuel. Iwuoha. *Graphene-functionalised LiMn<sub>2</sub>O<sub>4</sub> electrodes for high performance Li-ion capacitors*. 4<sup>th</sup> international symposium on electrochemistry: pure and applied electrochemistry. University of the Johannesburg, South Africa. 3-5 April 2018 (**Oral presentation**)

## LIST OF ABBREVIATIONS AND ACRONYMS

LICs	Lithium ion capacitors
LIBs	Lithium ion batteries
PCs	Pseudocapacitance
LiMnPO <sub>4</sub>	Lithium manganese phosphate
LiMn <sub>2</sub> O <sub>4</sub>	Spinel lithium manganese oxide
AC	Activated carbon
Li <sub>2</sub> SO <sub>4</sub>	Lithium sulphate
G-LMNP	Graphene coated lithium manganese phosphate doped with nickel
G-LMNO	Graphene coated spinel lithium manganese oxide doped with nickel
TEM	transmission electron microscopy)
SEM	scanning electron microscopy
XRD	X-ray powder diffraction
EDX	energy dispersive X-ray spectroscopy
NMR	Nuclear magnetic resonance spectroscopy
SAXS	Small-angle X-ray scattering
FTIR	Fourier transform infrared spectroscopy
CV	Cyclic voltammetry
EIS	Electrochemical Impedance spectroscopy
SAED	Selected area electron diffraction
E	Energy density
Pmax	Maximum power density
Csp	Specific capacitance

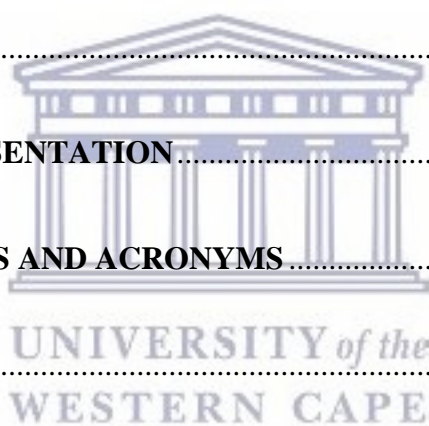


Rct	Charge transfer resistance
$\Delta E$	change in potential
JCPDS	Joint committee of power diffraction standards



# TABLE OF CONTENTS

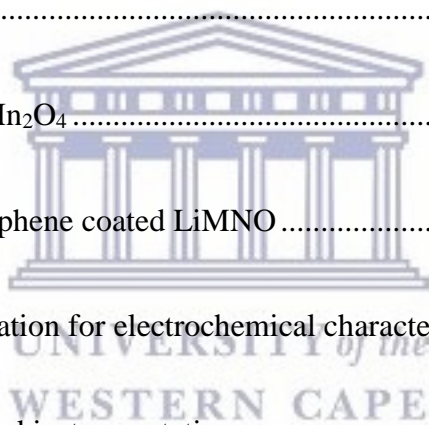
<b>KEYWORDS</b> .....	i
<b>ABSTRACT</b> .....	ii
<b>DECLARATION</b> .....	v
<b>ACKNOWLEDGEMENT</b> .....	vi
<b>DEDICATION</b> .....	viii
<b>LIST OF PUBLICATIONS</b> .....	ix
<b>LIST CONFERENCE PRESENTATION</b> .....	x
<b>LIST OF ABBREVIATIONS AND ACRONYMS</b> .....	xi
<b>TABLE OF CONTENTS</b> .....	xiii
<b>LIST OF FIGURES</b> .....	xviii
<b>CHAPTER ONE</b> .....	1
1 <b>Introduction</b> .....	1
1.1 <b>Background</b> .....	2
1.1.1 <b>Need for renewable energy production</b> .....	2
1.1.2 <b>Lithium ion capacitors for improved energy and power density</b> .....	3
1.2 <b>Problem Identification</b> .....	3



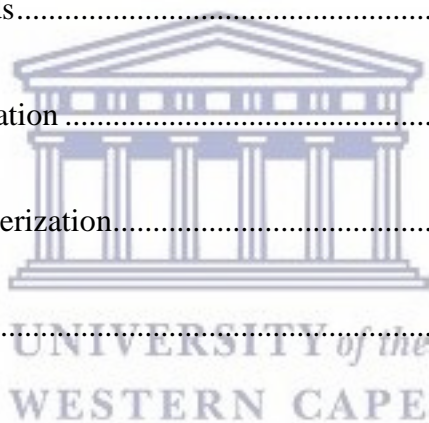
1.3	Rationale and Motivation .....	4
1.4	Research Aims and Objectives.....	5
1.5	Thesis lay-out .....	6
1.6	References .....	7
<b>CHAPTER TWO .....</b>		<b>14</b>
<b>2</b>	<b>Literature review .....</b>	<b>14</b>
<b>Lithiated manganese-based nanostructured electrode materials for high Energy density lithium ion capacitors .....</b>		<b>14</b>
2.1	Introduction .....	15
2.2	Electrochemical capacitors within energy storage systems .....	16
2.3	Lithium-ion capacitor materials for high power and energy density .....	18
2.3.1	The mechanism of the hybrid capacitor.....	18
2.3.2	Principles, requirements and limitations.....	19
2.4	Olivine and spinel materials as new electrode for Li-ion capacitors .....	22
2.4.1	Role of nanostructures and morphology on the electrode material .....	25
2.4.2	Effect of doping on the pristine material .....	26
2.4.3	Carbon coating .....	27
2.5	Summary .....	29

2.6	References .....	30
<b>CHAPTER THREE</b> .....		<b>42</b>
<b>3</b>	<b>Development of graphenised-lithium manganese phosphate doped with nickel with enhanced electrochemical performance for lithium ion capacitors .....</b>	<b>42</b>
	ABSTRACT.....	43
3.1	Introduction .....	43
3.2	Experimental .....	44
3.2.1	Chemical Reagents.....	45
3.2.2	Synthesis of $\text{LiMnPO}_4$ .....	45
3.2.3	Synthesis of Graphene coated LMNP.....	46
3.2.4	Electrode preparation for electrochemical characterization .....	46
3.2.5	Measurements and instrumentation .....	47
3.3	Material characterization.....	50
3.3.1	Structure and morphology characterisation of graphene .....	50
3.3.2	Morphology and structure of LMP, LMNP and G-LMNP nanocomposite.....	54
3.3.3	Electrochemical studies of single electrode $\text{LiMnPO}_4$ based electrodes .....	68
3.3.4	Lithium ion capacitor (LIC): $\text{LMP} \parallel \text{AC}$ .....	71
3.4	Summary .....	84

3.5	References .....	85
<b>CHAPTER FOUR.....</b>		<b>93</b>
<b>4</b>	<b>Energy storage performance of nickel doped graphene coated LiMn<sub>2</sub>O<sub>4</sub> material for Li-ion capacitors.....</b>	<b>93</b>
ABSTRACT.....		94
4.1	Introduction .....	95
4.2	Experimental .....	96
4.2.1	Chemicals.....	96
4.2.2	Synthesis of LiMn <sub>2</sub> O <sub>4</sub> .....	97
4.2.3	Synthesis of Graphene coated LiMNO .....	97
4.2.4	Electrode preparation for electrochemical characterization .....	98
4.2.5	Measurements and instrumentation .....	99
4.3	Materials characterization .....	102
4.3.1	Structure and morphology characterisation of graphene .....	102
4.3.2	Surface morphology, composition and structure of LMO and nickel doped derivatives.....	104
4.3.3	Electrochemical studies of single electrode LiMn <sub>2</sub> O <sub>4</sub> .....	116
4.3.4	Lithium ion capacitor (LIC): LMO    AC .....	120



4.4	Summary .....	133
4.5	Reference.....	135
<b>CHAPTER 5 .....</b>		<b>142</b>
<b>5 Development of copper manganese oxide and lithium manganese oxide-for thermochemical energy storage system .....</b>		<b>142</b>
ABSTRACT.....		143
5.1	Introduction .....	144
5.2	Experimental methods.....	147
5.2.1	Materials preparation .....	147
5.2.2	Material Characterization.....	147
5.2.3	Redox cycling .....	147
5.3	Results and Discussion.....	148
5.4	Summary .....	160
5.5	References .....	162
<b>CHAPTER SIX .....</b>		<b>166</b>
<b>6 Conclusion and Recommendations .....</b>		<b>165</b>
6.1	Conclusion.....	166
6.2	Recommendations .....	169



## LIST OF FIGURES

<b>Figure 2.1:</b> Ragone plot- comparison of performance of different energy storage devices[4] .....	15
<b>Figure 2.2:</b> Mechanism of working lithium ion capacitor[5].....	19
<b>Figure 2.3:</b> Cyclic voltammetry curves with increasing potential window [27].....	21
<b>Figure 2.4:</b> Structure of the $\text{LiMnPO}_4$ [43] .....	23
<b>Figure 2.5:</b> Structure of Spinel $\text{LiMn}_2\text{O}_4$ [43].....	24
<b>Figure 3.1:</b> FTIR spectra of graphene oxide (GO) and graphene .....	51
<b>Figure 3.2:</b> Raman spectra of graphene oxide and graphene .....	52
<b>Figure 3.4:</b> TEM image of the(a) and (b) $\text{LiMnPO}_4$ nanowires and [(c) and (d)] Nickel doped $\text{LiMnPO}_4$ and [(e) and (f)] G-LMNP .....	55
<b>Figure 3.5:</b> HRTEM images and SAED of (a) and (b) $\text{LiMnPO}_4$ , [(c) and (d)] LMNP and [(e) and (f)] G-LMNP .....	57
<b>Figure 3.6:</b> EDS of the synthesized $\text{LiMnPO}_4$ , LMNP and G-LMNP.....	58
<b>Figure 3.7:</b> (a) and (b) SEM image of the $\text{LiMnPO}_4$ nanowires, (c) and (d) nickel doped $\text{LiMnPO}_4$ and (c) and (d) Graphene coated LMNP .....	60
<b>Figure 3.8:</b> (a) SAXS Particle size distribution in number weighted, (b) volume weighted ..	62
<b>Figure 3.9:</b> $^7\text{Li}$ MAS NMR spectra for $\text{LiMnPO}_4$ , LMNP and G-LMNP at a MAS spinning speed of $\sim 15$ kHz. ....	63
<b>Figure 3.10:</b> XRD patterns of $\text{LiMnPO}_4$ , LMNP and G-LMNP.....	65

<b>Figure 3.11:</b> FTIR spectra of LiMnPO <sub>4</sub> , LMNP and G-LMNP .....	66
<b>Figure 3.12:</b> Raman spectra of LiMnPO <sub>4</sub> , LMNP and G-LMNP .....	67
<b>Figure 3.13:</b> Comparative curves for olivine LiMnPO <sub>4</sub> , nicked doped LiMnPO <sub>4</sub> and G-LMNP from cyclic voltammetry at a scan rate of 5 mV s <sup>-1</sup> .....	69
<b>Figure 3.14:</b> Comparative galvanostatic charge-discharge for LiMnPO <sub>4</sub> , nickel doped LiMnPO <sub>4</sub> and G-LMNP curves at a constant current density of 1 A g <sup>-1</sup> . .....	71
<b>Figure 3.15:</b> Comparative cyclic voltammograms of LiMnPO <sub>4</sub> and activated carbon (AC) at a scan rate of 5 mV.s <sup>-1</sup> in aqueous 1 M Li <sub>2</sub> SO <sub>4</sub> electrolyte. ....	72
<b>Figure 3.16:</b> Comparative curves for olivine LiMnPO <sub>4</sub>    AC, LMNP    AC and G-LMNP    AC lithium ion capacitors cyclic voltammetry at a scan rate of 5 mV.s <sup>-1</sup> .....	74
<b>Figure 3.17:</b> Comparison of cyclic voltammetry for (a) LiMnPO <sub>4</sub>    AC, (b) LMNP    AC, (c) G-LMNP    AC and (d) rate capability of lithium ion capacitors at various scan rates .....	76
<b>Figure 3.18:</b> Galvanostatic charge-discharge curves at constant current density for LiMnPO <sub>4</sub>    AC, LMNP    AC and G-LMNP    AC lithium ion capacitors. Electrolyte: aqueous 1 M Li <sub>2</sub> SO <sub>4</sub> .....	77
<b>Figure 3.19:</b> Comparison of galvanostatic charge-discharge for olivine (a) LiMnPO <sub>4</sub>    AC, (b) LMNP    AC, (c) G-LMNP    AC of lithium ion capacitors at various current densities and (d) capacitance curves (C <sub>sp</sub> vs. current densities .....	79
<b>Figure 3.20:</b> Ragone plots of LiMnPO <sub>4</sub>    AC, LMNP    AC and G-LMNP    AC at different density.....	80
<b>Figure 3.21:</b> Comparative Nyquist plots for LiMnPO <sub>4</sub>    AC, LMNP    AC and G-LMNP    AC and the inset show proposed equivalent circuit .....	81
<b>Figure 3.22:</b> Comparative Bode plots of LiMnPO <sub>4</sub>    AC, LMNP    AC, G-LMNP    AC.....	83



<b>Figure 3.23:</b> Cycling performance of $\text{LiMnPO}_4 \parallel \text{AC}$ , $\text{LMNP} \parallel \text{AC}$ , $\text{G-LMNP} \parallel \text{AC}$ lithium ion capacitor with continuous charge-discharge profiles as inset.....	84
<b>Figure 4.1:</b> FTIR spectra of graphene oxide (GO) and graphene .....	103
<b>Figure 4.2:</b> Raman spectra of graphene oxide and graphene .....	104
<b>Figure 4.3:</b> (a) and (b) SEM image of the $\text{LiMn}_2\text{O}_4$ , [(c) and (d)] LMNO and [(e) and (f)] G-LMNO.....	106
<b>Figure 4.4:</b> (a) and (b) TEM image of the $\text{LiMn}_2\text{O}_4$ , [(c) and (d)] nickel doped $\text{LiMn}_2\text{O}_4$ and [(c) and (d)] G-LMNO .....	108
<b>Figure 4.5:</b> EDS of the synthesized $\text{LiMn}_2\text{O}_4$ , nickel doped $\text{LiMn}_2\text{O}_4$ and G-LMNO.....	109
<b>Figure 4.6:</b> HRTEM image and selected area electron diffraction (SAED) patterns for $\text{LiMn}_2\text{O}_4$ , nickel doped $\text{LiMn}_2\text{O}_4$ and G-LMNO.....	111
<b>Figure 4.7:</b> SAXS Particle size distribution in (a) number weighted, (b) volume weighted	113
<b>Figure 4.8:</b> XRD patterns of $\text{LiMn}_2\text{O}_4$ , nickel doped $\text{LiMn}_2\text{O}_4$ and Graphene coated G-LMNO .....	114
<b>Figure 4.9:</b> FTIR spectra of $\text{LiMn}_2\text{O}_4$ , nickel doped $\text{LiMn}_2\text{O}_4$ and G-LMNO.....	115
<b>Figure 4.10:</b> Raman spectra of $\text{LiMn}_2\text{O}_4$ , nickel doped $\text{LiMn}_2\text{O}_4$ and G-LMNO .....	116
<b>Figure 4.11:</b> Comparative curves for olivine $\text{LiMn}_2\text{O}_4$ , nickel doped $\text{LiMn}_2\text{O}_4$ and G-LMNO from cyclic voltammetry at a scan rate of $5 \text{ mVs}^{-1}$ .....	118
<b>Figure 4.12:</b> Comparative of galvanostatic charge-discharge curves for spinel $\text{LiMn}_2\text{O}_4$ , nickel doped $\text{LiMn}_2\text{O}_4$ and G-LMNO nanocomposite at a constant current density of $1 \text{ A g}^{-1}$ .....	120
<b>Figure 4.13:</b> Comparative cyclic voltammetry curves for spinel $\text{LiMn}_2\text{O}_4$ and activated carbon (AC) at a scan rate of $5 \text{ mV s}^{-1}$ in aqueous $1 \text{ M Li}_2\text{SO}_4$ electrolyte .....	122

<b>Figure 4.14:</b> Comparative curves for spinel $\text{LiMn}_2\text{O}_4 \parallel \text{AC}$ , $\text{LMNO} \parallel \text{AC}$ and $\text{G-LMNO} \parallel \text{AC}$ lithium ion capacitors cyclic voltammetry at a scan rate of $5 \text{ mV s}^{-1}$ .....	123
<b>Figure 4.15:</b> Comparison of cyclic voltammetry for olivine (a) $\text{LiMn}_2\text{O}_4 \parallel \text{AC}$ , (b) $\text{LMNO} \parallel \text{AC}$ , (c) $\text{G-LMNO} \parallel \text{AC}$ and (d) rate capability of lithium ion capacitors at various scan rates .....	126
<b>Figure 4.16:</b> galvanostatic charge-discharge curves at constant current density for $\text{LiMn}_2\text{O}_4 \parallel \text{AC}$ , $\text{LMNO} \parallel \text{AC}$ and $\text{G-LMNO} \parallel \text{AC}$ lithium ion capacitors. Electrolyte: aqueous $1 \text{ M Li}_2\text{SO}_4$ .....	126
<b>Figure 4.17:</b> Comparison of galvanostatic charge-discharge for spinel (a) $\text{LiMn}_2\text{O}_4 \parallel \text{AC}$ , (b) $\text{LMNO} \parallel \text{AC}$ , (c) $\text{G-LMNO} \parallel \text{AC}$ of lithium ion capacitors at various current densities and (d) capacitance curves ( $C_{\text{sp}}$ vs. current densities).....	128
<b>Figure 4.18:</b> Ragone plots of $\text{LiMn}_2\text{O}_4 \parallel \text{AC}$ , $\text{LMNO} \parallel \text{AC}$ and $\text{G-LMNO} \parallel \text{AC}$ at different current densities .....	129
<b>Figure 4.19:</b> Comparative Nyquist plots of $\text{LiMn}_2\text{O}_4 \parallel \text{AC}$ , $\text{LMNO} \parallel \text{AC}$ and $\text{G-LMNO} \parallel \text{AC}$ and the inset of equivalent circuit.....	131
<b>Figure 4.20:</b> Comparative Bode plots of $\text{LiMn}_2\text{O}_4 \parallel \text{AC}$ , $\text{LMNO} \parallel \text{AC}$ and $\text{G-LMNO} \parallel \text{AC}$ .....	132
<b>Figure 5.1:</b> XRD pattern of synthesized $\text{CuMn}_2\text{O}_4$ ..... <b>Error! Bookmark not defined.</b>	
<b>Figure 5.2:</b> Five redox cycles performed to $\text{CuMn}_2\text{O}_4$ , heating up to $900 \text{ }^\circ\text{C}$ and cooling down to $700 \text{ }^\circ\text{C}$ in Ar/air flow .....	148
<b>Figure 5.3:</b> DSC analysis for the first cycle taken from <b>Figure 5.2</b> .....	151
<b>Figure 5.4:</b> XRD pattern of the reduced $\text{CuMn}_2\text{O}_4$ before and after five cycles.....	154
<b>Figure 5.5:</b> SEM of $\text{CuMn}_2\text{O}_4$ before and after five cycles .... <b>Error! Bookmark not defined.</b>	

**Figure 5.6:** XRD pattern of the  $\text{CuMn}_2\text{O}_4$  reduction in argon at  $900\text{ }^\circ\text{C}$  **Error! Bookmark not defined.**

**Figure 5.7:** XRD patterns of the synthesized  $\text{LiMn}_2\text{O}_4$ . ..... 152

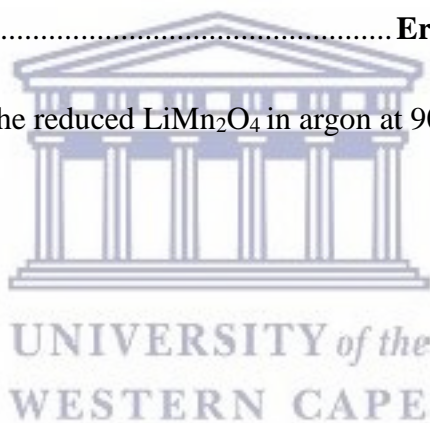
**Figure 5.8:** Five redox cycles performed to  $\text{LiMn}_2\text{O}_4$ , heating up to  $900\text{ }^\circ\text{C}$  and cooling down to  $700\text{ }^\circ\text{C}$  in Ar/air flow. .... 159

**Figure 5.9:** DSC analysis for the first cycle taken from **Figure 5.7**  
..... 155

**Figure 5.10:** XRD pattern of  $\text{LiMn}_2\text{O}_4$  after five redox cycles. .... 157

**Fig 5.11:** SEM images of synthesized  $\text{LiMn}_2\text{O}_4$ ; (A) as prepared material and (B) after 5 redox cycles. .... **Error! Bookmark not defined.**

**Figure 5.12:** XRD pattern of the reduced  $\text{LiMn}_2\text{O}_4$  in argon at  $900\text{ }^\circ\text{C}$ . .... 156

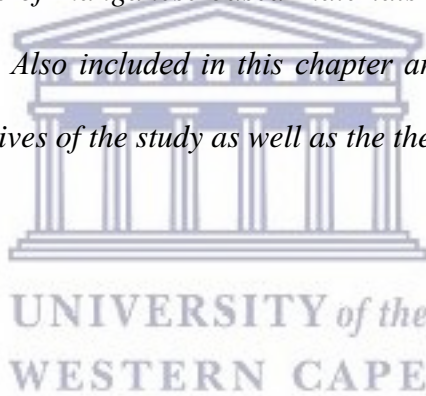


# CHAPTER ONE

## 1 Introduction

### Overview

*This chapter gives a brief background on the aspects involved in this project namely; energy storage devices, lithium ion capacitors,  $\text{LiMnPO}_4$  and  $\text{LiMn}_2\text{O}_4$ . It also deals with the enhancement of the properties of manganese-based materials through surface modification and design of nanostructures. Also included in this chapter are the project's rationale and motivation, the aim and objectives of the study as well as the thesis outline.*



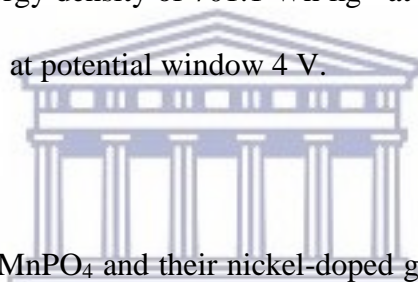
## 1.1 Background

### 1.1.1 Need for renewable energy production

Energy is very essential to societal development and technological advancement. The predicted depletion of non-renewable resources (fossil fuels) and issues with carbon dioxide (CO<sub>2</sub>) emissions upon fossil fuel combustion during electricity generation raises concerns for the future use of energy as well as the environment [1,2]. The global energy demand since 2011 has grown by an annual average of around 1.8% mainly in developing countries [3]. Solar and windmill are renewable energy sources viewed as alternatives in solving the issues associated with the use of fossil fuels. According to the global status report on renewable energy [3,4], CO<sub>2</sub> emission has been on the decline since the past three years mainly due to the global reduction in coal usage as well as increased generation of power from renewable sources. Renewable energy, as of 2015 provided an estimated 19.3% final global energy consumption [3,4]. The growth of renewable energy is hindered by cost in comparison to oil and natural gas. The establishment of suitable energy storage systems is a valuable approach for efficient utilization of renewable energy sources [5,6]. Highly efficient supercapacitors and lithium ion batteries can meet the demand for reliable energy storage system [7,8]. However, to acquire an established role in the commercial sector, lithium-ion batteries and supercapacitors need improvement with regards to power and energy density, cost, and particularly safety. Lithium ion capacitor development combines advantages of lithium ion batteries with supercapacitors electrodes. This device is attracting much interest due to their improved energy and power density with adequate cycling stability [6,9–11].

### **1.1.2 Lithium ion capacitors for improved energy and power density.**

Lithium ion capacitor (LICs) is a combination of EDLCs electrode materials and materials exhibiting battery-like redox characteristics. They can power and reinforce each other in a circuit. LICs offer better properties because of the synergistic behaviour with respect to their individual components [6]. Electroactive oxides (or phosphates) commonly used as cathode materials in lithium ion batteries [12,13], and conducting carbons used in EDLC, are the most utilised electrode materials in lithium ion capacitors [14–16]. Various works focus on materials such as  $\text{LiFePO}_4$ ,  $\text{LiMnPO}_4$ ,  $\text{LiMn}_2\text{O}_4$ ,  $\text{Li}_2\text{FeSiO}_4$  for LICs delivering encouraging results [17–20]. The choice for this study was  $\text{LiMnPO}_4$  and  $\text{LiMn}_2\text{O}_4$  due to their appealing properties.  $\text{LiMnPO}_4$  has a theoretical energy density of  $701.1 \text{ Wh kg}^{-1}$  at a voltage window 4.1 V while  $\text{LiMn}_2\text{O}_4$  delivers  $400 \text{ Wh kg}^{-1}$  at potential window 4 V.



In this study,  $\text{LiMn}_2\text{O}_4$  and  $\text{LiMnPO}_4$  and their nickel-doped graphene derivatives were used in LICs two electrode system in aqueous medium (1M  $\text{Li}_2\text{SO}_4$ ) and activated carbon as negative electrode materials. The fabricated LICs assembly displayed improved electrochemical performances, in terms of specific capacitance, energy density and power density.

## **1.2 Problem Identification**

$\text{LiMnPO}_4$  and  $\text{LiMn}_2\text{O}_4$  are environment-friendly, have low cost and good cycle stability. They have been studied extensively as positive electrode (cathode) materials for lithium ion battery rather than lithium ion capacitors. However, they have poor rate performance due to large lattice distortions by Jahn Teller active  $\text{Mn}^{3+}$  ions, which reduces conductance and blocks the transport of electrons or ions [21,22]. This phenomenon leads to low conductivity limiting their application in lithium ion capacitors. Many strategies have been employed to improve the rate

performances of  $\text{LiMn}_2\text{O}_4$  and  $\text{LiMnPO}_4$ . These include particle size reduction, carbon coating and metal cations doping. Carbon coating is essentially used to enhance the electronic conductivity of the material [23–25]. Metal cation doping which involves substitution of cations such as  $\text{Mg}^{2+}$ ,  $\text{Fe}^{2+}$ ,  $\text{Cu}^{2+}$ ,  $\text{Co}^{2+}$ ,  $\text{Ni}^{2+}$ ,  $\text{Ca}^{2+}$ ,  $\text{Zn}^{2+}$ ,  $\text{Ti}^{4+}$  and their combinations, have been studied [26–29]. Nickel-doped  $\text{LiMn}_2\text{O}_4$  and  $\text{LiMnPO}_4$  and their graphene derivatives were synthesized through solvothermal synthesis. The enhancing effect of graphene on the electrochemical performance of Li-ion capacitors that have Ni-doped and pristine  $\text{LiMnPO}_4$  and  $\text{LiMn}_2\text{O}_4$  were examined in this work.

### 1.3 Rationale and Motivation

The reduced dimensions of nanomaterials increase significantly the rate of lithium insertion/removal, because of the short distances for lithium-ion transport [12,30–32]. Electron transport within the particles is also enhanced by nanometer-sized particles, while high surface area allows active materials to absorb lithium ions more effectively hence increasing capacity [33]. Prabakaran *et al* designed nC- $\text{LiMnPO}_4$  exhibiting energy density of  $28.8 \text{ Wh kg}^{-1}$  with maximum specific power of  $14.6 \text{ kW kg}^{-1}$  [34]. Pazhamalai *et al* fabricated  $\text{LiMn}_2\text{O}_4$  || graphene which delivered energy and power densities of  $39.96 \text{ Wh kg}^{-1}$  and  $440 \text{ W kg}^{-1}$  respectively [9].

Doping is the addition of quantities of an element of a semiconductor which is used for modulating the electrical properties of the material [8,35–37]. This helps to decrease the manganese dissolution by decreasing the apparent contact area with the electrolyte [23]. Nickel doping in this work helped to improve the electrochemical performance of the manganese-based electrodes.

Graphene was used to coat LMNP and LMNO due to their interesting properties [39]. They have high electronic conductivity [9,40,41], structural flexibility, stability, and mechanical strength. They find use in various energy conversion and storage systems [42–44]. Lu and co-workers prepared  $\text{Li}_4\text{Ti}_5\text{O}_{12}$ /graphene nanosheets composite utilised for LICs obtaining specific energy of  $14 \text{ Wh kg}^{-1}$  and power density of  $2.7 \text{ kW kg}^{-1}$  at voltage of  $1 - 2.5 \text{ V}$  [45]. Kamari *et al* synthesized graphene-wrapped nanoporous  $\text{CuCo}_2\text{O}_4$  for LICs obtaining a specific energy of  $45.2 \text{ Wh kg}^{-1}$  at power density of  $15 \text{ kW kg}^{-1}$  at a potential window of  $0 - 1.6 \text{ V}$  [46].

## 1.4 Research Aims and Objectives

This research focussed on the development of lithium ion capacitor electrode materials for energy storage applications. This was achieved by fabricating G-LMNP || AC and G-LMNO || AC lithium ion capacitors and their electrochemical properties studied in  $1 \text{ M}$  aqueous  $\text{Li}_2\text{SO}_4$  electrolyte over the potential range of  $0 - 2 \text{ V}$ . Additionally, the properties of  $\text{LiMn}_2\text{O}_4$  and  $\text{CuMn}_2\text{O}_4$  were interrogated for use as thermochemical energy storage materials. Accordingly, the specific objectives are to:

1. Synthesize and characterization of  $\text{LiMn}_2\text{O}_4$  and  $\text{LiMnPO}_4$  and their nickel doped graphene derivatives.
2. Fabricate lithium ion capacitor for both spinels and olivines using Swagelok cell for the determination of the galvanostatic charge/discharge capacitance profiles.
3. Determine the power density and energy density of all the materials.
4. Synthesize and characterization of spinel  $\text{LiMn}_2\text{O}_4$  and  $\text{CuMn}_2\text{O}_4$  for thermochemical energy storage studies.



## 1.5 Thesis lay-out

This thesis is presented in six chapters.

**Chapter 1:** Gives brief background information on the project, problem statement and motivation as well as aims and objectives.

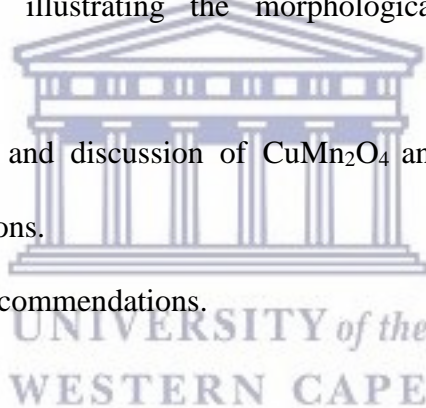
**Chapter 2:** Provides a detailed literature review for lithium ion capacitors.

**Chapter 3:** Provides results and discussion of the formed  $\text{LiMnPO}_4$  and nickel doped graphene coated derivatives illustrating the morphological, structural, spectroscopic, electrochemical properties.

**Chapter 4:** Provides results and discussion of the synthesized  $\text{LiMn}_2\text{O}_4$  and nickel doped graphene coated derivatives illustrating the morphological, structural, spectroscopic, electrochemical properties.

**Chapter 5:** Provides results and discussion of  $\text{CuMn}_2\text{O}_4$  and  $\text{LiMn}_2\text{O}_4$  synthesized, and thermochemical characterisations.

**Chapter 6:** Conclusion and recommendations.



## 1.6 References

- [1] B. Scrosati, J. Garche, Lithium batteries: Status, prospects and future, *J. Power Sources*. 195 (2010) 2419–2430. doi:<http://dx.doi.org/10.1016/j.jpowsour.2009.11.048>.
- [2] I. Hadjipaschalis, A. Poullikkas, V. Efthimiou, Overview of current and future energy storage technologies for electric power applications, *Renew. Sustain. Energy Rev.* 13 (2009) 1513–1522. doi:<http://dx.doi.org/10.1016/j.rser.2008.09.028>.
- [3] REN21, *Renewables 2017: global status report*, 2017. doi:10.1016/j.rser.2016.09.082.
- [4] A. McCrone, U. Moslener, F. D’Estais, C. Grünig, *Global Trends in Renewable Energy Investment 2017*, Frankfurt Sch. UNEP Collab. Cent. Clim. Sustain. Energy Financ. (2017) 90.  
<http://fsunepcentre.org/sites/default/files/publications/globaltrendsinrenewableenergyinvestment2017.pdf>  
<http://fs-unep-centre.org/publications/global-trends-renewable-energy-investment-2017>.
- [5] R.S. Disselkamp, Energy Storage using Aqueous Hydrogen Peroxide, *Energy & Fuels*. 22 (2008) 2771–2774. doi:10.1021/ef800050t.
- [6] D.P. Dubal, O. Ayyad, V. Ruiz, P. Gómez-Romero, Hybrid energy storage: the merging of battery and supercapacitor chemistries, *Chem. Soc. Rev.* 44 (2015) 1777–1790. doi:10.1039/C4CS00266K.
- [7] P. Alotto, M. Guarnieri, F. Moro, Redox flow batteries for the storage of renewable energy: A review, *Renew. Sustain. Energy Rev.* 29 (2014) 325–335. doi:<http://dx.doi.org/10.1016/j.rser.2013.08.001>.

- [8] C. Sronsri, P. Noisong, C. Danvirutai, Synthesis, characterization and vibrational spectroscopic study of Co, Mg co-doped  $\text{LiMnPO}_4$ , *Spectrochim. Acta Part A Mol. Biomol. Spectrosc.* 153 (2016) 436–444. doi:10.1016/j.saa.2015.08.046.
- [9] S.J.K. Parthiban Pazhamalai, Karthikeyan Krishnamoorthy, M.S.P. Sudhakaran, Fabrication of high performance aqueous Li-ion hybrid capacitor using  $\text{LiMn}_2\text{O}_4$  and graphene, *ChemElectroChem.* 4 (2017) 396–403. doi:10.1111/liv.12553.
- [10] X. Sun, X. Zhang, B. Huang, H. Zhang, D. Zhang, Y. Ma,  $(\text{LiNi}_{0.5}\text{Co}_{0.2}\text{Mn}_{0.3}\text{O}_2/\text{AC})/\text{graphite}$  hybrid energy storage device with high specific energy and high rate capability, *J. Power Sources.* 243 (2013) 361–368. doi:10.1016/j.jpowsour.2013.06.038.
- [11] D. Puthusseri, V. Aravindan, S. Madhavi, S. Ogale, Improving the energy density of Li-ion capacitors using polymer-derived porous carbons as cathode, *Electrochim. Acta.* 130 (2014) 766–770. doi:10.1016/j.electacta.2014.03.079.
- [12] J. Duan, G. Hu, Y. Cao, K. Du, Z. Peng, Synthesis of high-performance  $\text{LiMnPO}_4/\text{C}/\text{rGO}$  composite via a mechanical-activation-assisted polyol process, *Ionics (Kiel)*. (2016). doi:10.1007/s11581-016-1682-5.
- [13] Y. Gan, C. Chen, J. Liu, P. Bian, H. Hao, A. Yu, Enhancing the performance of  $\text{LiMnPO}_4/\text{C}$  composites through Cr doping, *J. Alloys Compd.* 620 (2015) 350–357. doi:10.1016/j.jallcom.2014.09.160.
- [14] F. Sun, J. Gao, Y. Zhu, X. Pi, L. Wang, X. Liu, Y. Qi., A high performance lithium ion capacitor achieved by the integration of a Sn-C anode and a biomass-derived microporous activated carbon cathode, *Nat. Publ. Gr.* 7 (2017) 40990. doi:10.1038/srep40990.

- [15] Q.Z. A. Yuan, A novel hybrid manganese dioxide / activated carbon supercapacitor using lithium hydroxide electrolyte using lithium hydroxide electrolyte, *Commun. Electrochem.* 8 (2015) 1173–1178. doi:10.1016/j.elecom.2006.05.018.
- [16] K.I. Ozoemena, K. Raju, P.M. Ejikeme, High-performance Mn<sub>3</sub>O<sub>4</sub>/onion-like carbon (OLC) nanohybrid pseudocapacitor: Unravelling the intrinsic properties of OLC against other carbon supports, *Carbon N. Y.* 117 (2017) 20–32. doi:10.1016/j.carbon.2017.02.050.
- [17] K. Karthikeyan, V. Aravindan, S.B. Lee, I.C. Jang, H.H. Lim, G.J. Park, M. Yashio, Y.S. Lee., A novel asymmetric hybrid supercapacitor based on Li<sub>2</sub>FeSiO<sub>4</sub> and activated carbon electrodes, *J. Alloys Compd.* 504 (2010) 224–227. doi:10.1016/j.jallcom.2010.05.097.
- [18] Y. Xie, F. Song, C. Xia, H. Du, Preparation of carbon-coated lithium iron phosphate/titanium nitride for a lithium-ion supercapacitor, *New J. Chem.* 39 (2015) 604–613. doi:10.1039/c4nj01169d.
- [19] K. Naoi, K. Kisu, E. Iwama, S. Nakashima, Y. Sakai, Y. Orikasa, P. Leone, N. Dupre, T. Brousse, , Ultrafast charge–discharge characteristics of a nanosized core–shell structured LiFePO<sub>4</sub> material for hybrid supercapacitor applications, *Energy Environ. Sci.* 9 (2016) 2143–2151. doi:10.1039/C6EE00829A.
- [20] J.-S. Zheng, L. Zhang, A. Shellikeri, W. Cao, Q. Wu, J.P. Zheng, A hybrid electrochemical device based on a synergetic inner combination of Li ion battery and Li ion capacitor for energy storage, *Sci. Rep.* 7 (2017) 41910. doi:10.1038/srep41910.
- [21] J. Chen, Recent Progress in Advanced Materials for Lithium Ion Batteries, *Materials (Basel)*. 6 (2013) 156–183. <http://www.mdpi.com/1996-1944/6/1/156>.

- [22] Y. Bi, W. Yang, B. Yang, C. Wang, D. Wang, S. Shi, Influence of  $\text{Li}_3\text{V}_2(\text{PO}_4)_3$  complexing on the performance of  $\text{LiMnPO}_4$  based materials utilized in lithium ion battery, *Ceram. Int.* 40 (2014) 7637–7641. doi:<http://dx.doi.org/10.1016/j.ceramint.2013.12.081>.
- [23] J. Liu, X. Liu, T. Huang, A. Yu, Synthesis of nano-sized  $\text{LiMnPO}_4$  and in situ carbon coating using a solvothermal method, *J. Power Sources.* 229 (2013) 203–209. doi:<http://dx.doi.org/10.1016/j.jpowsour.2012.11.093>.
- [24] Y. Dong, Y. Zhao, H. Duan, Z. Liang, Enhanced electrochemical performance of  $\text{LiMnPO}_4$  by  $\text{Li}^+$ -conductive  $\text{Li}_3\text{VO}_4$  surface coatings, *Electrochim. Acta.* 132 (2014) 244–250. doi:<http://dx.doi.org/10.1016/j.electacta.2014.03.171>.
- [25] Q. Zhu, S. Zheng, X. Lu, Y. Wan, Q. Chen, J. Yang, L. Zhang, Z. Lu, Improved cycle performance of  $\text{LiMn}_2\text{O}_4$  cathode material for aqueous rechargeable lithium battery by  $\text{LaF}_3$  coating, *J. Alloys Compd.* 654 (2016) 384–391. doi:[10.1016/j.jallcom.2015.09.085](http://dx.doi.org/10.1016/j.jallcom.2015.09.085).
- [26] L. Wu, S. Zhong, J. Lu, J. Liu, F. Lv, Synthesis of Cr-doped  $\text{LiMnPO}_4/\text{C}$  cathode materials by sol–gel combined ball milling method and its electrochemical properties, *Ionics (Kiel)*. 19 (2013) 1061–1065. doi:[10.1007/s11581-013-0919-9](http://dx.doi.org/10.1007/s11581-013-0919-9).
- [27] C. Hu, H. Yi, H. Fang, B. Yang, Y. Yao, W. Ma, Y. Dai., Mg Doping of  $\text{LiFePO}_4$  by co-Precipitation for Lithium Ion Batteries, *Int. J. Electrochem. Sci.* 5 (2010) 1457–1463.
- [28] Y. Fu, H. Jiang, Y. Hu, Y. Dai, L. Zhang, C. Li, Synergistic Enhancement Effect of Al Doping and Highly Active Facets of  $\text{LiMn}_2\text{O}_4$  Cathode Materials for Lithium-Ion Batteries, *Ind. Eng. Chem. Res.* (2015) 150407111022001. doi:[10.1021/ie504659h](http://dx.doi.org/10.1021/ie504659h).
- [29] Y. Zhang, Y. Zhao, L. Deng, Enhanced electrochemical properties of  $\text{LiMnPO}_4/\text{C}$  via doping with Cu, (2012) 573–578. doi:[10.1007/s11581-011-0655-y](http://dx.doi.org/10.1007/s11581-011-0655-y).

- [30] Z. Kai, W. Yang, Z. Shuang, Y. Yan, P. Hao, L. Guiwei, Synthesis of Single Crystalline Spinel  $\text{LiMn}_2\text{O}_4$  Nanorods for a Lithium Ion Battery, *Int. J. Electrochem. Sci.* 9 (2014) 5280–5288.
- [31] H. Zhao, F. Li, X. Liu, W. Xiong, B. Chen, H. Shao, D. Que, Z. Zhang, A simple, low-cost and eco-friendly approach to synthesize single-crystalline  $\text{LiMn}_2\text{O}_4$  nanorods with high electrochemical performance for lithium-ion batteries, *Electrochim. Acta.* 166 (2015) 124–133. doi:10.1016/j.electacta.2015.03.040.
- [32] X. Hu, X. Sun, M. Yang, H. Ji, X. Li, S. Cai, R. Guo, F. Hou, C. Zheng, Sandwich nanostructured  $\text{LiMnPO}_4/\text{C}$  as enhanced cathode materials for lithium-ion batteries, *J. Mater. Sci.* 52 (2017) 3597–3612. doi:10.1007/s10853-016-0417-3.
- [33] N.H. Kwon, K.M. Fromm, Enhanced electrochemical performance of thin  $\text{LiMnPO}_4$  nanorods with a reduced amount of carbon as a cathode for lithium ion batteries, *Electrochim. Acta.* 69 (2012) 38–44. doi:http://dx.doi.org/10.1016/j.electacta.2012.02.040.
- [34] M.S. Michael, A.R. Kulkarni, S.R.S. Prabaharan, Design of Monolayer Porous Carbon-Embedded Hybrid- $\text{LiMnPO}_4$  for High Energy Density Li-Ion Capacitors, *J. Nanosci. Nanotechnol.* 16 (2016) 7314–7324. doi:10.1166/jnn.2016.12081.
- [35] D.H. Wang, H.P. Jakobson, R. Kou, J. Tang, R.Z. Fineman, D.H. Yu, Y. Yu., Metal and semiconductor nanowire network thin films with hierarchical pore structures, *Chem. Mater.* 18 (2006) 4231–4237. Doi: 10.1021/Cm052216b.
- [36] Y.J. Wei, L.Y. Yan, C.Z. Wang, X.G. Xu, F. Wu, G. Chen, Effects of Ni Doping on [  $\text{MnO}_6$  ] Octahedron in  $\text{LiMn}_2\text{O}_4$ , *J. Phys. Chem. B.* 108 (2004) 18547–18551. doi:10.1021/jp0479522.

- [37] X.X. Dong, C.Y. Huang, Q. Jin, J. Zhou, P. Feng, F.Y. Shi, D. Y. Zhang., Enhancing the rate performance of spherical  $\text{LiFeBO}_3/\text{C}$  via Cr doping, *RSC Adv.* 7 (2017) 33745–33750. doi:10.1039/C7RA03028B.
- [38] X. Yang, F. Qu, H. Niu, Q. Wang, J. Yan, Z. Fan, High-performance aqueous asymmetric supercapacitor based on spinel  $\text{LiMn}_2\text{O}_4$  and nitrogen-doped graphene / porous carbon composite, *Electrochim. Acta.* 180 (2015) 287–294. doi:10.1016/j.electacta.2015.08.128.
- [39] R. Pitchai, V. Thavasi, S.G. Mhaisalkar, S. Ramakrishna, Nanostructured cathode materials: a key for better performance in Li-ion batteries, *J. Mater. Chem.* 21 (2011) 11040–11051. doi:10.1039/c1jm10857c.
- [40] V. Lakshmi, Y. Chen, A.A. Mikhaylov, A.G. Medvedev, I. Sultana, M.M. Rahman, O. Lev, P.V. Prikhodchenko, A.M. Glushenkov, Nanocrystalline  $\text{SnS}_2$  coated onto reduced graphene oxide: demonstrating the feasibility of a non-graphitic anode with sulfide chemistry for potassium-ion batteries, *Chem. Commun.* (2017). doi:10.1039/C7CC03998K.
- [41] J. Zong, X. Liu, Graphene nanoplates structured  $\text{LiMnPO}_4/\text{C}$  composite for lithium-ion battery, *Electrochim. Acta.* 116 (2014) 9–18. doi:10.1016/j.electacta.2013.10.176.
- [42] Y. Shao, M.F. El-Kady, L.J. Wang, Q. Zhang, Y. Li, H. Wang, M.F. Mousavi, R.B. Kane., Graphene-based materials for flexible supercapacitors, *Chem. Soc. Rev.* 44 (2015) 3639–3665. doi:10.1039/C4CS00316K.
- [43] J. Zong, X. Liu, Graphene nanoplates structured  $\text{LiMnPO}_4/\text{C}$  composite for lithium-ion battery, *Electrochim. Acta.* 116 (2014) 9–18. doi:10.1016/j.electacta.2013.10.176.



[44] H.-C. Tao, S.-C. Zhu, X.-L. Yang, L.-L. Zhang, S.-B. Ni, Systematic investigation of reduced graphene oxide foams for high-performance supercapacitors, *Electrochim. Acta.* 190 (2016) 168–177. doi:10.1016/j.electacta.2015.12.179.

[45] C. Lu, X. Wang, X. Zhang, H. Peng, Y. Zhang, G. Wang, G. Cao, N. Umirov, Z. Bakenov., Effect of graphene nanosheets on electrochemical performance of  $\text{Li}_4\text{Ti}_5\text{O}_{12}$  in lithium-ion capacitors, *Ceram. Int.* 43 (2017) 6554–6562.  
doi:10.1016/j.ceramint.2017.02.083.

[46] S.K. Kaverlavani, S.E. Moosavifard, A. Bakouei, Designing graphene-wrapped nanoporous  $\text{CuCo}_2\text{O}_4$  hollow spheres electrodes for high-performance asymmetric supercapacitors, *J. Mater. Chem. A.* 5 (2017) 14301–14309. doi:10.1039/C7TA03943C.





# CHAPTER TWO

## 2 Literature review

### **Lithiated manganese-based nanostructured electrode materials for high Energy density lithium ion capacitors**



*Overview*

*This chapter focuses on Li-ion capacitors specifically its positive electrode materials, their advantages, limitations and some of the paths that can be used to improve their shortcomings for better electrochemical performance.*

UNIVERSITY of the  
WESTERN CAPE

## 2.1 Introduction

The increasing reliance on new alternative forms of energy (e.g. solar and wind) means energy storage devices play a huge role in improving the utilization of this energy forms and boosting their storage efficiency. The Ragone plots shown on **Fig 2.1** illustrate the various comparisons within the energy system. Lithium ion batteries have high energy density and lower power density, while supercapacitors have high power density and lower energy density [1–3]. Hybrid capacitor devices are attracting much interest, due to improved energy and power density with adequate cycling stability.

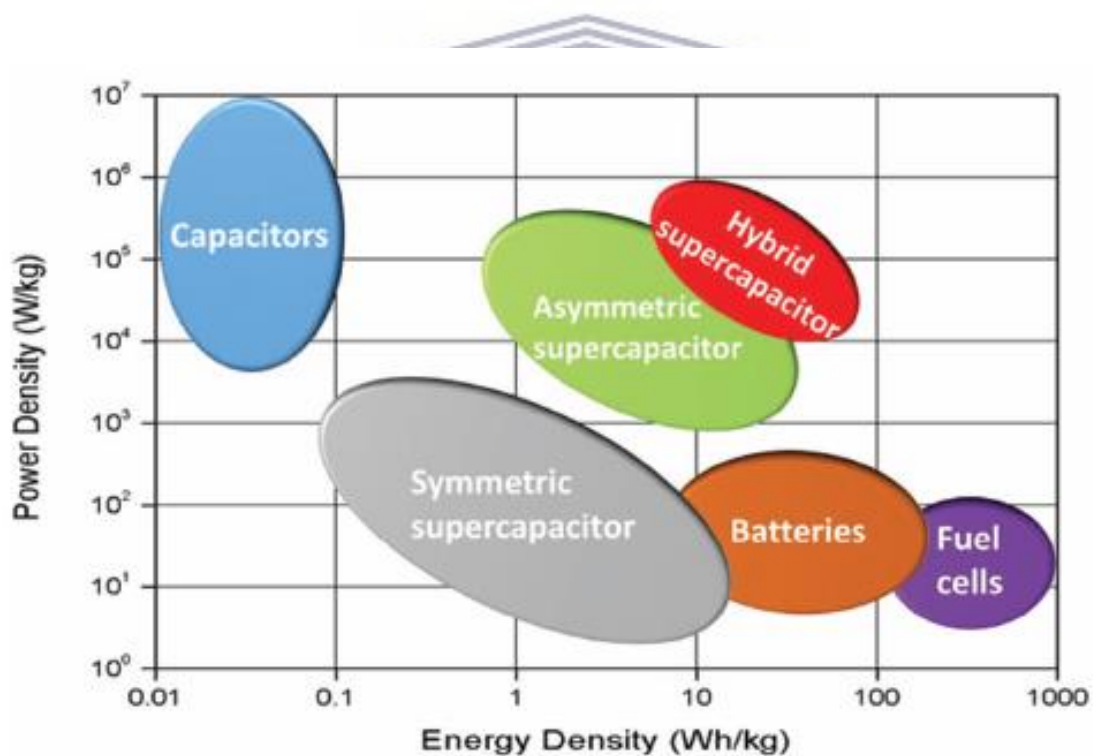


**Figure 2.1:** Ragone plot- comparison of performance of different energy storage devices [4]

## 2.2 Electrochemical capacitors within energy storage systems

Electrochemical capacitors also known as supercapacitors divided into three different groups according to the charge storage mechanisms; (i) electric double layer capacitors (EDLC), (ii) pseudocapacitors and (iii) hybrid capacitors. EDLCs store energy physically by the reversible adsorption of electrolyte ions on the surface of the active materials, thereby storing charge electrostatically with no Faradaic (redox) process involved [5–9].

Typically, EDLC cells comprise of two carbon based electrodes with a separator between them which is soaked in an electrolyte to prevent electrical contact between electrodes. High specific-surface area ( $> 1000 \text{ m}^2\text{g}^{-1}$ ) [10] nanoporous materials are considered as active materials for EDLCs. The energy storage mechanism for EDLCs was first defined by Helmholtz in 1879 and later refined by Stern and Geary. The capacitance is directly proportional to area of the electrodes and inversely proportional to the separation distance.

$$C = \frac{A\epsilon}{d} \quad (1)$$

Where  $A$  corresponds to the electrochemically active surface area of the electrode material,  $\epsilon$  is a dielectric constant of the vacuum. The capacitance of EDLC on carbon surface is in the range of 5 to 20  $\mu\text{Fcm}^{-2}$  depending on the electrolyte [11]. To increase capacitance, high surface area materials need to be employed and minimal magnitude of charge separation ( $d$ ) down to few Angstroms. Activated carbon (AC) is a commercially available EDLC electrode, which provides a cell voltage up to 2.7 V in organic electrolyte with high power density (up to  $10^8 \text{ W kg}^{-1}$ ) and good cycle life. However, the energy density still remains a challenge [12-14]. The lower energy density is due to low capacitance and high ionic resistance of the AC electrode

[15-16]. Research on EDLC electrode materials is now focused on novel materials like heteroatom doped carbon materials, conducting polymers and nano metal oxides to improve on the disadvantages.

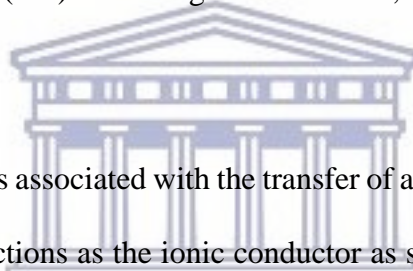
Pseudocapacitors (PCs) are based on Faradaic charge storage mechanism as a result of reversible reactions between the electrolyte and electrode surface. Pseudocapacitors utilize fast redox reaction [17-18]. Usually, materials such as conducting polymers, transition metal oxides, hydroxides, carbides and nitrides [19–23]. PC electrode materials can be differentiated from battery type materials through electroanalytical experiments, with their kinetics being limited by a surface-related process as opposed to diffusion controlled reactions governing the electrochemical response of battery electrodes [10]. They suffer from capacity fading due to very unstable cyclic performance over a few number of cycles but PCs based on transition metal oxide (TMO) electrode have a high reported capacitance between 300-1000 F g<sup>-1</sup> [17,18]. Pseudocapacitors based on symmetric configuration of two metal oxides can deliver specific energy density between 5-10 Wh kg<sup>-1</sup>. Asymmetric configuration can increase the specific energy, where two different types of electrode materials are used; one behaving like an electrochemical capacitor and the other performing like a battery, which leads us to hybrid capacitor which is the subject of this study.

Hybrid capacitors also known as lithium-ion capacitors (LICs) are combination of two electrode materials with one that stores charge electrostatically, and the other storing charge Faradaically. LICs are fabricated to bridge the gap between the tradition high energy Li-ion batteries and high power supercapacitors and combine the prime advantages to a single device [19].

## 2.3 Lithium-ion capacitor materials for high power and energy density

### 2.3.1 The mechanism of the hybrid capacitor

Hybrid capacitors or lithium ion capacitor integrate both the energy storage mechanisms of battery type and capacitive type electrode materials in an electrolyte containing Li ions. Charge storage mechanism in the Li-ion capacitors occurs by the formation of electrical double layer at the capacitive electrode and ion intercalation/de-intercalation at the battery type electrode [11,18,20]. Most LICs use the cathode materials of a lithium-ion battery (LIB) as positive electrode and activated carbon (AC) as the negative electrode, or vice versa [21].



The charge/discharge process is associated with the transfer of a Li ion between two electrodes, and the electrolyte mainly functions as the ionic conductor as seen in **Fig. 2.2**. LICs concepts were first introduced or proposed by Amatucci *et al.* when they produced a 2.8 V hybrid capacitors involving  $\text{Li}_4\text{Ti}_5\text{O}_{12}$  (LTO) [22]. Ohzuku *et al.* discovered  $\text{Li}_4\text{Ti}_5\text{O}_{12}$  as an excellent Li intercalating spinel anode material for Li-ion battery application owing to its zero-strain properties. It exhibits a specific capacity of  $>150 \text{ mA hg}^{-1}$  with high rate capability [23].

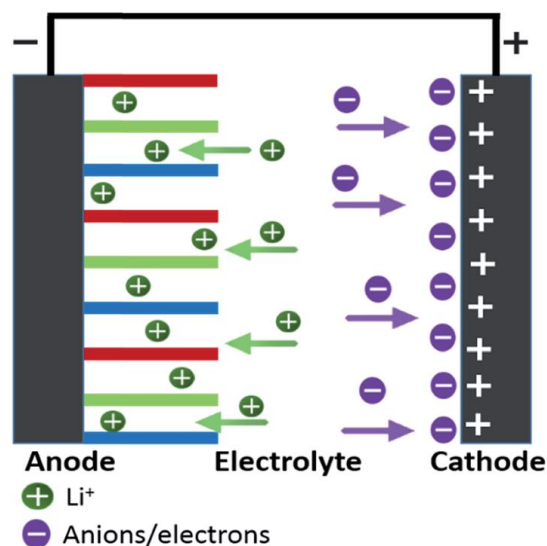


**Figure 2.2:** Mechanism of working lithium ion capacitor [5]

Lithium ion capacitors can operate on both aqueous and non-aqueous electrolytes. LICs using organic electrolytes have been well established and can operate at a maximum voltage of 3 – 4 V which leads to improved specific power [24]. However, the development of organic electrolyte application in electric vehicles and large scale power storage is affected by environmental concern. Aqueous electrolyte offers easy assembly processes in such way that there is no need for inert atmosphere, it is environmentally and user friendly, with higher conductivity leading to better power performance [25]. Therefore LICs utilising aqueous electrolyte should be of interest for development energy storage devices.

### 2.3.2 Principles, requirements and limitations

As already mentioned above the role of battery type (faradaic) electrode is to insert/de-insert Li ions while the function of capacitor type electrode (non-faradaic) is to adsorb/de-adsorb ions. These mechanisms occur reversibly in different ranges. The energy stored in a capacitor is related to the charge at each interface and the potential difference between two plates (+ve

and –ve). The following equations (2 and 3) can be used to determine the energy and power densities of the full cell (hybrid systems).

$$Power = \frac{V^2}{4R} \quad (2)$$

$$Energy = \frac{CV^2}{2} \quad (3)$$

Where  $V$  is the operating voltage,  $R$  is the equivalent series resistance (ESR) and  $C$  is the capacitance. Operating voltage play huge role in both energy and power as it has direct relationship. The Electrochemical performance of LICs is greatly enhanced by optimizing the voltage window. The use of high working voltage is crucial in order to increase the storable amount of energy. To achieve this, it is very essential to first do three electrode experiment for each electrode to determine the working voltage window and perform mass balancing. Li-ion capacitors can make full use of different potential windows of the two electrodes to provide a maximum operating voltage of the full cell as shown in **Fig.2.3**. The voltage split is dependent on the capacitance which is related to the mass and specific capacitance of the active material in each electrode in lithium ion capacitors [28,29]. The mass balancing is required to split the voltage equally between the two electrode using the following relationship:  $q_+ = q_-$ , where  $q_+$  stand for the charges stored at the positive electrode and  $q_-$  for the charges stored at the negative electrode. The equations are as follows for the charge stored.

$$q = C_{sp}.m.\Delta E \quad (4)$$

Or

$$\frac{m_+}{m_-} = \frac{C_{sp-} \times \Delta E_-}{C_{sp+} \times \Delta E_+} \quad (5)$$

Where  $m$  is the mass,  $C_{sp}$  is the specific capacitance,  $\Delta E$  is potential window received from charge/discharge profile of the three electrode configuration of the negative and positive electrode respectively. In general, the capacitance and stored energy essentially depend on the electrode material used. The two electrode used in LICs are in contact with the current collector (nickel foam as employed in this work) and separated by a porous separator in an electrolyte solution. The other important factors in improving LICs performance are specific capacitance ( $C_{sp}$ ) and equivalent series resistance, which are controlled by pore size distribution, specific surface area and conductivity of the electrode material [15,26,27]. The contact resistance between current collector and electrolyte also plays a crucial role in improving energy and power density of LICs.

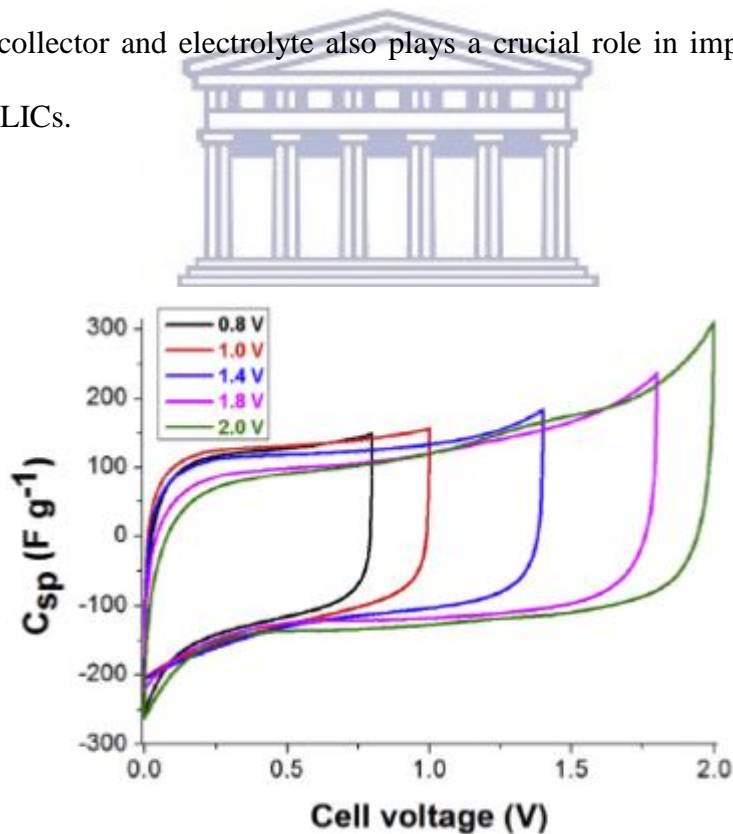
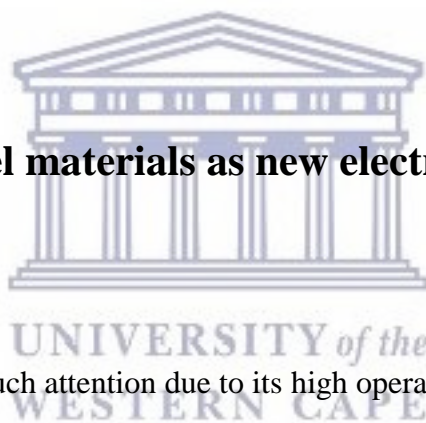


**Figure 2.3:** Cyclic voltammetry curves with increasing potential window [27].



The imbalance in the power capability and charge storage capacitance between the two electrode used is one of the difficulties which faces developing a high performance LICs. The biggest challenge associated with Li intercalation cathode is to restrain the cycling-induced electrode degradation, especially at high rates to match the high power characteristic of anode carbon based materials. The difficulties facing the carbon based anode is the lower capacity (30-35 mA hg<sup>-1</sup>) compared with the cathodes which further reduce the energy density [30]. This work focuses on doping both spinel and olivine manganese-based materials with nickel and coating with graphene in lithium ion capacitor with activated carbon as the negative electrode. The effect of coating as well as doping on the enhancement of electrochemical activity of spinel and olivine is reported [5,31–33].

## 2.4 Olivine and spinel materials as new electrode for Li-ion capacitors



LiMnPO<sub>4</sub> cathode received much attention due to its high operating voltage ~4.1 V vs. Li and capable of delivering a maximum energy density of ~700 Wh kg<sup>-1</sup>, which is higher than the commercialised cathodes, LiCoO<sub>2</sub> (518 Wh kg<sup>-1</sup>), LiMn<sub>2</sub>O<sub>4</sub> (400 Wh kg<sup>-1</sup>) and LiFePO<sub>4</sub> (495 Wh kg<sup>-1</sup>) [34–38]. Olivines compounds have been extensively studied as positive electrodes in lithium ion batteries and have proven to offer a lot of advantages due to their low-cost, non-toxicity, outstanding thermal stability [39–41]. In a LiMnPO<sub>4</sub> olivine structure Mn and Li occupy octahedral 4c and 4a sites, and P atom in 4c site, respectively, the O atoms are in a hexagonal close-packed arrangement and MnO<sub>6</sub> octahedral are separated by PO<sub>4</sub> polyanion [42]. LiMnPO<sub>4</sub> has all oxygen ions forming strong covalent bonds with P<sup>5+</sup> to form PO<sub>4</sub><sup>3-</sup> polyanion in the tetrahedra and this stabilizes the entire three dimensional frameworks as shown in **Fig. 2.4** [43–47]. This gives olivine cathode materials an advantage to work under

abusive conditions but still maintain safety due to their improved stability. The higher operating voltage of  $\text{LiMnPO}_4$  is 4.1 V which lies in the stability window of the common non-aqueous electrolyte and theoretical capacity of  $\leq 170 \text{ mA hg}^{-1}$  [48–50].

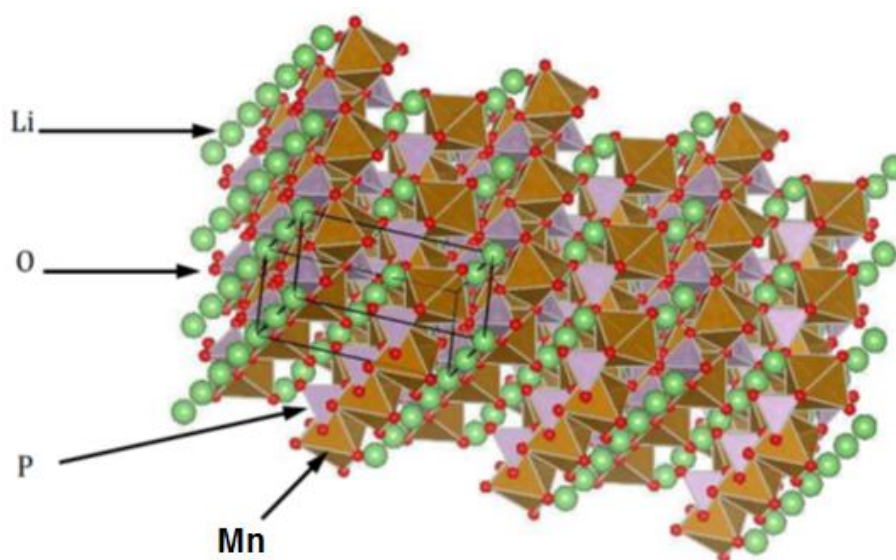


**Figure 2.4:** Structure of the  $\text{LiMnPO}_4$  [43]



$\text{LiMn}_2\text{O}_4$  with a spinel structure is one of the most promising cathodes of lithium ion battery. They are inexpensive, safe and produce theoretical energy of  $400 \text{ Wh kg}^{-1}$ . Spinel  $\text{LiMn}_2\text{O}_4$  has good structural stability with the lattice containing cubic close-packed oxygen ion with the distribution of the cations among the available octahedral and tetrahedral sites [51–54]. The Mn cations occupy half of the octahedral interstitial sites and Li cations occupy one eighth of the tetrahedral sites. The interstitial space in the  $[\text{Mn}_2]\text{O}_4$  framework represents a diamond type network of tetrahedral surrounding octahedral sites, sharing edges and faces in order to form 3D diffusion pathways for  $\text{Li}^+$  ions diffusion as shown in **Fig 2.5** [1,43,55,56]. The discharge occurs mainly in two steps, one around 4 V and the other around 3 V with capacity limited to  $\leq 120 \text{ mA hg}^{-1}$  [36,57–60]. Usually only the 4 V plateau is used, so that the cell is constructed

in the discharged state and must be charged before use. The cubic symmetry of the structure does not experience any change during cycling and with a minimal contraction of the unit cell over a wide ranges of compositions hence proving the structure stability.

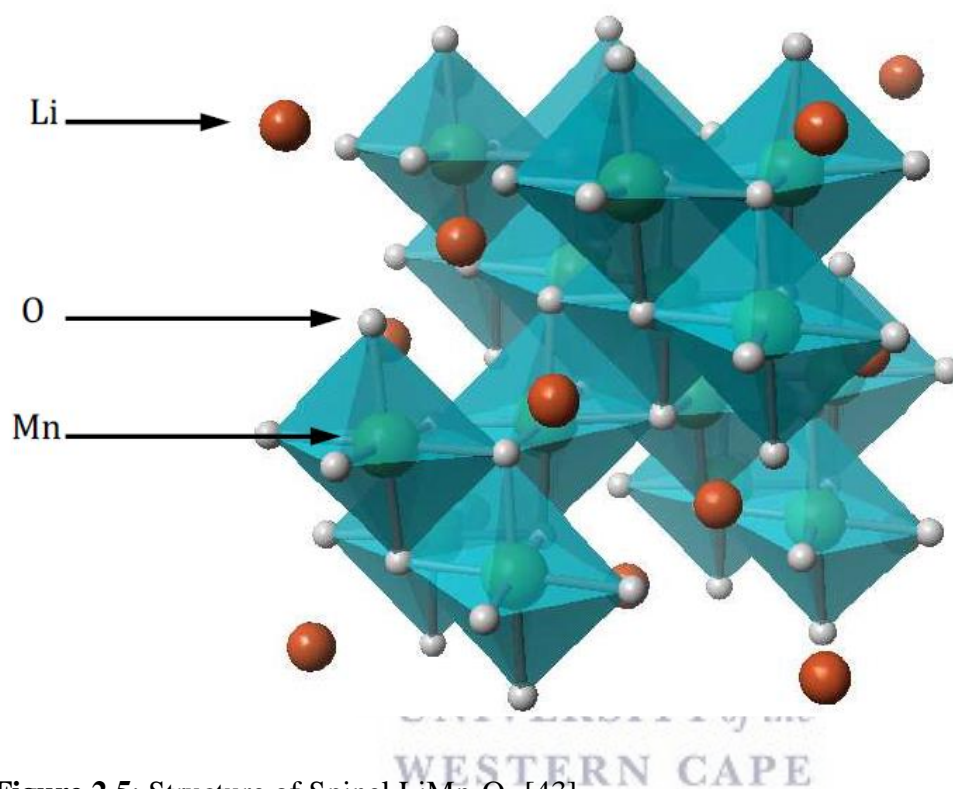
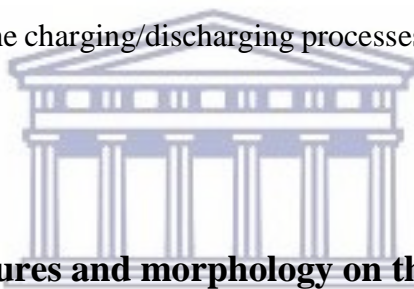


**Figure 2.5:** Structure of Spinel  $\text{LiMn}_2\text{O}_4$  [43]

Several studies have been conducted on lithium-based electrodes for the use to ascertain their usefulness in LICs. Wang *et al* did different experiments using other lithium-based positive electrode [61]. Various works on lithium ion capacitors have been reported with encouraging results, lithium metal phosphates or spinel oxides have been investigated as promising electrodes, mainly  $\text{LiFePO}_4$ ,  $\text{LiMnPO}_4$  and spinel  $\text{LiMn}_2\text{O}_4$  have also been studied in this field.. Yang *et al* reported  $\text{LiMn}_2\text{O}_4$  || nitrogen-doped graphene/porous carbon composite with specific energy of up to  $44.3 \text{ Wh kg}^{-1}$  at specific power of  $595 \text{ W kg}^{-1}$  with an output voltage of 1.8 V in aqueous 0.5  $\text{Li}_2\text{SO}_4$  electrolyte [62]. Yen-Po Lin and Nae-Lih Wu prepared

LiMn<sub>2</sub>O<sub>4</sub>||MnFe<sub>2</sub>O<sub>4</sub> cell under maximum operating voltage window of 1.3 V, exhibiting specific energy of 5.5 Wh kg<sup>-1</sup> and power density of 1.8 kW kg<sup>-1</sup> using aqueous LiNO<sub>3</sub> electrolyte. Pazhamalai and co-workers fabricated asymmetric LiMn<sub>2</sub>O<sub>4</sub>||graphene LIC which delivered high specific energy of 30.96 Wh kg<sup>-1</sup> at power density of 440 W kg<sup>-1</sup> using aqueous 1 M Li<sub>2</sub>SO<sub>4</sub> electrolyte with the operating voltage of 2.2 V [63]. Although LiMn<sub>2</sub>O<sub>4</sub> shows lots of promise, it suffers severe capacity fading during cycling which is mainly due to the occurrence of Jahn–Teller distortion, caused by Mn<sup>3+</sup> which led to the degraded cyclability during Li<sup>+</sup> diffusion process [56,64–66]. The olivine LiMnPO<sub>4</sub> also has intrinsically poor electronic and ionic conductivity govern by Jahn-Teller distortion caused by unstable Mn<sup>3+</sup> which arise from mechanical stress in the lattice and large volumetric change between LiMnPO<sub>4</sub> and MnPO<sub>4</sub> during the charging/discharging processes which leads to lower capacity [44,67–69].



#### **2.4.1 Role of nanostructures and morphology on the electrode material**

There are several potential advantages of forming cathode nanostructures in lithium ion battery such as: significant increase in the rate of lithium insertion/removal due to the reduced dimensions of nanomaterials; enhancement in the rate capacity as well as the cycle life [70]. Electron transport is also enhanced by nanometres-sized particles; the high surface area of nanosized species allow active material to absorb lithium ions more effectively thus leading to increased capacity with decrease in size; the chemical potentials for lithium ions and electrons may be modified resulting in a change of electrode potential (thermodynamics of the reaction) [71]. Nanomaterials provide new reactions which are not possible with bulk materials. Nanoparticles of different cathode materials can have higher electrode/electrolyte contact area leading to higher charge/discharge rates.

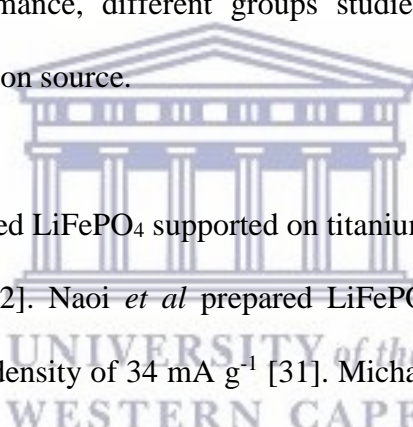
Paraharan *et al* synthesized nano-composite olivine  $\text{LiMnPO}_4$  using a solvothermal route for LMP || AC LICs and obtained a specific energy of  $16.5 \text{ Wh kg}^{-1}$  and power density of  $2.5 \text{ kW kg}^{-1}$  at a potential window of 2 V using aqueous 1 M  $\text{Li}_2\text{SO}_4$  electrolyte [72]. Li and co-workers synthesized  $\text{LiMn}_2\text{O}_4$  microspheres LICs LMO || AC using simple green process which showed the specific energy of  $26 \text{ Wh kg}^{-1}$  and power density of  $50 \text{ W kg}^{-1}$  with an organic electrolyte at voltage of (0.2-3V) [73]. For the purpose of this study nanoparticles and nanorods structures are synthesized using solvothermal route.

#### **2.4.2 Effect of doping on the pristine material**

Doping is the addition of quantities of an element of a semiconductor for modulating the electrical properties of the material being modified or to change its characteristics. Lightly doped semiconductors are referred to as extrinsic, while semiconductors doped to such high levels that act more like a conductor than a semiconductor is called a degenerate [74]. Doping can also be referred to as the activation of a particular material. Doping helps to reduce manganese dissolution and Jahn-Teller distortion experienced by manganese cathode materials. It enhances the conductivity, maintains and enhances the capacity of active materials, as well as enhance the power and energy density [75]. Many researchers have modified the surface of manganese-based cathode materials by using different doping modes. Xia *et al* prepared boron and nitrogen dual doped 3D porous carbon nanofibers. This LIC materials delivering specific energy of  $104 \text{ Wh kg}^{-1}$  and power density of  $22.5 \text{ kW kg}^{-1}$  [76]. In this work, nickel was used to dope the spinel  $\text{LiMn}_2\text{O}_4$  and olivine  $\text{LiMnPO}_4$  to further improve the electrochemical performance.

### 2.4.3 Carbon coating

Electrochemical reactions mainly occur at the electrode-electrolyte interface, hence control of the interfaces via coating can decrease the interface side-reactions with the electrolyte and improve the Li-ion diffusivity which therefore enhance the energy and power density of cathode material. The surface coating may also improve the electrochemical performance of manganese-based material (e.g. decrease the dissolution of  $\text{Mn}^{2+}$  and enhance the transportation of the lithium ions in  $\text{LiMn}_2\text{O}_4$  and  $\text{LiMnPO}_4$  cathode material) [76,77]. Carbon coating is essential for high rate manganese-based cathode materials and the quality of carbon coating has a great impact on the lithium ion cathode material. Carbon coating improves the conductivity and rate performance, different groups studied manganese-based materials synthesized with different carbon source.



Xie *et al* prepared carbon-coated  $\text{LiFePO}_4$  supported on titanium nitride obtaining  $972 \text{ F g}^{-1}$  at current density of  $1 \text{ A g}^{-1}$  [32]. Naoi *et al* prepared  $\text{LiFePO}_4$ /graphitic carbon composite displaying  $41 \text{ F g}^{-1}$  at current density of  $34 \text{ mA g}^{-1}$  [31]. Michael and co-workers synthesized  $\text{LiMnPO}_4$  coated with carbon monolayer attaining capacitance of  $622 \text{ F g}^{-1}$ , energy density of  $28.8 \text{ Wh kg}^{-1}$  with specific maximum power of  $3.3 \text{ kW kg}^{-1}$  [33]. Graphene was used to enhance the performance of olivine and spinel materials forming nanocomposite in this study.

Graphene has been used in many research fields especially in the energy storage field because of its exceptionally superior properties. It is a one-atom thick sheet made of  $\text{sp}^2$  bonded carbon atoms in a polyaromatic honeycomb crystal lattice [10]. It offers useful platform for the development of high capacitive hybrid energy storage devices due to its thin monolayer structure, with experimental specific surface area of  $1500 \text{ m}^2 \text{ g}^{-1}$ , high electrical conductivity of  $106 \text{ S cm}^{-1}$ , as well as good flexibility and tuneable structure, good chemical and thermal

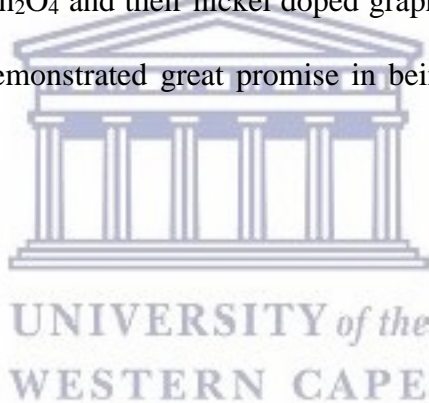


stability and wide potential window [19,78]. Graphene generally exhibit theoretical specific capacity of  $744 \text{ mA h g}^{-1}$  and specific capacitance of  $550 \text{ F g}^{-1}$  with high surface-volume ratio which makes it an ideal material for faster transportation of ionic species and electric charges in LIBs, supercapacitors and LICs [5]. Graphene is synthesized by different methods such as mechanical exfoliation of graphite, chemical vapour deposition (CVD), unzipping of carbon nanotubes, also through reduction of graphene oxide etc. The chemical method via reduction of graphene oxide is considered a scalable approach to synthesizing graphene and has been widely utilized to synthesize chemically derived graphene also known as reduced graphene oxide (rGO).

Lithium ion capacitors based on the use of graphene materials are reported to achieve enhanced performance, by displaying high energy and power density as well as rapid charging and discharging over a large number of cycles. Zhang *et al* synthesized nano-composite  $\text{Fe}_3\text{O}_4$ -graphene for LICs and displayed a specific energy of  $60.5 \text{ Wh kg}^{-1}$  at power density of  $45.4 \text{ kW kg}^{-1}$  at a potential window of  $1 - 4 \text{ V}$  [79]. Lu and co-workers prepared  $\text{Li}_4\text{Ti}_5\text{O}_{12}$ /graphene nanosheets composite utilized for LICs obtaining specific energy of  $14 \text{ Wh kg}^{-1}$  and power density of  $2.7 \text{ kW kg}^{-1}$  at voltage of  $1 - 2.5 \text{ V}$  [80]. Wang *et al* designed  $\text{MoS}_2$ -graphene for LICs and displaying a specific energy of  $45.3 \text{ Wh kg}^{-1}$  at power density of  $40 \text{ kW kg}^{-1}$  at a potential window of  $1 - 4.2 \text{ V}$  [81]. Kamari *et al* synthesized graphene-wrapped nanoporous  $\text{CuCo}_2\text{O}_4$  for LICs obtaining a specific energy of  $45.2 \text{ Wh kg}^{-1}$  at power density of  $15 \text{ kW kg}^{-1}$  at a potential window of  $0 - 1.6 \text{ V}$  [82].

## 2.5 Summary

The full potential of hybrid lithium ion capacitors electrodes materials have not been realized yet. Lithium ion capacitors are the only energy storage system which offers both high energy and power density in comparison with other energy storage devices like lithium ion batteries, supercapacitors, etc. In order to achieve high performance energy storage devices using LICs, a good understanding of surface chemistry between capacitors and battery components is important and crucial to improve the interfacial interactions and fabrication of uniform structures to enhance charge transfer. In this work, using activated carbon as negative electrode offered high thermal and physical stability, tuneable porous structure and high surface area. Olivine  $\text{LiMnPO}_4$ , spinel  $\text{LiMn}_2\text{O}_4$  and their nickel doped graphene derivatives were applied as positive electrode. They demonstrated great promise in being used as high performance energy storage devices.





## 2.6 References

- [1] I. Plitz, A. DuPasquier, F. Badway, J. Gural, N. Pereira, A. Gmitter, G.G. Amatucci, The design of alternative nonaqueous high power chemistries, *Appl. Phys. A.* 82 (2006) 615–626. doi:10.1007/s00339-005-3420-0.
- [2] P.R. Kumar, M. Venkateswarlu, M. Misra, A.K. Mohanty, N. Satyanarayana, Enhanced conductivity and electrical relaxation studies of carbon-coated LiMnPO<sub>4</sub> nanorods, *Ionics (Kiel)*. 19 (2012) 461–469. doi:10.1007/s11581-012-0778-9.
- [3] B. Scrosati, J. Garche, Lithium batteries: Status, prospects and future, *J. Power Sources*. 195 (2010) 2419–2430. doi:http://dx.doi.org/10.1016/j.jpowsour.2009.11.048.
- [4] N. Choudhary, C. Li, J. Moore, N. Nagaiah, L. Zhai, Y. Jung, J. Thomas., Asymmetric Supercapacitor Electrodes and Devices, *Adv. Mater.* 29 (2017) 1605336. doi:10.1002/adma.201605336.
- [5] S.W. Bokhari, A.H. Siddique, H. Pan, Y. Li, M. Imtiaz, Z. Chen, S.M. Zhu, D. Zhang., Nitrogen doping in the carbon matrix for Li-ion hybrid supercapacitors: state of the art, challenges and future prospective, *RSC Adv.* 7 (2017) 18926–18936. doi:10.1039/C7RA02296D.
- [6] L. Li, Z.A. Hu, N. An, Y.Y. Yang, Z.M. Li, H.Y. Wu, Facile Synthesis of MnO<sub>2</sub>/CNTs Composite for Supercapacitor Electrodes with Long Cycle Stability, (2014).
- [7] Y. Hou, L. Chen, A. Hirata, T. Fujita, M. Chen, Non-aqueous nanoporous gold based supercapacitors with high specific energy, *Scr. Mater.* 116 (2016) 76–81. doi:10.1016/j.scriptamat.2016.01.016.

- [8] P. Xiong, J. Zhu, X. Wang, Recent advances on multi-component hybrid nanostructures for electrochemical capacitors, *J. Power Sources*. 294 (2015) 31–50. doi:<http://dx.doi.org/10.1016/j.jpowsour.2015.06.062>.
- [9] Y.-Q. Zhao, M. Lu, P.-Y. Tao, Y.-J. Zhang, X.-T. Gong, Z. Yang, G. Zhang, H. Li, Hierarchically porous and heteroatom doped carbon derived from tobacco rods for supercapacitors, *J. Power Sources*. 307 (2016) 391–400. doi:10.1016/j.jpowsour.2016.01.020.
- [10] A. González, E. Goikolea, J.A. Barrena, R. Mysyk, Review on supercapacitors: Technologies and materials, *Renew. Sustain. Energy Rev.* 58 (2016) 1189–1206. doi:10.1016/j.rser.2015.12.249.
- [11] P. Simon, A. Burke, Nanostructured carbons: Double-layer capacitance and more, *Electrochem. Soc. Interface*. 17 (2008) 38–43. doi:10.1016/j.carbon.2005.06.046.
- [12] X. Xiao, B. Han, G. Chen, L. Wang, Y. Wang, Preparation and electrochemical performances of carbon sphere @ ZnO core-shell nanocomposites for supercapacitor applications, *Nat. Publ. Gr.* (2017) 1–13. doi:10.1038/srep40167.
- [13] C. Chen, D. Yu, G. Zhao, L. Sun, Y. Sun, K. Leng, M. Yu, Y. Sun., Hierarchical porous graphitic carbon for high-performance supercapacitors at high temperature, *RSC Adv.* 7 (2017) 34488–34496. doi:10.1039/C7RA06234F.
- [14] K. Wang, S. Gao, Z. Du, A. Yuan, W. Lu, L. Chen, MnO<sub>2</sub> -Carbon nanotube composite for high-areal-density supercapacitors with high rate performance, *J. Power Sources*. 305 (2016) 30–36. doi:10.1016/j.jpowsour.2015.11.064.

- [15] R.Q. and M.S. Xiuhua Wang, Bo Shi, Yao Fang, Fang Rong, Feifei Huang, High capacitance and rate capability of a Ni<sub>3</sub>S<sub>2</sub>@CdS core–shell nanostructure supercapacitor, *J. Mater. Chem. A*. 5 (2017) 7165–7172. doi:10.1039/C7TA00593H.
- [16] K. Makgopa, P.M. Ejikeme, C.J. Jafta, K. Raju, M. Zeiger, V. Presser, K.I. Ozoemena., A high-rate aqueous symmetric pseudocapacitor based on highly graphitized onion-like carbon/birnessite-type manganese oxide nanohybrids, *J. Mater. Chem. A*. (2015).
- [17] Y. Shao, M.F. El-Kady, L.J. Wang, Q. Zhang, Y. Li, H. Wang, M.F. Mousavi, R.B. Kaner., Graphene-based materials for flexible supercapacitors, *Chem. Soc. Rev.* 44 (2015) 3639–3665. doi:10.1039/C4CS00316K.
- [18] P. Suktha, N. Phattharasupakun, P. Dittanet, M. Sawangphruk, Charge storage mechanisms of electrospun Mn<sub>3</sub>O<sub>4</sub> nanofibres for high-performance supercapacitors, *RSC Adv.* 7 (2017) 9958–9963. doi:10.1039/C6RA28499J.
- [19] X. Lu, M. Yu, G. Wang, Y. Tong, Y. Li, Flexible solid-state supercapacitors: design, fabrication and applications, *Energy Environ. Sci.* 7 (2014) 2160. doi:10.1039/c4ee00960f.
- [20] M. Kim, J. Kim, Development of high power and energy density microsphere silicon carbide–MnO<sub>2</sub> nanoneedles and thermally oxidized activated carbon asymmetric electrochemical supercapacitors, *Phys. Chem. Chem. Phys.* 16 (2014) 11323. doi:10.1039/c4cp01141d.
- [21] N. Xu, X. Sun, X. Zhang, K. Wang, Y. Ma, A two-step method for preparing Li<sub>4</sub>Ti<sub>5</sub>O<sub>12</sub>-graphene as an anode material for lithium-ion hybrid capacitors, *RSC Adv.* 5 (2015) 94361–94368. doi:10.1039/c5ra20168c.

- [22] G.G. Amatucci, F. Badway, J. Shelburne, a Gozdz, I. Plitz, a DuPasquier, S.G. Menocal., The nonaqueous asymmetric hybrid technology: Materials, electrochemical properties and performance in plastic cells, *Electrochem. Capacit. Hybrid Power Sources*. 2002 (2002) 140–152\|r422.
- [23] T. Ohzuku, A. Ueda, N. Yamamoto, Zero-Strain Insertion Material of Li  $[\text{Li}_{1/3}\text{Ti}_{5/3}]\text{O}_4$  for Rechargeable Lithium Cells, *J. Electrochem. Soc.* 142 (1995) 1431–1435.  
doi:10.1149/1.2048592.
- [24] J. Yan, Y. Sun, L. Jiang, Y. Tian, R. Xue, L. Hao, W. Liu, B. Yi., Electrochemical performance of lithium ion capacitors using aqueous electrolyte at high temperature, *J. Renew. Sustain. Energy*. 5 (2013). doi:10.1063/1.4798432.
- [25] J. Menzel, K. Fic, E. Frackowiak, Hybrid aqueous capacitors with improved energy/power performance, *Prog. Nat. Sci. Mater. Int.* 25 (2015) 642–649.  
doi:10.1016/j.pnsc.2015.12.001.
- [26] P. Chen, G. Shen, Y. Shi, H. Chen, C. Zhou, Preparation and Characterization of Flexible Asymmetric Supercapacitors, *ACS Nano*. 4 (2010) 4403–4411.
- [27] D.B. T. Cottineau, M. Toupin, T. Delahaye, T. Brousse, Nanostructured transition metal oxides for aqueous hybrid electrochemical supercapacitors, *Appl. Phys. A*. 606 (2006) 599–606. doi:10.1007/s00339-005-3401-3.
- [28] H. Xiao, Y. Wang, K. Xie, S. Cheng, X. Cheng, High capacitance  $\text{LiMn}_2\text{O}_4$  microspheres with different microstructures as cathode material for aqueous asymmetric supercapacitors, *J. Alloys Compd.* 738 (2018) 25–31. doi:10.1016/j.jallcom.2017.12.143.

- [29] K. Makgopa. Raju, P.M. Ejikeme, K.I. Ozoemena, High-performance  $Mn_3O_4$ /onion-like carbon (OLC) nanohybrid pseudocapacitor: Unravelling the intrinsic properties of OLC against other carbon supports, *Carbon N. Y.* 117 (2017) 20–32.  
doi:10.1016/j.carbon.2017.02.050.
- [30] F. Sun, J. Gao, Y. Zhu, X. Pi, L. Wang, X. Liu, Y. Qin., A high performance lithium ion capacitor achieved by the integration of a Sn-C anode and a biomass-derived microporous activated carbon cathode, *Nat. Publ. Gr.* 7 (2017) 40990. doi:10.1038/srep40990.
- [31] K. Naoi, K. Kisu, E. Iwama, S. Nakashima, Y. Sakai, Y. Orikasa, P. Leone, N. Dupre, T. Brousse, P. Simon, Ultrafast charge–discharge characteristics of a nanosized core–shell structured  $LiFePO_4$  material for hybrid supercapacitor applications, *Energy Environ. Sci.* 9 (2016) 2143–2151. doi:10.1039/C6EE00829A.
- [32] Y. Xie, F. Song, C. Xia, H. Du, Preparation of carbon-coated lithium iron phosphate/titanium nitride for a lithium-ion supercapacitor, *New J. Chem.* 39 (2015) 604–613. doi:10.1039/c4nj01169d.
- [33] M.S. Michael, A.R. Kulkarni, S.R.S. Prabaharan, Design of Monolayer Porous Carbon-Embedded Hybrid- $LiMnPO_4$  for High Energy Density Li-Ion Capacitors, *J. Nanosci. Nanotechnol.* 16 (2016) 7314–7324. doi:10.1166/jnn.2016.12081.
- [34] V. Aravindan, J. Gnanaraj, Y.-S. Lee, S. Madhavi,  $LiMnPO_4$  - A next generation cathode material for lithium-ion batteries, *J. Mater. Chem. A.* 1 (2013) 3518–3539.  
doi:10.1039/c2ta01393b.
- [35] Z. Qin, X. Zhou, Y. Xia, C. Tang, Z. Liu, Morphology controlled synthesis and modification of high-performance  $LiMnPO_4$  cathode materials for Li-ion batteries, *J. Mater. Chem.* 22 (2012) 21144–21153. doi:10.1039/c2jm30821e.

- [36] T.F. Yi, J. Mei, Y.R. Zhu, Key strategies for enhancing the cycling stability and rate capacity of  $\text{LiNi}_{0.5}\text{Mn}_{1.5}\text{O}_4$  as high-voltage cathode materials for high power lithium-ion batteries, *J. Power Sources*. 316 (2016) 85–105. doi:10.1016/j.jpowsour.2016.03.070.
- [37] A.K. Shukla, S. Venugopalan, B. Hariprakash, Nickel-based rechargeable batteries, *J. Power Sources*. 100 (2001) 125–148. doi:http://dx.doi.org/10.1016/S0378-7753(01)00890-4.
- [38] H.M. Wu, J.P. Tu, X.T. Chen, Y. Li, X.B. Zhao, G.S. Cao, Effects of Ni-ion doping on electrochemical characteristics of spinel  $\text{LiMn}_2\text{O}_4$  powders prepared by a spray-drying method, *J. Solid State Electrochem.* 11 (2007) 173–176. doi:10.1007/s10008-005-0082-y.
- [39] Y. Dong, Y. Zhao, H. Duan, Z. Liang, Enhanced electrochemical performance of  $\text{LiMnPO}_4$  by  $\text{Li}^+$ -conductive  $\text{Li}_3\text{VO}_4$  surface coatings, *Electrochim. Acta*. 132 (2014) 244–250. doi:http://dx.doi.org/10.1016/j.electacta.2014.03.171.
- [40] J. Duan, G. Hu, Y. Cao, K. Du, Z. Peng, Synthesis of high-performance  $\text{LiMnPO}_4/\text{C}/\text{rGO}$  composite via a mechanical-activation-assisted polyol process, *Ionics (Kiel)*. (2016). doi:10.1007/s11581-016-1682-5.
- [41] Q.-Y. Huang, Z. Wu, J. Su, Y.-F. Long, X.-Y. Lv, Y.-X. Wen, Synthesis and electrochemical performance of Ti–Fe co-doped  $\text{LiMnPO}_4/\text{C}$  as cathode material for lithium-ion batteries, *Ceram. Int.* 42 (2016) 11348–11354. doi:10.1016/j.ceramint.2016.04.057.
- [42] Z. Bakenov, I. Taniguchi,  $\text{LiMnPO}_4$  Olivine as a Cathode for Lithium Batteries, *Open Mater. Sci. J.* 5 (2011) 222–227. doi:10.2174/1874088X01105010222.
- [43] Timothy John Patey, Oxide Nanoparticles for Electrodes in Lithium-Ion Batteries, A Diss. Submitt. to ETH ZURICH Degree Dr. Sci. (2009). doi:10.1016/j.jpowsour.2010.11.014.

- [44] J. Moskon, M. Pivko, I. Jerman, E. Tchernychova, N.Z. Logar, M. Zorko, V.S. Selih, R. Dominko, M. Geberscek, Cycling stability and degradation mechanism of  $\text{LiMnPO}_4$  based electrodes, *J. Power Sources*. 303 (2016) 97–108. doi:10.1016/j.jpowsour.2015.10.094.
- [45] R. Pitchai, V. Thavasi, S.G. Mhaisalkar, S. Ramakrishna, Nanostructured cathode materials: a key for better performance in Li-ion batteries, *J. Mater. Chem.* 21 (2011) 11040–11051. doi:10.1039/c1jm10857c.
- [46] A. Yamada, M. Hosoya, S.-C. Chung, Y. Kudo, K. Hinokuma, K.-Y. Liu, Y. Nishi., Olivine-type cathodes: Achievements and problems, *J. Power Sources*. 119–121 (2003) 232–238. doi:http://dx.doi.org/10.1016/S0378-7753(03)00239-8.
- [47] G.M. Nolis, F. Omenya, R. Zhang, B. Fang, S. Upreti, N. a. Chernova, F. Wang, J. Graetz, Y. Hu, M.S. Whittingham, Structure, defects and thermal stability of delithiated olivine phosphates, *J. Mater. Chem.* 22 (2012) 20482. doi:10.1039/c2jm33183g.
- [48] J. Kim, H. Kim, K.-Y. Park, Y.-U. Park, S. Lee, H.-S. Kwon, H. Yoo, K. Kang, Alluaudite  $\text{LiMnPO}_4$ : a new Mn-based positive electrode for Li rechargeable batteries, *J. Mater. Chem. A*. 2 (2014) 8632–8636. doi:10.1039/c4ta00955j.
- [49] C. Wang, Y. Bi, Y. Liu, Y. Qin, Y. Fang, D. Wang, Investigation of  $(1 - x)\text{LiMnPO}_4 \cdot x\text{Li}_3\text{V}_2(\text{PO}_4)_3/\text{C}$ : Phase composition and electrochemical performance, *J. Power Sources*. 263 (2014) 332–337. doi:http://dx.doi.org/10.1016/j.jpowsour.2014.04.044.
- [50] M. Park, X. Zhang, M. Chung, G.B. Less, A.M. Sastry, A review of conduction phenomena in Li-ion batteries, *J. Power Sources*. 195 (2010) 7904–7929. doi:10.1016/j.jpowsour.2010.06.060.



- [51] B. Hwang, S. Kim, Y. Lee, B. Han, S. Kim, W. Kim, K. Park., Mesoporous Spinel  $\text{LiMn}_2\text{O}_4$  Nanomaterial as a Cathode for High-Performance Lithium Ion Batteries, *Int. J. Electrochem. Sci.* 8 (2013) 9449–9458.
- [52] B. Put, P.M. Vereecken, N. Labyedh, A. Sepulveda, C. Huyghebaert, I.P. Radu, A. Stesmans., High Cycling Stability and Extreme Rate Performance in Nanoscaled  $\text{LiMn}_2\text{O}_4$  Thin Films, *ACS Appl. Mater. Interfaces.* 7 (2015) 22413–22420.  
doi:10.1021/acsami.5b06386.
- [53] I.M. Hung, Y.C. Yang, H.J. Su, J. Zhang, Influences of the surfactant on the performance of nano- $\text{LiMn}_2\text{O}_4$  cathode material for lithium-ion battery, *Ceram. Int.* 41 (2015) S779–S786. doi:10.1016/j.ceramint.2015.03.292.
- [54] S. Chen, Z. Chen, C. Cao, Mesoporous Spinel  $\text{LiMn}_2\text{O}_4$  Cathode Material by a Soft-templating Route, *Electrochim. Acta.* 199 (2016) 51–58. doi:10.1016/j.electacta.2016.03.135.
- [55] N. Arun, A. Jain, V. Aravindan, S. Jayaraman, W. Chui Ling, M.P. Srinivasan, S. Madhavi., Nanostructured spinel  $\text{LiNi}_{0.5}\text{Mn}_{1.5}\text{O}_4$  as new insertion anode for advanced Li-ion capacitors with high power capability, *Nano Energy.* 12 (2015) 69–75.  
doi:10.1016/j.nanoen.2014.12.006.
- [56] E.S. Lee, A. Huq, H.Y. Chang, A. Manthiram, High-voltage, high-energy layered-spinel composite cathodes with superior cycle Life for lithium-ion batteries, *Chem. Mater.* 24 (2012) 600–612. doi:10.1021/cm2034992.
- [57] J. Lu, Y.L. Chang, B. Song, H. Xia, J.R. Yang, K.S. Lee, High energy spinel-structured cathode stabilized by layered materials for advanced lithium-ion batteries, *J. Power Sources.* 271 (2014) 604–613. doi:10.1016/j.jpowsour.2014.08.037.



- [58] N. West, K.I. Ozoemena, C.O. Ikpo, P.G.L. Baker, E.I. Iwuoha, Transition metal alloy-modulated lithium manganese oxide nanosystem for energy storage in lithium-ion battery cathodes, *Electrochim. Acta.* 101 (2013) 86–92.  
doi:<http://dx.doi.org/10.1016/j.electacta.2012.11.085>.
- [59] D.K. Kim, P. Muralidharan, H.-W. Lee, R. Ruffo, Y. Yang, C.K. Chan., Spinel  $\text{LiMn}_2\text{O}_4$  Nanorods as Lithium Ion Battery Cathodes, *Nano Lett.* 8 (2008) 3948–3952.  
doi:10.1021/nl8024328.
- [60] C. Hu, Y. Wu, Spinel  $\text{LiMn}_2\text{O}_4$  nanohybrid as high capacitance positive electrode material for supercapacitors. *J Power Sources*, (2014). doi:10.1016/j.jpowsour.2013.07.046.
- [61] Y. Wang, Y. Wang, D. Jia, Z. Peng, Y. Xia, G. Zheng, All-nanowire based Li-ion full cells using homologous  $\text{Mn}_2\text{O}_3$  and  $\text{LiMn}_2\text{O}_4$ , *Nano Lett.* 14 (2014) 1080–1084.  
doi:10.1021/nl4047834.
- [62] X. Yang, F. Qu, H. Niu, Q. Wang, J. Yan, Z. Fan, High-performance aqueous asymmetric supercapacitor based on spinel  $\text{LiMn}_2\text{O}_4$  and nitrogen-doped graphene / porous carbon composite, *Electrochim. Acta.* 180 (2015) 287–294.  
doi:10.1016/j.electacta.2015.08.128.
- [63] S.J.K. Parthiban Pazhamalai, Karthikeyan Krishnamoorthy, M.S.P. Sudhakaran, Fabrication of high performance aqueous Li-ion hybrid capacitor using  $\text{LiMn}_2\text{O}_4$  and graphene, *ChemElectroChem.* 4 (2017) 396–403. doi:10.1111/liv.12553.
- [64] B.J. Kang, J.B. Joo, J.K. Lee, W. Choi, Surface modification of cathodes with nanosized amorphous  $\text{MnO}_2$  coating for high-power application in lithium-ion batteries, *J. Electroanal. Chem.* 728 (2014) 34–40. doi:10.1016/j.jelechem.2014.06.023.

- [65] M.D. Bhatt, C. O'Dwyer, Recent progress in theoretical and computational investigations of Li-ion battery materials and electrolytes, *Phys. Chem. Chem. Phys.* 17 (2015) 4799–844. doi:10.1039/c4cp05552g.
- [66] C.M. Julien, A. Mauger, K. Zaghib, H. Groult, Comparative Issues of Cathode Materials for Li-Ion Batteries, *Inorganics*. 2 (2014) 132–154. doi:10.3390/inorganics2020132.
- [67] M. Minakshi, A. Pandey, M. Blackford, M. Ionescu, Effect of  $\text{TiS}_2$  Additive on  $\text{LiMnPO}_4$  Cathode in Aqueous Solutions, *Energy & Fuels*. 24 (2010) 6193–6197. doi:10.1021/ef101063h.
- [68] H.-C. Dinh, S. Mho, Y. Kang, I.-H. Yeo, Large discharge capacities at high current rates for carbon-coated  $\text{LiMnPO}_4$  nanocrystalline cathodes, *J. Power Sources*. 244 (2013) 189–195. doi:http://dx.doi.org/10.1016/j.jpowsour.2013.01.191.
- [69] M.M. Doeff, *Encyclopedia of Sustainability Science and Technology*, 2012. doi:10.1007/978-1-4419-0851-3.
- [70] Z. Pei, X. Zhang, X. Gao, Shape-controlled synthesis of  $\text{LiMnPO}_4$  porous nanowires, *J. Alloys Compd.* 546 (2013) 92–94. doi:10.1016/j.jallcom.2012.08.080.
- [71] H. Zhang, C. Mao, J. Li, R. Chen, Advances in electrode materials for Li-based rechargeable batteries, *RSC Adv.* 7 (2017) 33789–33811. doi:10.1039/C7RA04370H.
- [72] S.R.S. Prabakaran, A. Anslin Star, A.R. Kulkarni, M.S. Michael, Nano-composite  $\text{LiMnPO}_4$  as New Insertion Electrode for Electrochemical Supercapacitors, *Curr. Appl. Phys.* 15 (2015) 1624–1633. doi:10.1016/j.cap.2015.09.009.

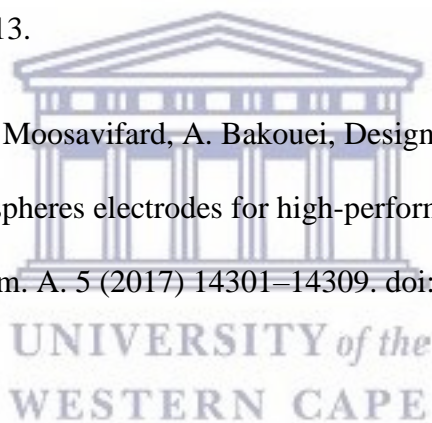
- [73] J. Li, X. Zhang, Y. Huang, L. Guo, Y. Qi,  $\text{LiMn}_2\text{O}_4/\text{Graphene}$  composites as cathode with enhanced electrochemical performance for lithium-ion capacitors, *RSC Adv.* 6 (2016) 54866–54873. doi:10.1039/C6RA09103B.
- [74] Y. Zhang, Y. Zhao, L. Deng, Enhanced electrochemical properties of  $\text{LiMnPO}_4/\text{C}$  via doping with Cu, *Ionics (Kiel)*. 18 (2012) 573–578. doi:10.1007/s11581-011-0655-y.
- [75] J. Liu, X. Liu, T. Huang, A. Yu, Synthesis of nano-sized  $\text{LiMnPO}_4$  and in situ carbon coating using a solvothermal method, *J. Power Sources*. 229 (2013) 203–209. doi:http://dx.doi.org/10.1016/j.jpowsour.2012.11.093.
- [76] Q. Xia, H. Yang, M. Wang, M. Yang, Q. Guo, L. Wan, H. Xia, Y. Yu, High Energy and High Power Lithium-Ion Capacitors Based on Boron and Nitrogen Dual-Doped 3D Carbon Nanofibers as Both Cathode and Anode, *Adv. Energy Mater.* 7 (2017) 1–9. doi:10.1002/aenm.201701336.
- [77] J. Lu, C. Zhan, T. Wu, J. Wen, Y. Lei, A.J. Kropf, et al., Effectively suppressing dissolution of manganese from spinel lithium manganate via a nanoscale surface-doping approach., *Nat. Commun.* 5 (2014) 5693. doi:10.1038/ncomms6693.
- [78] H.Q. Wang, F.Y. Lai, Y. Li, X.H. Zhang, Y.G. Huang, S.J. Hu, Q. Li., Excellent stability of spinel  $\text{LiMn}_2\text{O}_4$ -based cathode materials for lithium-ion batteries, *Electrochim. Acta.* 177 (2015) 290–297. doi:10.1016/j.electacta.2015.02.027.
- [79] C.J. Jafta, F. Nkosi, L. le Roux, M.K. Mathe, M. Kebede, K. Makgopa, K.I. Ozoemena., Manganese oxide/graphene oxide composites for high-energy aqueous asymmetric electrochemical capacitors, *Electrochim. Acta.* 110 (2013) 228–233. doi:http://dx.doi.org/10.1016/j.electacta.2013.06.096.

[80] S. Zhang, C. Li, X. Zhang, X. Sun, K. Wang, Y. Ma, High Performance Lithium-Ion Hybrid Capacitors Employing Fe<sub>3</sub>O<sub>4</sub>-Graphene Composite Anode and Activated Carbon Cathode, *ACS Appl. Mater. Interfaces*. 9 (2017) 17136–17144. doi:10.1021/acsami.7b03452.

[81] C. Lu, X. Wang, X. Zhang, H. Peng, Y. Zhang, G. Wang., Effect of graphene nanosheets on electrochemical performance of Li<sub>4</sub>Ti<sub>5</sub>O<sub>12</sub> in lithium-ion capacitors, *Ceram. Int.* 43 (2017) 6554–6562. doi:10.1016/j.ceramint.2017.02.083.

[82] R. Wang, S. Wang, D. Jin, Y. Zhang, Y. Cai, J. Ma, Z. Li., Engineering layer structure of MoS<sub>2</sub>-graphene composites with robust and fast lithium storage for high-performance Li-ion capacitors, *Energy Storage Mater.* 9 (2017) 195–205. doi:10.1016/j.ensm.2017.07.013.

[83] S.K. Kaverlavani, S.E. Moosavifard, A. Bakouei, Designing graphene-wrapped nanoporous CuCo<sub>2</sub>O<sub>4</sub> hollow spheres electrodes for high-performance asymmetric supercapacitors, *J. Mater. Chem. A*. 5 (2017) 14301–14309. doi:10.1039/C7TA03943C.



## CHAPTER THREE

### 3 Development of graphenised-lithium manganese phosphate doped with nickel with enhanced electrochemical performance for lithium ion capacitors

#### Overview

*This chapter provides a detailed account of the development of lithium ion capacitor based on G-LMNP||AC. Herein the morphological and structural studies of the developed graphene, LMP, LMNP and G-LMNP materials using HRSEM, HRTEM, XRD, FTIR, Raman and solid state NMR was discussed. Furthermore an in-depth discussion of the electrochemical properties (CV, EIS and GCD) of the developed LICs device. The important aspect of this section of the study was to construct a Ragone plots and see where the synthesized material fit with other devices*

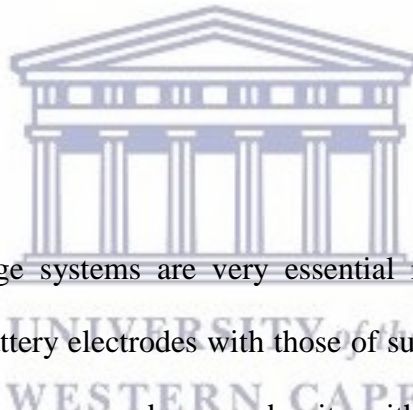


UNIVERSITY of the  
WESTERN CAPE

## ABSTRACT

Graphene coated olivine lithium manganese phosphate doped nickel was used as an electrode material for lithium-ion supercapacitor. Its electrochemical characteristics in  $\text{Li}_2\text{SO}_4$  aqueous electrolyte at a voltage window of 0 - 2 V were examined by cyclic voltammetry (CV), electrochemical impedance spectroscopy (EIS) and galvanostatic charge-discharge. The nanocomposite electrode gave a specific capacitance value of  $60 \text{ F g}^{-1}$  at a current density of  $0.1 \text{ A g}^{-1}$  and exhibited excellent capacitance retention after 750 cycles (floating) with a capacitance retention of 83%. It rendered a high power density of  $18 \text{ kW kg}^{-1}$  at  $0.5 \text{ A g}^{-1}$ . The G-LMNP presents a promising electrode material for applications in lithium-ion capacitors

### 3.1 Introduction



Electrochemical energy storage systems are very essential in everyday energy needs. A combination of lithium ion battery electrodes with those of supercapacitors can present very attractive devices having high energy and power density with satisfactory cycling stability, which is the so called hybrid Li-ion capacitors [1,2].

Various works on lithium ion supercapacitors have been reported with encouraging results [1,3–7]. Lithium metal phosphates ( $\text{LiMPO}_4$ ,  $M = \text{Fe, Mn, Co and Ni}$ ) have been investigated as promising electrodes, mainly  $\text{LiFePO}_4$  and  $\text{LiMnPO}_4$ . Xie *et al* designed carbon coated lithium iron phosphate (C-LFP) supported on a titanium nitride (TiN) substrate which exhibited high capacitance and excellent stability at a voltage window of -1 - 0 V due to carbon modification and the nano-network structure of TiN nanowires [8].

Parabakaran and co-workers made nanolayer carbon encompassed lithium manganese phosphate (LMP) for lithium ion hybrid capacitors which showed high specific capacitance and energy density with appreciable power and stability in aqueous electrolyte [9].

In this study, G-LMNP nanocomposite was used in two electrode lithium ion capacitor system in aqueous 1 M  $\text{Li}_2\text{SO}_4$ .  $\text{LiMnPO}_4$  has a theoretical energy density at  $701.1 \text{ Wh kg}^{-1}$  which is much higher than that of  $\text{LiFePO}_4$  at  $568.5 \text{ Wh kg}^{-1}$  as a result of the high operating voltage of LMP at 4.1 V. However, LMP shows less or poor electrochemical performance due to slow lithium ion diffusion kinetics within the crystals and very low intrinsic electronic conductivity [10–14]. It has been found that surface coating and reduced particle size enhance the electrochemical properties of LMP [15,16].  $\text{LiMnPO}_4$  structure was doped with nickel to decrease the Jahn Teller effect [16,17]. Nickel doping followed by graphene coating on the surface of LMP was the synthetic protocol used to enhance its electrochemical performance. This was due to the extraordinary properties of graphene like, large surface area, good flexibility, electric conductivity and good chemical and thermal stability [18,19]. In this study G-LMNP was designed as the electrode material for a lithium-ion capacitors for an energy storage application using a two electrode system in a 1 M  $\text{Li}_2\text{SO}_4$  aqueous medium.

## 3.2 Experimental

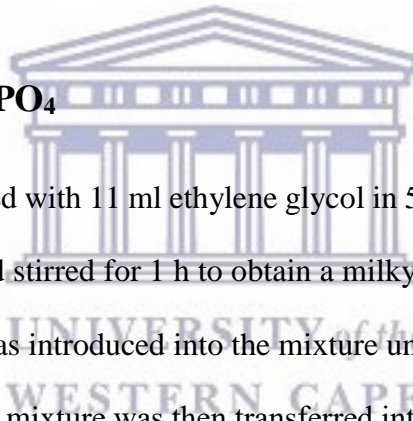
$\text{LiMnPO}_4$  was obtained using a solvothermal method and then it was doped with Nickel and coated with graphene.



### 3.2.1 Chemical Reagents

All chemicals used in this study were analytical reagent grade and used without further purification mostly obtained from Sigma-Aldrich. Lithium hydroxide (99.995 %) trace metal basis, manganese (II) sulfate monohydrate, ethylene glycol (99.0 %), phosphoric acid, crystalline ( $\geq 99.99$  %) trace metal basis, nickel(II) acetate tetrahydrate (98%), graphite powder  $\leq 20$   $\mu\text{m}$ , 96% ethanol from Saarchem, 37% hydrochloric acid from Saarchem, 65% nitric acid from KIMIX. Poly(vinylidene fluoride), Carbon black (CP), N-methyl-2-pyrrolidone, anhydrous (99.5 %), Activated carbon (AC) was purchased from SUPELCO analytical and used as received and ;Nickel foam purchased from MTI Corp.

### 3.2.2 Synthesis of $\text{LiMnPO}_4$



2.7 ml of 1 M  $\text{H}_3\text{PO}_4$  was mixed with 11 ml ethylene glycol in 50 ml round bottom flask. Then 3 ml 1 M LiOH was added and stirred for 1 h to obtain a milky solution. Subsequently 5.5 ml 0.5 M  $\text{MnSO}_4 \cdot \text{H}_2\text{O}$  solution was introduced into the mixture under vigorous stirring, resulting in a light pink suspension. The mixture was then transferred into a 25 ml autoclave sealed and heated at  $180^\circ\text{C}$  and maintained at the same temperature for 12 h. Afterwards the autoclave was allowed to cool to room temperature. The resultant products were collected via centrifugation and washed three times with ethanol and water. The off white product was dried under vacuum at  $80^\circ\text{C}$  for 12 h [15]. The powder as produced was then calcined at  $500^\circ\text{C}$  for 5h. Synthesis of Ni doped  $\text{LiMnPO}_4$  followed the same procedure with stoichiometric amount of  $\text{Ni}(\text{CH}_3\text{COO})_2$  added to form LMNP.



### 3.2.3 Synthesis of Graphene coated LMNP

Graphene nanosheets were prepared from graphite powder in a two-step process, involving the oxidation and/or exfoliation of graphite to graphene oxide by modified Hummer's method and chemical reduction of graphene oxide to graphene according to literature [20–22]. To prepare the graphene coated LMNP, 50 mg graphene is dispersed in 50 ml of ethanol under ultrasonication for 30 min. Then 1 g of LMNP was added, after that the mixture was vigorously stirred at 70 °C for 12 h to obtain a uniform dispersion of G-LMNP. The final product was dried in the vacuum oven at 80 °C overnight.

### 3.2.4 Electrode preparation for electrochemical characterization

All electrochemical measurements were carried out using a Bio-Logic VMP 300 potentiostat/galvanostat using three (half-cell) and two-electrode (full cell) configuration. The half-cell was done in three electrode system where the active material was coated on the nickel foam which acted as substrate, the reference electrode was Ag/AgCl (3M KCl) and platinum wire as counter electrode. The two electrode system assembled in Swagelok cell consist of the active material (LMP, LMNP and G-LMNP) coated on the nickel foam and the negative electrode made up of activated carbon coated on nickel form.

#### 3.2.4.1 Preparation of electrodes for three electrode configuration

The  $\text{LiMnPO}_4$  and composite electrodes were prepared from a mixture of active (LMP), carbon black (CB, Degussa), and polyvinylidene fluoride (PVDF) in a mass ratio of 70:30:10, respectively, using anhydrous N-methyl-2-pyrrolidone as the solvent. The slurry was coated

on a nickel foam (1 cm x 0.5 cm) substrate with the mass loading ranged between 8 mg.cm<sup>-2</sup> to 20 mg.cm<sup>-2</sup>. The prepared electrode was dried at 70 °C for 12 h [7, 8].

#### **3.2.4.2 Preparation of electrodes for two-electrode configuration (LICs)**

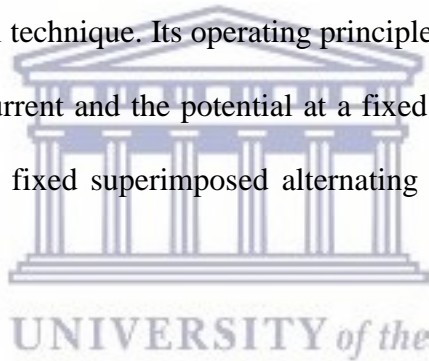
The positive electrode was prepared by mixing 70 wt% LMP composite, 30 wt% carbon black (CB, Degussa), and 10 wt% polyvinylidene fluoride (PVDF) in anhydrous N-methyl-2-pyrrolidone to form homogeneous slurry which was coated on a nickel foam substrate (3 cm<sup>2</sup>) with a mass loading of 7 – 12 mg.cm<sup>-2</sup>. The negative electrode was prepared using similar procedure but with activated carbon, carbon black and PVDF at a mass ratio of 80:15:5, respectively [6,9]. The cell was tested after 24 h of fabrication. In all the experiments, 1 M Li<sub>2</sub>SO<sub>4</sub> was used as electrolyte and a porous glass fiber (Whatman Grade GF/D Glass Microfiber Filters, Sigma-Aldrich) served as the separator.

#### **3.2.5 Measurements and instrumentation**

The surface morphology and internal ultra-structure of the synthesized materials was evaluated by the use of scanning electron microscopy (SEM) and high resolution transmission electron microscopy (HRTEM), respectively. Scanning electron microscopic (SEM) images were obtained using a Hitachi model X-650 ZEISS ULTRA scanning electron microscope. The sample was placed on a carbon supported by alumina and then placed in a sputter coater to make the material conductive. The samples were then coated for 30 seconds using gold-palladium alloy. The high resolution transmission electron microscopic images were obtained by Tecnai G2 F20 X-TWIN MAT equipped with an energy-dispersed spectroscopy (EDS) for Elemental mapping. Characterisation here was performed by coating a copper- carbon grid with a drop of the sample solution and drying with an electric lamp for 10 min. HRTEM

provides information on particle size, shape and crystallography of nanoparticles. It can measure particle sizes to as low as 1 nm. HRTEM was used to identify the size, shape and structure of the products. X-ray powder diffraction (XRD) is a rapid analytical technique primarily used for phase identification of a crystalline material and provides information on unit cell dimensions. The sample was finely ground, homogenized, and average bulk composition determined. XRD reveals information on the structure, crystallinity and lattice spacing of the material. X-ray diffraction (XRD) measurements were carried out with a BRUKER AXS (Germany), D8 Advance diffractometer, using Cu K $\alpha$  radiation of wavelength 1.5418 Å and scanned from 80° to 10° with a step size of 0.02°. FTIR spectra were obtained using a perkin elmer spectrum 100 series attenuated total reflection (ATR) FTIR spectrometer. Infrared spectroscopy reveals information about the vibrational states of a molecule and functional groups. Solid state NMR experiments were performed on a Bruker Avance III HD Ascend standard bore 500 MHz spectrometer operating at (<sup>7</sup>Li) 194 MHz. Direct polarization solid state <sup>7</sup>Li NMR as well as Hahn Echo experiments were carried out using a 4 mm MAS BB NMR probe using an excitation pulse length of 2.4 us at 120 W with a recycle delay of 50 ms. Sample spectra were acquired at spinning speeds of 11 kHz and 15 kHz. The samples were packed into 4.0 mm zirconia rotors. Small-Angle X-Ray Scattering (SAXS) measurements for LiMnPO<sub>4</sub> and nanocomposites were obtained using a 1 mm thin walled capillary (solid powder samples) at the beamline ID09B. We used the CCD 161 detector (Anton Paar, GmbH, Australia, 133 mm diameter, 2048 × 2048 pixels) at a distance of 0.6 m and an X-ray energy of 10 keV. The electrochemical properties of the nanocomposite and pristine LMP were studied by cyclic voltammetry, galvanostatic charge-discharge and electrochemical impedance spectroscopy (EIS) using the full and half-cells prepared above. The nickel foam served as the current collector. Cyclic voltammetry (CV) is a technique which is widely used in the study of oxidation/reduction reactions and the detection of reaction intermediates. This technique

indicates the potentials at which processes occur. The cyclic voltammetry (CV), tests for full cell were carried out in the potential range of 0 to 2 V at various scan rates from 5 mV s<sup>-1</sup> to 50 mV s<sup>-1</sup>. Galvanostatic charge-discharge (GCD) technique is the widely used method in supercapacitors application and the most important characterisation tool for the determination of the electrochemical performance of the electrode materials. To gain understanding of the power, energy performance and ability of the electrode material to retain its capacitance, a variation of current density on the GCD technique must be employed. The GCD tests were carried out at varying current densities between 0.1 A g<sup>-1</sup> to 1 A g<sup>-1</sup>. Electrochemical impedance spectroscopy measurements were conducted at amplitude of 5 mV and frequency range of 100 mHz to 100 kHz. EIS provides a more thorough understanding of an electrochemical system than any other electrochemical technique. Its operating principle involves the measurement of the impedance between the current and the potential at a fixed direct current (DC) potential during frequency scan with a fixed superimposed alternating current (AC) signal of small amplitude.



The specific capacitance ( $C_{sp}$ ), maximum specific power density ( $P_{max}$ ) and specific energy density ( $E_{sp}$ ) were determined from the discharge curves using the established equations (1 to 5) for a two electrode system [23–26].

$$C(F) = \frac{i}{\frac{\Delta V}{\Delta t}} \quad (1)$$

$$C_{sp} = \frac{4.C}{m} \quad (2)$$

$$P_{max} (W/Kg) = \frac{V^2}{4mR_{ir}} \quad (3)$$

$$E(\text{Wh/kg}) = \frac{CV^2}{2m} \quad (4)$$

Where  $i$  (A) is the applied current,  $\Delta V$  (V) /  $\Delta t$  (s) is the slope of the discharge curve after the initial  $iR$  drop and  $m$  (g) the mass of both electrodes.  $V$  (V) is the maximum voltage obtained during charge and  $C$  (F) the calculated capacitance. The internal resistance ( $R_{ir}$ ) can be calculated from the voltage drop at the beginning of a discharge curve:

$$R_{ir} (\Omega) = \frac{\Delta V_{iR}}{2i} \quad (5)$$

Where  $\Delta V_{iR}$  is the voltage drop between the first two points from the start of the discharge curve.



### 3.3 Material characterization

#### 3.3.1 Structure and morphology characterisation of graphene

**Fig. 3.1** shows the Fourier transformed infrared (FTIR) spectra of graphene and graphene oxide. The spectrum of graphene oxide is characterized by the band at  $1026 \text{ cm}^{-1}$  due to the C-O stretching vibration occurring in epoxides and alcohols within the graphite structure. The absorption band at  $1715 \text{ cm}^{-1}$  due to C=O stretch, the band at  $1503 \text{ cm}^{-1}$  associated with bending COOH vibrations. Upon reduction using  $\text{NaBH}_4$  as reducing agent, a considerable decrease or complete removal of the above mentioned oxygen containing functionalities is noted in graphene spectrum. Graphene is characterized by band at  $1556 \text{ cm}^{-1}$  representing the aromatic C-C stretch, band at  $620 \text{ cm}^{-1}$  indicating =C-H bend vibration confirming the unsaturation  $\text{sp}^2$  bending to bond to  $\text{sp}^3$  carbon molecule. The carboxyl COOH stretching vibration band at  $1495$

$\text{cm}^{-1}$ , the absorption band at  $1715 \text{ cm}^{-1}$  due to  $\text{C}=\text{O}$  stretch which is attributed to accumulation of oxygen atoms on the sheets [27,28]

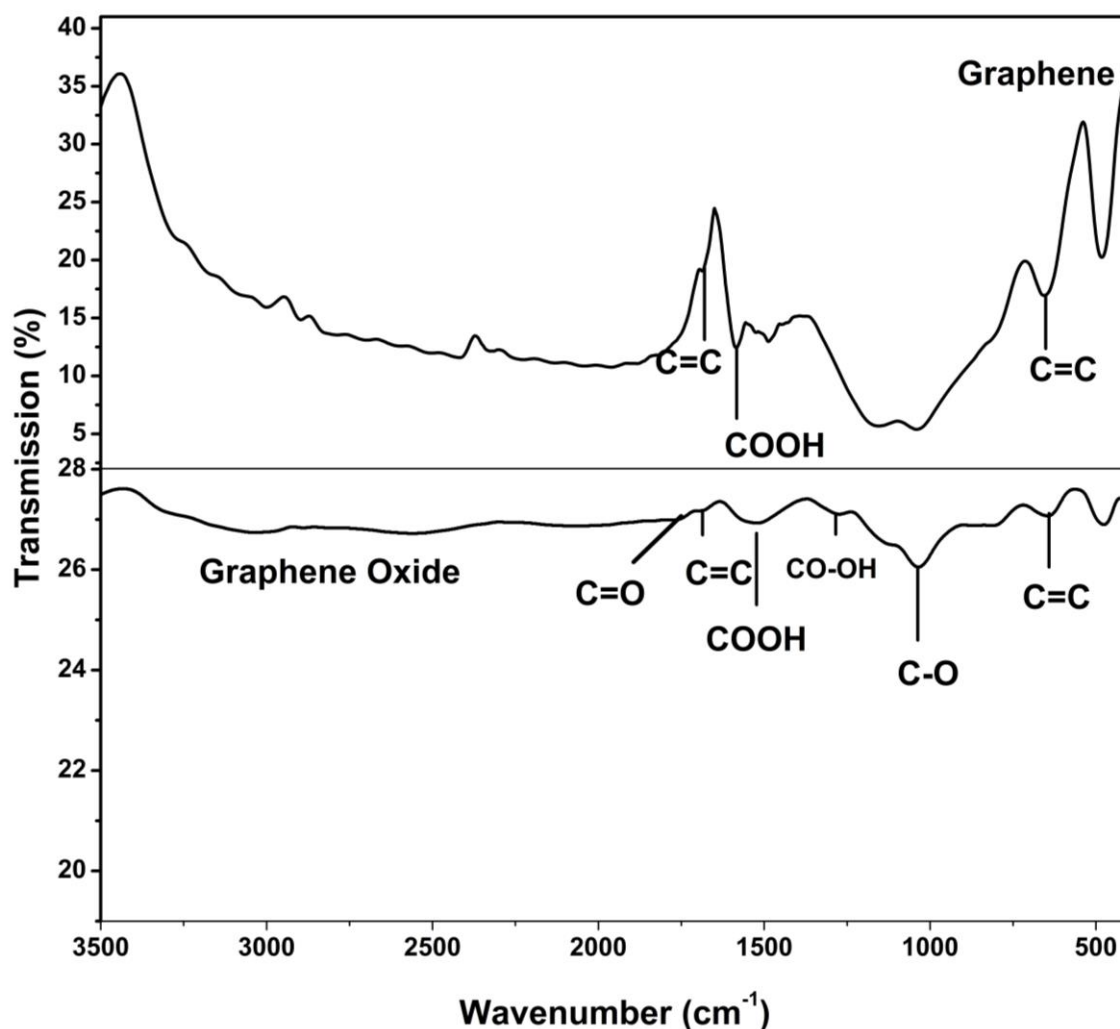


**Figure 3.1:** FTIR spectra of graphene oxide (GO) and graphene

**Fig. 3.2** shows the Raman spectra of graphene oxide and graphene. Graphene oxide showed a Raman shift to  $1600 \text{ cm}^{-1}$  for the G band while the D band at  $1360 \text{ cm}^{-1}$  is considerably larger. The Raman spectrum of graphene showed a decrease in intensity and slightly shift to lower frequencies indicating the reduction process was successful. Raman shift of the D peak is located at  $1348 \text{ cm}^{-1}$  and G peak at  $1593 \text{ cm}^{-1}$ . The D band is allocated to the breathing mode

of k-point phonons of  $A_{1g}$  symmetry from the aromatic rings which show the defects in these materials, whereas the G band is assigned to the  $E_{2g}$  phonons from the stretching of C  $sp^2$  atoms in both the rings and chains [29,30]. The Raman and FTIR results showed the successful synthesis of graphene oxide and graphene.

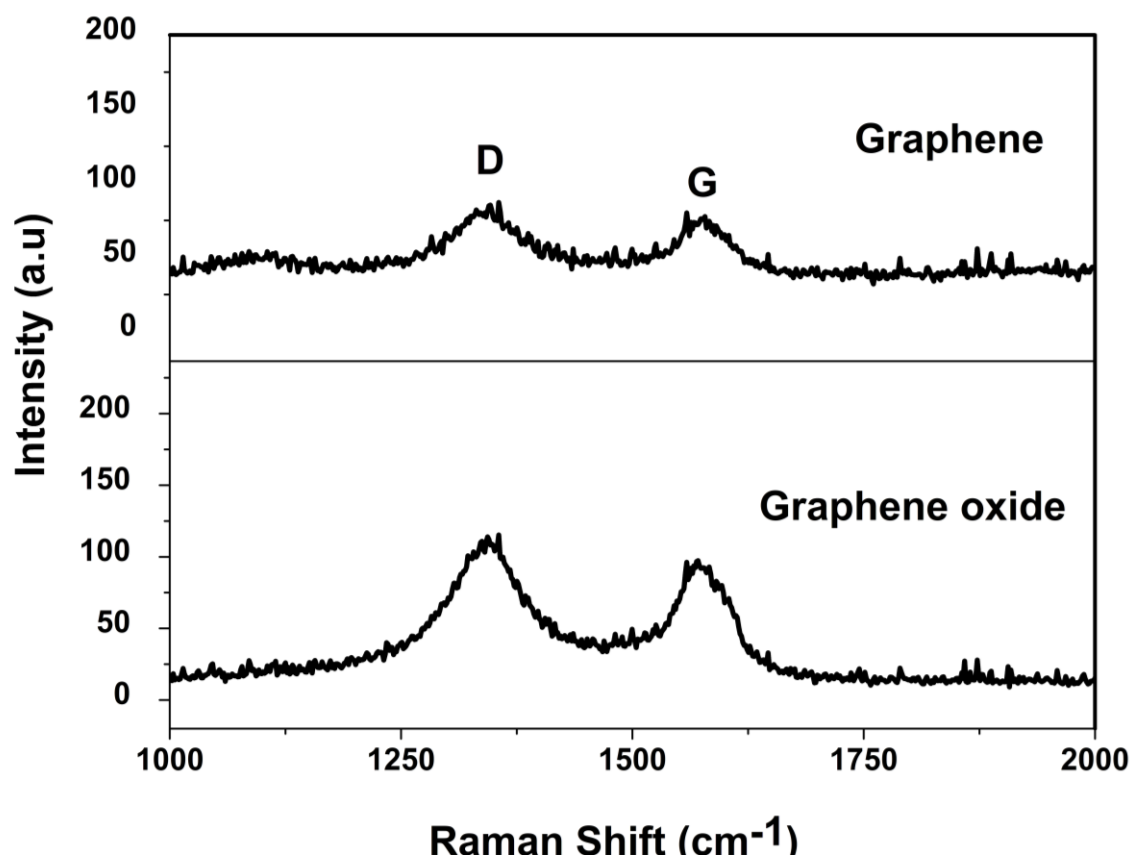


**Figure 3.2:** Raman spectra of graphene oxide and graphene

The surface morphologies of graphene were investigated by high resolution scanning electron microscopy (HRSEM) and high transmission electron microscopy (HTEM) represented in **Fig. 3.3** below. The HRSEM image of graphene demonstrates that the material consists of thin, haphazardly aggregated, wrinkly sheets closely linked with each other forming a lawless solid. TEM images of graphene reveal exfoliation of individual packed graphene sheets. The EDS spectra of Graphene are represented in **Fig. 3.3(d)**. The EDS confirms the presence of Cu, O,



and C elements. Copper present is attributed to the choice of Cu mesh grids used for analysis. The incomplete removal of oxygen is a draw-back to the chemical synthesis approach as well as the use of  $\text{NaBH}_4$  as reducing agent but is to be expected. The large intensity of carbon further proves graphene is made of carbon rings.

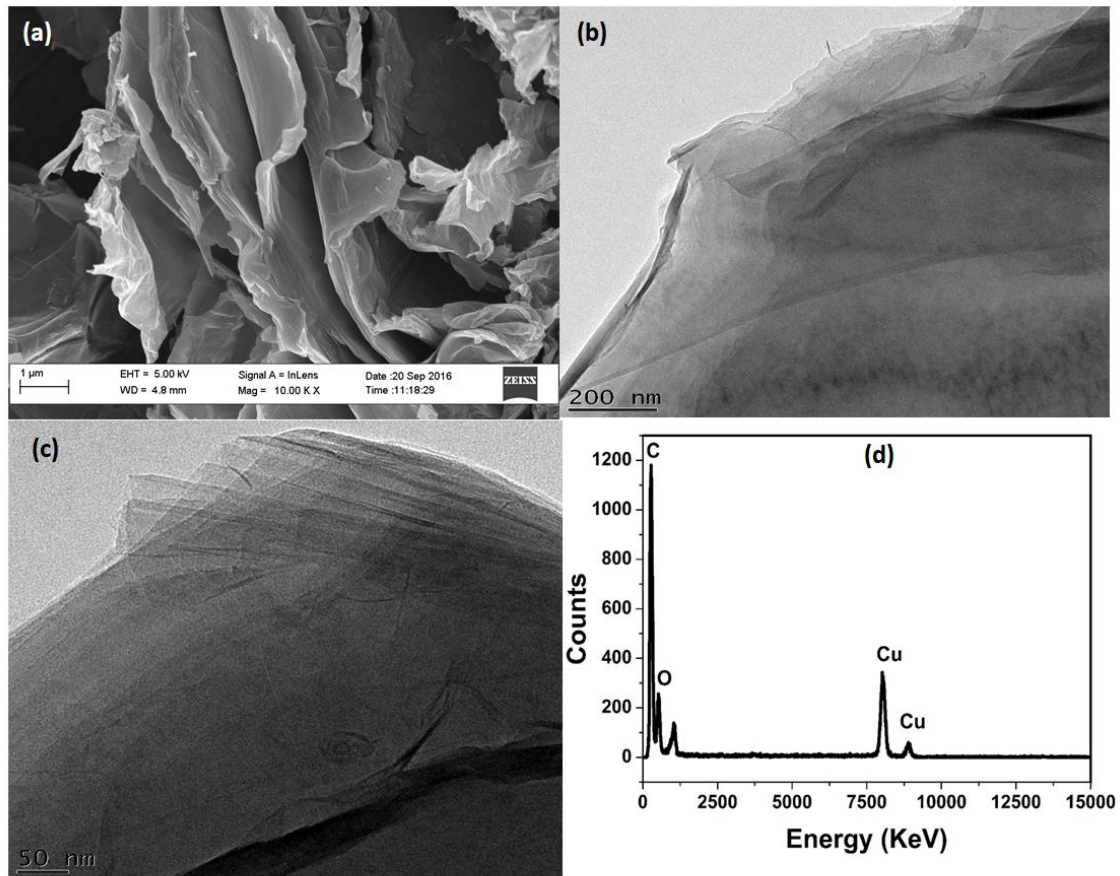
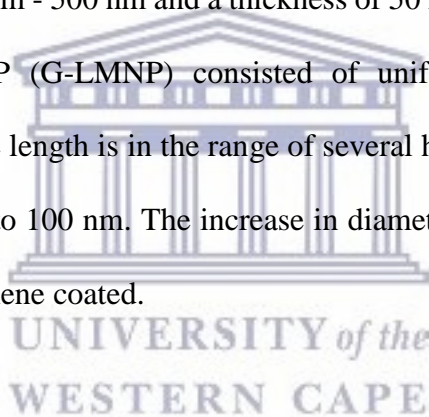


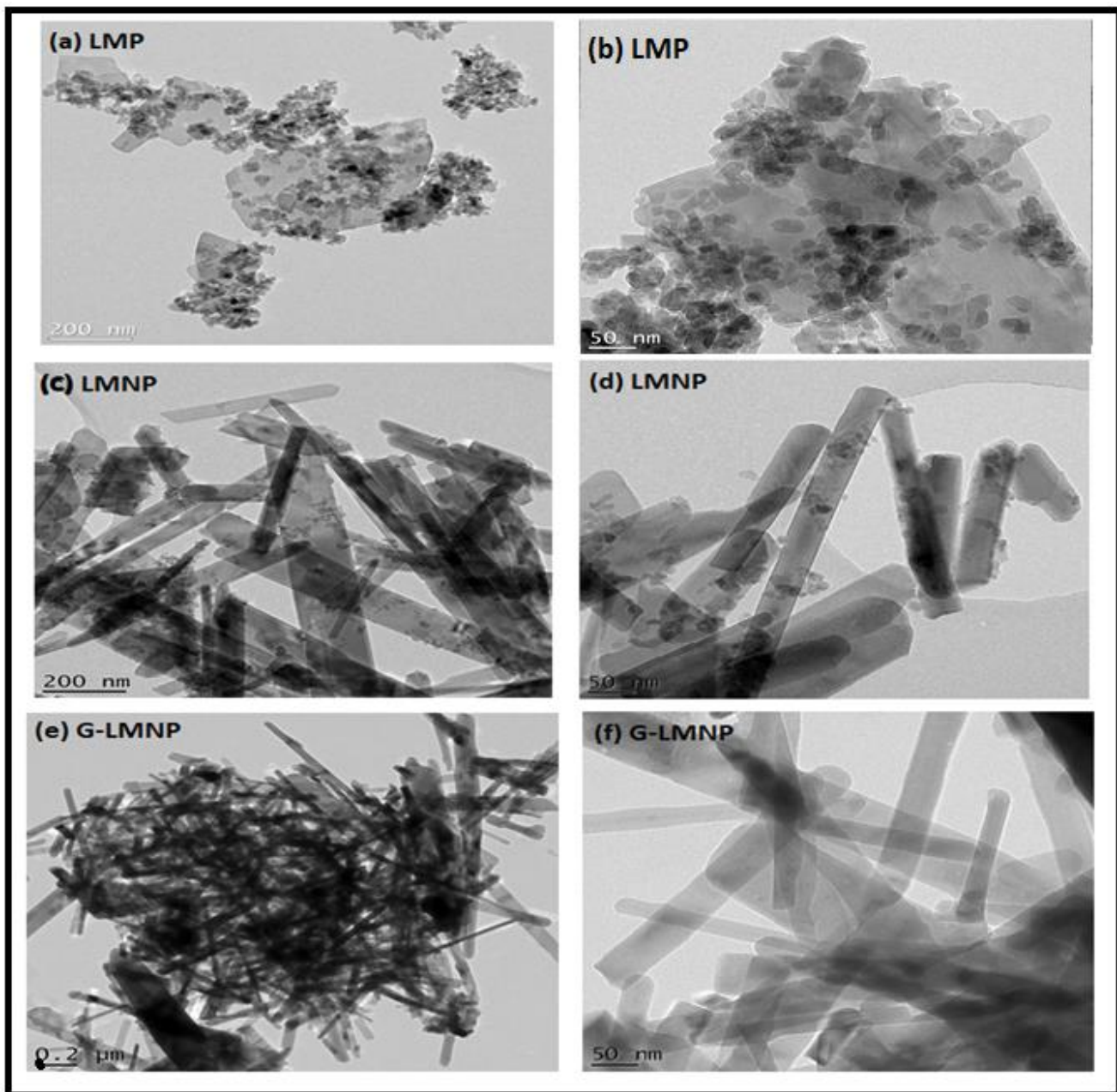
**Figure 3.3:** (a) HRSEM, [(b) and (c)] HRTEM and (d) EDS spectra of graphene.



### 3.3.2 Morphology and structure of LMP, LMNP and G-LMNP nanocomposite

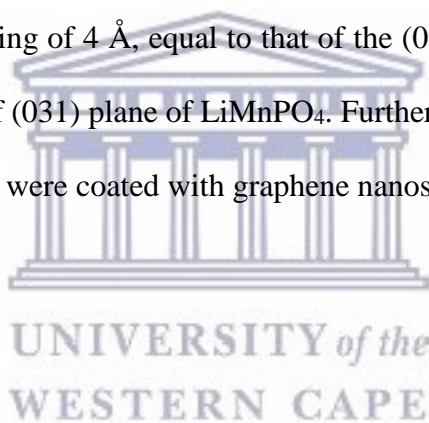
Using a solvothermal method, the morphology and the particle size of LMP was investigated as shown in transmission electron microscopy (TEM). **Fig. 3.4** compares the TEM images of the synthesized  $\text{LiMnPO}_4$  and its composites. **Fig. 3.4 (a) and (b)** shows the typical TEM images of  $\text{LiMnPO}_4$ . The micrographs revealed that the particles are randomly-sized crystals with dimensions ranging from nanometres to a few in a micrometres-sized particle. The interconnected LMP nanoparticles with diameters range 100 nm - 10 nm formed a porous structure. **Fig. 3.4(c) and (d)** revealed that nickel doped  $\text{LiMnPO}_4$  (LMNP) exhibited a rod-like shape with length of 100 nm - 500 nm and a thickness of 50 nm. **Fig. 3.4 (e) and (f)** shows that Graphene coated LMNP (G-LMNP) consisted of uniform, ultrafine nanorods-like structures with high yield. The length is in the range of several hundred nm to 3  $\mu\text{m}$  while the thickness ranges from 20 nm to 100 nm. The increase in diameter and length of rod is due to the structural features of graphene coated.





**Figure 3.4:** TEM images of (a) and (b)  $\text{LiMnPO}_4$  nanowires, [(c) and (d)] Nickel doped  $\text{LiMnPO}_4$  and [(e) and (f)] G-LMNP

The fine structure and crystal orientation of  $\text{LiMnPO}_4$  nanocrystals were investigated using electron diffraction and high resolution TEM (HRTEM) and selected area electron diffraction (SAED) on an individual LMP nanorods or LMP sphere. **Fig.3.5 (a)** showed clear lattice fringes indicating formation of pure crystallites of  $\text{LiMnPO}_4$ . The observed d-spacing at  $6 \text{ \AA}$  of neighbouring lattice fringes corresponds to the (031) plane of  $\text{LiMnPO}_4$  and well defined diffraction spots (**Fig. 3.5 (b)**), revealing a highly ordered single crystalline nature of the particles. The diffraction patterns were indexed according to the  $Pnmb$  space group with the selected area diffraction (SAD) pattern corresponding to the (011) facet plane of the orthorhombic lattice of  $\text{LiMnPO}_4$  [31]. All three samples displayed perfect lattice fringes distributed within the entire particle while LMNP and G-LMNP showed parallel crystal planes with identical inter-plane spacing of  $4 \text{ \AA}$ , equal to that of the (020) plane and LMP showed d spacing of  $6 \text{ \AA}$ , equal to that of (031) plane of  $\text{LiMnPO}_4$ . Furthermore, G-LMNP (**Fig. 3.5 (e)**) revealed that the nanoparticles were coated with graphene nanosheets.



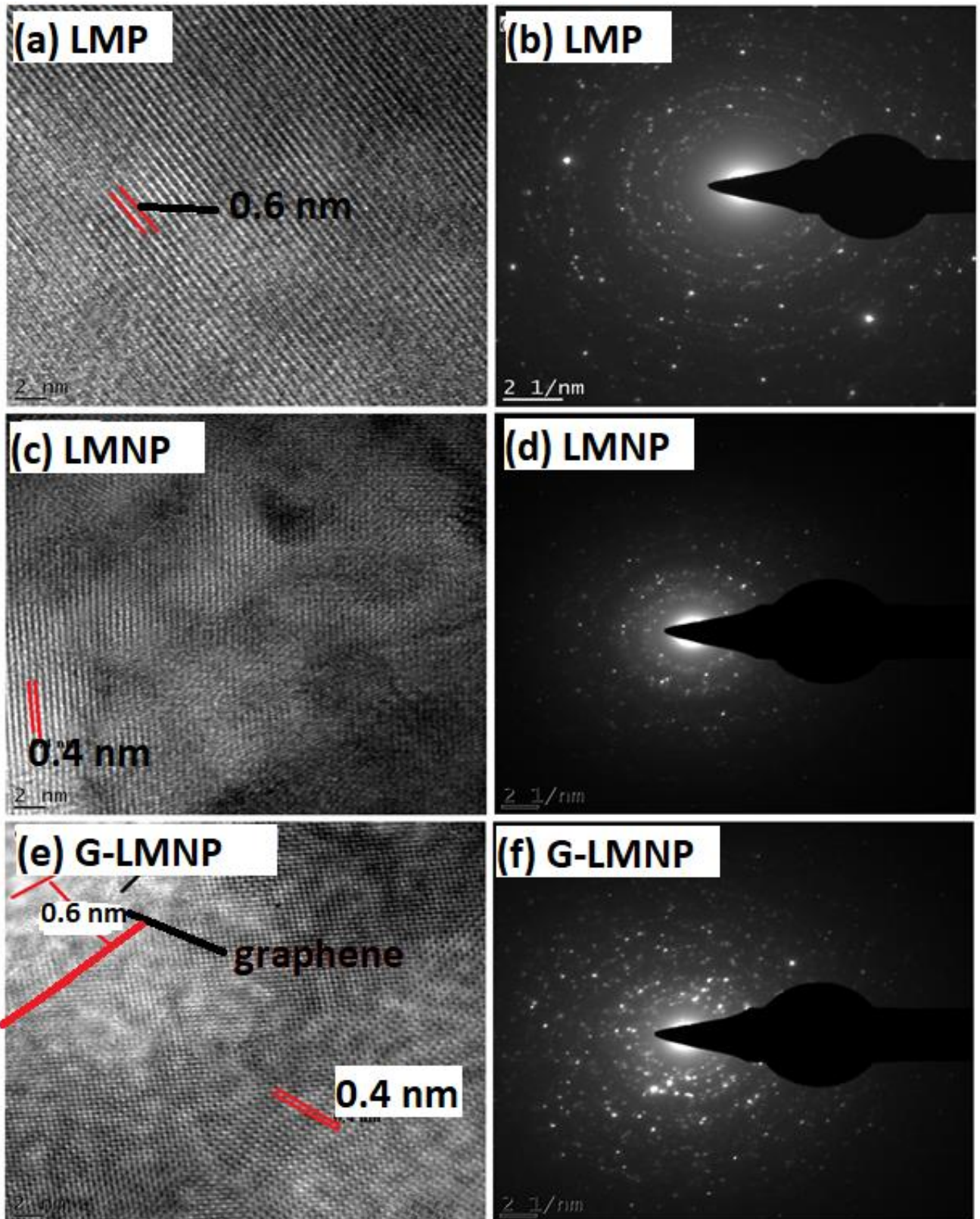


**Figure 3.5:** HRTEM images and SAED of (a) and (b)  $\text{LiMnPO}_4$ , [(c) and (d)] LMNP and [(e) and (f)] G-LMNP

**Fig. 3.6** showed the TEM-EDS spectrum of the nickel doped graphene coated  $\text{LiMnPO}_4$  nanorods confirming the presence of Mn, P, O, Ni and C. TEM-EDS showed the present of nickel in spectrum, the c observed is the carbon coated on the copper grid. The FTIR and Raman spectra were used to confirm graphene present on G-LMNP.

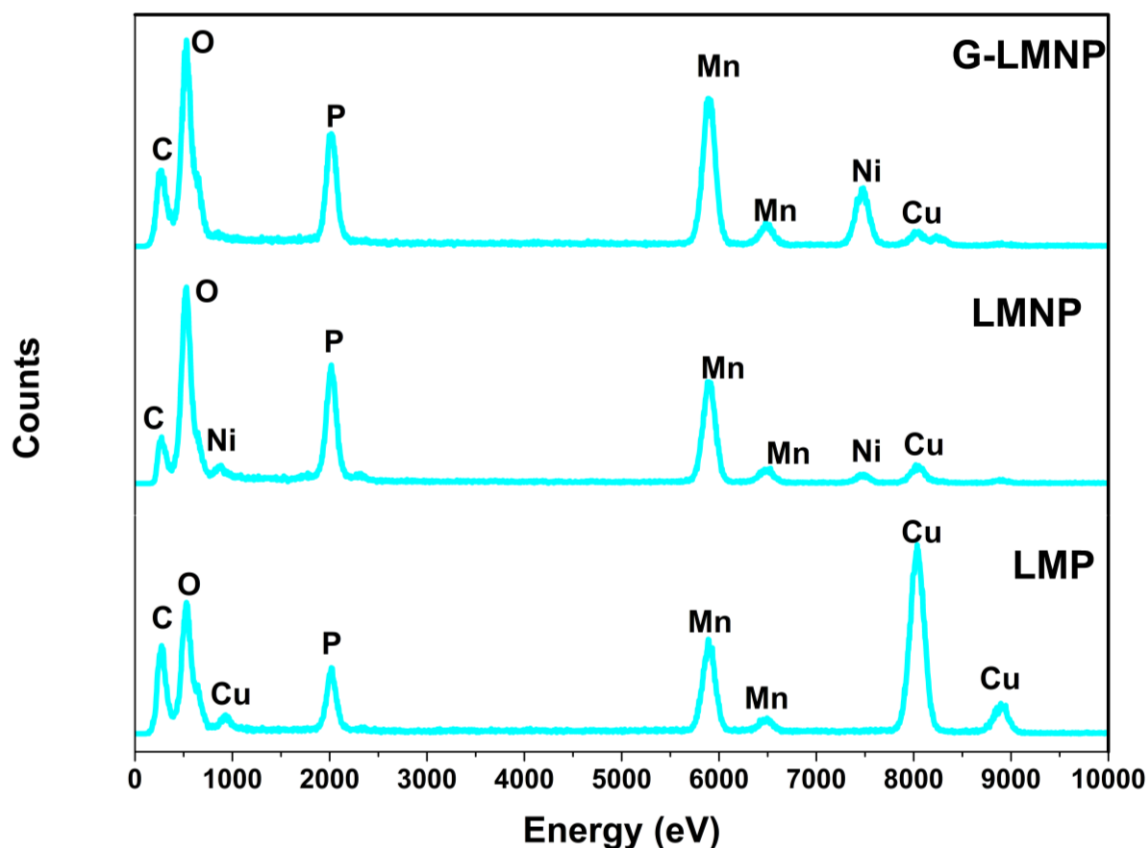


**Figure 3.6:** EDS of the synthesized  $\text{LiMnPO}_4$ , LMNP and G-LMNP

The HRSEM micrograph is shown in **Fig. 3.7**. The figure shows spherically-shaped, pure  $\text{LiMnPO}_4$  with primary particles size of  $\sim 100$  nm. The secondary particles of  $\text{LiMnPO}_4$  that form from aggregation of the primary particles are randomly sized and range between 200 - 350 nm indicating the crystals growth of the  $\text{LiMnPO}_4$  [32]. LMNP sample showed agglomerated nanorods morphology which was also evident from TEM. The observed SEM images shown in **Fig 3.7 (e) and f)** revealed ultrafine nanorods found to have a diameter of



ranges from 50 -100 nm and length of  $\sim 2 \mu\text{m}$ . The bright white region observed on G-LMNP SEM image maybe due to the coating of carbon on the nanorods [33]. Nanoparticles are essential for high accessibility of  $\text{Li}^+$  ion to the electrode material during lithiation/delithiation process due to increased surface-to-volume ratios [34].



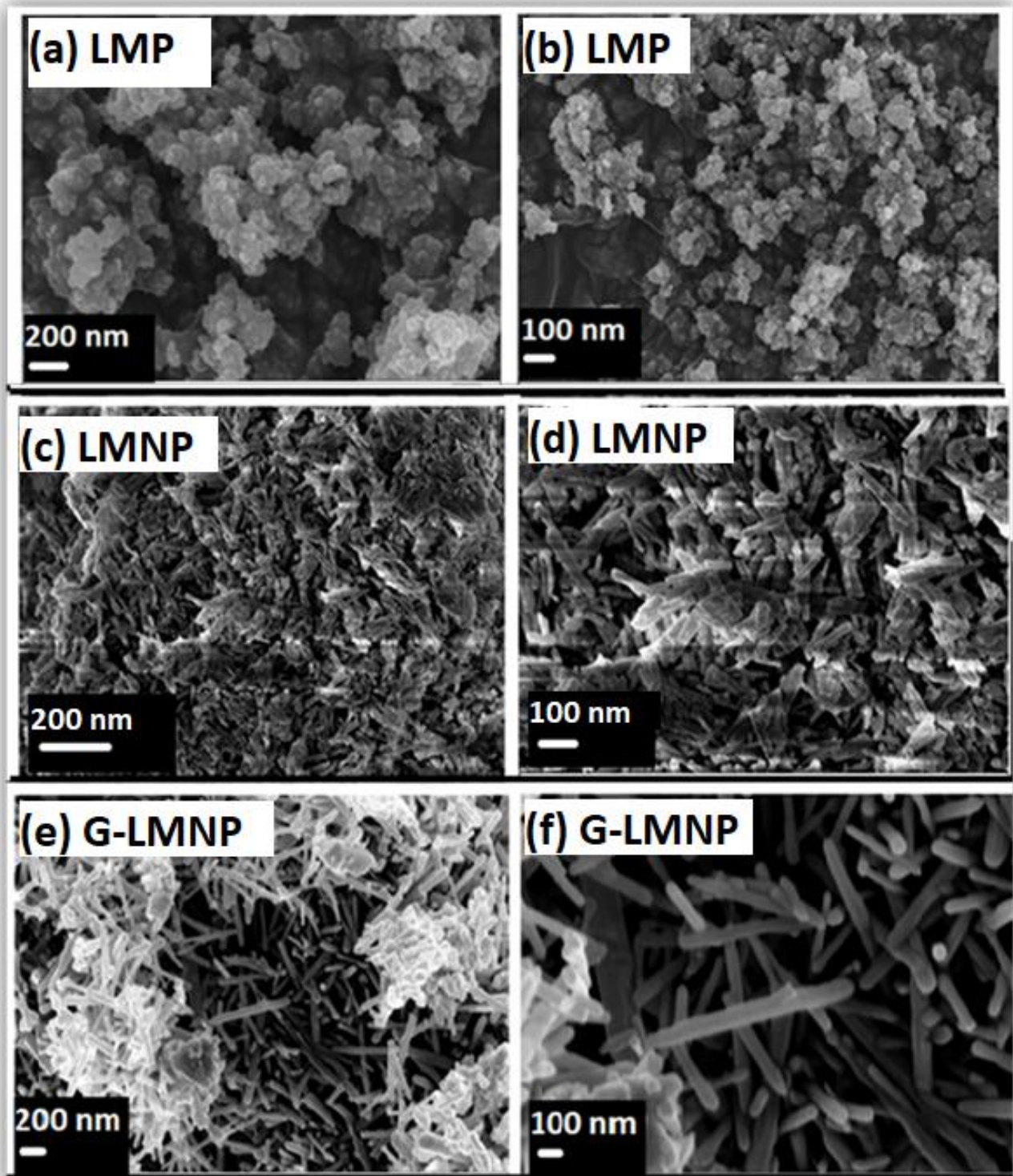


**Figure 3.7:** SEM image of (a) and (b) the  $\text{LiMnPO}_4$  nanowires, [(c) and (d)] nickel doped  $\text{LiMnPO}_4$  and [(e) and (f)] graphene coated LMNP

**Fig. 3.8** showed  $\text{LiMnPO}_4$ , LMNP and G-LMNP particle size measured by Small-angle X-ray scattering (SAXS) system. SAXS proved to be well-suited method for determining the size of materials with very small particle size. In **Fig 3.8 (a)**, the LMP exhibited slightly bell shaped peak of pair distance distribution functions confirming a spherically-shaped material with diameter 50 nm. The majority of LMNP nanoparticles appeared at small-angle scattering patterns with the average sizes ranging from 58-70 nm. G-LMNP average size is at 60 – 80 nm followed by the decreased scattering fraction number ( $P$ ) of bigger particles observed at 120-135 nm. Normally, small angle scattering pattern can be considered as the sum of the scattering patterns of the individual particles contained in the scattering volume fraction [35]. Thus, the scattered intensity generally decreases with scattering angle and the investigation is established on assessment of the scattering by a single particle.

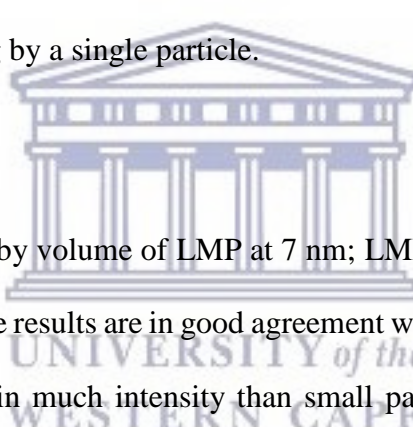


**Fig 3.8 (b)** revealed weighted by volume of LMP at 7 nm; LMNP at 7 nm and 70 nm; and G-LMNP at 90 and 130 nm. These results are in good agreement with HRTEM results. The bigger particles at larger angles obtain much intensity than small particles at small angles [35,36] Therefore, as seen in **Fig. 3.8 (b)**, the intensity signal obtained from LMP and LMNP at 7 nm was clearly invisible in G-LMNP than the intensity at large angles (i.e 90 nm and 130 nm in diameter). This, therefore, concluded that larger particles overshadowed the intensity signal of the particles at small angles.



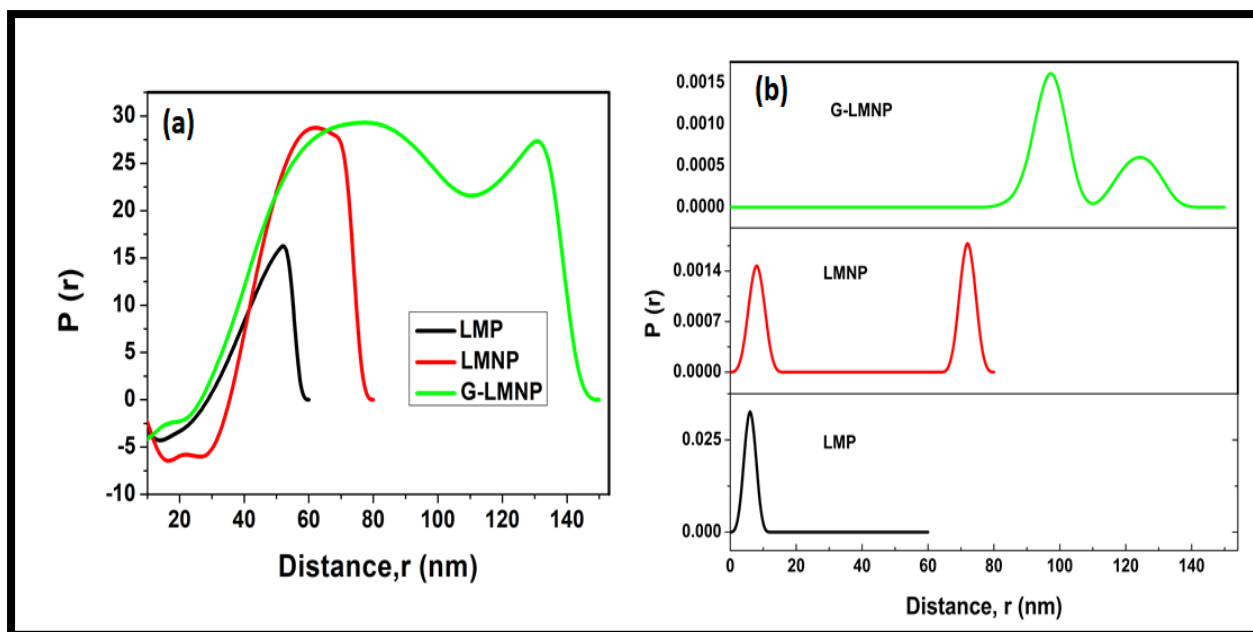


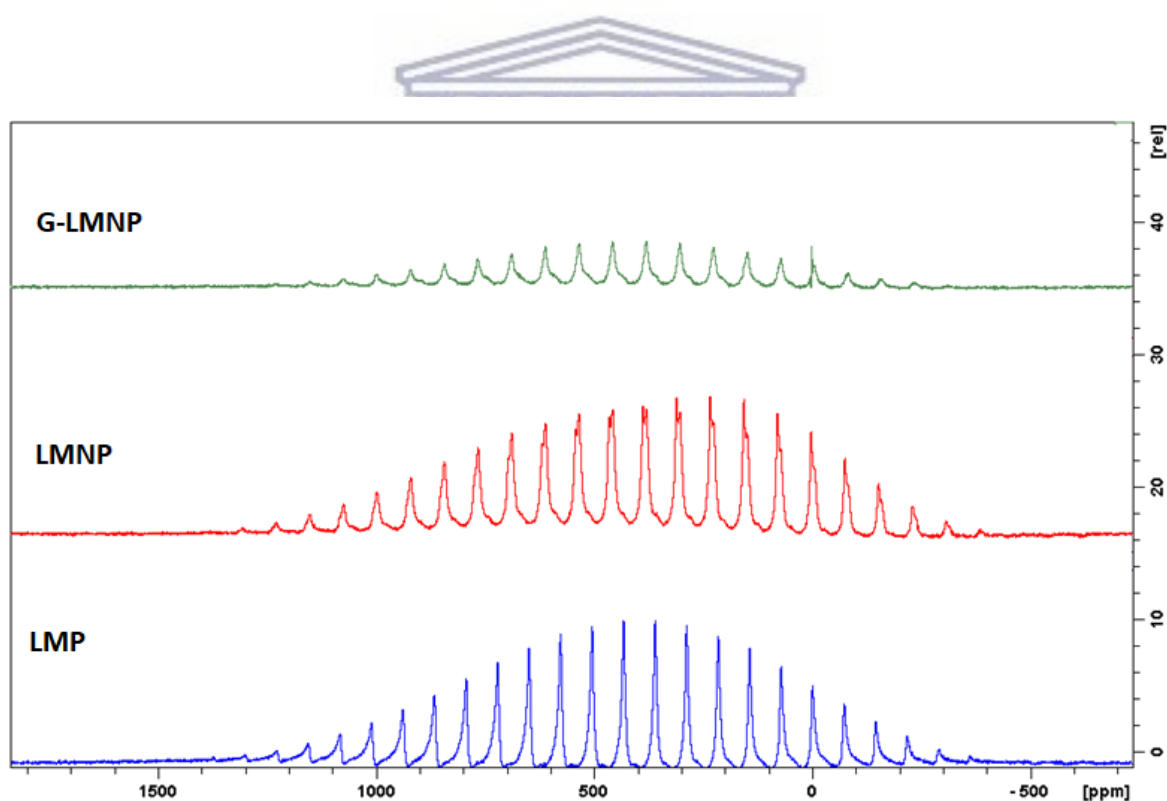
**Figure 3.8:** (a) SAXS Particle size distribution in number weighted, (b) volume weighted

The lithium local environment with structural and electronic anisotropies of the as-prepared materials was explored using Solid-state Nuclear Magnetic Resonance (SSNMR) Spectroscopy. The  $^7\text{Li}$  MAS NMR spectra of  $\text{LiMnPO}_4$ , LMNP and G-LMNP are shown in **Fig. 3.9**. All spectra are dominated by the interaction of the lithium nuclei with magnetic moments of the unpaired electron spins [37]. The isotropic peaks was identified by varying the spin rate whilst the magnetic field strength was varied to distinguish the interaction between chemical shift and quadrupolar effect strength

All the materials displayed three isotropic  $^7\text{Li}$  resonance and broad spinning sideband manifolds arising from the paramagnetic interaction between the lithium nucleus and transition metal unpaired electrons [38]. The isotropic peaks for LMP are at 360, 583 and 869 ppm, where the intense peak at 583 ppm is assigned to the lithium ions in the tetrahedral site of the olivine structure, peak at 360 ppm arises from the majority of Pnmb polymorph [39], which was also

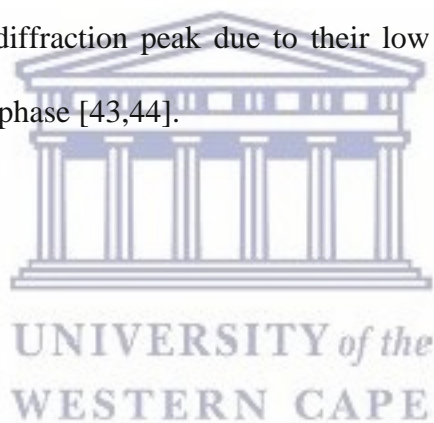
observed in XRD investigations. The peak at 869 ppm generally originate from vacancies on both the lithium and manganese sites (i.e., Mn 16d site and the interstitial 16c sites) [40].

The  $^7\text{Li}$  MAS NMR shifts in  $\text{LiMPO}_4$  are assigned to the hyperfine interaction of the  $^7\text{Li}$  nuclei with the unpaired electrons on the transition metal atom through a Li-O-M bond. Whereby, a transfer of unpaired electron density occurs from the metal d-orbitals, through the oxygen p-orbitals to the lithium s-orbital, resulting in paramagnetic susceptibility [41,42]. It is known that the governing interactions between the Li nuclear spins and Mn electron spins should be through-bond (Fermi-contact) or through-space (dipolar). With the Fermi-contact interactions, the peak shifts to  $>500$  ppm [37].



**Figure 3.9:**  $^7\text{Li}$  MAS NMR spectra for  $\text{LiMnPO}_4$ , LMNP and G-LMNP at a MAS spinning speed of  $\sim 15$  kHz.

X-ray powder diffraction (XRD) is a rapid analytical technique primarily used for phase identification of a crystalline material and provides information on unit cell dimensions. The sample was finely ground, homogenized, and average bulk composition determined. XRD reveals information on the structure, crystallinity and lattice spacing of the material. **Fig 3.10** showed the XRD patterns of  $\text{LiMnPO}_4$ , LMNP and G-LMNP. LMP showed strong intensities of (011), (111), (200), (131) and (042) patterns indexed into an orthorhombic  $Pnmb$  space group olivine structure (JCPDC 74-0375). XRD pattern of LMNP exhibited two extra peaks at  $2\theta = 23^\circ\text{C}$  and  $34^\circ\text{C}$  which are due to the crystalline  $\text{LiNiPO}_4$  (JCPDS# 881297) which is formed by nickel-doped LMP. The XRD patterns of G-LMNP exhibited single phase of LMP, all diffraction peaks are strong and narrow, indicating highly crystalline sample. There is no obvious graphene or carbon diffraction peak due to their low content or it may be due to graphene being in amorphous phase [43,44].



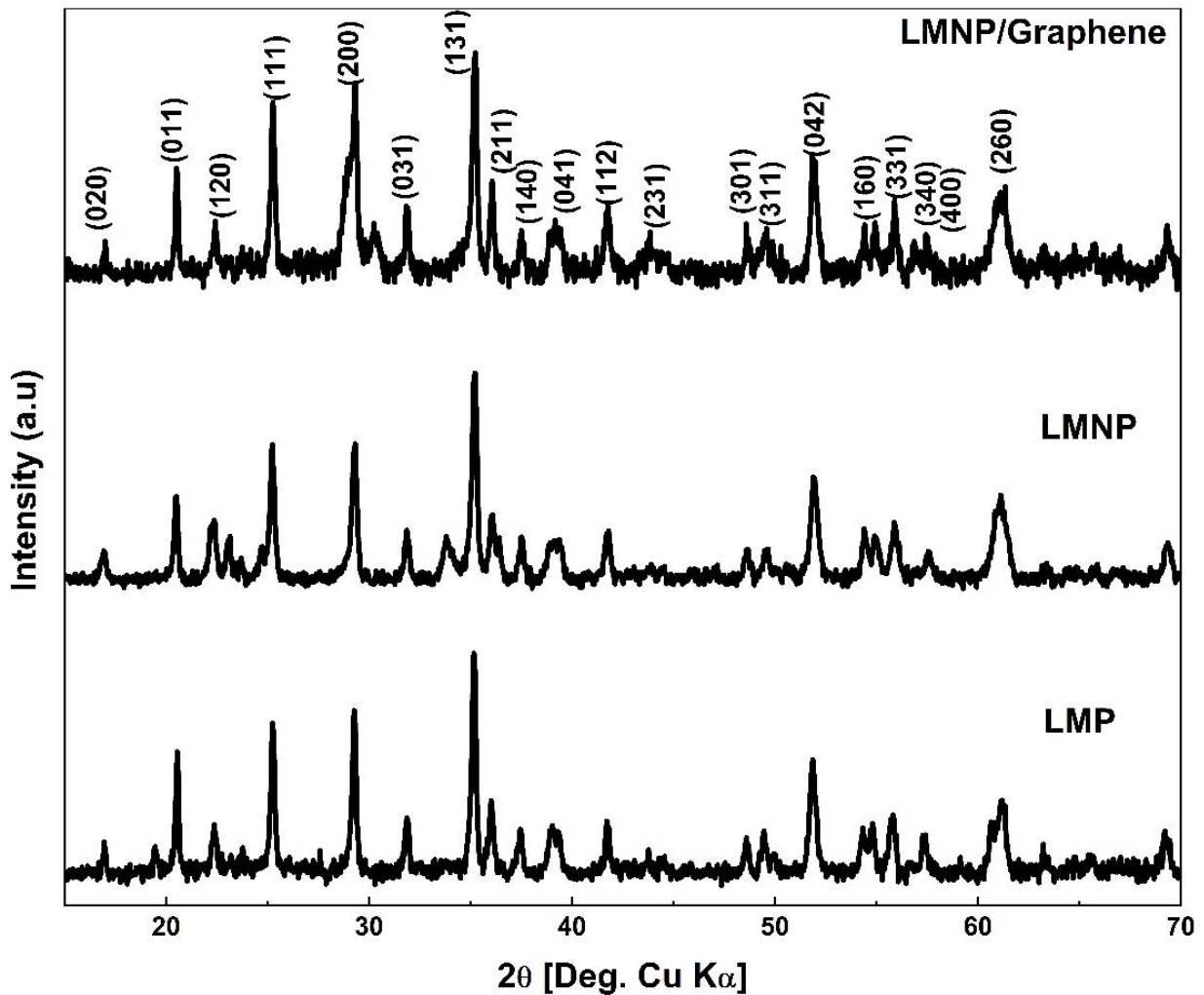


**Figure 3.10:** XRD patterns of  $\text{LiMnPO}_4$ , LMNP and G-LMNP

The IR spectrum features of  $\text{LiMnPO}_4$  have been previously assigned based on group theory analysis, isotope studies, and direct comparison to similar olivine structures ( $\text{LiMePO}_4$ ; Me = Fe, Mg, Ni) [45]. **Fig. 3.11** showed that the spectra are dominated by the intramolecular vibrations of the  $\text{PO}_4^{3-}$  anion which confirm the presence of phospho-olivine phase in  $\text{LiMnPO}_4$ . These internal vibrations consist of three components; the antisymmetric  $\text{PO}_4^{3-}$  stretching mode at  $1065\text{ cm}^{-1}$ , the symmetric  $\text{PO}_4^{3-}$  stretching mode around  $974\text{ cm}^{-1}$  and the antisymmetric bending mode between  $650\text{ cm}^{-1}$  and  $530\text{ cm}^{-1}$  [17,33]. The  $3431\text{ cm}^{-1}$  band is attributed to the O-H stretching vibration. Nickel doped  $\text{LiMnPO}_4$  FTIR spectrum displayed

the same spectrum as LMP meaning the structure of olivine was not affected by the modification. G-LMNP is dominated by intramolecular vibration bands of the  $\text{PO}_4^{3-}$  anion at  $650 - 530 \text{ cm}^{-1}$  which confirm the presence of phospho-olivine phase in the material. Also the C-C vibrational frequency occurred at  $1630 \text{ cm}^{-1}$  thus confirming the presence of graphene in G-LMNP [17]. The FTIR results are in good accordance with the observed XRD results.

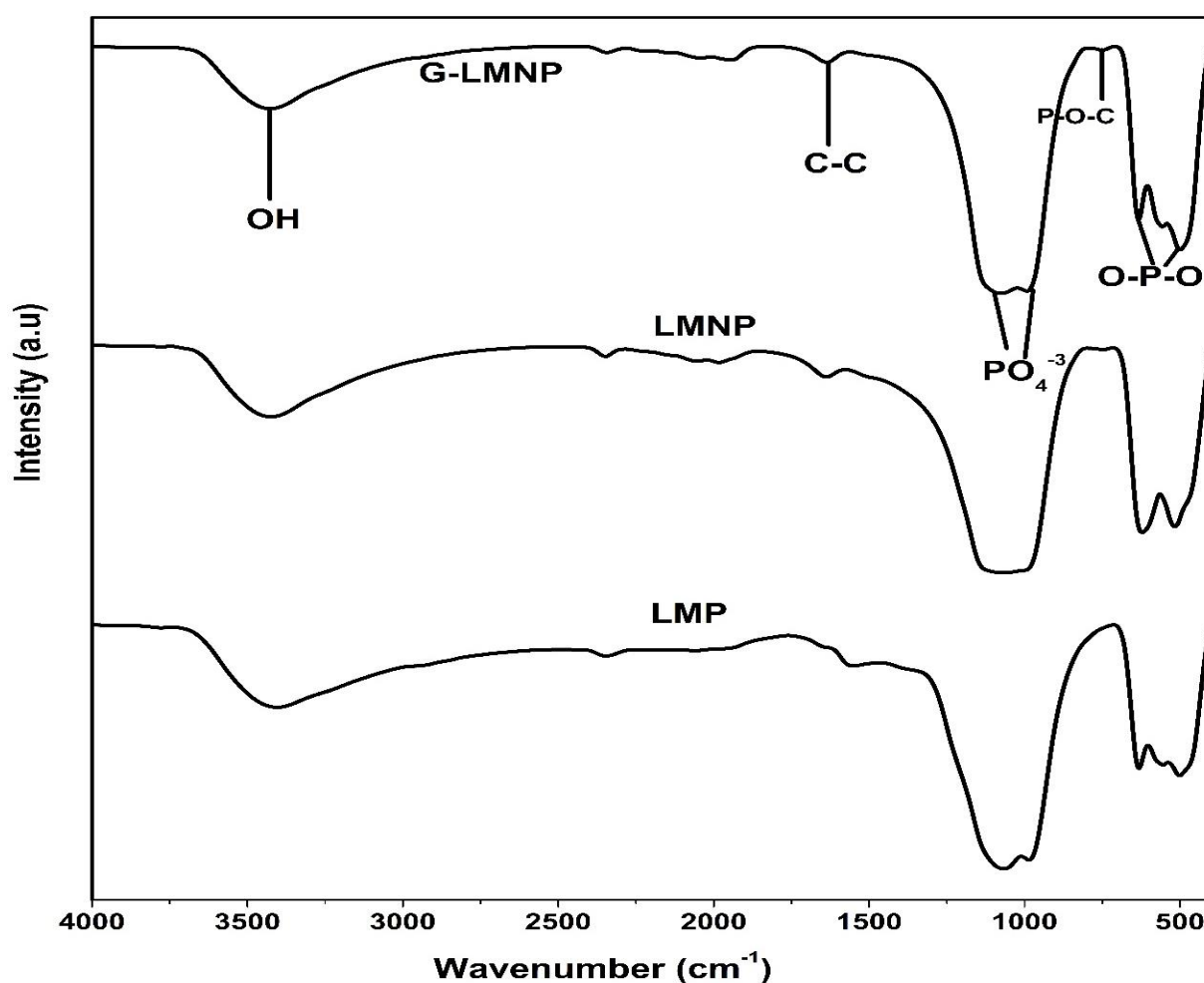


**Figure 3.11:** FTIR spectra of  $\text{LiMnPO}_4$ , LMNP and G-LMNP

**Fig. 3.12** showed the Raman spectra of the  $\text{LiMnPO}_4$ , nickel doped  $\text{LiMnPO}_4$  and G-LMNP.

From **Fig. 3.7**, the Raman spectra of the LMP and LMNP nanorods showed the band at 950

$\text{cm}^{-1}$  corresponding to the symmetric  $A_g$  mode, and the two low intensity bands at 983 and  $1006 \text{ cm}^{-1}$  due to the asymmetric stretching modes of the  $\text{PO}_4^{-3}$  anion.

Raman spectrum of the G-LMNP sample showed two bands at 1463 and  $1526 \text{ cm}^{-1}$  representing D and G bands, respectively, along with  $\text{PO}_4^{-3}$  anion bands. D is disordered band of  $\text{sp}^3$  and G is the graphene band of  $\text{sp}^2$ -type. Hence, the Raman spectra of G-LMNP confirmed successful coating of graphene on LMNP.

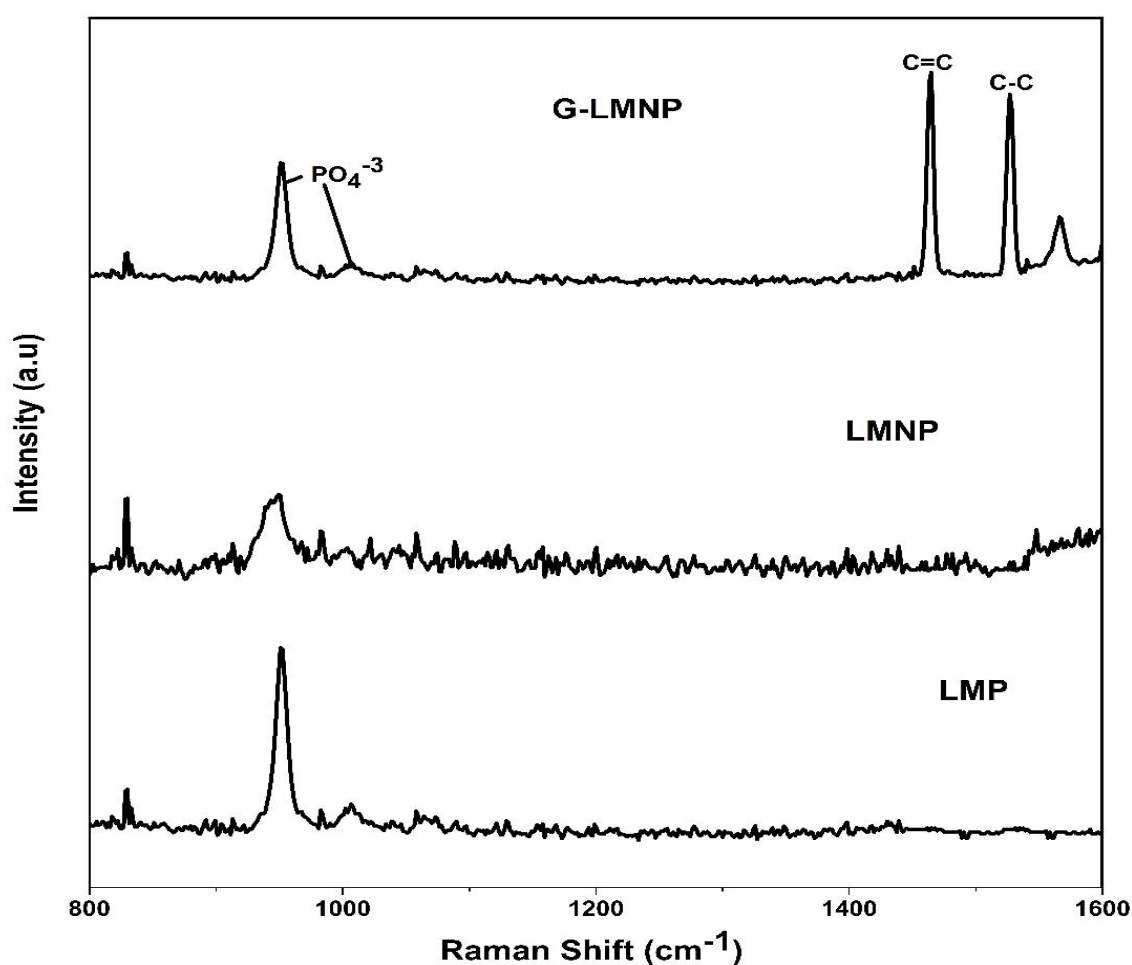


**Figure 3.12:** Raman spectra of  $\text{LiMnPO}_4$ , LMNP and G-LMNP

### 3.3.3 Electrochemical studies of single electrode LiMnPO<sub>4</sub> based electrodes

The investigation of LiMnPO<sub>4</sub>, nickel doped LiMnPO<sub>4</sub> and G-LMNP as working electrode against Ag/AgCl (3 M KCl) in the three electrode system was carried out using nickel foam as the current collector and 1 M Li<sub>2</sub>SO<sub>4</sub> aqueous electrolyte in the voltage window of 0.2 – 1.2 V.

**Fig. 3.13** compared the CV curves of LiMnPO<sub>4</sub>, LMNP and G-LMNP at 5 mV s<sup>-1</sup>. All the CV curves exhibited a redox peaks attributed to surface oxidation/reduction of Mn<sup>2+</sup>/Mn<sup>3+</sup> due to the charge transfer across the electrode/electrolyte interface during insertion of Li<sup>+</sup> into LiMnPO<sub>4</sub> [46]. The pair of redox peaks further revealed the Faradaic battery nature of the charge storage mechanism in these materials. The possible charge storage mechanism can be considered according to the following reaction.



The peak potential difference ( $\Delta E_p$ ) in the redox peaks has been considerably decreased in the nanocomposite sample (from 0.22 V in LMP to 0.19 V in G-LMNP) which suggest an improved electrochemical reversibility. This may be due to the fact that conducting graphene layers provided new pathways for electron transfer thus facilitating the redox reaction. It can be clearly observed that the peak current intensities have remarkably increased for the G-LMNP material. This indicates more facile lithium ion transfer will result in the better reaction kinetics.

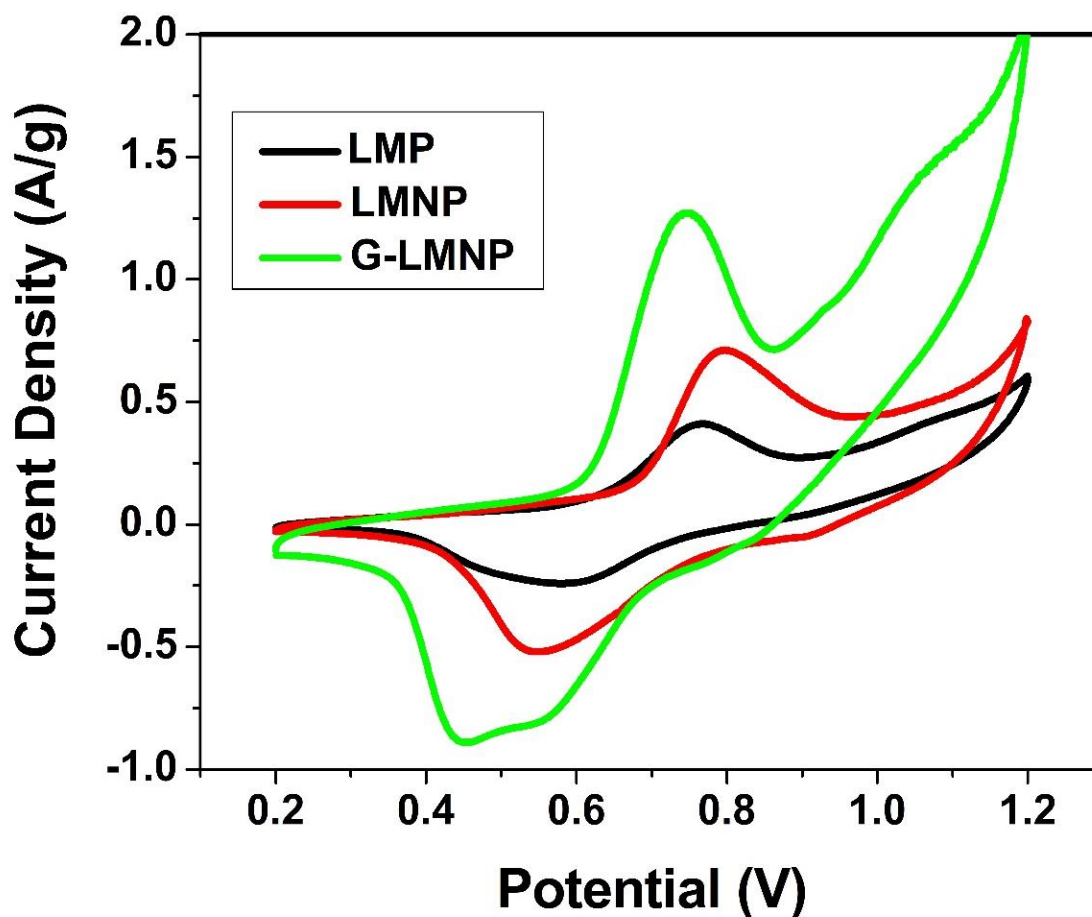


**Figure 3.13:** Comparative curves for olivine LiMnPO<sub>4</sub> nicked doped LiMnPO<sub>4</sub> and G-LMNP from cyclic voltammetry at a scan rate of 5 mV s<sup>-1</sup>.

Cyclic voltammetry was also used to calculate the capacitance of all the samples. The charge stored during forward and backward scans directly corresponds to the area under the CV curves. The capacitances were calculated according to the following equation:

$$C_{sp} = \frac{Q}{mV} \tag{8}$$



$C_{sp}$  is the specific capacitance,  $Q$  is the charge obtained from CV results,  $m$  is the mass of the electrode and  $V$  is potential window. The capacitance obtained from the integrated area under the cathodic peak at the scan rate of  $5 \text{ mV s}^{-1}$  indicate that the nanocomposite G-LMNP exhibited higher capacitance of  $138 \text{ F g}^{-1}$  for the insertion of lithium and reduction of  $\text{Mn}^{3+}$  to  $\text{Mn}^{2+}$ , and the corresponding values for LMP and LMNP were  $44.1 \text{ F g}^{-1}$  and  $60.7 \text{ F g}^{-1}$  respectively. G-LMNP revealed higher capacitance than in the pristine  $\text{LiMnPO}_4$  at the same scan rates which suggests an improvement in electrochemical performance. This can be attributed to the conducting graphene which enhanced its conductivity.

Galvanostatic charge-discharge technique is a reliable electrochemical method for the evaluation of electro-capacitive behaviour of electrode materials in energy storage device and also complements the cycling characteristics. **Fig. 3.14** represented the respective galvanostatic charge/discharge curves of  $\text{LiMnPO}_4$ , LMNP and G-LMNP at the same current density of  $1 \text{ A g}^{-1}$ . The nonlinear charge/discharge profiles further demonstrates the pseudo capacitive behaviour of  $\text{LiMnPO}_4$ . The charge-discharge curves further showed plateau observed at about  $0.5 \text{ V}$  and  $0.75 \text{ V}$  corresponding to deintercalation/intercalation  $\text{Li}^+$  in  $\text{LiMnPO}_4$ . These results are in good agreement with redox peaks observed in the CV curves above. The G-LMNP revealed superior electrochemical performance of the nanocomposite electrode. The specific capacitance  $C_{sp}$  ( $\text{F g}^{-1}$ ), calculated from the three electrode materials were found to be  $30 \text{ F g}^{-1}$ ,  $37 \text{ F g}^{-1}$  and  $60 \text{ F g}^{-1}$  at  $1 \text{ A g}^{-1}$  for LMP, LMNP and G-LMNP respectively. This proves the conductivity of graphene played a major role in enhancing electrochemical performance of  $\text{LiMnPO}_4$  as witnessed by the increase in specific capacitance.

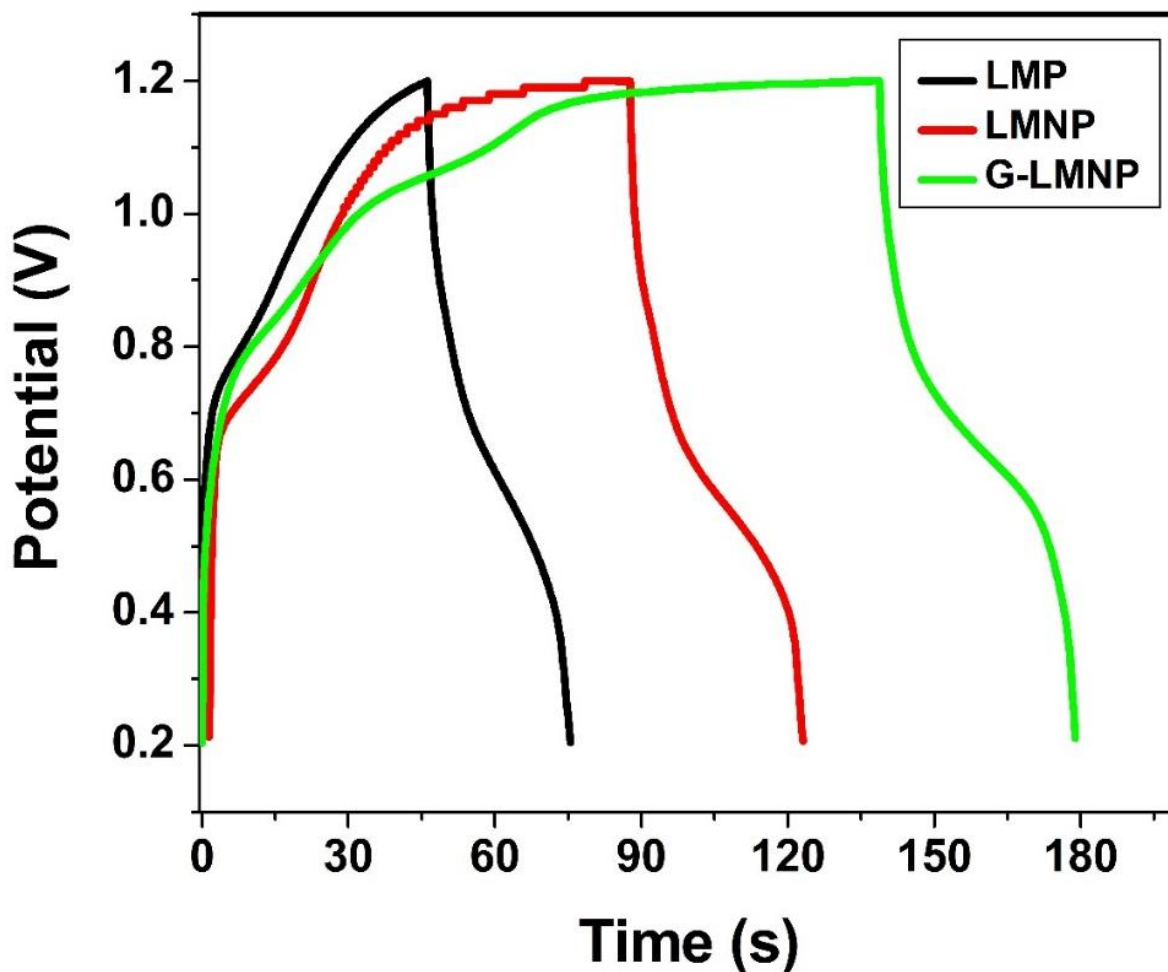


**Figure 3.14:** Comparative galvanostatic charge-discharge for LiMnPO<sub>4</sub>, nickel doped LiMnPO<sub>4</sub> and G-LMNP curves at a constant current density of 1 A g<sup>-1</sup>.

### 3.3.4 Lithium ion capacitor (LIC): LMP || AC

LIC was composed of LMP, LMNP and G-LMNP as positive-working electrode and AC as negative-counter electrode in 1 M Li<sub>2</sub>SO<sub>4</sub> electrolyte. Properly balancing the weight of both electrodes based on their specific capacitance is essential for constructing lithium ion capacitor.

### 3.3.4.1 Estimation of electrochemical potential window

LiMnPO<sub>4</sub> and the modified materials were further interrogated as an asymmetric lithium ion capacitor in aqueous 1 M Li<sub>2</sub>SO<sub>4</sub> electrolyte solution. **Fig. 3.15** compared the CV curves of LMP (between 0.2 and 1.2V vs Ag/AgCl) and AC (between -0.2 and 0.7 V vs Ag/AgCl). CV curve of AC showed a perfect rectangular shaped voltammogram indicating non-faradaic charge transfer reaction. This indicates the desirable fast charging/discharging capability derived from high power density.

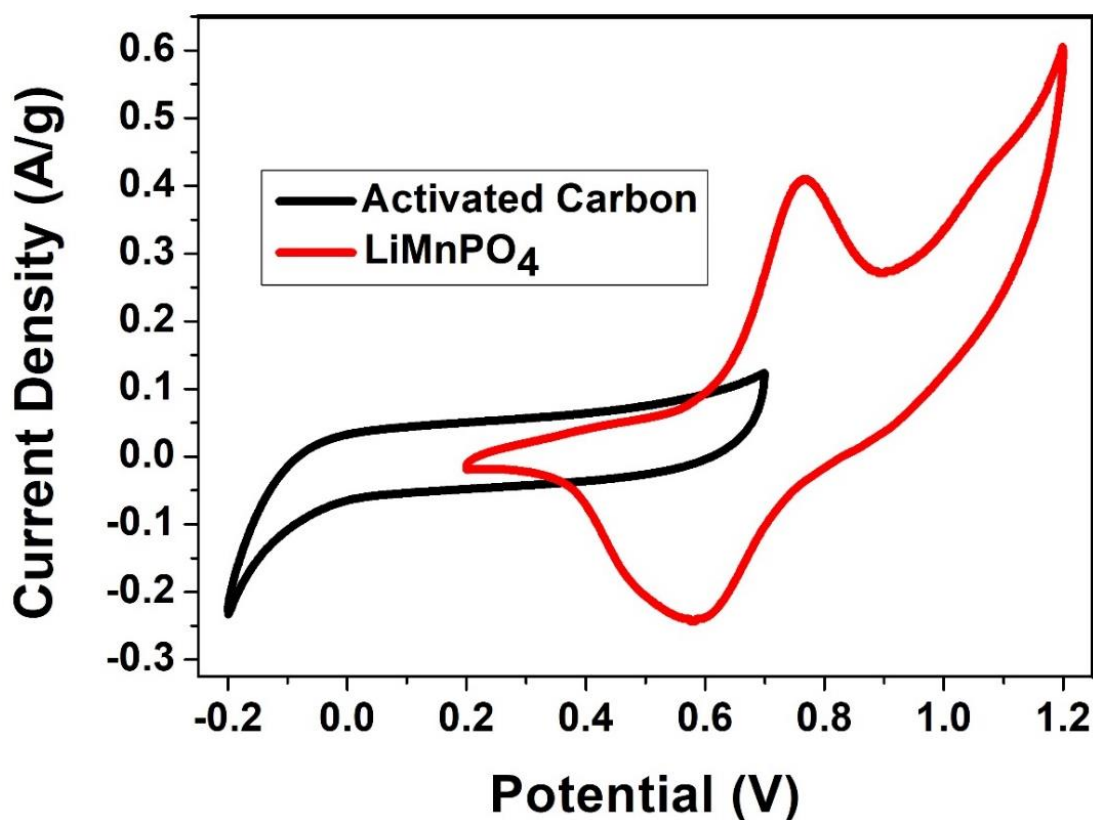


**Figure 3.15:** Comparative cyclic voltammograms of LiMnPO<sub>4</sub> and activated carbon (AC) at a scan rate of 5 mV.s<sup>-1</sup> in aqueous 1 M Li<sub>2</sub>SO<sub>4</sub> electrolyte.

The calculated  $C_{sp}$  from CV was  $30 \text{ F g}^{-1}$  at  $5 \text{ mV s}^{-1}$ . The mass balancing of the two electrodes in LICs is  $q_+ = q_-$ , where  $q_+$  represent the charges stored at the positive electrode and  $q_-$  represent the charge stored at the negative electrode. The mass balancing was:

$$\frac{m_+}{m_-} = \frac{C_{sp-} \times \Delta E_-}{C_{sp+} \times \Delta E_+} \quad (9)$$

$$\text{Thus } \frac{m_{LMP}}{m_{AC}} = \frac{30 \text{ F g}^{-1} \times 0.9 \text{ V}}{44.1 \text{ F g}^{-1} \times 1 \text{ V}} \quad (10)$$

$$\frac{m_{LMP}}{m_{AC}} = 0.61 \quad (11)$$

$$m_{LMP} = 0.61 m_{AC} \quad (12)$$



The same procedure was adopted for all mass ratio calculations with data obtained from CV. The mass ratio obtained for LMNP || AC was  $m_{LMNP} = 0.44.m_{AC}$  and for G-LMNP || AC was  $m_{G-LMNP} = 0.20.m_{AC}$ . The lithium ion capacitor cell was assembled at 2 V.

### 3.3.4.2 Electrochemical performance of $\text{LiMnPO}_4$ || AC, LMNP || AC and G-LMNP || AC lithium ion capacitors.

**Fig. 3.16** compared CV curves for LMP || AC, LMNP || AC and G-LMNP || AC lithium ion capacitors in 1 M  $\text{Li}_2\text{SO}_4$  aqueous electrolyte at scan rates of  $5 \text{ mV s}^{-1}$ . All the CV curves showed large current response and exhibits nearly rectangular shape in voltage range of 0 – 1

V, characteristic of double layer capacitive material attributed to the AC low contact resistance. The deviation from the rectangular shape observed around 1 to 1.75 V is due to Faradic pseudo capacitive contribution arising from  $\text{LiMnPO}_4$  redox reaction. G-LMNP displayed largest enclosed area in CV than other materials. Generally the performance trend follows as: G-LMNP > LMNP > LMP at the same scan rates. The CV curve for G-LMNP nanocomposite revealed that synergistic effects between LMNP and graphene resulted in improved conductivity and enhanced specific capacitance.

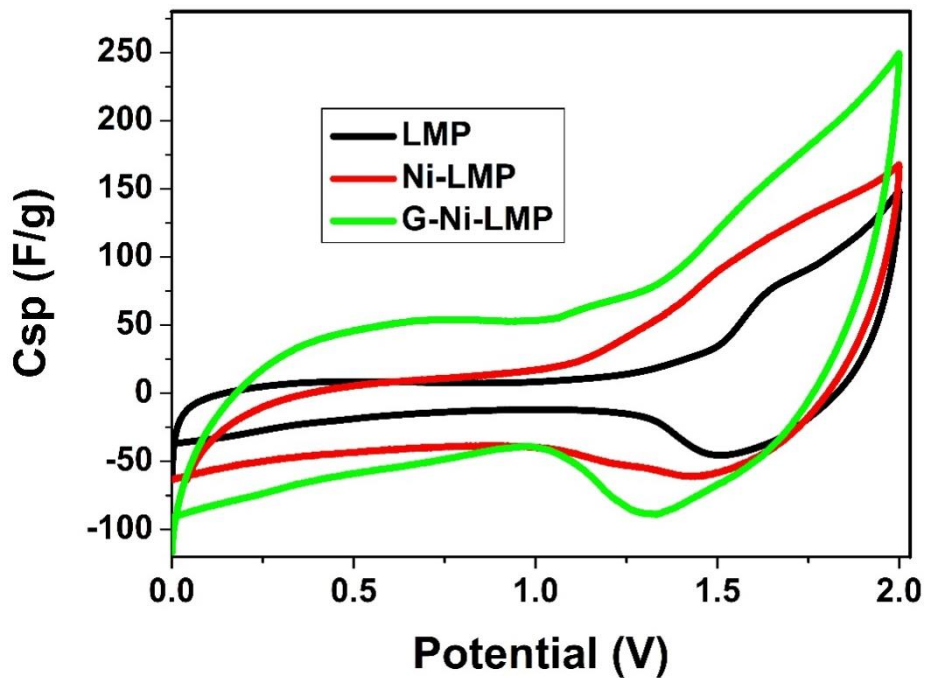


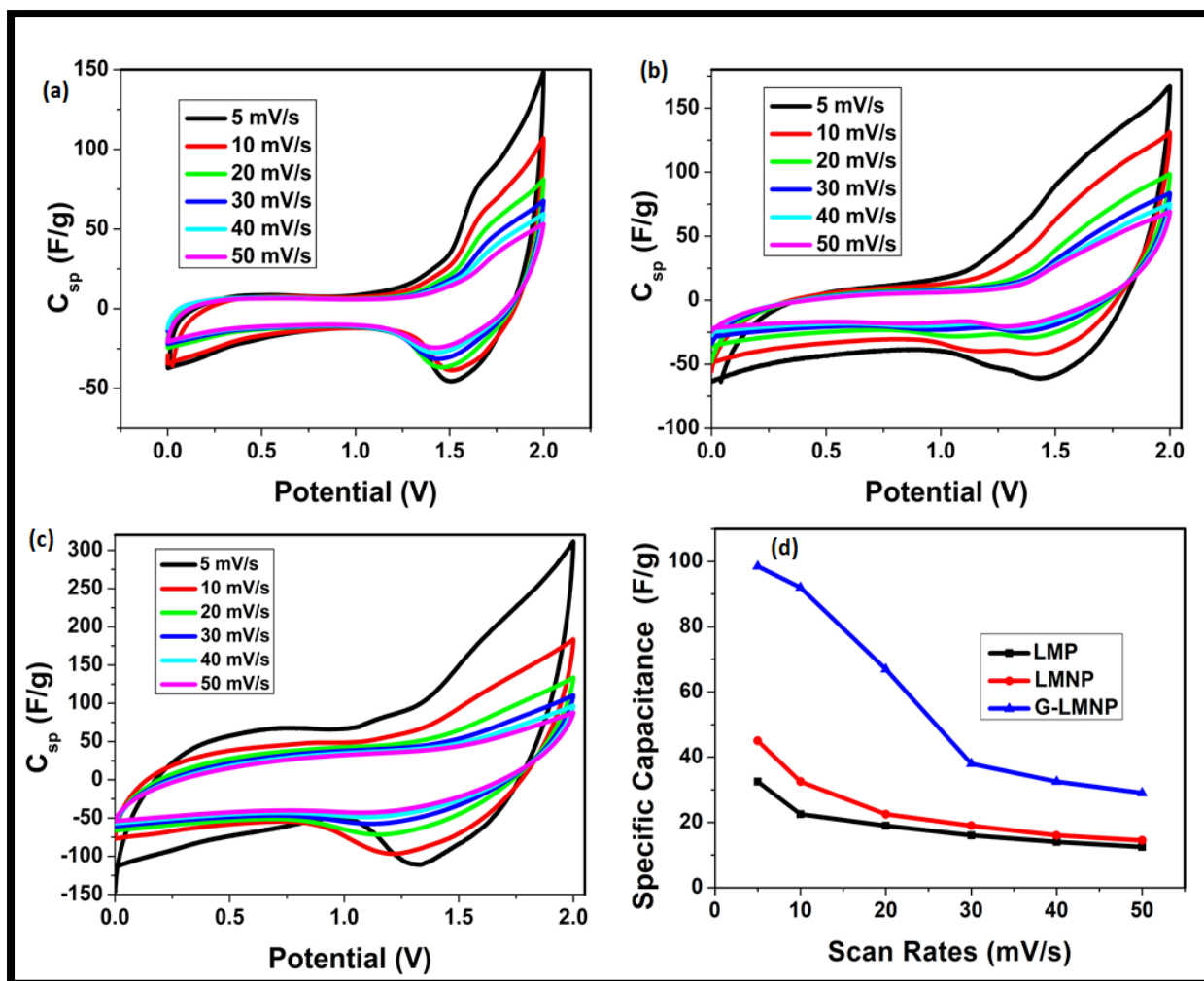
**Figure 3.16:** Comparative curves for olivine  $\text{LiMnPO}_4 \parallel \text{AC}$ , LMNP  $\parallel \text{AC}$  and G-LMNP  $\parallel \text{AC}$  lithium ion capacitors cyclic voltammetry at a scan rate of  $5 \text{ mV} \cdot \text{s}^{-1}$ .

**Fig 3.17** showed cyclic voltammograms of LMP  $\parallel \text{AC}$ , LMNP  $\parallel \text{AC}$  and G-LMNP  $\parallel \text{AC}$  at the scan rates of  $5 - 50 \text{ mV s}^{-1}$ . It is clearly visible that CV profile exhibit redox peaks at around 1.5/1.55 V revealing the faradaic signature in LMP  $\parallel \text{AC}$  full device. The shape of the CV

curves didn't change as the scan rates was increased suggesting good rate capability. LMNP||AC and G-LMNP||AC CV curves resemble that of LMP except that at higher scan rates of 40 – 50 mV s<sup>-1</sup>, they showed typical capacitor profiles indicating fast charge/discharge properties leading to improved power density.

**Fig. 3.17 (d)** showed the calculated specific capacitance from CV profiles for all the system. An increase in  $C_{sp}$  as the scan rate decreased was observed, revealing that at slow scan rates there was more time for the electrolyte ions to diffuse to the electrode materials. G-LMNP||AC device exhibited high specific capacitance of 98 F g<sup>-1</sup> than 35 F g<sup>-1</sup> for LMP||AC and 48 F g<sup>-1</sup> for LMNP||AC achieved at 5 mV s<sup>-1</sup>.





UNIVERSITY of the  
WESTERN CAPE

**Figure 3.17:** Comparison of cyclic voltammetry for (a) LiMnPO<sub>4</sub> || AC, (b) LMNP || AC, (c) G-LMNP || AC and (d) rate capability of lithium ion capacitors at various scan rates

Furthermore, the electrochemical performance was investigated using galvanostatic charge/discharge (GCD) measurements. **Fig. 3.18** depicted GCD profiles for LMP || AC, LMNP || AC and G-LMNP || AC lithium ion capacitors at current density of 0.1 A g<sup>-1</sup>. The obtained charge/discharge curves showed nearly identical counterparts during charge and discharge, suggesting excellent reversibility. The nonlinear charge-discharge profile demonstrates the pseudocapacitive behaviour of LMP as seen in the single electrode GCD results (see **Fig 3.14**). For better analysis of the capacitive behaviour of the synthesised LMP,

LMNP and G-LMNP materials, studies were made using various current densities (see **Fig 3.19**)

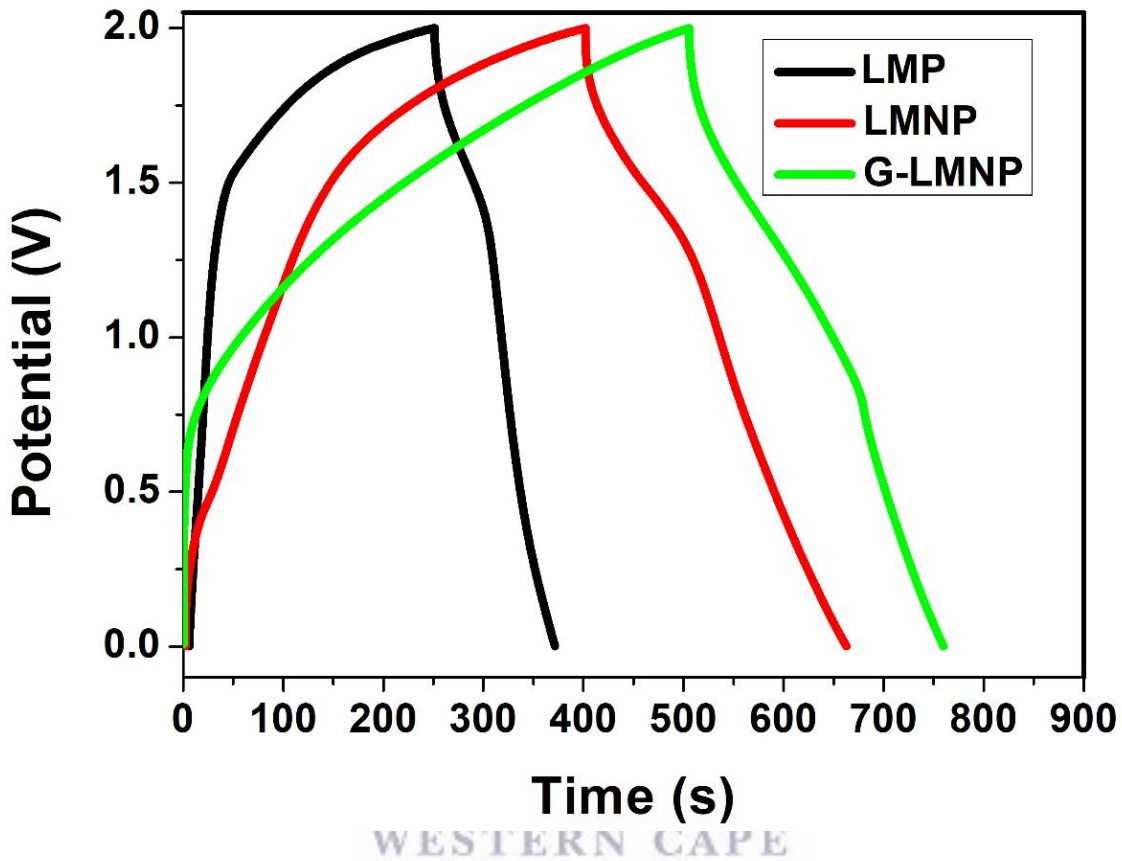


**Figure 3.18:** Galvanostatic charge-discharge curves at constant current density for  $\text{LiMnPO}_4 \parallel \text{AC}$ ,  $\text{LMNP} \parallel \text{AC}$  and  $\text{G-LMNP} \parallel \text{AC}$  lithium ion capacitors. Electrolyte: aqueous 1 M  $\text{Li}_2\text{SO}_4$

**Fig. 3.19** (a) -(c) showed the galvanostatic charge- discharge curves from  $0.1 \text{ A g}^{-1}$  to  $0.5 \text{ A g}^{-1}$  current densities. The discharge curves nearly symmetric with their corresponding charging counterpart, which showed excellent electrochemical reversibility for LIC device. The nonlinear charge-discharge profiles further indicate the pseudo capacitive behaviour of LMP and composites. The specific capacitance values were calculated using equation 2 mentioned



above for full cell. **Fig 3.19 (d)** shows rate capability at various current densities. G-LMNP||AC LIC achieved maximum specific capacitance of  $60 \text{ F g}^{-1}$  followed by LMNP||AC with specific capacitance of  $54 \text{ F g}^{-1}$  and LMP||AC exhibited the least value of  $24 \text{ F g}^{-1}$  at current density of  $0.1 \text{ A g}^{-1}$ . All the materials displayed an initial decay with a large decrease in specific capacitance ( $C_{sp}$ ) and then reached a stable level at high current densities. The gradually decreased capacitance as the current density increases is due to the diffusion-controlled kinetics process for the electrode reactions of LMP electrode. The G-LMNP exhibit low internal resistance compared to other electrodes due to the conductivity nature of graphene, enhancing the electrochemical performance of the electrode material.



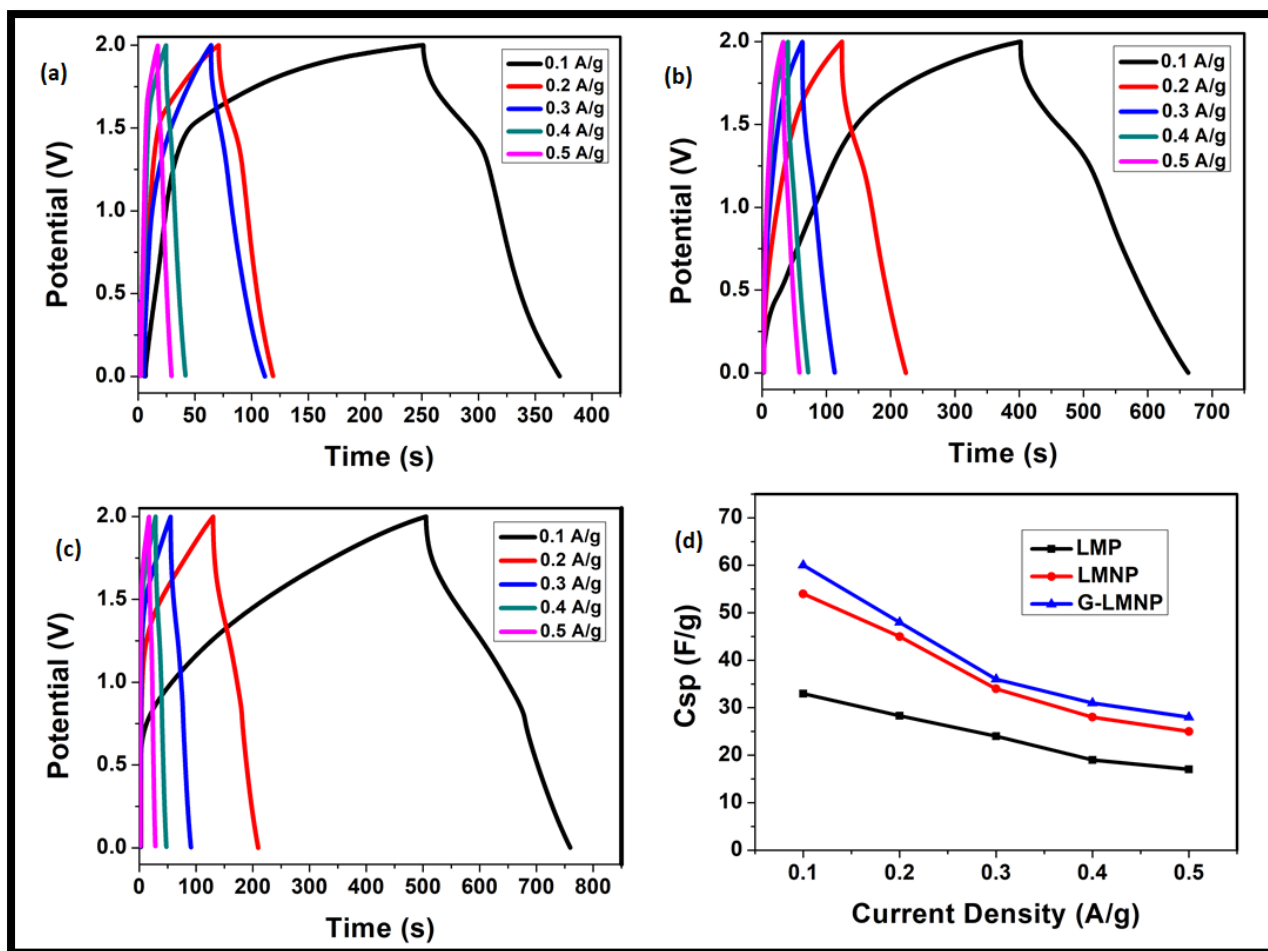


**Figure 3.19:** Comparison of galvanostatic charge-discharge for olivine (a)  $\text{LiMnPO}_4 \parallel \text{AC}$ , (b)  $\text{LMNP} \parallel \text{AC}$ , (c)  $\text{G-LMNP} \parallel \text{AC}$  of lithium ion capacitors at various current densities and (d) capacitance curves ( $C_{sp}$  vs. current densities)

According to the galvanostatic discharge curves, maximum specific energy and power densities can be calculated using the equations 3 and 4 mentioned above. **Fig. 3.20** showed the graphical correlation of energy and power densities. The Ragone plot is a common tool for evaluating the performance of energy storage devices. The energy density for the  $\text{G-LMNP} \parallel \text{AC}$  LIC device is about  $14 \text{ Wh kg}^{-1}$  at current density of  $0.1 \text{ A g}^{-1}$ . The specific energy is still  $5 \text{ Wh kg}^{-1}$  with a power density of  $19 \text{ kW kg}^{-1}$  at  $0.5 \text{ A g}^{-1}$  current density. The  $\text{G-LMNP} \parallel \text{AC}$  LIC performance is comparable to other works reported on lithium ion capacitor devices [9,47–49].

This results compared with the ones reported on literature suggests that this LIC device is suitable for high power energy storage applications. The LMNP || AC exhibited energy density and maximum power density of  $9.4 \text{ Wh kg}^{-1}$  and  $16.1 \text{ kW kg}^{-1}$ , respectively. The LMP || AC exhibited, energy density and maximum power density of  $5.7 \text{ Wh kg}^{-1}$  and  $8 \text{ kW kg}^{-1}$ , respectively. The remarkably enhanced energy and power density observed in G-LMNP electrode is assigned to good electronic conductivity graphene.

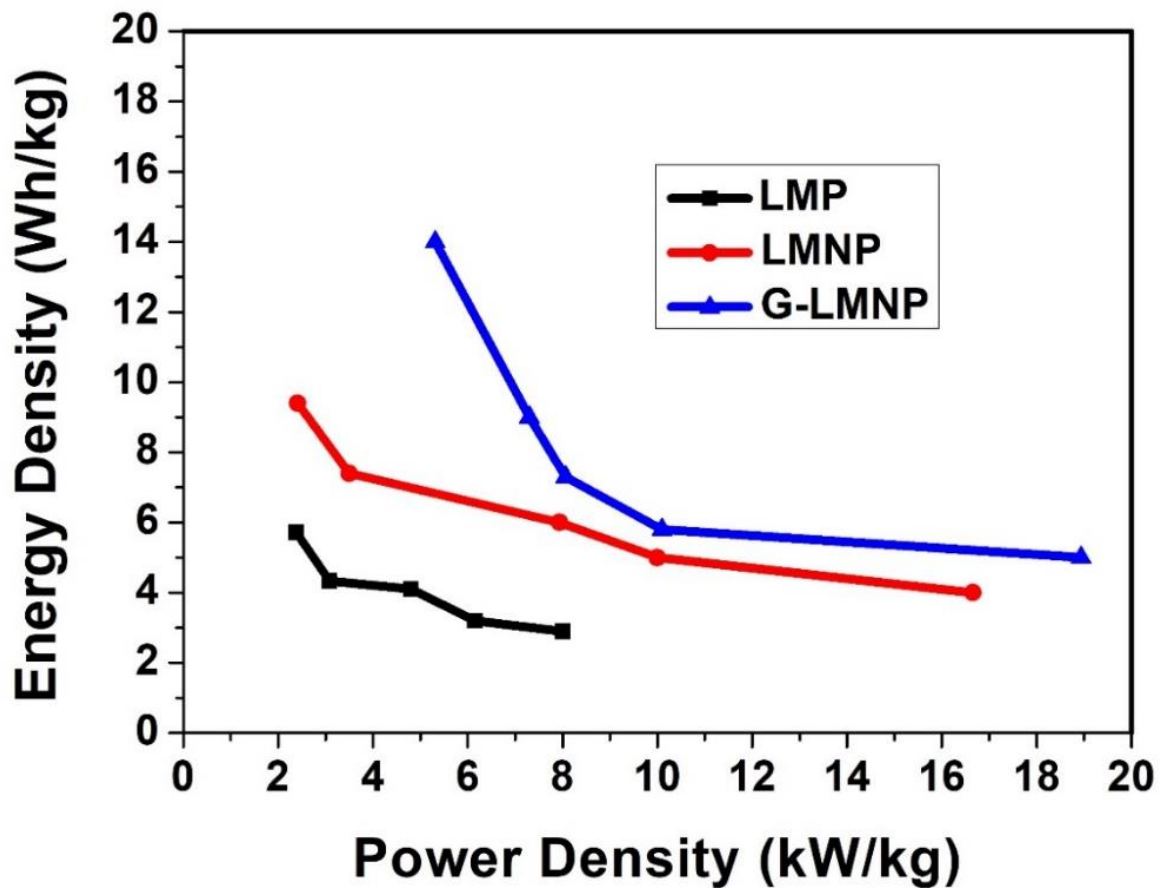


**Figure 3.20:** Ragone plots of  $\text{LiMnPO}_4$  || AC, LMNP || AC and G-LMNP || AC at different density

Electrochemical impedance spectroscopy (EIS) provides information on impedance changes of the electrode surface after each modification step. **Fig. 3.21** showed Nyquist plot of LMP || AC, LMNP || AC and G-LMNP || AC.

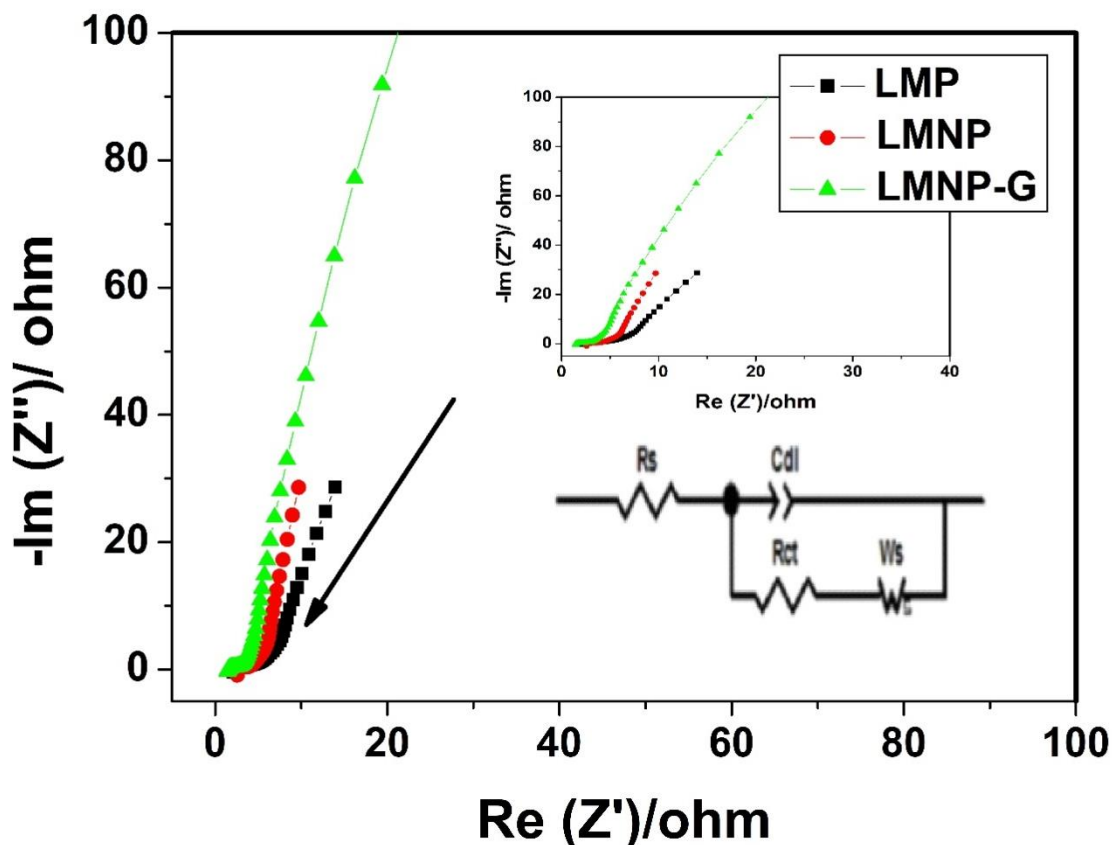


**Figure 3.21:** Comparative Nyquist plots for  $\text{LiMnPO}_4$  || AC, LMNP || AC and G-LMNP || AC and the inset show proposed equivalent circuit.

Each plot gave a well-defined single semi-circle at high frequency and an inclined line at low frequency attributed to Warburg impedance associated with lithium ion diffusion in the bulk of the electrode. This is an indication that during lithium deinsertion/insertion, the kinetics of the electrode process is controlled by the diffusion process in the low frequency region and by the charge transfer in the high frequency region. A possible equivalent circuit is provided as

the inset of **Fig. 3.21** for interpretation.  $R_s$  represent internal resistance which has a total of intrinsic resistance of active materials.  $R_{ct}$  denotes faradaic charge transfer resistance which is equivalent to the semicircle diameter of impedance.  $C_{dl}$  is the double layer capacitance and  $W_s$  represents Warburg impedance [50]. All the electrodes showed the semi-circle with LMNP-G nanocomposite exhibiting smaller semicircle corroborated by obtained fitted parameters.

The  $R_{ct}$  for LMP || AC, LMNP || AC and G-LMNP || AC lithium ion capacitor was 23.5, 3.9 and 1.4  $\Omega$ , respectively. It can be observed that the  $R_{ct}$  for G-LMNP || AC is smaller than that of LMNP || AC and LMP || AC, suggesting that the modified nanocomposite electrode has low charge transfer resistance indicating fast kinetics. Moreover, the low frequency line is more vertical in G-LMNP nanocomposite, showing better capacitive behaviour and lower ionic diffusion resistance due to the addition of graphene [51]. The results further confirm improved electrochemical performance of G-LMNP || AC lithium ion capacitor attributed to surface coating of graphene nanosheets. The wider conduction bands of graphene sheets contributed in the enhancement of the electrochemical performance of G-LMNP nanocomposite.

The high performance of G-LMNP electrode material is further highlighted using the bode plots. **Fig. 3.22** represented the Bode phase-impedance plots for LMP || AC, LMNP || AC and G-LMNP || AC. The lower  $R_{ct}$  observed from the Nyquist plot corresponds to the shift of phase angle to high frequency observed from Bode plots of G-LMNP nanocomposite associated with fast electron transfer.

The phase angle obtained for LMP || AC, LMNP || AC and G-LMNP || AC lithium ion capacitor were 65, 71 and 80°, respectively. The G-LMNP positive electrode showed higher phase angle revealing improved conductivity of the material. As it is known that between 20 - 45° the

material possess semiconductor characteristics compared to  $0^\circ$  (insulator) and  $90^\circ$  which is of pure metal (more conducting). This values may be further compared to that of an ideal EDLC which is close to  $90^\circ$  [49]. The lower phase angle suggest the electrodes possesses pseudo capacitive behaviour due to the faradaic reaction occurring at the positive electrode

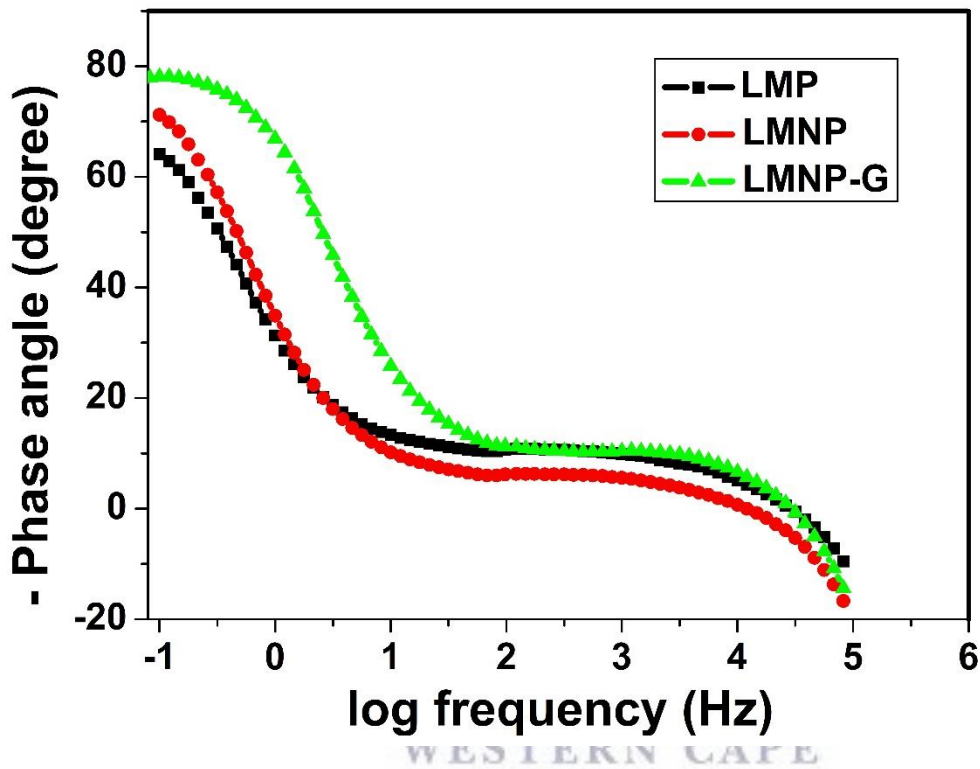


**Figure 3.22:** Comparative Bode plots of  $\text{LiMnPO}_4 \parallel \text{AC}$ ,  $\text{LMNP} \parallel \text{AC}$ ,  $\text{G-LMNP} \parallel \text{AC}$

### 3.3.4.3 Cycling performance

The cycle life is an important factor in energy storage electrode material; cyclic stability experiments measured by galvanostatic charge-discharge represented a reliable analysis method for establishing the long-term stability of LICs electrodes. **Fig. 3.23** shows the specific capacitance of the three electrodes within 750 cycles at  $0.4 \text{ A g}^{-1}$ . As cycle number is increased, the specific capacitance gradually decreased. The capacitance retention for  $\text{LMP} \parallel \text{AC}$ ,  $\text{LMNP} \parallel \text{AC}$  and  $\text{G-LMNP} \parallel \text{AC}$  were 61%, 71% and 83%, respectively after 750 cycles. The

excellent stability of the G-LMNP || AC lithium ion capacitor showed the device can be charged and discharged without significant deterioration. The values obtained after 750 cycles correspond to a specific energy of 4.49 Wh kg<sup>-1</sup> and power density of 10 kW kg<sup>-1</sup>.

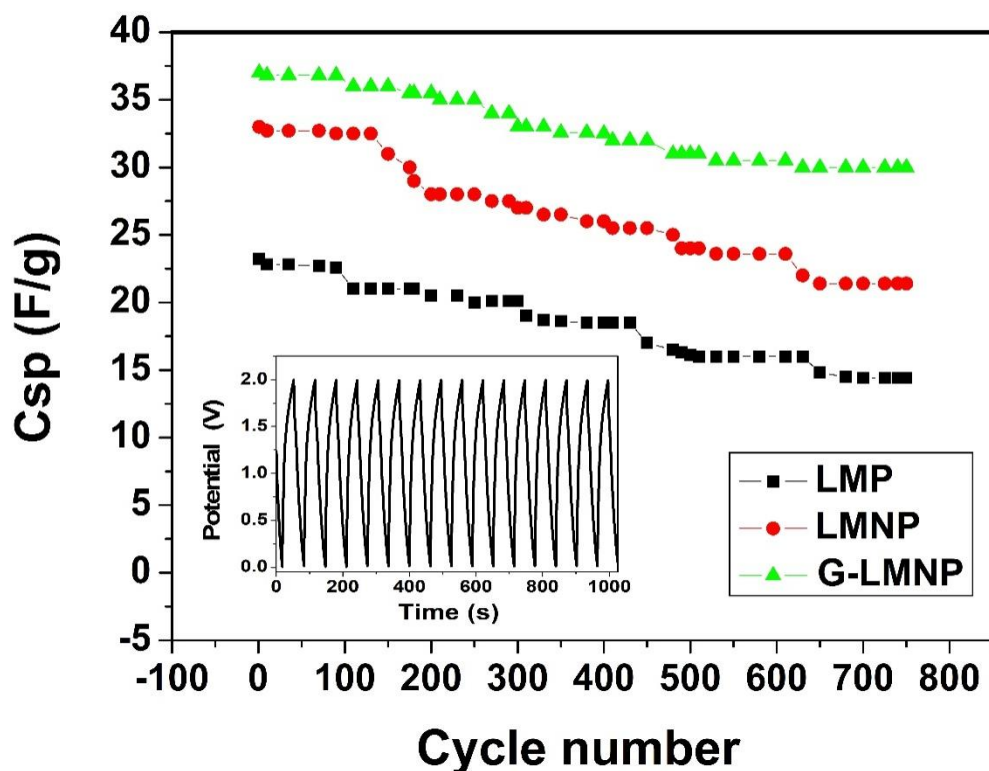


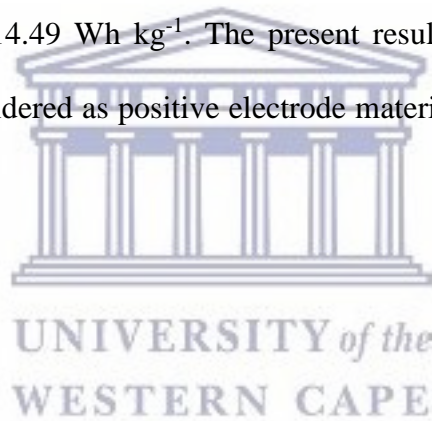
**Figure 3.23:** Cycling performance of LiMnPO<sub>4</sub> || AC, LMNP || AC, G-LMNP || AC lithium ion capacitor with continuous charge-discharge profiles as inset

### 3.4 Summary

The goal of this work was to explore and study the electrochemical performance of lithium manganese phosphate (LiMnPO<sub>4</sub>) and its nickel and graphene derivatives as lithium ion capacitor electrode materials. Nickel foam was used as a current collector because of its excellent performance. G-LMNP exhibited better performance when compared to LMP and LMNP. The LMP || AC exhibited specific capacitance, energy density and maximum power



density of 30 F g<sup>-1</sup>, 5.7 Wh kg<sup>-1</sup> and 6.1 kW kg<sup>-1</sup>, respectively. The LMNP||AC exhibited specific capacitance, energy density and maximum power density of 54 F g<sup>-1</sup>, 9.4 Wh kg<sup>-1</sup> and 16.7 kW kg<sup>-1</sup>, respectively. The G-LMNP exhibited a high capacitance of 60 F g<sup>-1</sup> at the current density of 0.1 A g<sup>-1</sup> and excellent cycle stability when 750 cycle experiment was conducted with 17 % capacitance loss. The improved capacitance performance of G-LMNP was influenced by surface coating of graphene which is conductive in nature. Furthermore, the improved conductivity was observed from *R<sub>ct</sub>* obtained in EIS. The *R<sub>ct</sub>* values for G-LMNP, LMNP and LMP were 1.4, 3.9 and 23.5 Ω, respectively. Noting that there has been no known report on G-LMNP||AC lithium ion capacitor in the literature so far; yet, the work is important because it showed good stability, high rates capability, high maximum power density (18 kW kg<sup>-1</sup>) and energy density of 14.49 Wh kg<sup>-1</sup>. The present results suggest that the G-LMNP nanocomposite could be considered as positive electrode material for high power lithium ion capacitors.



### 3.5 References

- [1] N. Böckenfeld, R.S. Kühnel, S. Passerini, M. Winter, A. Balducci, Composite LiFePO<sub>4</sub>/AC high rate performance electrodes for Li-ion capacitors, J. Power Sources. 196 (2011) 4136–4142. doi:10.1016/j.jpowsour.2010.11.042.
- [2] L. Xu, S. Wang, X. Zhang, T. He, F. Lu, H. Li, J. Ye., A facile method of preparing

- LiMnPO<sub>4</sub>/reduced graphene oxide aerogel as cathodic material for aqueous lithium-ion hybrid supercapacitors, *Appl. Surf. Sci.* 428 (2017) 977–985. doi:10.1016/j.apsusc.2017.09.247.
- [3] L. Ye, Q. Liang, Y. Lei, X. Yu, C. Han, W. Shen, Z. Huang, F. Kang, Q. Yang, A high performance Li-ion capacitor constructed with Li<sub>4</sub>Ti<sub>5</sub>O<sub>12</sub>/C hybrid and porous graphene macroform, *J. Power Sources.* 282 (2015) 174–178. doi:http://dx.doi.org/10.1016/j.jpowsour.2015.02.028.
- [4] N. Arun, A. Jain, V. Aravindan, S. Jayaraman, W. Chui Ling, M.P. Srinivasan, Nanostructured spinel LiNi<sub>0.5</sub>Mn<sub>1.5</sub>O<sub>4</sub> as new insertion anode for advanced Li-ion capacitors with high power capability, *Nano Energy.* 12 (2015) 69–75. doi:10.1016/j.nanoen.2014.12.006.
- [5] H. Du, H. Yang, C. Huang, J. He, H. Liu, Y. Li, Graphdiyne applied for lithium-ion capacitors displaying high power and energy densities, *Nano Energy.* 22 (2016) 615–622. doi:10.1016/j.nanoen.2016.02.052.
- [6] C. Liu, C. Zhang, H. Song, C. Zhang, Y. Liu, X. Nan, Guozhang Cao, Mesocrystal MnO cubes as anode for Li-ion capacitors, *Nano Energy.* 22 (2016) 290–300. doi:10.1016/j.nanoen.2016.02.035.
- [7] D. Puthusseri, V. Aravindan, S. Madhavi, S. Ogale, Improving the energy density of Li-ion capacitors using polymer-derived porous carbons as cathode, *Electrochim. Acta.* 130 (2014) 766–770. doi:10.1016/j.electacta.2014.03.079.
- [8] Y. Xie, F. Song, C. Xia, H. Du, Preparation of carbon-coated lithium iron phosphate/titanium nitride for a lithium-ion supercapacitor, *New J. Chem.* 39 (2015) 604–613. doi:10.1039/c4nj01169d.

- [9] S.R.S. Prabaharan, A. Anslin Star, A.R. Kulkarni, M.S. Michael, Nano-composite  $\text{LiMnPO}_4$  as New Insertion Electrode for Electrochemical Supercapacitors, *Curr. Appl. Phys.* 15 (2015) 1624–1633. doi:10.1016/j.cap.2015.09.009.
- [10] V. Aravindan, J. Gnanaraj, Y.-S. Lee, S. Madhavi,  $\text{LiMnPO}_4$  – A next generation cathode material for lithium-ion batteries, *J. Mater. Chem. A*. 1 (2013) 3518–3539. doi:10.1039/c2ta01393b.
- [11] Y. Bi, W. Yang, B. Yang, C. Wang, D. Wang, S. Shi, Influence of  $\text{Li}_3\text{V}_2(\text{PO}_4)_3$  complexing on the performance of  $\text{LiMnPO}_4$  based materials utilized in lithium ion battery, *Ceram. Int.* 40 (2014) 7637–7641. doi:http://dx.doi.org/10.1016/j.ceramint.2013.12.081.
- [12] C. Chen, A. Yuan, H. Zhao, J. Xu, Electrochemical behavior of olivine-type  $\text{LiMnPO}_4$ -based material in a mild aqueous electrolyte, *Ionics (Kiel)*. 18 (2012) 635–641. doi:10.1007/s11581-012-0677-0.
- [13] H. Guo, C. Wu, L. Liao, J. Xie, S. Zhang, P. Zhu., Performance Improvement of Lithium Manganese Phosphate by Controllable Morphology Tailoring with Acid-Engaged Nano Engineering, *Inorg. Chem.* 54 (2015) 667–674. doi:10.1021/ic5026075.
- [14] Y. Dong, Y. Zhao, H. Duan, Z. Liang, Enhanced electrochemical performance of  $\text{LiMnPO}_4$  by  $\text{Li}^+$ -conductive  $\text{Li}_3\text{VO}_4$  surface coatings, *Electrochim. Acta*. 132 (2014) 244–250. doi:http://dx.doi.org/10.1016/j.electacta.2014.03.171.
- [15] Z. Qin, X. Zhou, Y. Xia, C. Tang, Z. Liu, Morphology controlled synthesis and modification of high-performance  $\text{LiMnPO}_4$  cathode materials for Li-ion batteries, *J. Mater. Chem.* 22 (2012) 21144–21153. doi:10.1039/c2jm30821e.

- [16] C. Neef, C. Jähne, H.-P. Meyer, R. Klingeler, Morphology and Agglomeration Control of LiMnPO<sub>4</sub> Micro- and Nanocrystals, *Langmuir*. 29 (2013) 8054–8060. doi:10.1021/la3046498.
- [17] N.S. Norberg, R. Kostecki, FTIR spectroscopy of a LiMnPO<sub>4</sub> composite cathode, *Electrochim.Acta*. 56 (2011) 9168–9171. doi:http://dx.doi.org/10.1016/j.electacta.2011.07.116.
- [18] A. González, E. Goikolea, J.A. Barrena, R. Mysyk, Review on supercapacitors: Technologies and materials, *Renew. Sustain. Energy Rev.* 58 (2016) 1189–1206. doi:10.1016/j.rser.2015.12.249.
- [19] Y. Sun, J. Tang, F. Qin, J. Yuan, K. Zhang, J. Li, et al., Hybrid Lithium-Ion Capacitors with Asymmetric Graphene Electrodes, *J. Mater. Chem. A*. 5 (2017) 13601–13609. doi:10.1039/C7TA01113J.
- [20] A.K. Geim, K.S. Novoselov, The rise of graphene, *Nat. Mater.* 6 (2007) 183–191.
- [21] A. Zhamu, Graphene Surface-enabled lithium ion-exchanging cells: next-generation high-power energy storage devices, (2011) 3785–3791.
- [22] H. Yu, K. Xie, J. Hu, C. Shen, J. Wang, B. Wei, The importance of raw graphite size to the capacitive properties of graphene oxide, *RSC Adv.* 6 (2016) 17023–17028. doi:10.1039/C5RA24501J.
- [23] K. Makgopa, P.M. Ejikeme, C.J. Jafta, K. Raju, M. Zeiger, V. Presser, K. Ozoemena, A high-rate aqueous symmetric pseudocapacitor based on highly graphitized onion-like carbon/birnessite-type manganese oxide nanohybrids, *J. Mater. Chem. A*. (2015).

- [24] C.J. Jafta, F. Nkosi, L. le Roux, M.K. Mathe, M. Kebede, K. Makgopa, K. Ozoemena., Manganese oxide/graphene oxide composites for high-energy aqueous asymmetric electrochemical capacitors, *Electrochim. Acta.* 110 (2013) 228–233. doi:<http://dx.doi.org/10.1016/j.electacta.2013.06.096>.
- [25] W.K. Chee, H.N. Lim, I. Harrison, K.F. Chong, Z. Zainal, C.H. Ng, Performance of Flexible and Binderless Polypyrrole/Graphene Oxide/Zinc Oxide Supercapacitor Electrode in a Symmetrical Two-Electrode Configuration, *Electrochim. Acta.* 157 (2015) 88–94. doi:<http://dx.doi.org/10.1016/j.electacta.2015.01.080>.
- [26] M.S. Michael, Role of Cu substitution on the pseudocapacitive performance of nanoplatelet shaped spinels,  $\text{Ni}_x\text{Cu}_z\text{Co}_y\text{O}_4$  { $x=1-z$ ,  $y=2-z$ ,  $z=0.2$ }, *Electrochim. Acta.* 120 (2014) 350–358. doi:[10.1016/j.electacta.2013.12.056](http://dx.doi.org/10.1016/j.electacta.2013.12.056).
- [27] A.K. Nanjundan, R.R. Gaddam, M. Suresh, S.R. Varanasi, D. Yang, S. Bhatia, Porphyrin-graphene oxide frameworks for long life sodium ion batteries, *J. Mater. Chem. A.* (2017). doi:[10.1039/C7TA02370G](http://dx.doi.org/10.1039/C7TA02370G).
- [28] C. Lu, X. Wang, X. Zhang, H. Peng, Y. Zhang, G. Wang, G. Cao, N. Umirov, Z. Bakenov, Effect of graphene nanosheets on electrochemical performance of  $\text{Li}_4\text{Ti}_5\text{O}_{12}$  in lithium-ion capacitors, *Ceram. Int.* 43 (2017) 6554–6562. doi:[10.1016/j.ceramint.2017.02.083](http://dx.doi.org/10.1016/j.ceramint.2017.02.083).
- [29] S. Yaragalla, A.P. Meera, N. Kalarikkal, S. Thomas, Chemistry associated with natural rubber – graphene nanocomposites and its effect on physical and structural properties, *Ind. Crop. Prod.* 74 (2015) 792–802. doi:[10.1016/j.indcrop.2015.05.079](http://dx.doi.org/10.1016/j.indcrop.2015.05.079).
- [30] R. Ramachandran, M. Saranya, V. Velmurugan, B.P.C. Raghupathy, S. Kwan, A. Nirmala, Effect of reducing agent on graphene synthesis and its influence on charge storage

towards supercapacitor applications q, Appl. Energy. 153 (2015) 22–31.  
doi:10.1016/j.apenergy.2015.02.091.

[31] M. Zhao, G. Huang, B. Zhang, F. Wang, X. Song, Characteristics and electrochemical performance of  $\text{LiFe}_{0.5}\text{Mn}_{0.5}\text{PO}_4/\text{C}$  used as cathode for aqueous rechargeable lithium battery, J. Power Sources. 211 (2012) 202–207. doi:http://dx.doi.org/10.1016/j.jpowsour.2012.03.049.

[32] J. Chen, M.J. Vacchio, S. Wang, N. Chernova, P.Y. Zavalij, M.S. Whittingham, The hydrothermal synthesis and characterization of olivines and related compounds for electrochemical applications, Solid State Ionics. 178 (2008) 1676–1693.  
doi:http://dx.doi.org/10.1016/j.ssi.2007.10.015.

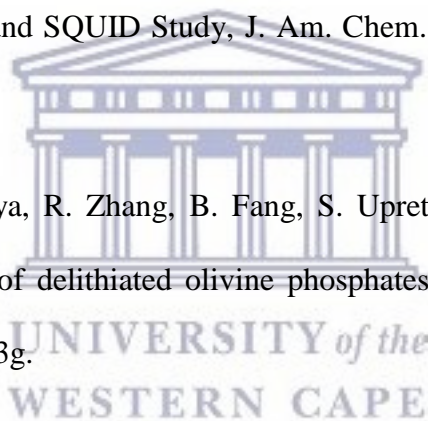
[33] P.R. Kumar, M. Venkateswarlu, M. Misra, A.K. Mohanty, N. Satyanarayana, Enhanced conductivity and electrical relaxation studies of carbon-coated  $\text{LiMnPO}_4$  nanorods, Ionics (Kiel). 19 (2012) 461–469. doi:10.1007/s11581-012-0778-9.

[34] Y.J. Yun, M. Wu, J.K. Kim, J.Y. Ju, S.S. Lee, K.W. Kim, Morphology Effect on Enhanced  $\text{Li}^+$  -Ion Storage Performance for  $\text{Ni}^{2+/3+}$  and/or  $\text{Co}^{2+/3+}$  Doped  $\text{LiMnPO}_4$  Cathode Nanoparticles, J. Nanomater. 2015 (2015) 970856.

[35] H. Schablegger, Y. Singh, The SAXS Guide, Ant. Paar. (2011) 1–99.

[36] X. Small-angle, X. Di, B. Fleury, R. Cortes-huerto, O. Tache, F. Testard, Gold Nanoparticle Internal Structure and Symmetry Probed by Unified Small-Angle X - ray Scattering and X - ray Diffraction Coupled with Molecular Dynamics Analysis, Nano Lett. 15 (2015) 6088–6094. doi:10.1021/acs.nanolett.5b02924.

- [37] S.L. Wilcke, Y. Lee, E.J. Cairns, J.A. Reimer, Covalency Measurements via NMR in Lithium Metal Phosphates, *Appl. Magn. Reson.* 32 (2007) 547–563. doi:10.1007/s00723-007-0032-1.
- [38] L.J.M. Davis, I. Heinmaa, B.L. Ellis, L.F. Nazar, G.R. Goward, Influence of particle size on solid solution formation and phase interfaces in  $\text{Li}_{0.5}\text{FePO}_4$  revealed by  $^{31}\text{P}$  and  $^7\text{Li}$  solid state NMR spectroscopy., *Phys. Chem. Chem. Phys.* 13 (2011) 5171–7. doi:10.1039/c0cp01922d.
- [39] M.C. Tucker, M.M. Doeff, T.J. Richardson, R. Fiñones, E.J. Cairns, J. A. Reimer, Hyperfine Fields at the Li Site in  $\text{LiFePO}_4$  -Type Olivine Materials for Lithium Rechargeable Batteries: A  $^7\text{Li}$  MAS NMR and SQUID Study, *J. Am. Chem. Soc.* 124 (2002) 3832–3833. doi:10.1021/ja017838m.
- [40] G.M. Nolis, F. Omenya, R. Zhang, B. Fang, S. Upreti, N. a. Chernova, Structure, defects and thermal stability of delithiated olivine phosphates, *J. Mater. Chem.* 22 (2012) 20482. doi:10.1039/c2jm33183g.
- [41] C. Pan, Y.J. Lee, B. Ammundsen, C.P. Grey,  $^6\text{Li}$  MAS NMR Studies of the Local Structure and Electrochemical Properties of Cr-doped Lithium Manganese and Lithium Cobalt Oxide Cathode Materials for Lithium-Ion Batteries, *Chem. Mater.* 14 (2002) 2289–2299. doi:10.1021/cm011623u.
- [42] A.J. Pell, D.S. Middlemiss, F.C. Strobridge, J.K. Miller, J. Cle, M.S. Whittingham, Spin-Transfer Pathways in Paramagnetic Lithium Transition-Metal Phosphates from Combined Broadband Isotropic Solid-State MAS NMR Spectroscopy and DFT Calculations *Rapheae I*, *J. Am. Chem. Soc.* 134 (2012) 17178–17185.





- [43] S. Geller, J.L. Durand, Refinement of the Structure of  $\text{LiMnPO}_4$ , *Acta Crystallogr.* 13 (1960) 325–331.
- [44] A.K. Padhi, K.S. Nanjundaswamy, J.B. Goodenough, Phospho-olivines as Positive-Electrode Materials for Rechargeable Lithium Batteries, *J. Electrochem. Soc.* 144 (1997) 1188–1194. doi:10.1684/agr.2014.0700.
- [45] C. Burda, X. Chen, R. Narayanan, M.A. El-Sayed, Chemistry and properties of nanocrystals of different shapes, *Chem. Rev.* 105 (2005) 1025–1102.
- [46] H. Manjunatha, T. V Venkatesha, G.S. Suresh, Electrochemical studies of  $\text{LiMnPO}_4$  as aqueous rechargeable lithium-ion battery electrode, *J. Solid State Electrochem.* 16 (2012) 1941–1952. doi:10.1007/s10008-011-1593-3.
- [47] Y.-Q. Zhao, M. Lu, P.-Y. Tao, Y.-J. Zhang, X.-T. Gong, Z. Yang, Hierarchically porous and heteroatom doped carbon derived from tobacco rods for supercapacitors, *J. Power Sources.* 307 (2016) 391–400. doi:10.1016/j.jpowsour.2016.01.020.
- [48] H.-C. Tao, S.-C. Zhu, X.-L. Yang, L.-L. Zhang, S.-B. Ni, Systematic investigation of reduced graphene oxide foams for high-performance supercapacitors, *Electrochim. Acta.* 190 (2016) 168–177. doi:10.1016/j.electacta.2015.12.179.
- [49] M.S. Michael, A.R. Kulkarni, S.R.S. Prabaharan, Design of Monolayer Porous Carbon-Embedded Hybrid- $\text{LiMnPO}_4$  for High Energy Density Li-Ion Capacitors, *J. Nanosci. Nanotechnol.* 16 (2016) 7314–7324. doi:10.1166/jnn.2016.12081.
- [50] C.O. Ikpo, C.J. Jafta, K.I. Ozoemena, N. West, N. Njomo, N. Jahed, P.G. Baker, E. I. Iwuoha, Novel iron-cobalt derivatised lithium iron phosphate nanocomposite for lithium ion battery cathode, *Int. J. Electrochem. Sci.* 8 (2013) 753–772.

[51] J.S. Sanchez, A. Pendashteh, J. Palma, M. Anderson, R. Marcilla, Anchored Fe<sub>3</sub>O<sub>4</sub> Nanoparticles on rGO Nanosheets as High-Power Negative Electrodes for Aqueous Batteries, *ChemElectroChem*. (2017). doi:10.1002/celec.201700048.

[52] K. Makgopa, K. Raju, P.M. Ejikeme, K.I. Ozoemena, High-performance Mn<sub>3</sub>O<sub>4</sub>/onion-like carbon (OLC) nanohybrid pseudocapacitor: Unravelling the intrinsic properties of OLC against other carbon supports, *Carbon* N. Y. 117 (2017) 20–32. doi:10.1016/j.carbon.2017.02.050.



## **CHAPTER FOUR**

### **4 Energy storage performance of nickel doped graphene coated LiMn<sub>2</sub>O<sub>4</sub> for Li-ion capacitors**

## Overview

*This chapter provides a detailed account of the development of lithium ion capacitor based on G-LMNO||AC. Herein the morphological and structural studies of the synthesized LMO, LMNO and G-LMNO using HRSEM, HRTEM, XRD, FTIR and Raman were discussed. G-LMNO was used as the positive electrode material for the lithium-ion capacitor developed in this work in a two-electrode system of 1M Li<sub>2</sub>SO<sub>4</sub> electrolyte. Furthermore an in-depth discussion of the electrochemical properties (CV, EIS and GCD) of the developed LIC device was evaluated as well as calculation of energy and maximum power densities.*



## ABSTRACT

Graphene coated spinel lithium manganese oxide doped nickel was used as the positive electrode material for the lithium-ion capacitor studied in this work. Its electrochemical characteristics in 1M Li<sub>2</sub>SO<sub>4</sub> aqueous electrolyte at a voltage window of 0 - 2 V were examined by cyclic voltammetry (CV), electrochemical impedance spectroscopy (EIS) and galvanostatic charge-discharge. The nanocomposite electrode gave a specific capacitance value of 80 F g<sup>-1</sup> at current density of 0.1 A g<sup>-1</sup> and exhibited capacitance retention of 70% after 1000 cycles. It rendered a high power density of 19.6 kW kg<sup>-1</sup> at 0.5 A g<sup>-1</sup> and maximum energy density of

12.32 Wh kg<sup>-1</sup>. The G-LMNO presents a promising electrode material for applications in lithium-ion capacitors.

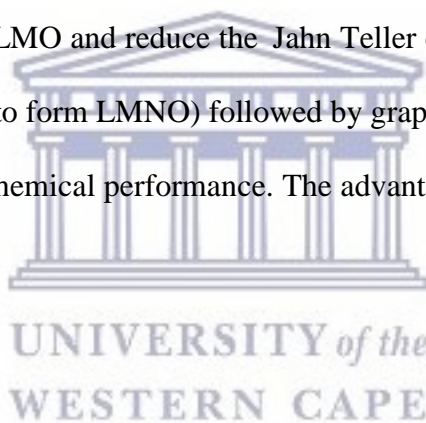
## 4.1 Introduction

Electrochemical energy storage devices with high capacitance and fast charge-discharge ability are essential for meeting the need and rapidly increasing demands for energy and power energy storage systems [1]. The major electrochemical energy storage devices are supercapacitors and batteries. Lithium ion batteries can deliver high energy densities (150-200 Wh kg<sup>-1</sup>) with limited power densities (less than 1000 W.kg<sup>-1</sup>) and poor cycle life (less than 1000 cycles) due to sluggish Li-ion diffusion and structural degradation in Faradaic redox reaction taking place on the surface of active material [2]. Supercapacitors offer high power and good long cycle life (up to 10 000 W kg<sup>-1</sup> and more than 100 000 cycles) but suffers from low energy densities (5-10 Wh kg<sup>-1</sup>) [2-4]. A Combination of lithium ion battery electrodes with those of supercapacitors can present very attractive devices having high energy and power density with satisfactory cycling stability [5,6]. In this regard, lithium ion capacitors are an important class of energy storage devices.

So far, various lithium-ion capacitor work has been done such as LiMn<sub>2</sub>O<sub>4</sub> nanohybrid || AC system at a voltage of 1.8 V and delivered energy density of 29.8 Wh kg<sup>-1</sup> at a power density of 90 W.Kg<sup>-1</sup> [7]. LiMn<sub>2</sub>O<sub>4</sub>-microsphere || AC delivered energy density of 38.8 Wh kg<sup>-1</sup> at power density of 12.6 Wh kg<sup>-1</sup> in the voltage range of 0-2.3 V [8], Pazhamalai *et al* designed LiMn<sub>2</sub>O<sub>4</sub> || graphene lithium ion capacitor device which delivered energy density of 40 Wh kg<sup>-1</sup> at a power density of 440 Wh kg<sup>-1</sup> in the voltage range of 0-2.2 V [9]. However, the search

for new electrode material with lower cost and better properties is still important in the development of lithium-ion capacitors.

In this study, G-LMNO was used in Li-ion capacitors two electrode system under aqueous medium (1M Li<sub>2</sub>SO<sub>4</sub>). As a cathode material, LiMn<sub>2</sub>O<sub>4</sub> (LMO) with spinel structure has been widely used in lithium ion batteries because they are inexpensive and safe [10]. It has a theoretical energy density at 400 Wh kg<sup>-1</sup> as a result of the high operating voltage of LMO at 4 V. However, it shows less or poor electrochemical performance due to slow lithium ion diffusion kinetics within the crystals and very low intrinsic electronic conductivity [11–14]. It has been found that surface coating, reduced particle size and doping can enhance the electrochemical properties of LMO and reduce the Jahn Teller effect [3,15–17]. In this work, LMO was doped with nickel (to form LMNO) followed by graphene coating on the surface of LMNO to enhance its electrochemical performance. The advantageous properties of graphene are widely reported [18,19].



## 4.2 Experimental

### 4.2.1 Chemicals

All chemicals used in this study were analytical reagent grade and used without further purification mostly obtained from Sigma-Aldrich. Lithium hydroxide monohydrate (99.995 %) trace metal basis, Potassium permanganate (97%), nickel(II) acetate tetra hydrate (98%), graphite powder  $\leq 20 \mu\text{m}$ , 96% ethanol from Saarchem, 37% hydrochloric acid from Saarchem, 65% nitric acid from KIMIX, Poly(vinylidene fluoride), Carbon black (CP), N-methyl-2-pyrrolidone, anhydrous (99.5 %), Activated carbon (AC) was purchased from SUPELCO analytical and used as received and ;Nickel foam purchased from MTI Corp.

### 4.2.2 Synthesis of $\text{LiMn}_2\text{O}_4$

0.75 g of  $\text{KMnO}_4$  was dissolved in 17 ml deionized water, and then 1.25 ml anhydrous ethanol was added to the above mixture. After well dispersion under magnetic stirring the obtained mixed solution was transferred into 25 ml Teflon-lined stainless steel autoclave, which was sealed and heated in an oil bath at  $180^\circ\text{C}$  for 20 h. The khaki products were collected by filtration after it naturally cooled down, washed with deionized water for several times and then dried at  $80^\circ\text{C}$  for 12 h in a vacuum oven. Typically a certain amount of obtained product and  $\text{LiOH}\cdot\text{H}_2\text{O}$  (Li/Mn= 1.05:2 with the molar ratio) was dispersed into 3 ml ethanol to form thick slurry, which was further ground for a few hours to a fine mixture and then dried at room temperature. The above procedure was repeated two times to obtain a well-mixed powder. Subsequently, the powder was sintered at  $700^\circ\text{C}$  for 10 h in muffle furnace [20]. Synthesis of Ni doped  $\text{LiMn}_2\text{O}_4$  followed the same procedure with the stoichiometric amount of  $\text{Ni}(\text{CH}_3\text{COO})_2$  added to form LMNO. Synthesis of Ni doped  $\text{LiMn}_2\text{O}_4$  followed the same procedure with the stoichiometric amount of  $\text{Ni}(\text{CH}_3\text{COO})_2$  added to form LMNO.

### 4.2.3 Synthesis of Graphene coated LMNO

Graphene nanosheets were prepared from graphite powder in a two-step process, involving the oxidation and/or exfoliation of graphite to graphite oxide by Hummer's method and chemical reduction of graphite oxide to graphene according to literature [21–23]. To prepare the graphene coated LMNO, 50 mg graphene is dispersed in 50 ml of ethanol under ultrasonication for 30 min. Then 1g of LMNO was added, after that the mixture was vigorously stirred at  $70^\circ\text{C}$  for 12 h to obtain a uniform dispersion of G-LMNO. The final product was dried in the vacuum oven at  $80^\circ\text{C}$  overnight.

## **4.2.4 Electrode preparation for electrochemical characterization**

All electrochemical measurements were carried out using a Bio-Logic VMP 300 potentiostat/galvanostat using three (half-cell) and two-electrode (full cell) configuration. The half-cell was done in three electrode system where the active material was coated on the nickel foam which acted as substrate; the reference electrode was Ag/AgCl (3M KCl) and platinum wire as counter electrode. The two electrode system assembled in Swagelok cell consist of the active material (LMO, LMNO and G-LMNO) coated on the nickel foam and the negative electrode made up of activated carbon coated on nickel foam.

### **4.2.4.1 Preparation of electrodes for three electrode configuration**

The  $\text{LiMn}_2\text{O}_4$  and composite electrodes were prepared from a mixture of active (LMO), carbon black (CB, Degussa), and polyvinylidene fluoride (PVDF) in a mass ratio of 70:30:10, respectively, using anhydrous N-methyl-2-pyrrolidone as the solvent. The slurry was coated on a nickel foam (1 cm x 0.5 cm) substrate with the mass loading ranged between  $8 \text{ mg}\cdot\text{cm}^{-2}$  to  $20 \text{ mg}\cdot\text{cm}^{-2}$ . The prepared electrode was dried at  $70^\circ\text{C}$  for 12 h.

### **4.2.4.2 Preparation of electrodes for two-electrode configuration (LICs)**

The positive electrode was prepared by mixing 70 wt% LMO composite, 30 wt% carbon black (CB, Degussa), and 10 wt% polyvinylidene fluoride (PVDF) in anhydrous N-methyl-2-pyrrolidone to form homogeneous slurry which was coated on a nickel foam substrate ( $3 \text{ cm}^2$ ) with a mass loading of  $7 - 12 \text{ mg}\cdot\text{cm}^{-2}$ . The negative electrode was prepared using similar procedure but with activated carbon, carbon black and PVDF at a mass ratio of 80:15:5, respectively. The cell was tested after 24 h of fabrication. In all the experiments, 1 M  $\text{Li}_2\text{SO}_4$



was used as electrolyte and a porous glass fiber (Whatman Grade GF/D Glass Microfiber Filters, Sigma-Aldrich) served as the separator.

#### **4.2.5 Measurements and instrumentation**

The surface morphology and internal ultra-structure of the synthesized materials was evaluated by the use of scanning electron microscopy (SEM) and high resolution transmission electron microscopy (HRTEM), respectively. Scanning electron microscopic (SEM) images were obtained using a Hitachi model X-650 ZEISS ULTRA scanning electron microscope. The sample was placed on a carbon supported by alumina and then placed in a sputter coater to make the material conductive. The samples were then coated for 30 seconds using gold-palladium alloy. The high resolution transmission electron microscopic images were obtained by Tecnai G2 F20 X-TWIN MAT equipped with an energy-dispersed spectroscopy (EDS) for Elemental mapping. Characterisation here was performed by coating a copper- carbon grid with a drop of the sample solution and drying with an electric lamp for 10 min. HRTEM provides information on particle size, shape and crystallography of nanoparticles. It can measure particle sizes to as low as 1 nm. HRTEM was used to identify the size, shape and structure of the products.

X-ray powder diffraction (XRD) is a rapid analytical technique primarily used for phase identification of a crystalline material and provides information on unit cell dimensions. The sample was finely ground, homogenized, and average bulk composition determined. XRD reveals information on the structure, crystallinity and lattice spacing of the material. X-ray diffraction (XRD) measurements were carried out with a BRUKER AXS (Germany), D8 Advance diffractometer, using Cu K $\alpha$  radiation of wavelength 1.5418 Å and scanned from 80°

to  $10^\circ$  with a step size of  $0.02^\circ$ . FTIR spectra were obtained using a perkin elmer spectrum 100 series attenuated total reflection (ATR) FTIR spectrometer. Infrared spectroscopy reveals information about the vibrational states of a molecule and functional groups. Solid state. Small-Angle X-Ray Scattering (SAXS) measurements for  $\text{LiMn}_2\text{O}_4$  and nanocomposites were obtained using a 1 mm thin walled capillary (solid powder samples) at the beamline ID09B. We used the CCD 161 detector (Anton Paar, GmbH, Australia, 133 mm diameter,  $2048 \times 2048$  pixels) at a distance of 0.6 m and an X-ray energy of 10 keV.

Cyclic voltammetry (CV) is a technique which is widely used in the study of oxidation/reduction reactions and the detection of reaction intermediates. This technique indicates the potentials at which processes occurs. The CV, tests for the full cell were carried out in the potential range of 0 to 2 V at various scan rates from  $5 \text{ mV s}^{-1}$  to  $50 \text{ mV s}^{-1}$ . Galvanostatic charge-discharge (GCD) technique is the widely used method in supercapacitors application and the most important characterisation tool for the determination of the electrochemical performance of the electrode materials.

To gain understanding of the power, energy performance and ability of the electrode material to retain its capacitance, a variation of current density on the GCD technique must be employed. The GCD tests were carried out at varying current densities between  $0.1 \text{ A g}^{-1}$  to  $1 \text{ A g}^{-1}$ . EIS measurements were conducted at amplitude of 5 mV and frequency range of 100 mHz to 100 kHz. EIS provides a more thorough understanding of an electrochemical system than any other electrochemical technique. Its operating principle involves the measurement of the impedance between the current and the potential at a fixed direct current (DC) potential during frequency scan with a fixed superimpose alternating current (AC) signal of small amplitude.

The specific capacitance ( $C_{sp}$ ), maximum specific power density ( $P_{max}$ ) and specific energy density ( $E_{sp}$ ) were determined from the discharge curves using the established Equations (1) to (4) for a two electrode system [24–27]

$$C(F) = \frac{i}{\frac{\Delta V}{\Delta t}} \quad (1)$$

$$C_{sp} = \frac{4.C}{m} \quad (2)$$

$$P_{max} (W/Kg) = \frac{V^2}{4mR_{ir}} \quad (3)$$

$$E(Wh/kg) = \frac{CV^2}{2m} \quad (4)$$

Where  $i$  (A) is the applied current,  $\Delta V$  (V) /  $\Delta t$  (s) is the slope of the discharge curve after the initial  $iR$  drop and  $m$  (g) the mass of both electrodes.  $V$  (V) is the maximum voltage obtained during charge and  $C$  (F) the calculated capacitance. The internal resistance ( $R_{ir}$ ) can be calculated from the voltage drop at the beginning of a discharge curve:

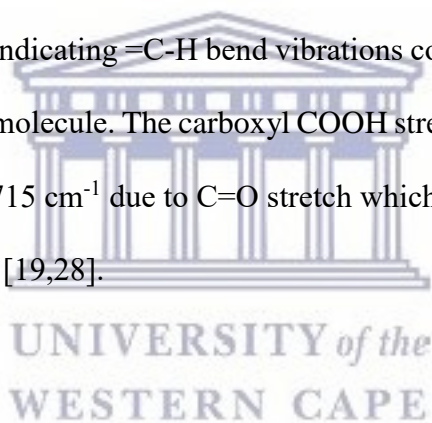
$$R_{ir} (\Omega) = \frac{\Delta V_{iR}}{2i} \quad (5)$$

Where  $\Delta V_{iR}$  is the voltage drop between the first two points from the start of the discharge curve.

## 4.3 Materials characterization

### 4.3.1 Structure and morphology characterisation of graphene

**Fig. 4.1** shows the Fourier transformed infrared (FTIR) spectra of graphene and graphene oxide. The spectrum of graphene oxide is characterized by the band at  $1026\text{ cm}^{-1}$  due to the C-O stretching vibration occurring in epoxides and alcohols within the graphite structure. The absorption band at  $1715\text{ cm}^{-1}$  due to C=O stretch, the band at  $1503\text{ cm}^{-1}$  associated with bending COOH vibrations. Upon reduction using  $\text{NaBH}_4$  as reducing agent, a considerable decrease or complete removal of the above mentioned oxygen containing functionalities is noted in graphene spectrum. Graphene is characterized by band at  $1556\text{ cm}^{-1}$  representing the aromatic C-C stretch, band at  $620\text{ cm}^{-1}$  indicating =C-H bend vibrations confirming the unsaturation  $\text{sp}^2$  bending to bond to  $\text{sp}^3$  carbon molecule. The carboxyl COOH stretching vibration band at  $1495\text{ cm}^{-1}$ , the absorption band at  $1715\text{ cm}^{-1}$  due to C=O stretch which is attributed to accumulation of oxygen atoms on the sheets [19,28].



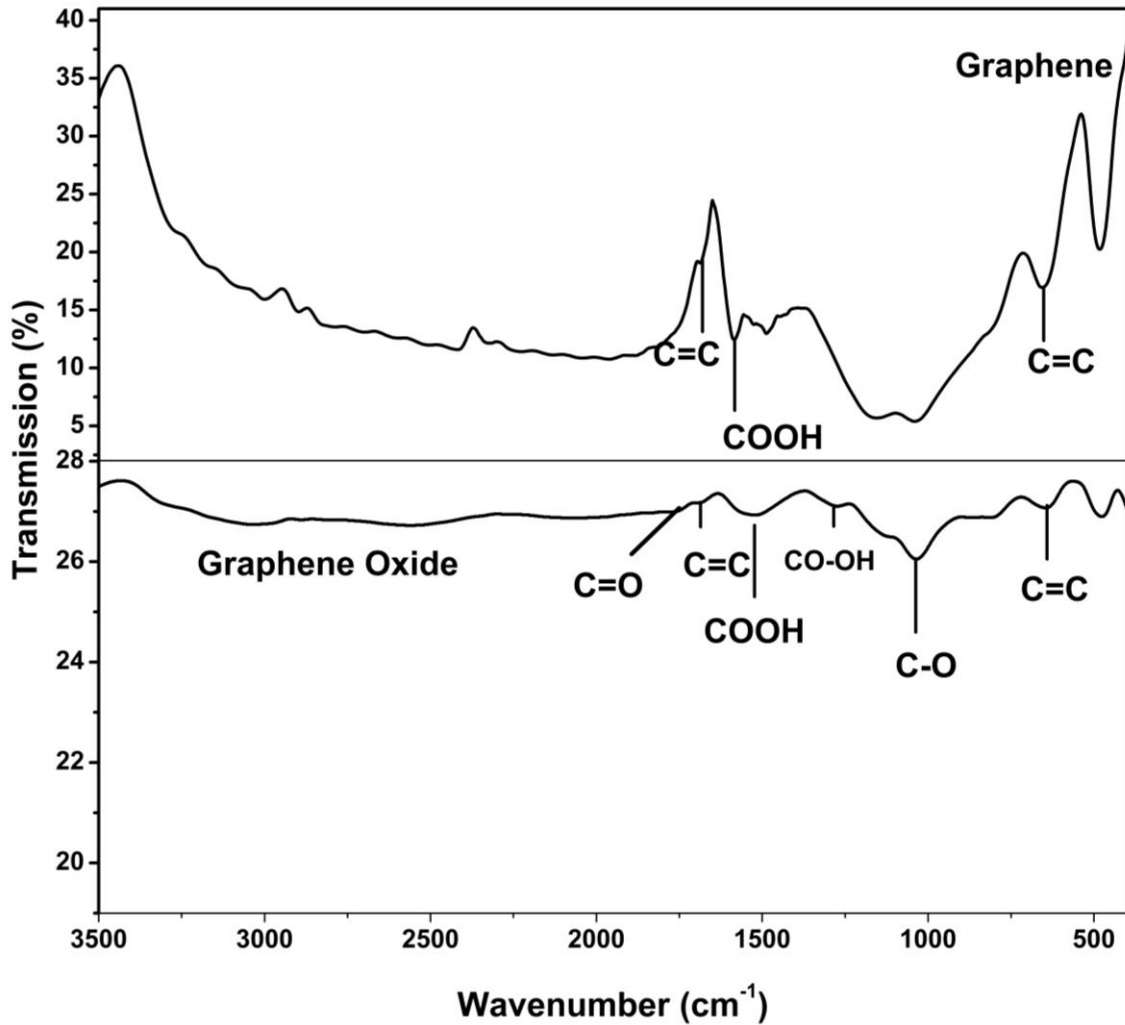


**Figure 4.1:** FTIR spectra of graphene oxide (GO) and graphene

**Fig. 4.2** shows the Raman spectra of graphene oxide and graphene. Graphene oxide showed a broadening and Raman shift to  $1600\text{ cm}^{-1}$  for the G band while the D band at  $1360\text{ cm}^{-1}$  is considerably larger. The Raman spectrum of graphene showed a decrease in intensity and slightly shifts to lower frequencies indicating the reduction process was successful. Raman shift of the D peak is located at  $1348\text{ cm}^{-1}$  and G peak at  $1593\text{ cm}^{-1}$ . The D band is allocated to the breathing mode of k-point phonons of  $A_{1g}$  symmetry from the aromatic rings which show the defects in these materials, whereas the G band is assigned to the  $E_{2g}$  phonons from the stretching of C  $sp^2$  atoms in both the rings and chains [29,30]. The Raman and FTIR results show the successful synthesis of graphene oxide and graphene.

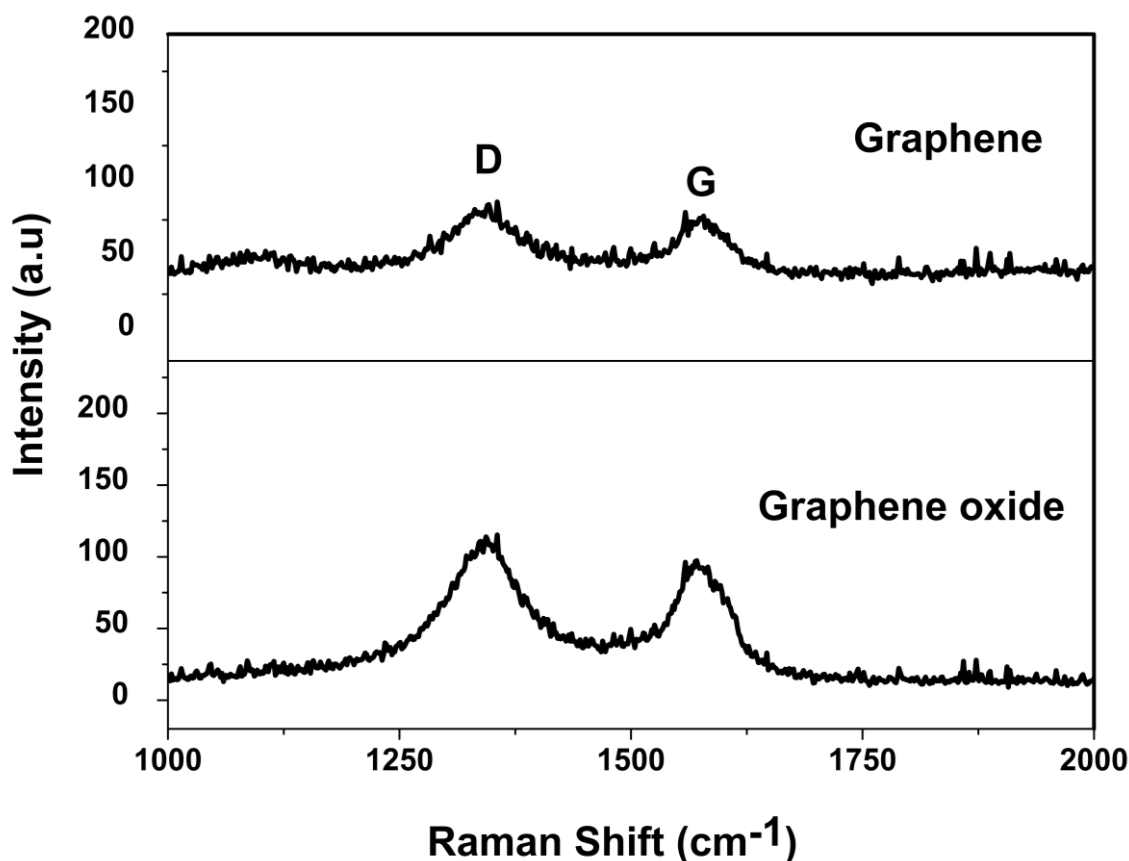


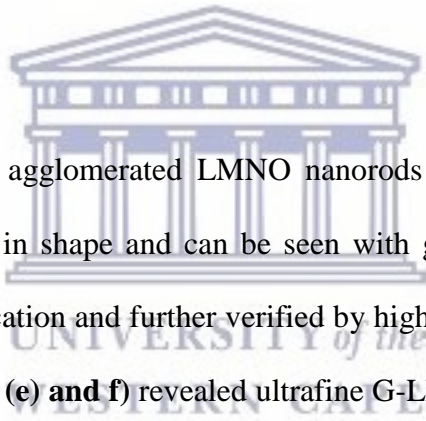
**Figure 4.2:** Raman spectra of graphene oxide and graphene

UNIVERSITY of the  
WESTERN CAPE

### 4.3.2 Surface morphology, composition and structure of LMO and nickel doped derivatives

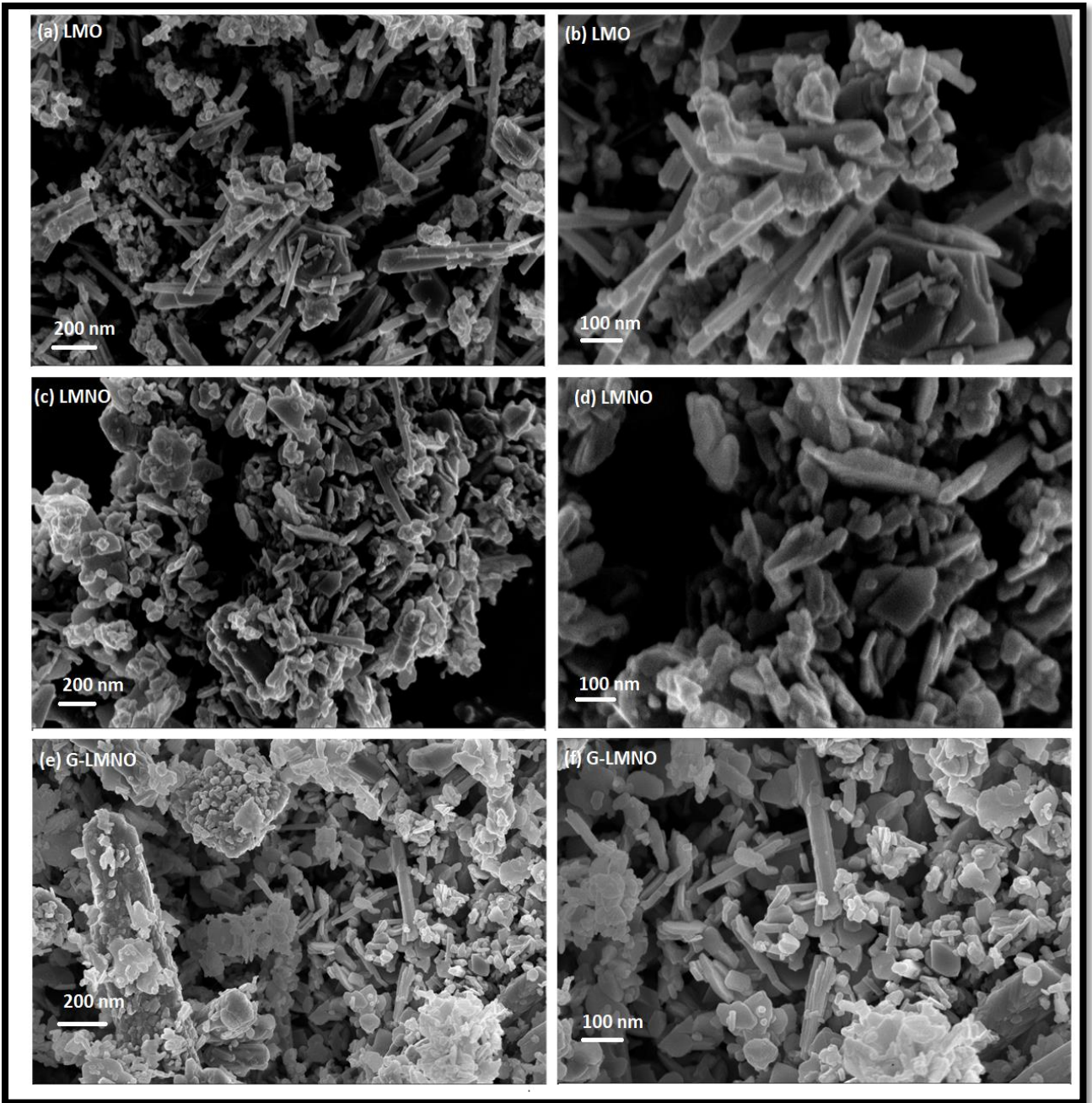
High resolution scanning electron microscopy (HRSEM) was used in order to get high definition morphology of the synthesized spinel  $\text{LiMn}_2\text{O}_4$  (LMO), and nanocomposites. Since the particle properties such as morphology and size have great effect on the performance of Li-ion capacitor electrode, therefore LMO, LMNO and G-LMNO may exhibit different electrochemical features. Scaling down the particle to nanoscale is essential which might lead to high accessibility of  $\text{Li}^+$  ion to the electrode material during lithiation/delithiation process due to that surface-to-volume ratios increases [20].

**Fig. 4.3** showed the corresponding morphology of LMO, LMNO and G-LMNO derived from hydrothermal synthesis as explained in the experimental part. HRSEM micrograph of the pristine  $\text{LiMn}_2\text{O}_4$  shows that the nanoparticles have a rough surface and that two types of particles are seen: primary particles with well-shaped nanorods morphology with a diameter 20 nm and an average length of  $\sim 10 \mu\text{m}$ . The secondary particles which are much bigger having a size of  $\sim 200 \text{ nm}$  interspersed with agglomerated nanoparticles due to higher temperature sintering that caused uncontrollable particle growth on the surface. One of the most significant effects of small particles is their ability to support higher rate of lithium intercalation / deintercalation from the oxide host.



**Fig. 4.3 (c & d)** still showed agglomerated LMNO nanorods morphology with secondary particle which are plates like in shape and can be seen with good dispersability of nearly uniform plates at low magnification and further verified by high magnification. The observed SEM images shown in **Fig 4.3 (e) and f)** revealed ultrafine G-LMNO agglomerated nanorods found to have a diameter of ranges from 20 -100 nm and length of  $\sim 2 - 10 \mu\text{m}$ . The bright white region observed on the graphene coated SEM image maybe due to the coating of carbon on the nanorods

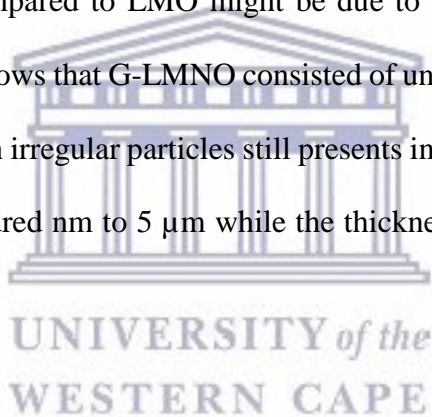




**Figure 4.3:** (a) and (b) SEM image of the  $\text{LiMn}_2\text{O}_4$ , [(c) and (d)] LMNO and [(e) and (f)] G-LMNO

**Fig. 4.4** compared the TEM images of the synthesized  $\text{LiMn}_2\text{O}_4$  and its composite. **Fig 4.4 (a) and (b)** shows the typical TEM images of LMO. It can be observed that the obtained  $\text{LiMn}_2\text{O}_4$  product consists mainly of nanorods, appearing to have a larger diameter  $\sim 100$  nm and an average length of  $\sim 6$   $\mu\text{m}$ .  $\text{LiMn}_2\text{O}_4$  also consists of many irregular and aggregated particles, as can be seen in **Fig 4.4 (b)**, which may be due to high temperature where the material was calcined.

Nickel doped LMO TEM image consists of many irregular and aggregated particles with nanorods still visible in the image, meaning the material is composed of different particles. The difference in morphology compared to LMO might be due to altered synthetic route of the material. **Fig 4.4 (e) and (f)** shows that G-LMNO consists of uniform, ultrafine nanorods-like structures with high yield, with irregular particles still present in image **Fig 4.4 (e)**. The length is in the range of several hundred nm to  $5$   $\mu\text{m}$  while the thickness ranges from  $35$  nm to  $120$  nm.



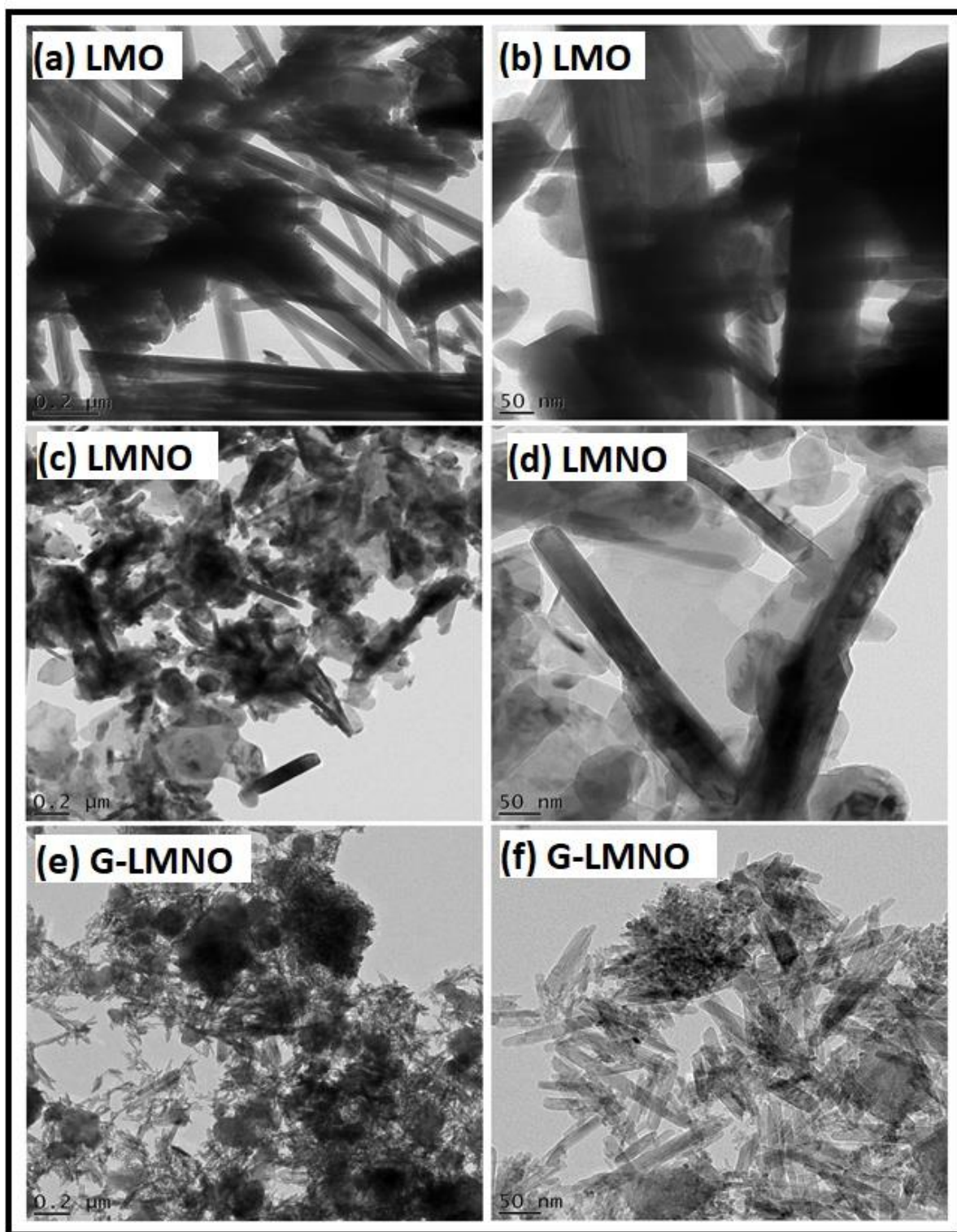


**Figure 4.4:** (a) and (b) TEM image of the  $\text{LiMn}_2\text{O}_4$ , [(c) and (d)] nickel doped  $\text{LiMn}_2\text{O}_4$  and [(e) and (f)] G-LMNO

**Fig. 4.5** showed the TEM-EDS spectrum of the LMO, LMNO and graphene-coated LMNO which confirmed the presence of Mn, Ni, O, and C and some impurities peaks of potassium (K) from the precursor. LMNO TEM-EDS revealed the presence of nickel due to doping. The presence of C was due to the C-coated Cu grids. The presences of graphene were confirmed from FTIR and Raman spectroscopy.

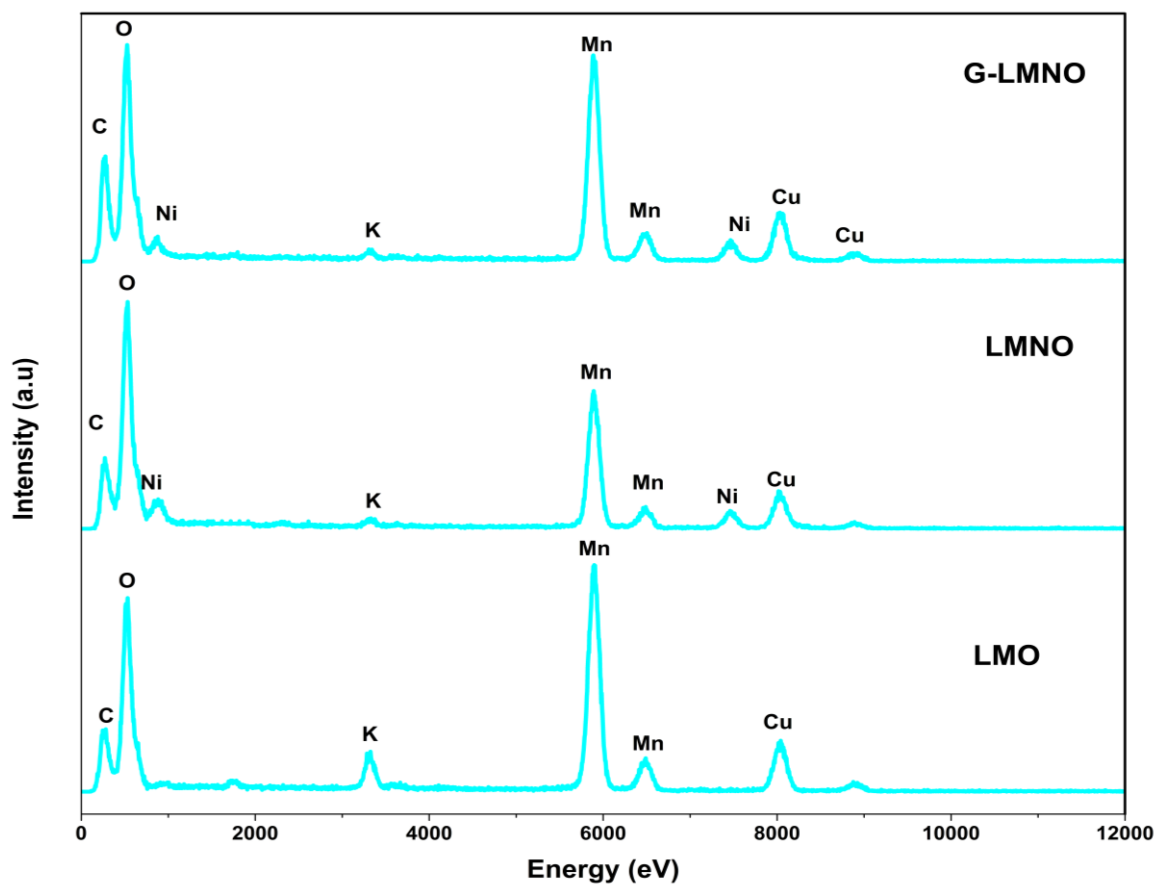


**Figure 4.5:** EDS of the synthesized  $\text{LiMn}_2\text{O}_4$ , nickel doped  $\text{LiMn}_2\text{O}_4$  and G-LMNO

**Fig 4.6** shows the high resolution transmission electron microscopy (HRTEM) image and selected area electron diffraction (SAED) pattern of the resulting  $\text{LiMn}_2\text{O}_4$  and nanocomposites. It can be observed that all the materials display perfect lattice fringes distributed within the entire particle with the size of 0.47 nm toward the (111) direction and have a good consistency with the spacing of the (111) plane of  $\text{LiMn}_2\text{O}_4$  (JCPDS No. 35-0782). The corresponding SAED pattern reveals that the obtained product is single-crystalline  $\text{LiMn}_2\text{O}_4$  nanorods with the cubic spinel structure [31,32]. **Fig 4.6 (e)** reveals two layers, where one is layer of graphene coated into the surface of LMNO.





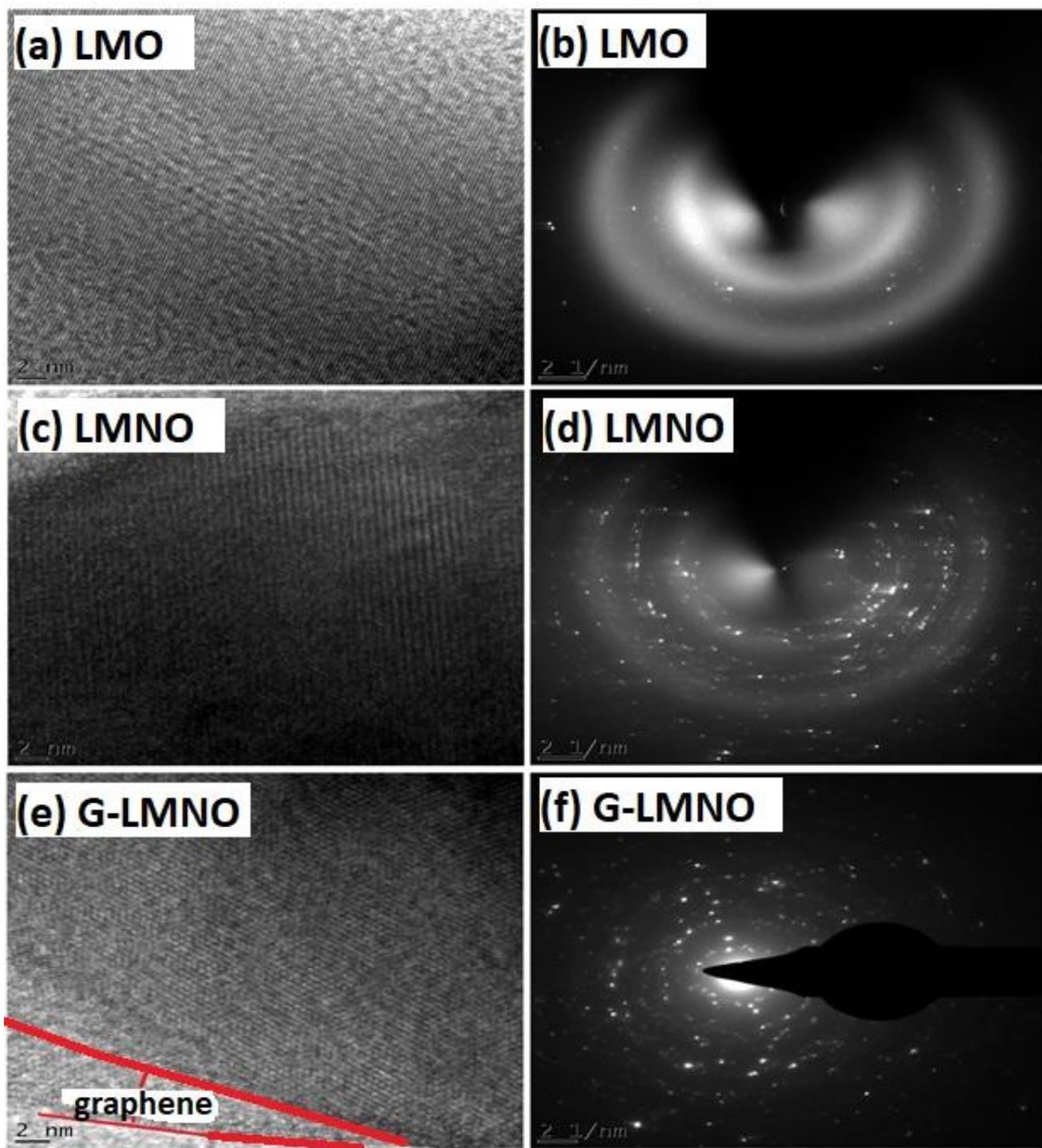


**Figure 4.6:** HRTEM image and selected area electron diffraction (SAED) patterns for  $\text{LiMn}_2\text{O}_4$ , nickel doped  $\text{LiMn}_2\text{O}_4$  and G-LMNO

Fig. 4.7 showed  $\text{LiMn}_2\text{O}_4$ , LMNO and G-LMNO particle size distribution measured by Small-angle X-ray scattering (SAXS) system. SAXS proved to be well-suited method for determining the size of materials with very small particle size. Fig 4.7 (a) revealed LMO nanoparticles appeared at small-angle scattering pattern with the average size from 75 – 120 nm. LMNO average size is at 120 nm and G-LMNO is at 75 nm followed by the decreased scattering fraction number ( $P$ ) of bigger particles observed at 120 nm. Normally, small angle scattering pattern can be considered as the sum of the scattering patterns of the individual particles contained in the scattering volume fraction [33]. Thus, the scattered intensity generally decreases with scattering angle and the investigation is established on assessment of the scattering by a single particle.

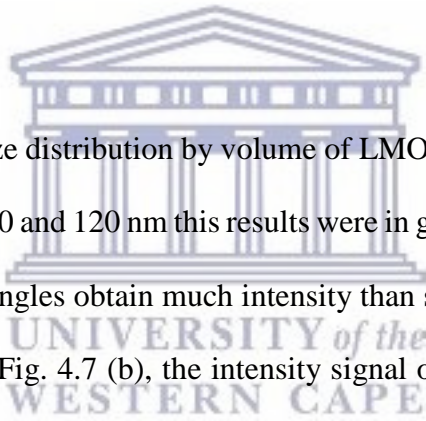
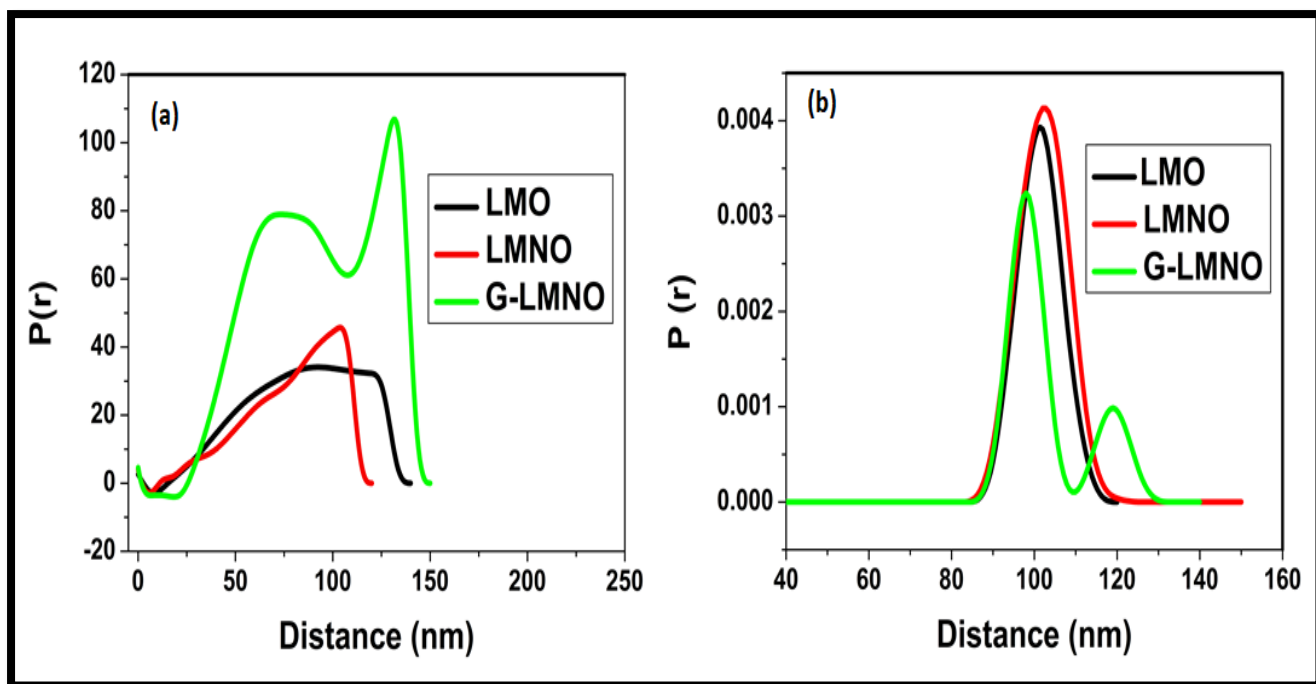


Fig 4.7 (b) revealed particle size distribution by volume of LMO was at 100 nm, for LMNO at 100 nm and for G-LMNO at 100 and 120 nm this results were in good agreement with HRTEM. The bigger particles at larger angles obtain much intensity than small particles at small angles [33,34]. Therefore, as seen in Fig. 4.7 (b), the intensity signal obtained at 75 nm was clearly invisible in G-LMNO than the intensity at large angles (i.e 100 nm and 120 nm in diameter). This, therefore, concluded that larger particles overshadowed the intensity signal of the particles at small angles.





**Figure 4.7:** SAXS Particle size distribution in (a) number weighted, (b) volume weighted

In order to confirm the phase composition and the crystallinity of the heat-treated powder, analysis by XRD is an important technique. **Fig. 4.8** displayed the XRD patterns for  $\text{LiMn}_2\text{O}_4$ , nickel doped  $\text{LiMn}_2\text{O}_4$  and G-LMNO. All the diffraction peaks of LMO, LMNO and G-LMNO could be readily indexed to the cubic spinel  $\text{LiMn}_2\text{O}_4$  structure with a space group of  $Fd3m$ . The XRD pattern showed strong intensities of (111), (311) and (400) planes with close agreement to the standard JCPDS file number: 35-0782, lattice constant:  $a = 0.8248 \text{ nm}$  [1], as seen from TEM results. There are no peaks related to lithium oxide, manganese oxide and any hydroxides in the XRD pattern, thus suggesting the formation of  $\text{LiMn}_2\text{O}_4$  with high purity. The diffraction peaks of LMNO and G-LMNO are stronger and narrow, which indicate that nickel and graphene were successfully doped and coated respectively, on the surface of LMO nanorods, the diffraction peak still matches that of  $\text{LiMn}_2\text{O}_4$ . There is no obvious graphene or carbon diffraction peak due to their low content or it may be due to graphene coated being in amorphous phase [35–37]

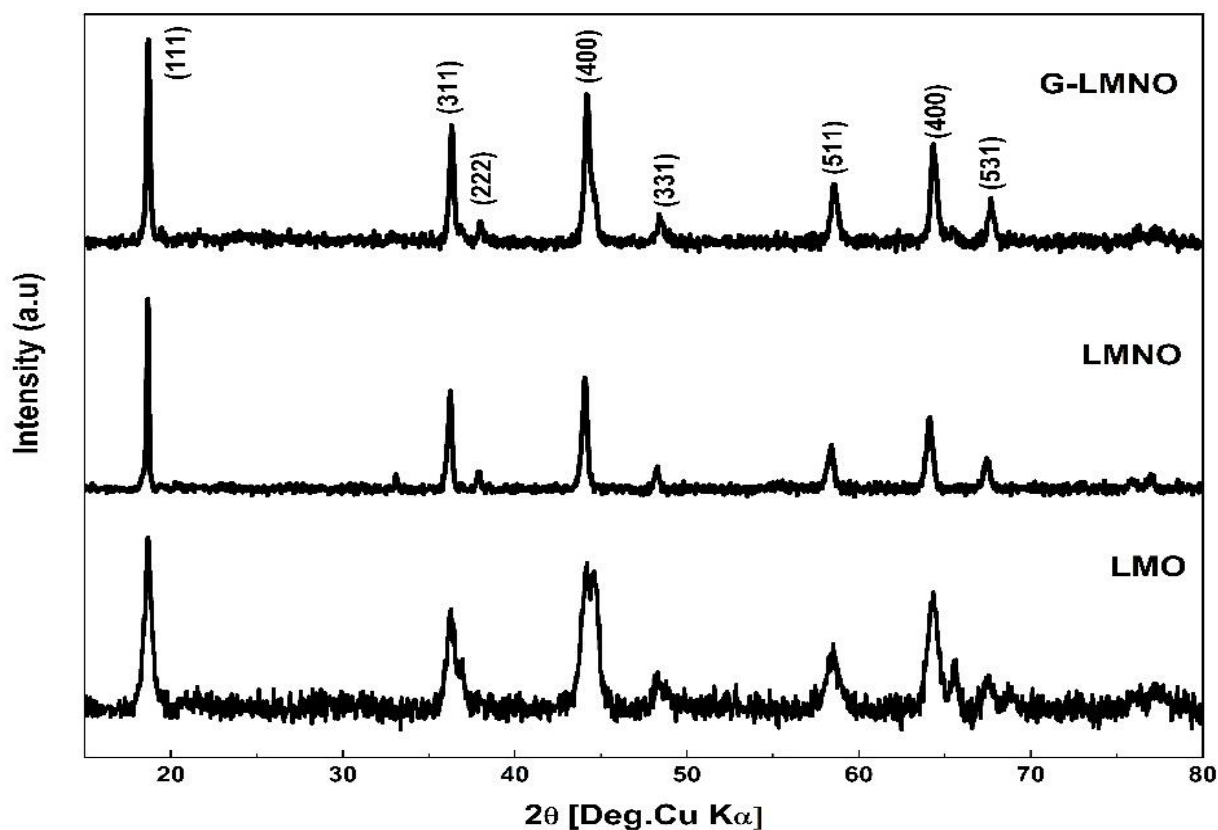


**Figure 4.8:** XRD patterns of  $\text{LiMn}_2\text{O}_4$ , nickel doped  $\text{LiMn}_2\text{O}_4$  and Graphene coated G-LMNO

Fourier transform infrared (FTIR) spectroscopy was used to study the structure coordination of the obtained powder in the range  $450 - 3000 \text{ cm}^{-1}$  and also employed to understand the metal-oxygen and metal-metal bond in prepared samples. **Fig.4.9** showed FTIR spectrum of LMO, LMNO and G-LMNO which is dominated by stretching modes of  $\text{MnO}_6$  which is responsible for the formation of spinel  $\text{LiMn}_2\text{O}_4$  structure. The characteristic two strong absorption bands are at  $510$  and  $620 \text{ cm}^{-1}$  which are attributed to the asymmetric stretching modes of  $\text{MnO}_6$  octahedral structure [9].

The bands around  $1000 \text{ cm}^{-1}$  are due to the metal oxygen vibrational frequencies [38]. All the samples showed a similar IR pattern with the typical peaks in the range between  $400$  and  $750$

$\text{cm}^{-1}$  characteristics of the disordered  $Fd3m$  crystalline structure. This indicates that graphene coating did not affect cation ordering in the crystallographic structure of LMNO [39]. The graphene coated LMNO FTIR spectra shows bands at  $1600 \text{ cm}^{-1}$  which is assigned to the symmetrical stretching C-C. From the FTIR spectra, it is revealed that the synthesized product is a single phase  $\text{LiMn}_2\text{O}_4$  compound as can be seen from XRD and TEM results.

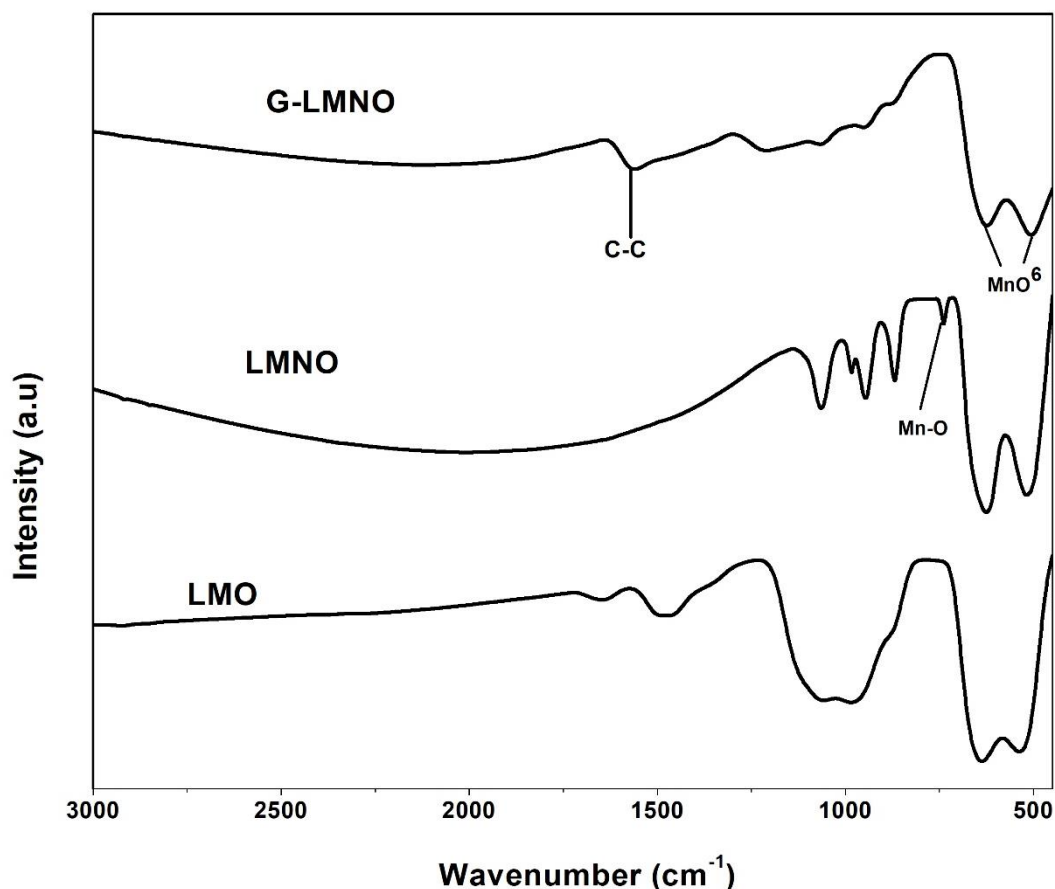


**Figure 4.9:** FTIR spectra of  $\text{LiMn}_2\text{O}_4$ , nickel doped  $\text{LiMn}_2\text{O}_4$  and G-LMNO

**Fig. 4.10** showed the Raman spectra of the  $\text{LiMn}_2\text{O}_4$ , nickel doped  $\text{LiMn}_2\text{O}_4$  and G-LMNO nanocomposite which was recorded at  $250 - 1600 \text{ cm}^{-1}$ . The Raman spectra of the LMO and LMNO nanorods showed the broad band at  $485 \text{ cm}^{-1}$  which correspond to  $F^{(2)}_{2g}$  mode of strong vibrational band of Mn-O stretching in  $\text{MnO}_6$  [9]. The assignment of Mn-O bands confirms

that the  $\text{LiMn}_2\text{O}_4$  spinel structure is successfully synthesized. The spectrum corresponding to G-LMNO nanocomposite still exhibit the Mn-O bands which is evidence of the structure of  $\text{LiMn}_2\text{O}_4$  with two extra bands at  $1464$  and  $1529\text{ cm}^{-1}$  which represent D and G bands D represents the disordered band of  $\text{sp}^3$  and G is for the graphene band of  $\text{sp}^2$ -type, [37]. Hence, the Raman spectra of G-LMNO confirmed the presence of graphene in accordance with FTIR spectra

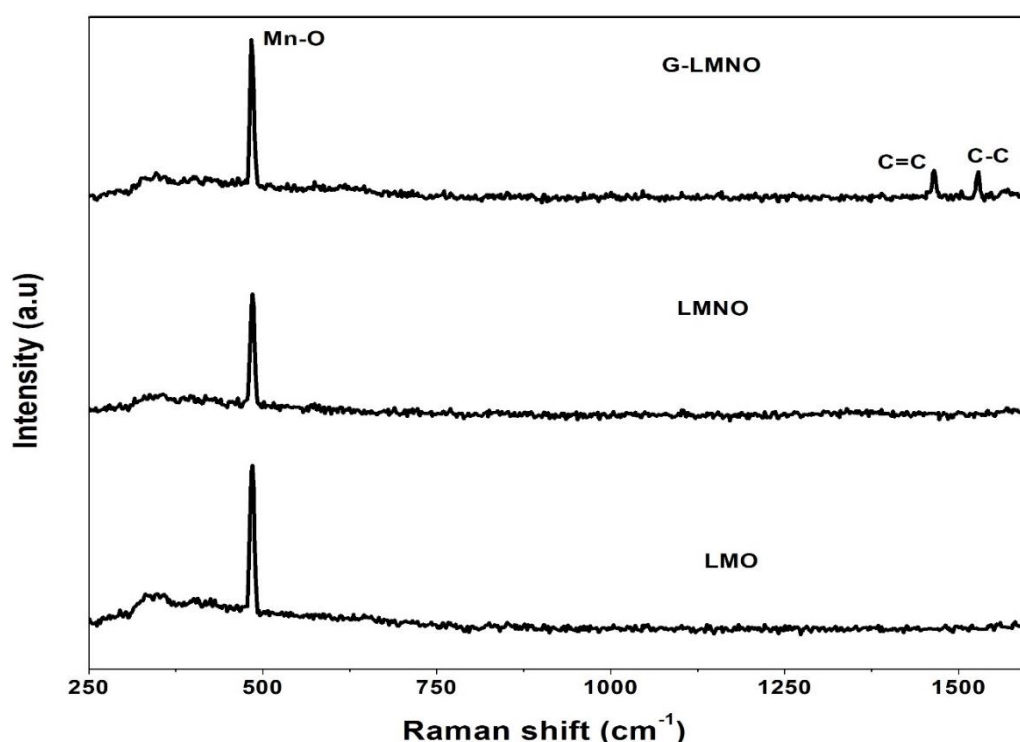


**Figure 4.10:** Raman spectra of  $\text{LiMn}_2\text{O}_4$ , nickel doped  $\text{LiMn}_2\text{O}_4$  and G-LMNO

### 4.3.3 Electrochemical studies of single electrode $\text{LiMn}_2\text{O}_4$

The investigation of  $\text{LiMn}_2\text{O}_4$ , LMNO and G-LMNO nanocomposite as working electrode against Ag/AgCl (3 M KCl) in the three electrode system was carried out using nickel foam as the current collector and 1 M  $\text{Li}_2\text{SO}_4$  aqueous electrolyte in the voltage window of 0.2 – 1.2 V.

**Fig. 4.11** compares the CV curves of LMO, LMNO and G-LMNO nanocomposite at  $5\text{ mVs}^{-1}$ .

All the CV curves exhibited redox peaks attributed to surface oxidation/reduction of  $\text{Mn}^{3+} / \text{Mn}^{4+}$  due to the insertion / deinsertion of  $\text{Li}^+$  at  $\text{LiMn}_2\text{O}_4$  which can be summarized by the following equation:



The above is a typical characteristic equation attributed to the deintercalation process of Li ion in 8a tetrahedral sites of  $\text{LiMn}_2\text{O}_4$  spinel [40]. The cathodic peak is attributed to the removal of lithium ions from the tetrahedral sites where Li – Li interactions occur, whereas the anodic peak is attributed to the gaining of lithium ions from the tetrahedral sites. The peak separation  $\Delta E_p$  ( $\Delta E_p = E_{pa} - E_{pc}$ ) in the redox peaks has been considerably decreased in the nanocomposite sample, the values are 0.25 V, 0.12 V and 0.1 V for LMO, LMNO and G-LMNO respectively, which suggest an improved in electrochemical reversibility. Consequently, the least  $\Delta E_p$  would shorten the Li-ion path responsible for the faster reaction. This may be due to the presence of the conducting graphene layers providing new pathways for electron transfer thus facilitating the redox reaction. It can be clearly be observed that the peak currents intensities have remarkably increase for the G-LMNO. This indicates that the conductivity of  $\text{LiMn}_2\text{O}_4$  has been improved and more facile lithium ion transfer will result in better reaction kinetics. The large area of CV of the G-LMNO compared to LMO and LMNO curves implies a higher specific capacitance of the electrode material at the same scan rate.

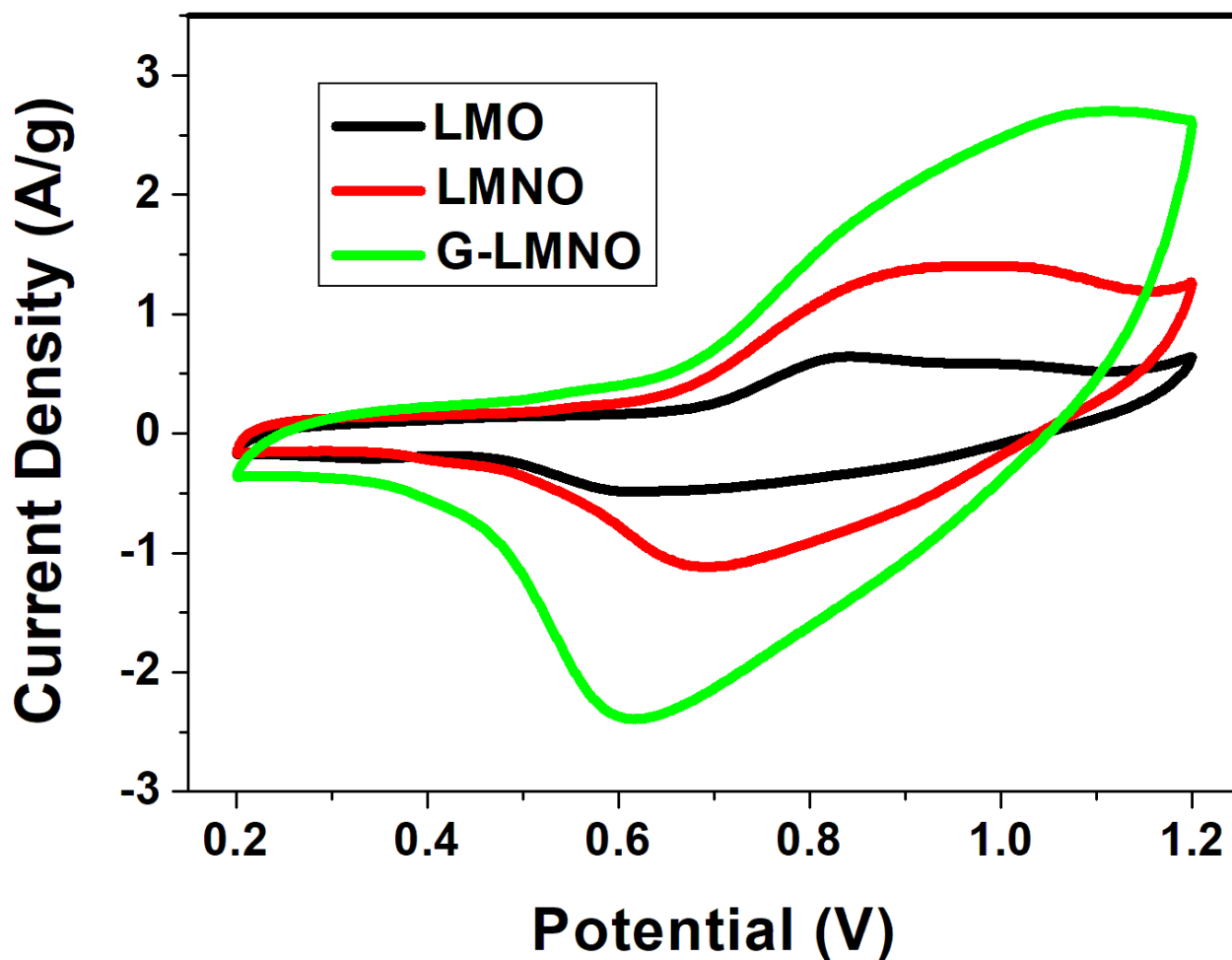


**Figure 4.11:** Comparative curves for olivine  $\text{LiMn}_2\text{O}_4$ , nickel doped  $\text{LiMn}_2\text{O}_4$  and G-LMNO from cyclic voltammetry at a scan rate of  $5 \text{ mVs}^{-1}$

Cyclic voltammetry was also used to calculate the capacitance of all the samples. The charge stored during forward and backward scans directly corresponds to the area under the CV curves. The capacitance obtained from the integrated area under the cathodic peak at the scan rate of  $5 \text{ mV/s}$  indicate that the nanocomposite G-LMNO exhibited better higher capacitance of  $195.2 \text{ F g}^{-1}$  for the insertion of lithium and reduction of  $\text{Mn}^{4+}$  to  $\text{Mn}^{3+}$ , and the corresponding values for LMO and LMNO were  $66.4 \text{ F g}^{-1}$  and  $138 \text{ F g}^{-1}$  respectively. G-LMNO revealed higher capacitance than in the pristine  $\text{LiMn}_2\text{O}_4$  at the same scan rates which suggests an improvement in electrochemical performance.

The capacitances were calculated according to the following equation:

$$C_{\text{sp}} = \frac{Q}{mV} \quad (6)$$

$C_{\text{sp}}$  is the specific capacitance,  $Q$  is the charge obtained from CV results,  $m$  is the mass of the electrode and  $V$  is potential window. Furthermore, the electrochemical performance was investigated using galvanostatic charge/discharge experiment. Galvanostatic charge-discharge technique is a reliable electrochemical method for the evaluation of electro-capacitive behaviour of electrode materials in energy storage device and also complements the cycling characteristics. **Fig. 4.12** represents the comparison of galvanostatic charge/discharge curves of  $\text{LiMn}_2\text{O}_4$ , LMNO and G-LMNO at the same current density of  $1 \text{ A g}^{-1}$ . The nonlinear charge/discharge profile demonstrates the pseudo capacitive behaviour of  $\text{LiMn}_2\text{O}_4$ . The charge-discharge curves further show plateau at about 0.48 and 0.7 V corresponding to deintercalation/intercalation, which is in good agreement with the CV curve above.

The G-LMNO electrode showed greater discharging time as illustrated on **Fig. 4.12** than the pristine material LMO indicating the superior electrochemical performance of the nanocomposite electrode. The specific capacitance  $C_{\text{sp}}$  ( $\text{F g}^{-1}$ ), calculated from the three different electrode materials were found to be  $25 \text{ F g}^{-1}$ ,  $50 \text{ F g}^{-1}$  and  $70 \text{ F g}^{-1}$  at  $1 \text{ A g}^{-1}$  for LMO, LMNO and G-LMNO respectively. The graphene coated derivative (G-LMNO) exhibited higher specific capacitance compared to LMO and LMNO due to conductive properties of graphene highlighted previously.



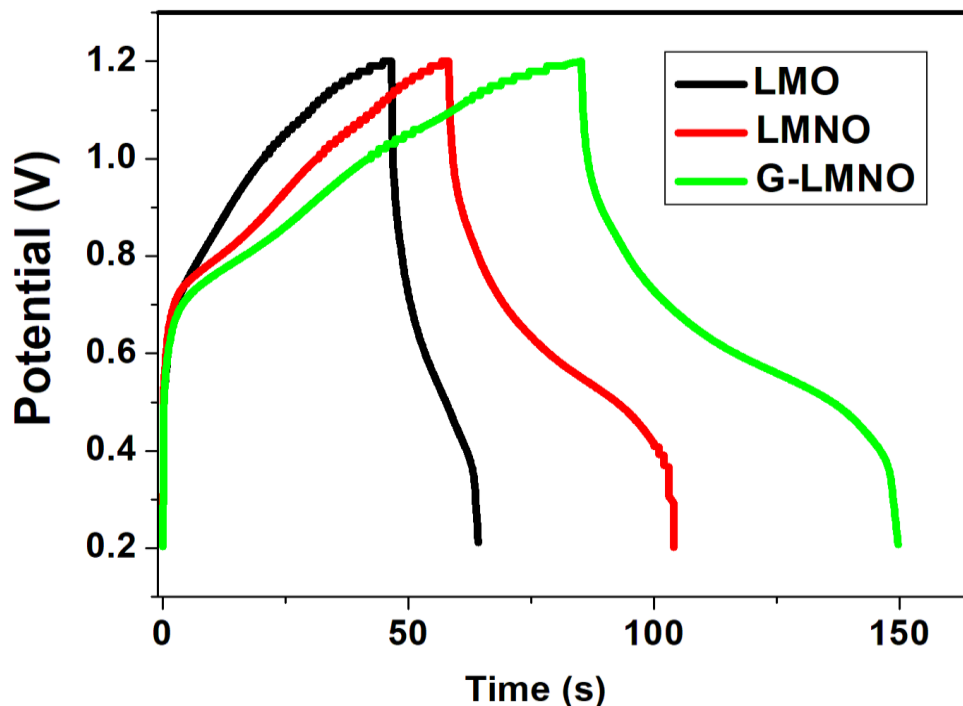


**Figure 4.12:** Comparative of galvanostatic charge-discharge curves for spinel  $\text{LiMn}_2\text{O}_4$ , nickel doped  $\text{LiMn}_2\text{O}_4$  and G-LMNO nanocomposite at a constant current density of  $1 \text{ A g}^{-1}$

#### 4.3.4 Lithium ion capacitor (LIC): LMO || AC

LIC was composed of LMO, LMNO and G-LMNO positive-working electrode and AC negative-counter electrode in  $1 \text{ M Li}_2\text{SO}_4$  electrolyte. Properly balancing the weight of both electrodes based on their specific capacitance is essential for constructing lithium ion capacitor [38].

##### 4.3.4.1 Estimation of electrochemical potential window

$\text{LiMn}_2\text{O}_4$  and the modified materials were further interrogated as an asymmetric lithium ion capacitor in aqueous  $1 \text{ M Li}_2\text{SO}_4$  electrolyte solution. **Fig. 4.13** compared the CV curves of LMO (between  $0.2$  and  $1.2 \text{ V vs Ag/AgCl}$ ) and AC (between  $-0.2$  and  $0.7 \text{ V vs Ag/AgCl}$ ). CV

curve of AC showed a perfect rectangular shaped voltammogram indicating non-faradic charge transfer reaction. This indicates the desirable fast charging/discharging capability derived from high power density. The specific capacitance calculated from CV for AC was found out to be  $30 \text{ F g}^{-1}$  at  $5 \text{ mV s}^{-1}$ . The mass balancing of the two electrodes in LIC is  $q_+ = q_-$ , where  $q_+$  represent the charges stored at the positive electrode and  $q_-$  represent the charge stored at the negative electrode [10]. In order for  $q_+ = q_-$ . The mass balancing was:

$$\frac{m_+}{m_-} = \frac{C_{sp-} \times \Delta E_-}{C_{sp+} \times \Delta E_+} \quad (7)$$

$$\text{Thus } \frac{m_{LMO}}{m_{AC}} = \frac{30 \text{ F g}^{-1} \times 0.9 \text{ V}}{66.4 \text{ F g}^{-1} \times 1 \text{ V}} \quad (8)$$

$$\frac{m_{LMO}}{m_{AC}} = 0.41 \quad (9)$$

$$m_{LMO} = 0.41 \cdot m_{AC} \quad (10)$$

The same procedure was adopted for all mass ratio calculations with data obtained from CV. The mass ratio obtained for LMNP||AC was  $m_{LMNO} = 0.20 \cdot m_{AC}$  and G-LMNO||AC was  $m_{G-LMNO} = 0.14 \cdot m_{AC}$ . The lithium ion capacitor cell system was assembled at 2 V.

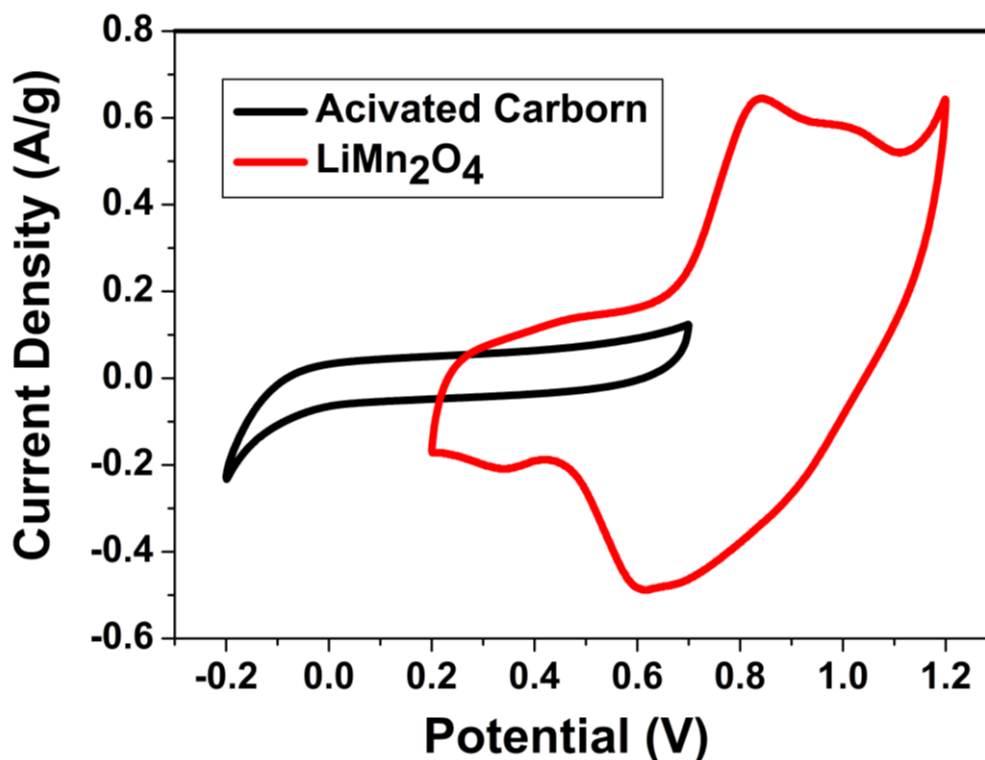


**Figure 4.13:** Comparative cyclic voltammetry curves for spinel  $\text{LiMn}_2\text{O}_4$  and activated carbon (AC) at a scan rate of  $5 \text{ mV s}^{-1}$  in aqueous  $1\text{M Li}_2\text{SO}_4$  electrolyte

#### 4.3.4.2 Electrochemical performance of spinel $\text{LiMn}_2\text{O}_4 \parallel \text{AC}$ , $\text{LMNP} \parallel \text{AC}$ and $\text{G-LMNP} \parallel \text{AC}$ lithium ion capacitors.

In the Lithium ion capacitor, upon charging,  $\text{Li}^+$  cations are deintercalated from the positive electrode and migrate into the solution phase, while a similar amount of  $\text{Li}^+$  cations are adsorbed on the surface of the negative electrode by capacitive (electrostatic) interactions [10]. Upon discharge, the  $\text{Li}^+$  cations desorb from the negative electrode and intercalate back into the  $\text{LiMn}_2\text{O}_4$  positive electrode. The CV is a suitable tool to investigate the capacitive behaviour of any material. **Fig. 4.14** compared the CV curves of  $\text{LiMn}_2\text{O}_4 \parallel \text{AC}$ ,  $\text{LMNO} \parallel \text{AC}$  and  $\text{G-LMNO} \parallel \text{AC}$  LICs in  $1 \text{ M Li}_2\text{SO}_4$  aqueous electrolyte at a scan rates of  $5 \text{ mV s}^{-1}$ . The voltammogram of all the materials retained the faradaic nature as seen in the single electrode voltammetric profile. The faradaic adsorption and desorption reaction of Li ions on the surface

of LMO makes the major contribution on the cell capacitance. G-LMNO had largest enclosed area in CV compared with LMO and LMNO, indicating a higher specific capacitance of the material. Generally the performance trend follows as: G-LMNO > LMNO > LMO at the same scan rates. CV curve for G-LMNO nanocomposite indicate that they is a synergy in LMNO and graphene which results in a combined effect and improve in conductivity.

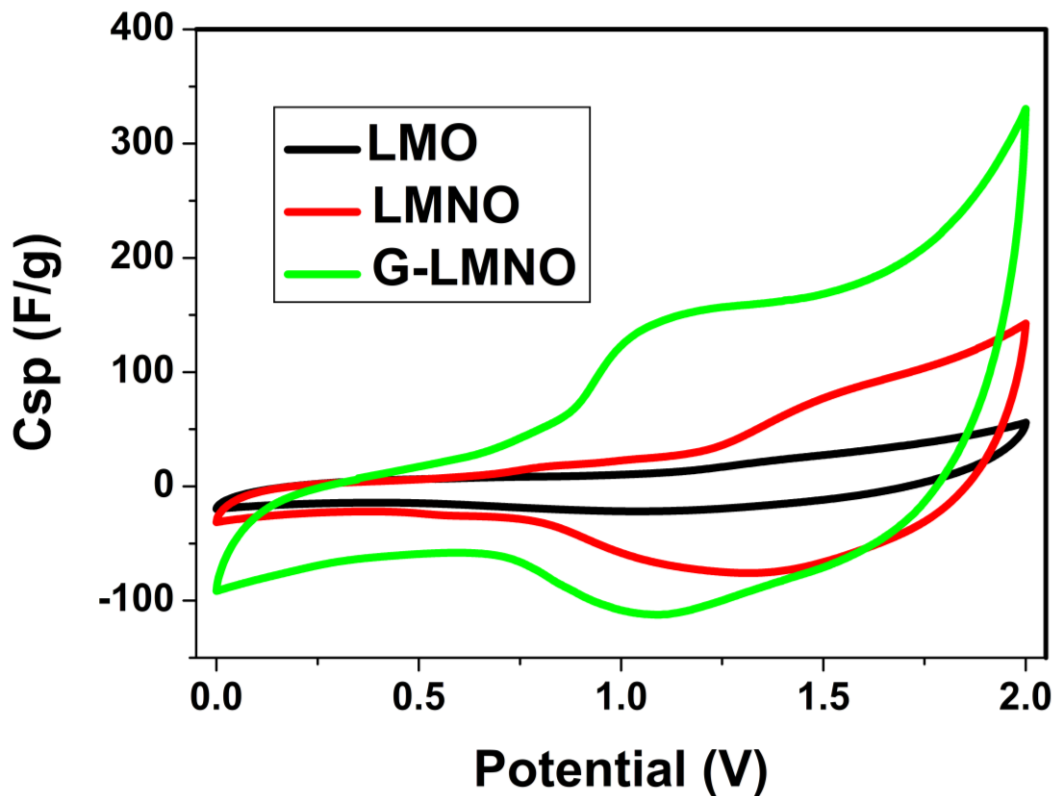
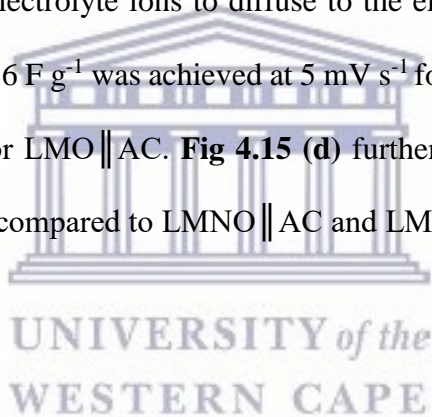


**Figure 4.14:** Comparative curves for spinel  $\text{LiMn}_2\text{O}_4 \parallel \text{AC}$ ,  $\text{LMNO} \parallel \text{AC}$  and  $\text{G-LMNO} \parallel \text{AC}$  lithium ion capacitors cyclic voltammetry at a scan rate of  $5 \text{ mV s}^{-1}$

**Fig 4.15** showed a typical cyclic voltammograms of  $\text{LMO} \parallel \text{AC}$ ,  $\text{LMNO} \parallel \text{AC}$  and  $\text{G-LMNO} \parallel \text{AC}$  with potential window of 0 - 2 V at the scan rates of 5 - 50  $\text{mVs}^{-1}$ . All the CV profile revealed two different shapes as seen in **Fig 4.15 (a), (b) and (c)**. At lower scan rates exhibit redox peaks showing the dominance of faradaic charge storage mechanism in

resembling the behaviour of cathode material in lithium ion battery. The CV shapes changed as the scan rates was increase from 20 - 50  $\text{mV s}^{-1}$ , the shapes are almost rectangular in shape. These possess capacitive nature proving the dominance of activated carbon at high scan rates, resembling the characteristics of EDLC material. This change may be caused by internal resistance of the electrode material inhibiting the charge movements within their porous structure.

**Fig. 4.15 (d)** showed the calculated specific capacitance from CV profiles for all the system. The increase in  $C_{sp}$  as the scan rate decreased was observed revealing that at slow scan rates there was more time for the electrolyte ions to diffuse to the electrode materials. As seen, a high specific capacitance of  $156 \text{ F g}^{-1}$  was achieved at  $5 \text{ mV s}^{-1}$  for G-LMNO || AC,  $51 \text{ F g}^{-1}$  for LMNO || AC and  $25.4 \text{ F g}^{-1}$  for LMO || AC. **Fig 4.15 (d)** further showed that G-LMNO || AC possess superior performance compared to LMNO || AC and LMO || AC at same scan rates.



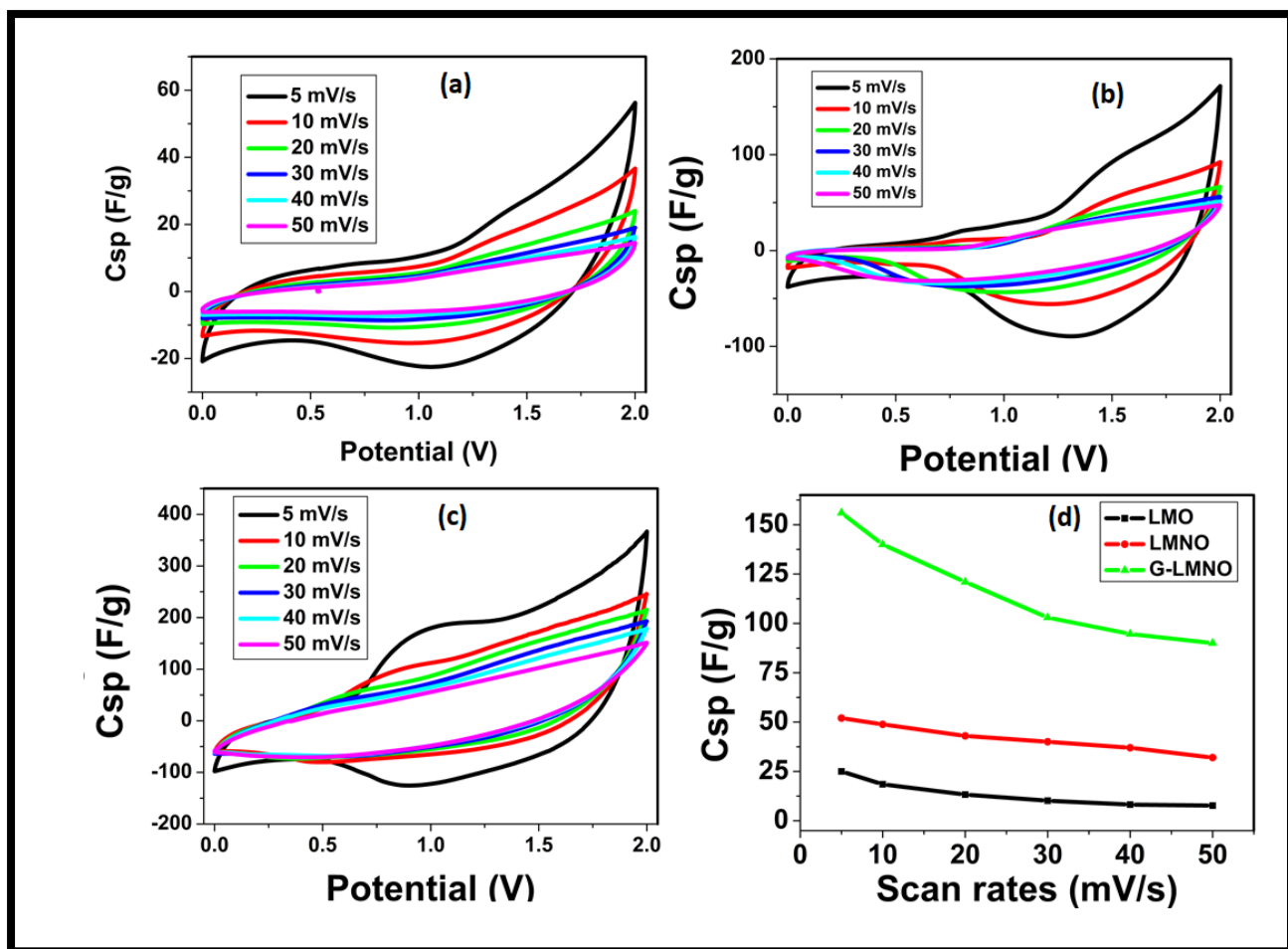


**Figure 4.15:** Comparison of cyclic voltammetry for olivine (a)  $\text{LiMn}_2\text{O}_4 \parallel \text{AC}$ , (b)  $\text{LMNO} \parallel \text{AC}$ , (c)  $\text{G-LMNO} \parallel \text{AC}$  and (d) rate capability of lithium ion capacitors at various scan rates

Furthermore, the electrochemical performance was investigated using galvanostatic charge/discharge (GCD) measurements. **Fig. 4.16** depicts GCD profiles  $\text{LMO} \parallel \text{AC}$ ,  $\text{LMNO} \parallel \text{AC}$  and  $\text{G-LMNO} \parallel \text{AC}$  LICs at current density of  $0.1 \text{ A g}^{-1}$ . The obtained charge/discharge curves showed nearly identical counterparts during charge and discharge, suggesting excellent reversibility. The charge-discharge profile displayed Faradaic mechanism showing slope-changing points at 1.36 V for charging curve and 0.8 V for discharge curve matching the observed peaks in the cyclic voltammograms (**Fig. 4.12**) at same current density

$0.1 \text{ Ag}^{-1}$ . The specific capacitance of LMO || AC, LMNO || AC and G-LMNO || AC lithium ion capacitor were 21, 56 and  $80 \text{ F g}^{-1}$ , respectively. Galvanostatic charge – discharge curve is in good agreement with CV due to that G-LMNO has capacitance improvement compared with LMP and LMNO at the same current density ( $0.1 \text{ A g}^{-1}$ ). The G-LMNO material showed to be stable at higher working potential under aqueous electrolyte. This is mainly due to the well coated graphene on the LMNO surface reducing the dissolution of Mn ions for electrode accessibility.

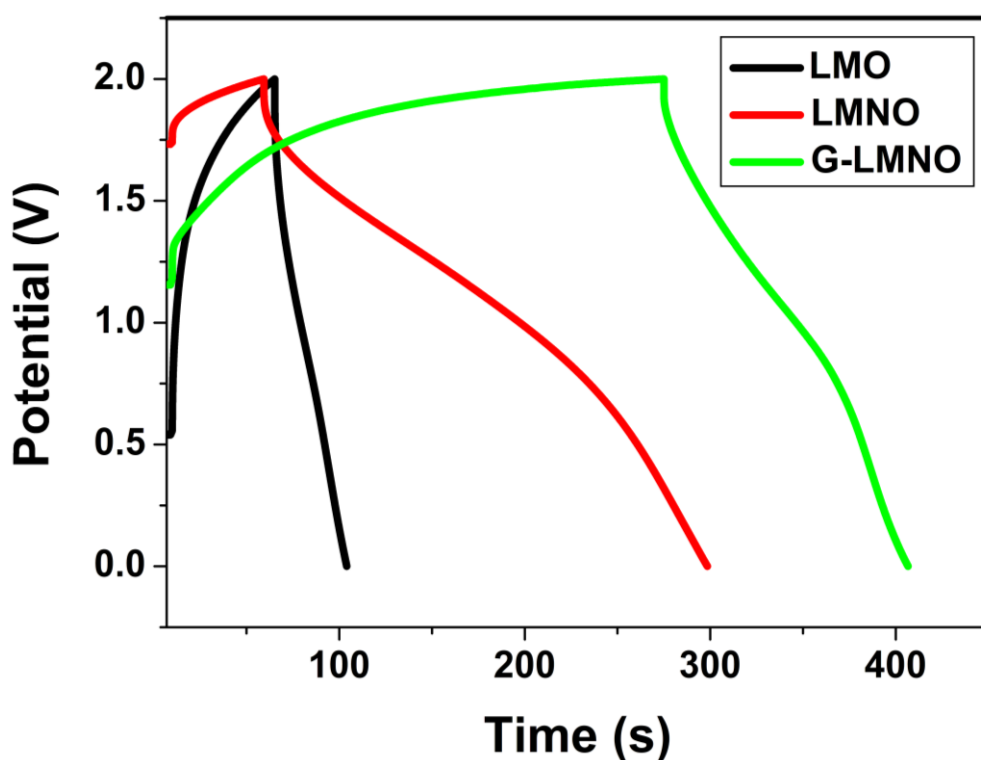


**Figure 4.16:** galvanostatic charge-discharge curves at constant current density for  $\text{LiMn}_2\text{O}_4$  || AC, LMNO || AC and G-LMNO || AC lithium ion capacitors. Electrolyte: aqueous 1 M  $\text{Li}_2\text{SO}_4$



**Fig. 4.17** showed the rate properties of LMO || AC, LMNO || AC and G-LMNO || AC lithium ion capacitors. The charge/discharge curves are obtained at varying current densities from 0.1  $\text{A g}^{-1}$  to 0.5  $\text{A g}^{-1}$ . The nonlinear charge-discharge profiles further indicate the pseudo capacitive behaviour of LMO and nanocomposites. The specific capacitance values were calculated using equation 2 mentioned above for full cell. **Fig 4.17 (d)** showed rate capability at various current densities. All the materials displayed an initial decay with a large decrease in specific capacitance ( $C_{sp}$ ) and then reached a stable level as the current density increases. G-LMNO || AC LIC achieves maximum specific capacitance of 80  $\text{F g}^{-1}$  at current density of 0.1  $\text{A g}^{-1}$  and remains 33  $\text{F g}^{-1}$  at 0.5  $\text{A g}^{-1}$ . The G-LMNO nanocomposite exhibits much high specific capacitance and rate capability compared to LMNO and LMO.



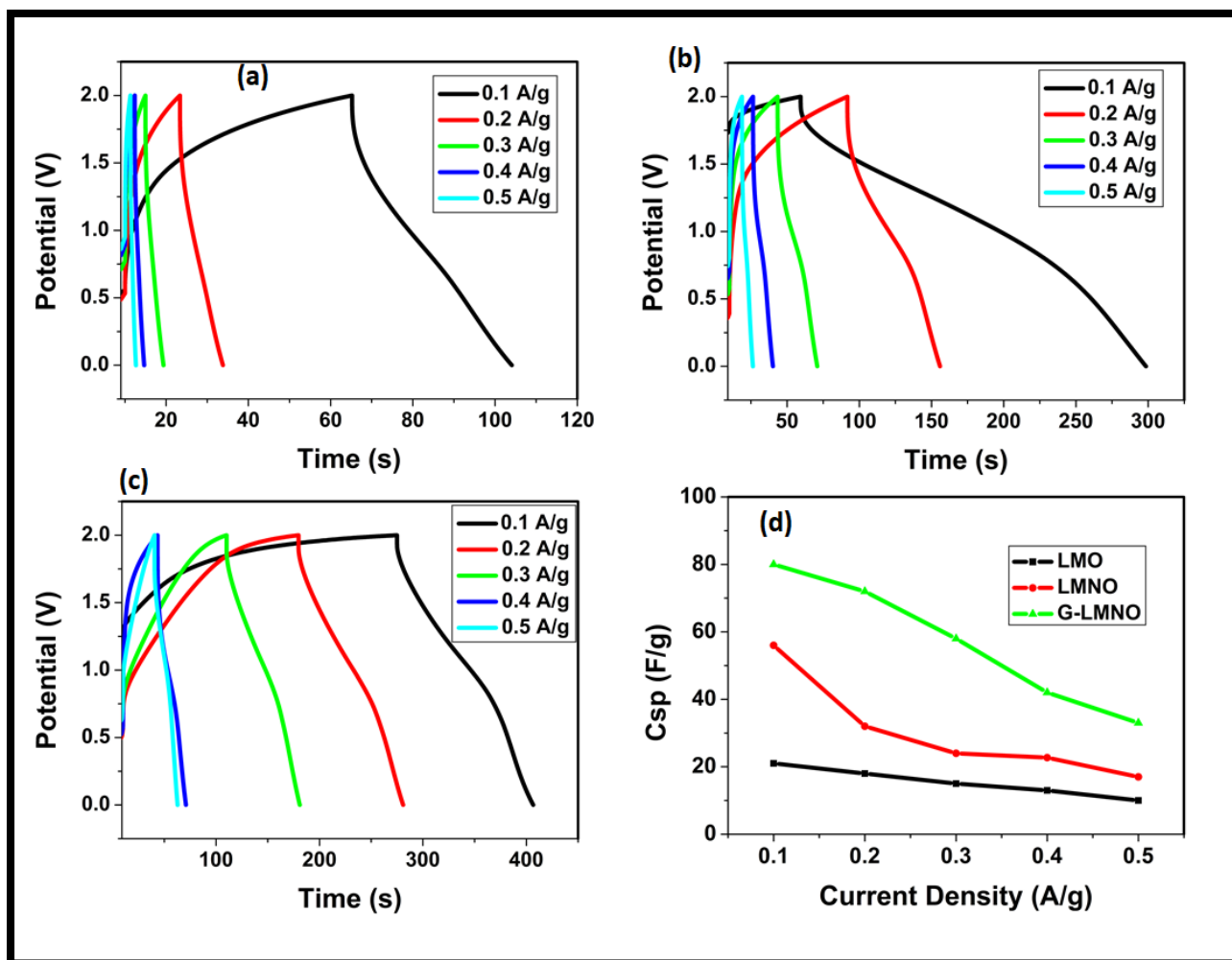


**Figure 4.17:** Comparison of galvanostatic charge-discharge for spinel (a)  $\text{LiMn}_2\text{O}_4 \parallel \text{AC}$ , (b)  $\text{LMNO} \parallel \text{AC}$ , (c)  $\text{G-LMNO} \parallel \text{AC}$  of lithium ion capacitors at various current densities and (d) capacitance curves ( $C_{\text{sp}}$  vs. current densities)

Lithium ion capacitors combine lithium ion battery electrodes with those of supercapacitors that can produce high energy and power density with satisfactory cycling stability. The energy and power densities were calculated using the data from **Fig 4.17** and equations 3 and 4 mentioned above. **Fig. 4.18** showed the relationship of energy and power densities of electrochemical power sources. Ragone plot is a common tool for evaluating the performance of energy storage devices.

The energy density and maximum power density for the G-LMNO||AC LIC device is apparently high with values of 12.32 Wh kg<sup>-1</sup> at current density of 0.1 A g<sup>-1</sup> and 19.6 kW kg<sup>-1</sup>, respectively. The maximum energy and power density values of LMO were found to be 3.1 Wh kg<sup>-1</sup> and 9.2 kW kg<sup>-1</sup>, respectively. The LMNO nanostructure showed maximum energy and power density values of 7.84 Wh kg<sup>-1</sup> and 10.6 kW kg<sup>-1</sup>, respectively. It was observed that G-LMNO||AC LIC exhibited better performance in terms of energy, power or rate capability. The G-LMNO||AC results compared with ones reported on literature suggest that this LIC device is suitable for high power energy storage application [8,9,42–44]. The improved energy and power density are attributed to good electronic conductivity graphene.

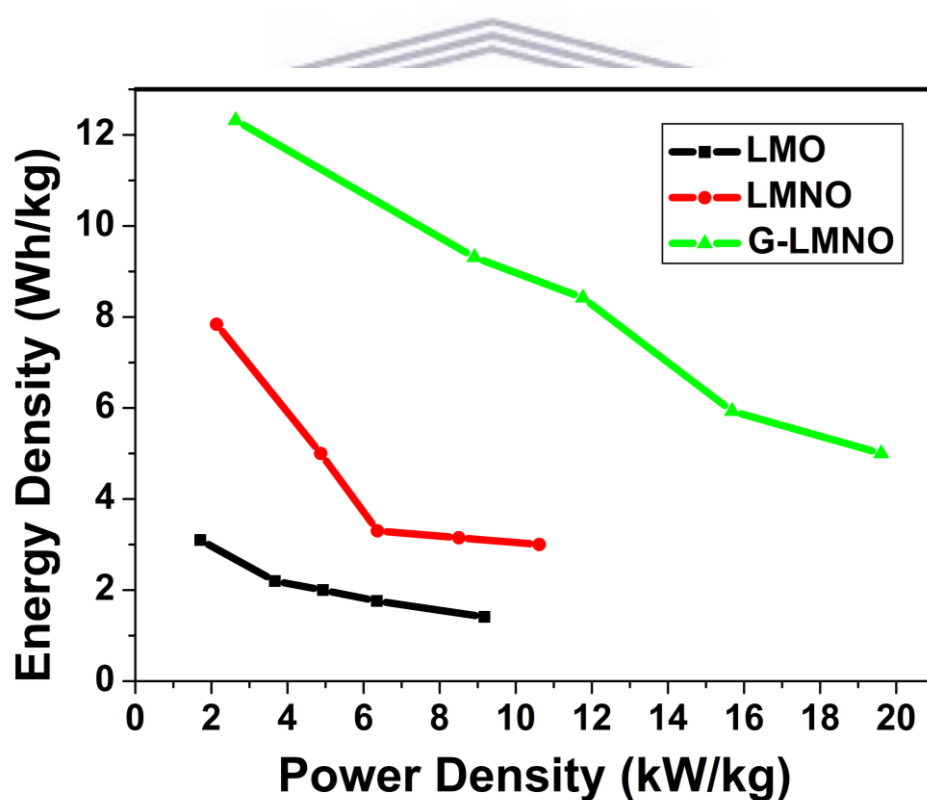


**Figure 4.18:** Ragone plots of LiMn<sub>2</sub>O<sub>4</sub>||AC, LMNO||AC and G-LMNO||AC at different current densities

**Fig. 4.19** showed EIS Nyquist plot comparison of LMO || AC, LMNO || AC and G-LMNO || AC and a possible equivalent circuit as an inset. Each curve gave almost vertical line at lower frequency region attributed to Warburg impedance associated with lithium ion diffusion in the bulk of the electrode, and a small semicircle in the high frequency region. Charge transfer resistance ( $R_{ct}$ ) is the diameter of the semicircle, which controls the transfer kinetics at the electrode interface and it reflects the electrode transfer kinetics of the redox probe at the electrode interface.  $R_s$  represent internal resistance which has a total of intrinsic resistance of active materials.  $C_{dl}$  is the double layer capacitance and  $W_s$  represents Warburg impedance.

The  $R_{ct}$  for LMO || AC, LMNO || AC and G-LMNO || AC lithium ion capacitor obtained were 8.31, 3.51 and 0.92  $\Omega$ , respectively. The G-LMNO || AC  $R_{ct}$  is smaller than that of LMO || AC and LMNO || AC, revealing that the modified nanocomposite electrode has better charge transfer kinetics than the  $\text{LiMn}_2\text{O}_4$  electrode. This suggests that the conducting graphene coated on the surface of  $\text{LiMn}_2\text{O}_4$  facilitates the transfer of electrons between electrodes and Li-ions during the charge-discharge process. These results further confirm improved electrochemical performance of G-LMNO || AC lithium ion capacitor as a result of synergetic relationship between graphene and LMNO which was seen on evident on both GCD and CV.

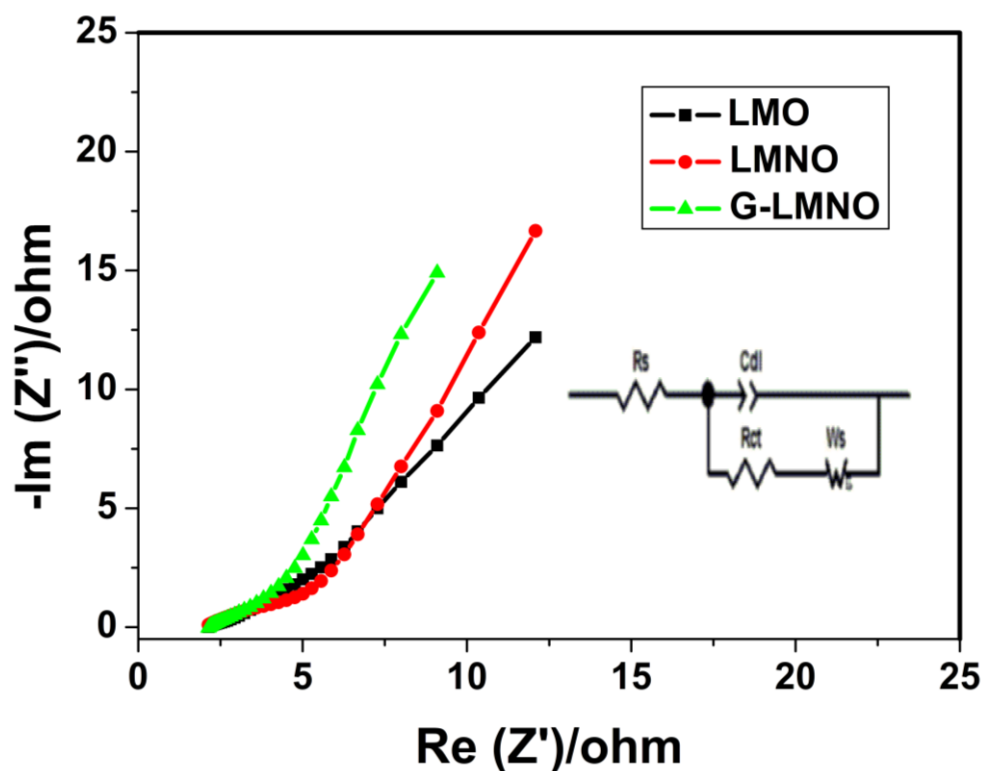


**Figure 4.19:** Comparative Nyquist plots of  $\text{LiMn}_2\text{O}_4 \parallel \text{AC}$ ,  $\text{LMNO} \parallel \text{AC}$  and  $\text{G-LMNO} \parallel \text{AC}$  and the inset of equivalent circuit.

The pseudocapacitive behaviour of all the materials synthesized for lithium ion capacitors was further emphasized by the bode plot. **Fig. 4.20** displayed the Bode phase angle plot for  $\text{LMO} \parallel \text{AC}$ ,  $\text{LMNO} \parallel \text{AC}$  and  $\text{G-LMNO} \parallel \text{AC}$  LICs. The lower  $R_{ct}$  observed from the Nyquist plot corresponds to the shift of phase angle to high frequency which was observed from Bode plots of  $\text{G-LMNO}$  nanocomposite and therefore, associated with fast electron transfer. The phase angle obtained for  $\text{LMO} \parallel \text{AC}$ ,  $\text{LMNO} \parallel \text{AC}$  and  $\text{G-LMNO} \parallel \text{AC}$  LICs was 45, 52 and 56°, respectively. The  $\text{G-LMNO} \parallel \text{AC}$  exhibited improved conductivity based on higher phase angle compared to other materials. As it is known that between 20 - 45° the material possesses semiconductor characteristic compared to 0° (insulator) and 90° which is of pure metal (more conducting). These values may be further compared to that of an ideal EDLC which is close to 90° [45]. The lower phase angle suggest the electrodes possesses pseudo capacitive behaviour due to the faradaic reaction occurring at the positive electrode

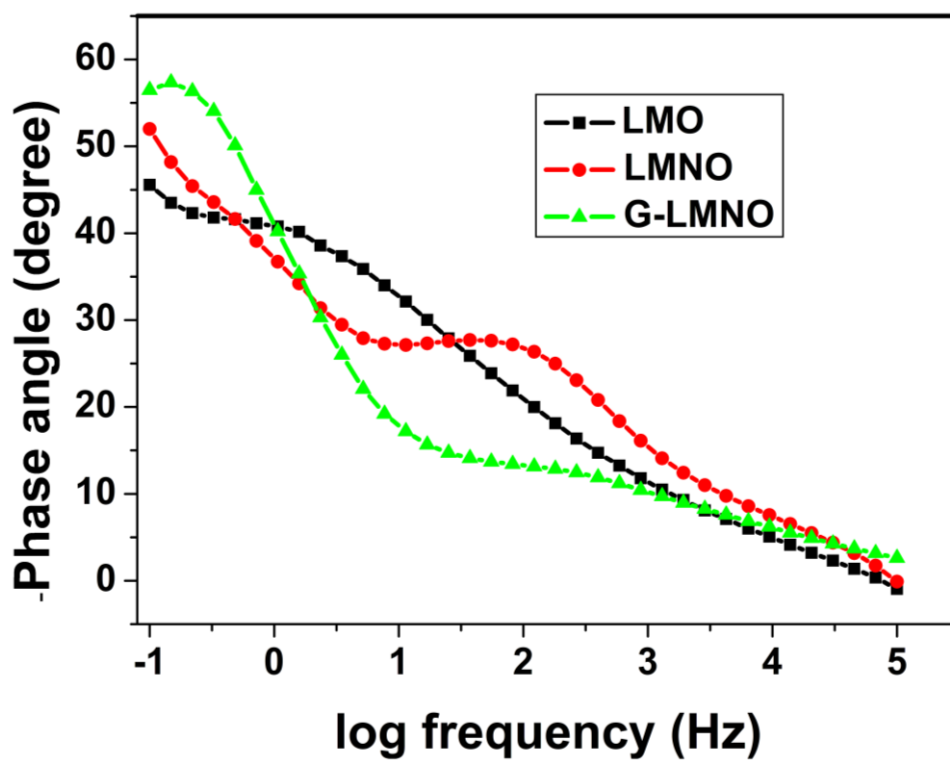


**Figure 4.20:** Comparative Bode plots of  $\text{LiMn}_2\text{O}_4 \parallel \text{AC}$ ,  $\text{LMNO} \parallel \text{AC}$  and  $\text{G-LMNO} \parallel \text{AC}$

UNIVERSITY of the  
WESTERN CAPE

#### 4.3.4.3 Cycling performance

The cycle life is an important factor in supercapacitors electrode material, cyclic stability experiments measured by galvanostatic charge-discharge represent a reliable analysis method for establishing the long-term stability of LICs electrodes. **Fig. 4.21** showed the specific capacitance of the three electrodes within 1000 cycles at  $0.4 \text{ A g}^{-1}$ . All materials showed a capacitance decay, as cycle number is increase. The  $\text{G-LMNO} \parallel \text{AC}$  exhibited excellent stability during 1000 cycles compared to LMO and LMNO electrodes. The device delivered a capacitance of  $47 \text{ F g}^{-1}$  during the first cycle and  $33.2 \text{ F g}^{-1}$  at the 1000<sup>th</sup> cycle. The capacitive retention was 61%, 67% and 70% for  $\text{LMO} \parallel \text{AC}$ ,  $\text{LMNO} \parallel \text{AC}$  and  $\text{G-LMNO} \parallel \text{AC}$  respectively, indicating favourable cyclability. The excellent stability of the  $\text{G-LMNP} \parallel \text{AC}$

lithium ion capacitor showed that this device can be charged and discharged without significant deterioration. The values obtained from cycling performance correspond with a specific energy of  $5.93 \text{ Wh kg}^{-1}$  and power density of  $15.7 \text{ kW kg}^{-1}$ .

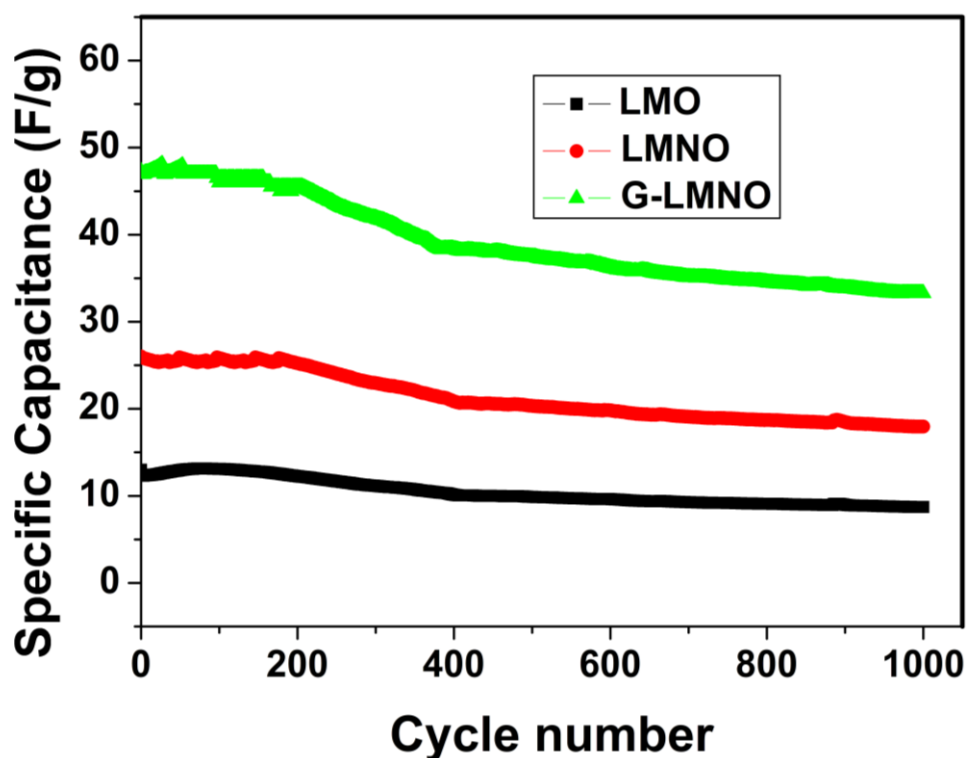


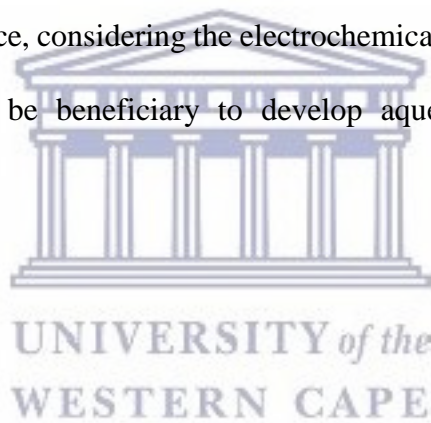
**Figure 4.21:** Comparative cycling performance at current density of  $0.4 \text{ Ag}^{-1}$  of  $\text{LiMn}_2\text{O}_4 \parallel \text{AC}$ ,  $\text{LMNO} \parallel \text{AC}$  and  $\text{G-LMNO} \parallel \text{AC}$

#### 4.4 Summary

The G-LMNO nanocomposite was prepared by a facile hydrothermal, coating and calcination treatment processes. Nickel foam acted as the current collector; AC as negative electrode, and 1 M  $\text{Li}_2\text{SO}_4$  aqueous electrolyte. The  $\text{G-LMNO} \parallel \text{AC}$  displayed an improved electrochemical performance compared to  $\text{LMO} \parallel \text{AC}$  and  $\text{LMNO} \parallel \text{AC}$ . The  $\text{LMO} \parallel \text{AC}$  exhibited specific capacitance, energy density and maximum power density of  $21 \text{ F g}^{-1}$ ,  $3.1 \text{ Wh kg}^{-1}$  and  $9.1 \text{ kW}$



kg<sup>-1</sup>, respectively. The LMNO||AC displayed specific capacitance, energy density and maximum power density of 56 F g<sup>-1</sup>, 7.8 Wh kg<sup>-1</sup> and 10.6 kW kg<sup>-1</sup>, respectively. The G-LMNO||AC exhibited a high capacitance at 80 F g<sup>-1</sup> at the current density 0.1 Ag<sup>-1</sup> and excellent cycle stability after 1000 cycles at a current density of 0.4 A g<sup>-1</sup>. The improved capacitance performance of G-LMNO was ascribed to the graphene modification and the doping of nickel. This contributed to the improved conductivity and fast diffusion of electrolyte ions on the surface of the electrode. Furthermore, the improved conductivity was observed from *R*<sub>ct</sub> obtained in EIS. The *R*<sub>ct</sub> values for G-LMNO, LMNO and LMO were 0.92, 3.51 and 8.31 Ω, respectively. The G-LMNO||AC exhibited high capacitance, good cycle stability and high rate capability, showed by high maximum power density (19.6 kW kg<sup>-1</sup>) and energy density of 12.32 Wh kg<sup>-1</sup>. Hence, considering the electrochemical performance of G-LMNO as positive electrode, it would be beneficiary to develop aqueous type LIC for practical application.



## 4.5 Reference

- [1] X. Yang, F. Qu, H. Niu, Q. Wang, J. Yan, Z. Fan, High-performance aqueous asymmetric supercapacitor based on spinel  $\text{LiMn}_2\text{O}_4$  and nitrogen-doped graphene / porous carbon composite, *Electrochim. Acta.* 180 (2015) 287–294.
- [2] F. Zhang, Y. Tang, H. Liu, H. Ji, C. Jiang, J. Zhang, X. Zhang, X. Lee., Uniform Incorporation of Flocculent Molybdenum Disulfide Nanostructure into Three-Dimensional Porous Graphene as an Anode for High-Performance Lithium Ion Batteries and Hybrid Supercapacitors, *ACS Appl. Mater. Interfaces.* 8 (2016) 4691–4699.
- [3] J. Lu, Y.L. Chang, B. Song, H. Xia, J.R. Yang, K.S. Lee, L. Lu., High energy spinel-structured cathode stabilized by layered materials for advanced lithium-ion batteries, *J. Power Sources.* 271 (2014) 604–613. doi:10.1016/j.jpowsour.2014.08.037.
- [4] W. He, C. Wang, F. Zhuge, X. Deng, X. Xu, T. Zhai, Nano Energy Flexible and high energy density asymmetrical supercapacitors based on core / shell conducting polymer nanowires / manganese dioxide nano flakes, *Nano Energy.* 35 (2017) 242–250.
- [5] N. Böckenfeld, R.S. Kühnel, S. Passerini, M. Winter, A. Balducci, Composite  $\text{LiFePO}_4/\text{AC}$  high rate performance electrodes for Li-ion capacitors, *J. Power Sources.* 196 (2011) 4136–4142. doi:10.1016/j.jpowsour.2010.11.042.
- [6] L. Xu, S. Wang, X. Zhang, T. He, F. Lu, H. Li, J. Ye., A facile method of preparing  $\text{LiMnPO}_4/\text{reduced}$  graphene oxide aerogel as cathodic material for aqueous lithium-ion hybrid supercapacitors, *Appl. Surf. Sci.* 428 (2017) 977–985.
- [7] C. Hu, Y. Wu, Spinel  $\text{LiMn}_2\text{O}_4$  nanohybrid as high capacitance positive electrode material for supercapacitors. *J Power Sources*, (2014).

- doi:10.1016/j.jpowsour.2013.07.046.
- [8] J. Li, X. Zhang, Y. Huang, L. Guo, Y. Qi, LiMn<sub>2</sub>O<sub>4</sub>/Graphene composites as cathode with enhanced electrochemical performance for lithium-ion capacitors, *RSC Adv.* 6 (2016) 54866–54873. doi:10.1039/C6RA09103B.
- [9] S.J.K. Parthiban Pazhamalai, Karthikeyan Krishnamoorthy, M.S.P. Sudhakaran, Fabrication of high performance aqueous Li-ion hybrid capacitor using LiMn<sub>2</sub>O<sub>4</sub> and graphene, *ChemElectroChem.* 4 (2017) 396–403. doi:10.1111/liv.12553.
- [10] O. Hanna, S. Luski, T. Brousse, D. Aurbach, Aqueous energy-storage cells based on activated carbon and LiMn<sub>2</sub>O<sub>4</sub> electrodes, *J. Power Sources.* 354 (2017) 148–156. doi:10.1016/j.jpowsour.2017.04.039.
- [11] N. Ross, M. Nzaba, W. Ntuthuko, C. Ikpo, P. Baker, E. Iwuoha, Palladium-Gold Nanoalloy Surface Modified LiMn<sub>2</sub>O<sub>4</sub> Cathode for Enhanced Li-Ion Battery, *J. Nanomaterials* 2015 (2015).
- [12] X. Li, Y. Xu, Enhanced cycling performance of spinel LiMn<sub>2</sub>O<sub>4</sub> coated with ZnMn<sub>2</sub>O<sub>4</sub> shell, *J. Solid State Electrochem.* 12 (2007) 851–855. doi:10.1007/s10008-007-0426-x.
- [13] Q. Zhu, S. Zheng, X. Lu, Y. Wan, Q. Chen, J. Yang, Improved cycle performance of LiMn<sub>2</sub>O<sub>4</sub> cathode material for aqueous rechargeable lithium battery by LaF<sub>3</sub> coating, *J. Alloys Compd.* 654 (2016) 384–391. doi:10.1016/j.jallcom.2015.09.085.
- [14] N. West, K.I. Ozoemena, C.O. Ikpo, P.G.L. Baker, E.I. Iwuoha, Transition metal alloy-modulated lithium manganese oxide nanosystem for energy storage in lithium-ion battery cathodes, *Electrochim. Acta.* 101 (2013) 86–92. doi:http://dx.doi.org/10.1016/j.electacta.2012.11.085.
- [15] H. Liu, R. Tian, Y. Jiang, X. Tan, J. Chen, L. Zhang, Y. Guo, H. Wang, L. Sun, W.

- Chu, On the drastically improved performance of Fe - Doped  $\text{LiMn}_2\text{O}_4$  nanoparticles prepared by a facile solution - Gelation route, *Electrochim. Acta.* 180 (2015) 138–146. doi:10.1016/j.electacta.2015.08.123.
- [16] Y. Fu, H. Jiang, Y. Hu, Y. Dai, L. Zhang, C. Li, Synergistic Enhancement Effect of Al Doping and Highly Active Facets of  $\text{LiMn}_2\text{O}_4$  Cathode Materials for Lithium-Ion Batteries, *Ind. Eng. Chem. Res.* (2015) 150407111022001. doi:10.1021/ie504659h.
- [17] D. Tang, Y. Sun, Z. Yang, L. Ben, L. Gu, X. Huang, Surface Structure Evolution of  $\text{LiMn}_2\text{O}_4$  Cathode Material upon Charge/Discharge, *Chem. Mater.* 26 (2014) 3535–3543. doi:10.1021/cm501125e.
- [18] A. González, E. Goikolea, J.A. Barrena, R. Mysyk, Review on supercapacitors: Technologies and materials, *Renew. Sustain. Energy Rev.* 58 (2016) 1189–1206. doi:10.1016/j.rser.2015.12.249.
- [19] Y. Sun, J. Tang, F. Qin, J. Yuan, K. Zhang, J. Li, D. Zhu, L. Qin., Hybrid Lithium-Ion Capacitors with Asymmetric Graphene Electrodes, *J. Mater. Chem. A.* 5 (2017) 13601–13609. doi:10.1039/C7TA01113J.
- [20] H. Zhao, F. Li, X. Liu, W. Xiong, B. Chen, H. Shao, A simple, low-cost and eco-friendly approach to synthesize single-crystalline  $\text{LiMn}_2\text{O}_4$  nanorods with high electrochemical performance for lithium-ion batteries, *Electrochim. Acta.* 166 (2015) 124–133. doi:10.1016/j.electacta.2015.03.040.
- [21] A.K. Geim, K.S. Novoselov, The rise of graphene. *Nat. Mater.* 6 (2007) 183–191.
- [22] D. Chen, H. Quan, S. Luo, X. Luo, F. Deng, H. Jiang, Reduced graphene oxide enwrapped vanadium pentoxide nanorods as cathode materials for lithium-ion batteries, *Phys.*

E Low-Dimensional Syst. Nanostructures. 56 (2014) 231–237.  
doi:10.1016/j.physe.2013.09.009.

[23] H. Yu, K. Xie, J. Hu, C. Shen, J. Wang, B. Wei, The importance of raw graphite size to the capacitive properties of graphene oxide, RSC Adv. 6 (2016) 17023–17028.  
doi:10.1039/C5RA24501J.

[24] K. Makgopa, P.M. Ejikeme, C.J. Jafta, K. Raju, M. Zeiger, V. Presser, K.I. Ozoemena, A high-rate aqueous symmetric pseudocapacitor based on highly graphitized onion-like carbon/birnessite-type manganese oxide nanohybrids, J. Mater. Chem. A. (2015).

[25] C.J. Jafta, F. Nkosi, L. le Roux, M.K. Mathe, M. Kebede, K. Makgopa, K.I. Ozoemena, Manganese oxide/graphene oxide composites for high-energy aqueous asymmetric electrochemical capacitors, Electrochim. Acta. 110 (2013) 228–233.  
doi:http://dx.doi.org/10.1016/j.electacta.2013.06.096.

[26] W.K. Chee, H.N. Lim, I. Harrison, K.F. Chong, Z. Zainal, C.H. Ng, Performance of Flexible and Binderless Polypyrrole/Graphene Oxide/Zinc Oxide Supercapacitor Electrode in a Symmetrical Two-Electrode Configuration, Electrochim. Acta. 157 (2015) 88–94.  
doi:http://dx.doi.org/10.1016/j.electacta.2015.01.080.

[27] M.S. Michael, Role of Cu substitution on the pseudocapacitive performance of nanoplatelet shaped spinels,  $\text{Ni}_x\text{Cu}_z\text{Co}_y\text{O}_4$  { $x=1-z$ ,  $y=2-z$ ,  $z=0.2$ }, Electrochim. Acta. 120 (2014) 350–358. doi:10.1016/j.electacta.2013.12.056.

[28] A.K. Nanjundan, R.R. Gaddam, M. Suresh, S.R. Varanasi, D. Yang, S. Bhatia, Porphyrin-graphene oxide frameworks for long life sodium ion batteries, J. Mater. Chem. A. (2017). doi:10.1039/C7TA02370G.

- [29] S. Yaragalla, A.P. Meera, N. Kalarikkal, S. Thomas, Chemistry associated with natural rubber – graphene nanocomposites and its effect on physical and structural properties, *Ind. Crop. Prod.* 74 (2015) 792–802. doi:10.1016/j.indcrop.2015.05.079.
- [30] R. Ramachandran, M. Saranya, V. Velmurugan, B.P.C. Raghupathy, S. Kwan, A. Nirmala, Effect of reducing agent on graphene synthesis and its influence on charge storage towards supercapacitor applications, *Appl. Energy.* 153 (2015) 22–31. doi:10.1016/j.apenergy.2015.02.091.
- [31] Y. Cai, Y. Huang, X. Wang, D. Jia, X. Tang, Long cycle life, high rate capability of truncated octahedral  $\text{LiMn}_2\text{O}_4$  cathode materials synthesized by a solid-state combustion reaction for lithium ion batteries, *Ceram. Int.* 40 (2014) 14039–14043. doi:10.1016/j.ceramint.2014.05.130.
- [32] D. Zhan, F. Yang, Q. Zhang, X. Hu, T. Peng, Effect of solid-state reaction temperature on electrochemical performance of  $\text{LiMn}_2\text{O}_4$  submicro-rods as cathode material for Li-ion battery by using  $\text{MnOOH}$  submicro-rods as self-template, *Electrochim. Acta.* 129 (2014) 364–372. doi:10.1016/j.electacta.2014.02.141.
- [33] H. Schablegger, Y. Singh, *The SAXS Guide*, Ant. Paar. (2011) 1–99.
- [34] X. Small-angle, X. Di, B. Fleury, R. Cortes-huerto, O. Tache, F. Testard, Gold Nanoparticle Internal Structure and Symmetry Probed by Unified Small-Angle X - ray Scattering and X - ray Diffraction Coupled with Molecular Dynamics Analysis, *Nano Lett.* 15 (2015) 6088–6094. doi:10.1021/acs.nanolett.5b02924.
- [35] S. Geller, J.L. Durand, Refinement of the Structure of  $\text{LiMnPO}_4$ , *Acta Crystallogr.* 13 (1960) 325–331.

- [36] A.K. Padhi, K.S. Nanjundaswamy, J.B. Goodenough, Phospho-olivines as Positive-Electrode Materials for Rechargeable Lithium Batteries, *J. Electrochem. Soc.* 144 (1997) 1188–1194. doi:10.1684/agr.2014.0700.
- [37] X.-M. Liu, Z.-D. Huang, S. Oh, P.-C. Ma, P.C.H. Chan, G.K. Vedam, K. Kang, J. Kim, Sol-gel synthesis of multiwalled carbon nanotube-LiMn<sub>2</sub>O<sub>4</sub> nanocomposites as cathode materials for Li-ion batteries, *J. Power Sources.* 195 (2010) 4290–4296. doi:10.1016/j.jpowsour.2010.01.068.
- [38] A. Lagashetty, V. Havanoor, S. Basavaraja, A. Venkataraman, Combustion synthesis of LiMn<sub>2</sub>O<sub>4</sub> by thermal decomposition of oxalate precursors, *Indian J. Chem. Technol.* 15 (2008) 41–44.
- [39] S. Niketic, M. Couillard, D. MacNeil, Y. Abu-Lebdeh, Improving the performance of high voltage LiMn<sub>1.5</sub>Ni<sub>0.5</sub>O<sub>4</sub> cathode material by carbon coating, *J. Power Sources.* 271 (2014) 285–290. doi:10.1016/j.jpowsour.2014.08.015.
- [40] H. Xiao, Y. Wang, K. Xie, S. Cheng, X. Cheng, High capacitance LiMn<sub>2</sub>O<sub>4</sub> microspheres with different microstructures as cathode material for aqueous asymmetric supercapacitors, *J. Alloys Compd.* 738 (2018) 25–31. doi:10.1016/j.jallcom.2017.12.143.
- [41] S.R.S. Prabaharan, A. Anslin Star, A.R. Kulkarni, M.S. Michael, Nano-composite LiMnPO<sub>4</sub> as New Insertion Electrode for Electrochemical Supercapacitors, *Curr. Appl. Phys.* 15 (2015) 1624–1633. doi:10.1016/j.cap.2015.09.009.
- [42] C. Chen, D. Yu, G. Zhao, L. Sun, Y. Sun, K. Leng, et al., Hierarchical porous graphitic carbon for high-performance supercapacitors at high temperature, *RSC Adv.* 7 (2017) 34488–34496. doi:10.1039/C7RA06234F.



- [43] H.-C. Tao, S.-C. Zhu, X.-L. Yang, L.-L. Zhang, S.-B. Ni, Systematic investigation of reduced graphene oxide foams for high-performance supercapacitors, *Electrochim. Acta.* 190 (2016) 168–177. doi:10.1016/j.electacta.2015.12.179.
- [44] M.S. Michael, A.R. Kulkarni, S.R.S. Prabaharan, Design of Monolayer Porous Carbon-Embedded Hybrid-LiMnPO<sub>4</sub> for High Energy Density Li-Ion Capacitors, *J. Nanosci. Nanotechnol.* 16 (2016) 7314–7324. doi:10.1166/jnn.2016.12081.
- [45] K. Makgopa, K. Raju, P.M. Ejikeme, K.I. Ozoemena, High-performance Mn<sub>3</sub>O<sub>4</sub>/onion-like carbon (OLC) nanohybrid pseudocapacitor: Unravelling the intrinsic properties of OLC against other carbon supports, *Carbon N. Y.* 117 (2017) 20–32. doi:10.1016/j.carbon.2017.02.050.



## CHAPTER 5

### 5 Development of copper manganese oxide and lithium manganese oxide-for thermochemical energy storage system

#### Overview

*Development of thermal energy storage (TES) systems for concentrated solar power (CSP) is essential in order to match a variable electricity demand with an intermittent energy source supply thereby enhancing energy generation dispatchability. In this chapter, we further studied additionally the effect that doping of Mn oxides with Li and Cu has on the redox temperatures and reaction enthalpies of both forward and reverse reactions. Lithium manganese oxides and copper manganese oxide were synthesized by a modified Pechini method and their redox cycle stability characterized in order to evaluate their suitability as thermochemical storage (TCS) materials.*

## ABSTRACT

At present, there is a clear interest in developing redox materials with improved properties for high temperature thermochemical energy storage. Chemical modification of manganese oxides with cations such as Li and Cu can produce, among other phases,  $\text{LiMn}_2\text{O}_4$  and  $\text{CuMn}_2\text{O}_4$  spinels, which are feasible candidates for heat storage due to their redox capacity. In this work, these materials were synthesised by a modified Pechini method, and the characterization results confirmed the formation of the targeted phases with some minor contribution of  $\text{Mn}_3\text{O}_4$ . Thermogravimetric redox tests in air established that both materials experience fully reversible redox transformations when the temperature is varied between 900 and 1000 °C. These assays showed the stability of both Cu and Li mixed oxides after five consecutive redox cycles and, in accordance, the XRD confirmed the spinels retaining their crystal structures after the treatment. However, in these conditions, reduction temperatures are higher than 940 °C. Alternatively, if the reduction is performed in argon and the oxidation in air, it is possible to increase the amount of oxygen exchanged in the gas-solids reactions and, accordingly, the heat storage capacity. Therefore, the heat recovered in the re-oxidation of  $\text{CuMn}_2\text{O}_4$  at 700 °C was  $144 \text{ kJ kg}^{-1}$ , while  $\text{LiMn}_2\text{O}_4$  showed an enthalpy of  $209 \text{ kJ kg}^{-1}$  ( $37 \text{ kJ mol}^{-1}$ ). These changes in the composition of the atmosphere do not affect the stability of the system and the conversion is maintained after five consecutive cycles. In all cases, the initial spinel phase is recovered after re-oxidation, which takes place at remarkably fast rates. Analysis of the intermediate reduced materials reveals a significant complexity of the redox transformations, which imply the formation of  $\text{LiMnO}_2$  and  $\text{CuMnO}_2$  among other phases. Accordingly, considering the stability of these systems as well as the relatively high enthalpies,  $\text{CuMn}_2\text{O}_4$  and  $\text{LiMn}_2\text{O}_4$  appear to be promising materials for thermochemical energy storage.

## 5.1 Introduction

The continuous demand for energy as well as environmental concerns due to global warming places an urgent need for sustainable and efficient energy systems. Solar radiation can provide enough energy to meet the world's demand. Concentrated solar power (CSP) plays a huge role for prospective renewable energy and heat generation [1]. Nevertheless, solar power presents the limitation of being an intermittent energy source. In this respect built-in energy storage technologies research is undergoing tremendous development because they allow CSP plants to supply power on demand [2].

Thermal energy storage systems are a key component of concentrated solar power plants [3], since its implementation increases the energy generation dispatch ability [4]. Heat is stored in three different mechanisms which are sensible heat storage, latent heat storage and thermochemical heat storage. The most widely studied and commercialised technology is sensible heat storage but it suffers from low energy density [5]. The less matured technologies are both latent heat storage and thermochemical heat storage which still need further research. Physical thermal storage systems (sensible heat or phase change) would gradually lose their thermal energy [6]. Therefore this leads to thermochemical energy storage which is the less developed between the three due to the fact that latent and sensible heat storage are not suitable for long-term energy storage. In contrast with other more developed technologies for thermal storage based on latent or sensible heat, TCS presents relatively high energy densities.

Thermochemical heat storage (TCS) stores energy by using reversible chemical reactions to store thermal energy in the form of chemical compound and have high density and potential low cost energy storage [7]. High amounts of thermal energy can be stored by thermochemical

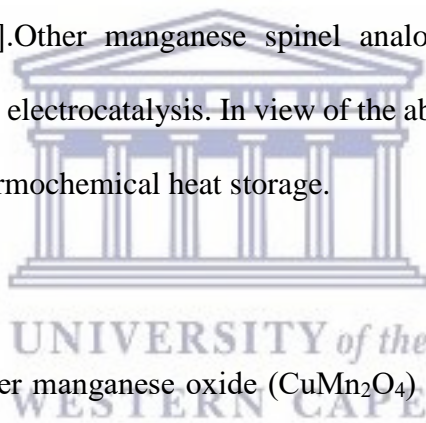
reaction while using various chemical reactions for heat absorption and subsequent heat release.

Many systems based on redox chemical reaction which can reversibly loose and gain oxygen have been proposed as candidates for high temperature range (700-1000 °C) solar polar towers [8]. Several pure metal oxides have been analysed as possible suitable oxides for this application. In particular, manganese oxide, iron oxide and copper oxide redox reactions appear most appropriate for temperatures in 700-1000 °C [9,10]. TCS based on redox cycles of metal oxides consists of two steps. During the charge step (endothermic process), part of the hot air generated from renewable energy sources or conventional energy sources like fossil fuels is used to supply enough heat to carry out the reduction. Surplus heat produced at the CSP plant is partly stored by means of chemical reaction as in equation 1 below. Then during the discharge step, (off-sun periods) the reversible oxidation of the reduced form of the metal oxide releases the heat previously stored as shown in equation 2. The redox reaction can be described as follows (M = Metal):



TSC are basically focused on three directly interrelated aspects, storage [11–14], reactor concept [15,16], and system integration [17]. The work conducted in this segment of the thesis utilized the redox cycle of manganese oxide ( $\text{Mn}_2\text{O}_3/\text{Mn}_3\text{O}_4$ ) in the development of materials for thermochemical heat storage at high temperatures. The oxide pair have the advantages of being less expensive and more abundant than other existing pairs [18]. Previous works proved that too high temperatures required for the application led to a decrease in the oxidation rate during first cycle assay [10]. Stability of the oxidation rates over long-term cycling was needed

to provide proper control of the discharge process to guarantee the commercial viability of TCS. Metal doping has been generally studied as the first approach because it can be beneficial for oxygen diffusion through the crystal lattice as the incorporation of cations of different oxidation states and radii could create charge imbalances [8]. Carrillo *et al* showed that the incorporation of Fe was especially beneficial in the enhancement of the oxidation rates and improvement of its stability over 30 redox cycles [18]. Varsano *et al* confirmed that the addition of lithium to the conventional manganese oxide thermochemical cycle is highly beneficial due to the fact that various redox cycles were performed and the material showed great stability [8]. Carrillo *et al* revealed that metal co-doping by Cu-Fe can narrow the thermal hysteresis which means that heat is stored and released in closer range of temperatures which boosted the energy storage efficiency [6]. Other manganese spinel analogues such as  $ZnMn_2O_4$  and  $CaMn_2O_4$  have been studied in electrocatalysis. In view of the above, spinel manganese oxides are considered suitable for thermochemical heat storage.



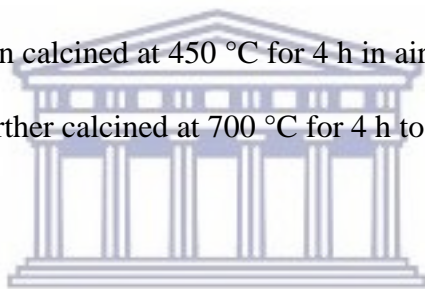
The utilization of spinel copper manganese oxide ( $CuMn_2O_4$ ) and lithium manganese oxide ( $LiMn_2O_4$ ) as thermal energy storage materials was explored in this research. Spinel structured copper manganese oxide ( $CuMn_2O_4$ ) is an important inorganic functional semiconductor material and has been widely studied and applied in various areas [19–21].  $LiMn_2O_4$  has been vastly used as a cathode material in lithium ion batteries [22–25].

The properties of these spinel oxides were studied for applications in thermochemical energy storage. Redox cycling was monitored by thermogravimetric analysis. Structure and morphology were characterized by powder X-ray diffraction and scanning electron microscopy before and after reaction. Finally, the thermochemical heat storage/release capacity of the as prepared materials was analysed by differential scanning calorimetry.

## 5.2 Experimental methods

### 5.2.1 Materials preparation

LiMn<sub>2</sub>O<sub>4</sub> and CuMn<sub>2</sub>O<sub>4</sub> were synthesized by a modification of Pechini method [26]. The metal (Me) precursors, namely Mn(NO<sub>3</sub>)<sub>2</sub>·4H<sub>2</sub>O (97%, Sigma–Aldrich), Cu(NO<sub>3</sub>)<sub>2</sub>·3H<sub>2</sub>O (99%, Sigma–Aldrich) and LiNO<sub>3</sub> (99%, Sigma–Aldrich) were added to an aqueous solution of citric acid (CA, ≥99.5%, Scharlab) in a Me: CA molar ratio of 1:5 with constant stirring for 3 h at 70 °C. Afterwards, ethylene glycol (EG, ≥99.5%, Sigma–Aldrich) was added (in a CA: EG molar ratio of 3:2) with continued stirring for further 2 h at 90 °C to achieve gelification. The gel was dried at 200 °C for 3 h and then calcined at 450 °C for 4 h in air. Finally, the calcined gel was ground to fine powders and further calcined at 700 °C for 4 h to obtain the products.



### 5.2.2 Material Characterization

X-ray diffraction (XRD) analyses were performed using a Philips PW 3040/00 X'Pert MPD/MRD diffractometer with Cu K $\alpha$  radiation ( $\lambda = 1.54178 \text{ \AA}$ ) at a scanning rate of  $0.2^\circ\text{s}^{-1}$  and using a secondary monochromator. Hitachi TM-100 microscope was used for scanning electron microscopy (SEM) images without any previous treatment of the samples.

### 5.2.3 Redox cycling

Thermogravimetric analysis (TGA) using a SDT Q-600 from TA instruments was used to monitor the stability of redox cycle. During cyclability studies, 15-20 mg of sample were placed in a 90  $\mu\text{l}$  alumina crucibles and subjected to 5 charging–discharging cycles. Each cycle involved heating up to 900 °C and cooling down to 700 °C both at a rate of  $5 \text{ deg min}^{-1}$ , under



Argon flow at  $100 \text{ ml min}^{-1}$  ( $p\text{O}_2 \leq 5 \cdot 10^{-3} \text{ bar}$ ) after which the sample was kept in air flow for 30 min. The heating and cooling process continued until the fifth cycle was completed. Differential scanning calorimetry (DSC) was carried out simultaneously with TGA in order to study the heat effects during reduction and oxidation reactions. DSC was calibrated under Ar atmosphere using the melting temperatures and enthalpies of Zn and Ag along the temperature range utilized for redox cycling [6, 18, 27].

### 5.3 Results and Discussion

Fig 5.1 showed X-ray diffraction patterns of  $\text{CuMn}_2\text{O}_4$  which indicated that the phases identified are crystal planes of cubic  $\text{CuMn}_2\text{O}_4$  spinel structure (JCPDS74-2422). In addition, some reflections corresponding to the peaks of the  $\text{Mn}_3\text{O}_4$  tetragonal phase (JCPDS024-0734) observed at  $2\theta = 28^\circ$  and  $33^\circ$ . These results suggest that higher temperature ( $\geq 900^\circ \text{C}$ ) and longer calcination times (more than 10 h) are required to obtain the spinel as a single phase.

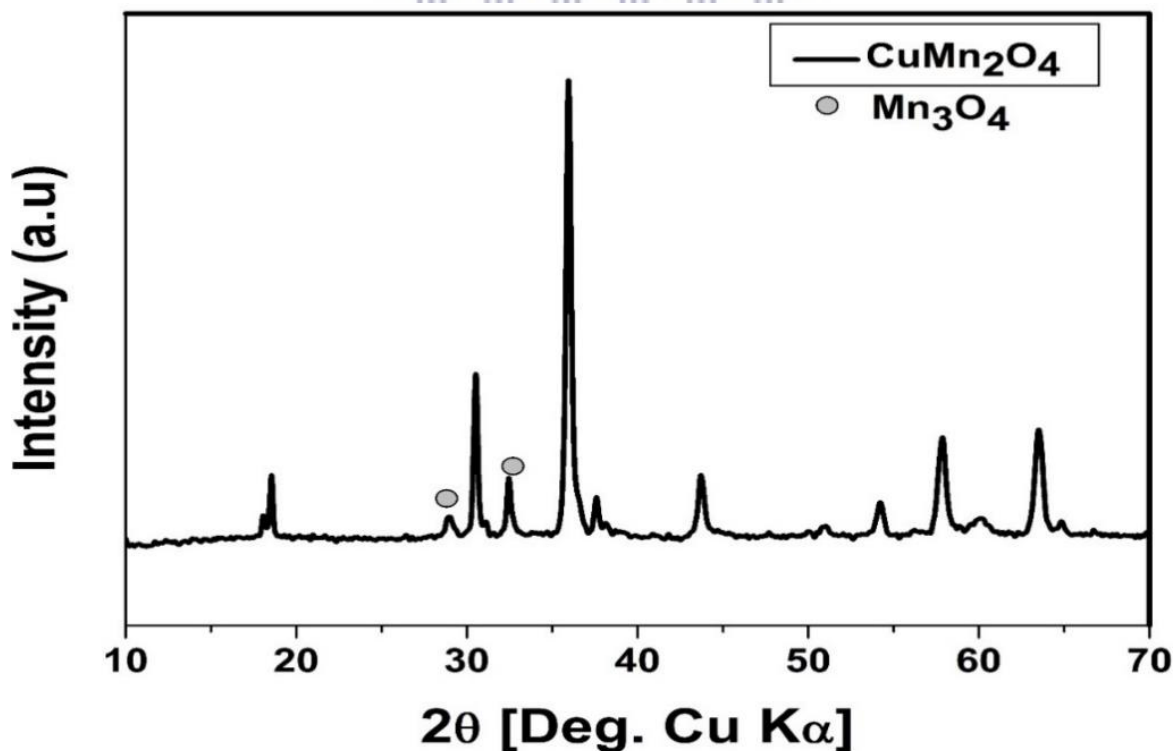
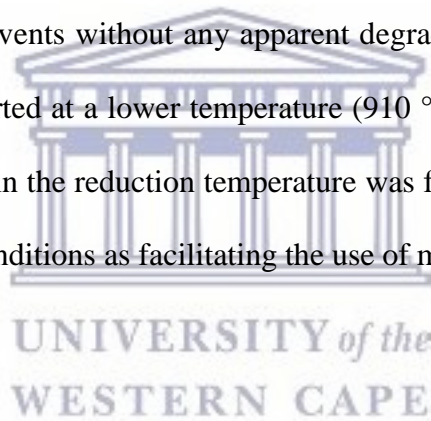
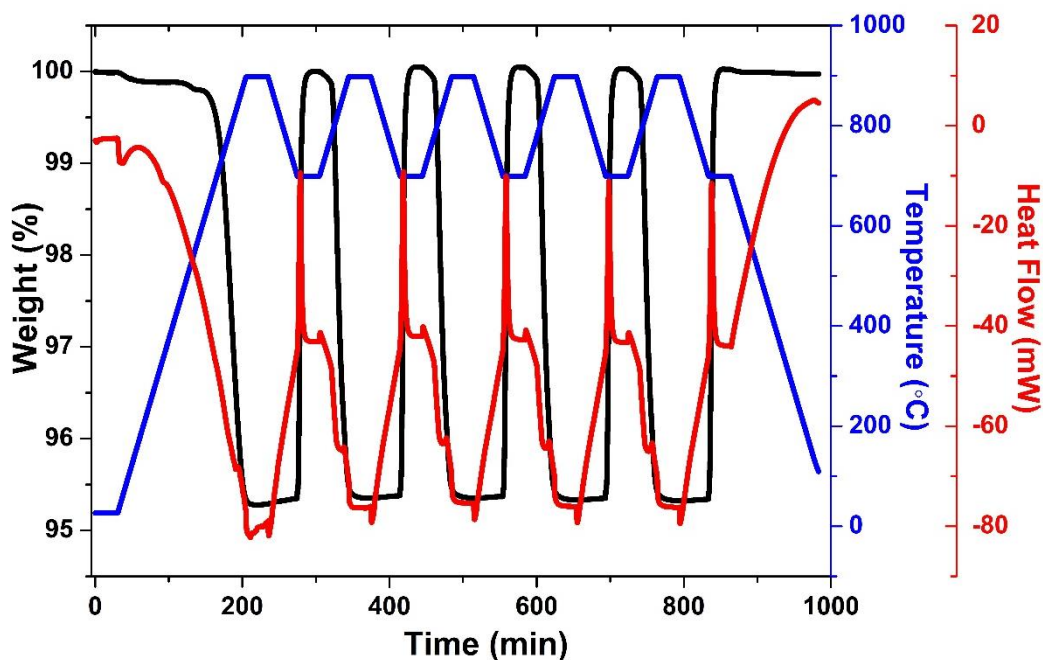


Figure 5.1: XRD pattern of synthesized  $\text{CuMn}_2\text{O}_4$

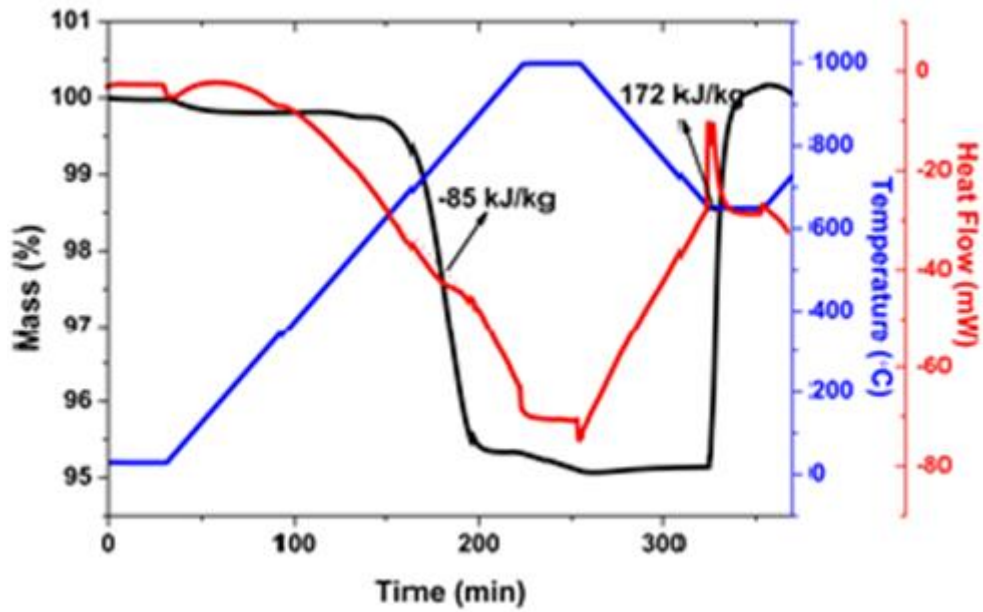
In order to study the redox behaviour of  $\text{CuMn}_2\text{O}_4$ , this material was subjected to heating up to  $900\text{ }^\circ\text{C}$  and then, after cooling the sample down to  $700\text{ }^\circ\text{C}$ , swapping to air flow in order to allow re-oxidation and continuous cycling. **Fig 5.2** showed the results obtained under these conditions, where a sharp decrease in mass and the subsequent recovery in air atmospheres can be appreciated for five consecutive cycles. Total weight loss in the first cycle was 4.67 wt%, which implies a deep reduction of the  $\text{CuMn}_2\text{O}_4$  phase. The reduction onset appears at  $650\text{ }^\circ\text{C}$ , and this is reflected in the temperature of the maximum reduction rate. On the other hand, re-oxidation is remarkably rapid once air is introduced at  $700\text{ }^\circ\text{C}$ , as indicated by the weight recovery which is complete in less than 10 min.  $\text{CuMn}_2\text{O}_4$  demonstrated good characteristics to be considered as material for heat storage applications because it was able to withstand five successive charge-discharge events without any apparent degradation. The other observation made is that the reduction started at a lower temperature ( $910\text{ }^\circ\text{C}$ ) compared to the un-doped  $\text{Mn}_2\text{O}_3$  at  $950\text{ }^\circ\text{C}$ . Decreasing in the reduction temperature was favourable because this would allow working in moderate conditions as facilitating the use of more conventional materials in the reactor fabrication.





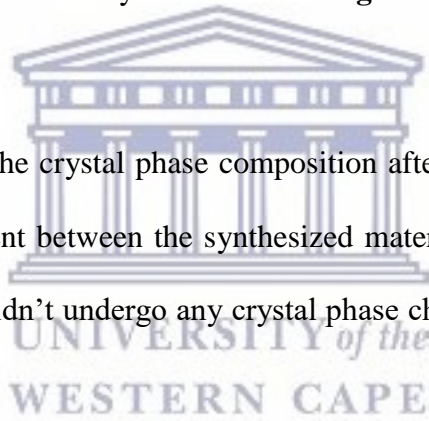
**Figure 5.2:** Five redox cycles performed to  $\text{CuMn}_2\text{O}_4$ , heating up to  $900\text{ }^\circ\text{C}$  and cooling down to  $700\text{ }^\circ\text{C}$  in Ar/air flow.

DSC (discussed in section 5.2.3) results were used to determine the enthalpy. **Fig 5.3** showed that the area under the endothermic peak was  $85\text{ kJ kg}^{-1}$  which was determined by tangential-sigmoidal integration. The oxidation enthalpy obtained was  $172\text{ kJ kg}^{-1}$ . The value for reduction enthalpy is very low when compared to the theoretical values of pure Mn oxide, which is because of the presence of Cu cations [6]. The solid recovered after the reduction step, was cooled down in inert atmosphere to avoid re-oxidation and it was subjected to XRD analysis in order to determine its phase composition.



**Figure. 5.3:** DSC analysis for the first cycle taken from **Figure 5.2**.

XRD was used to determine the crystal phase composition after the 5 redox cycles. **Fig 5.4** revealed no significant different between the synthesized material as well as the cycled one which shows that  $\text{CuMn}_2\text{O}_4$  didn't undergo any crystal phase change, proving the stability of the material.



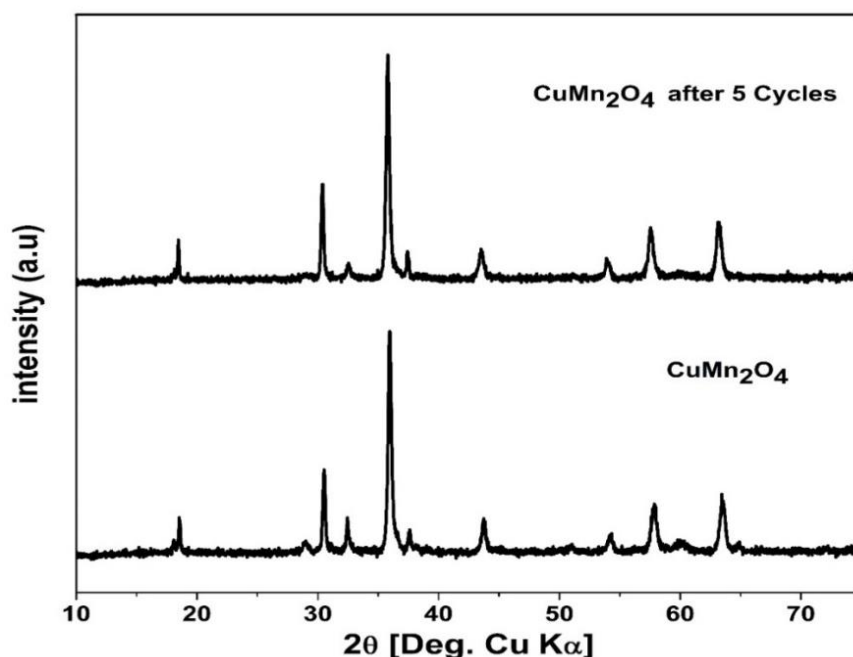


**Figure 5.4:** XRD pattern of CuMn<sub>2</sub>O<sub>4</sub> before and after five cycles.

**Fig 5.5** displayed the SEM morphology before and after 5 redox cycles. **Fig 5.5 A** showed that the material consists of agglomerates of particles with irregular shape of several microns of diameter. **Fig 5.5 B** showed that the reaction condition lead to a complete morphology change due to sintering processes. It can be seen that coarsening occurs in CuMn<sub>2</sub>O<sub>4</sub> particles which results in a more open structure with large pores. The sintering that occurred because of high temperature did not have an effect on the re-oxidation rate in any of the five cycles. However, these extensive changes induced by high temperature cycling did not have a negative effect on the re-oxidation rate. On the contrary, as mentioned above, oxidation rate slightly increases for successive cycles for this spinel.

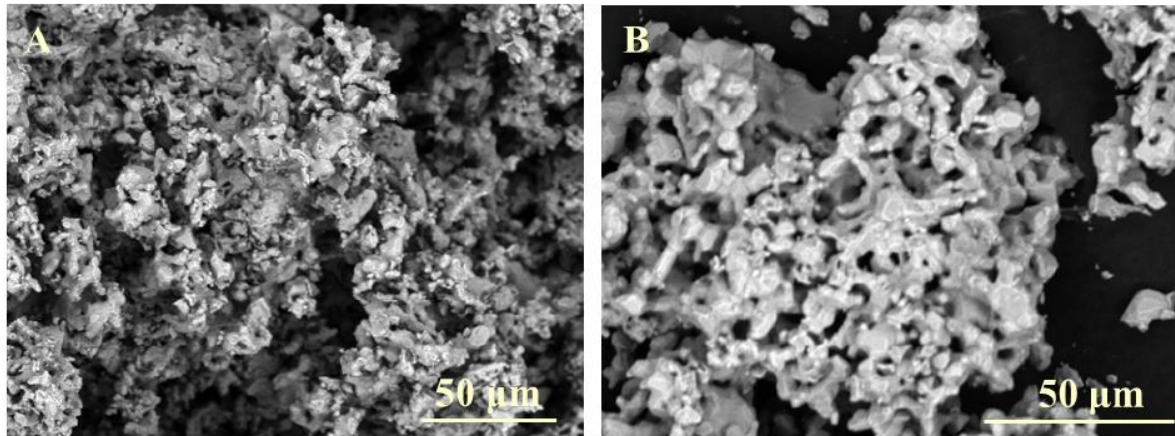


**Figure 5.5:** SEM of  $\text{CuMn}_2\text{O}_4$  before and after five cycles

The powder materials recovered after reduction was subjected to XRD. **Fig 5.6** displayed that monoclinic  $\text{CuMnO}_2$  crystal phase coexist with  $\text{Mn}_3\text{O}_4$ . The high temperature phase  $\text{CuMnO}_2$  would gain oxygen during cooling and form  $\text{CuMn}_2\text{O}_4$ . Accordingly, the whole redox process taking place at high temperature in argon can be described by the following equation:



However, considering that the theoretical mass loss for this process is 4.49 wt%. It appears that conversion in Ar is not complete. This is at least partly due to the initial presence of  $\text{Mn}_3\text{O}_4$  impurities.



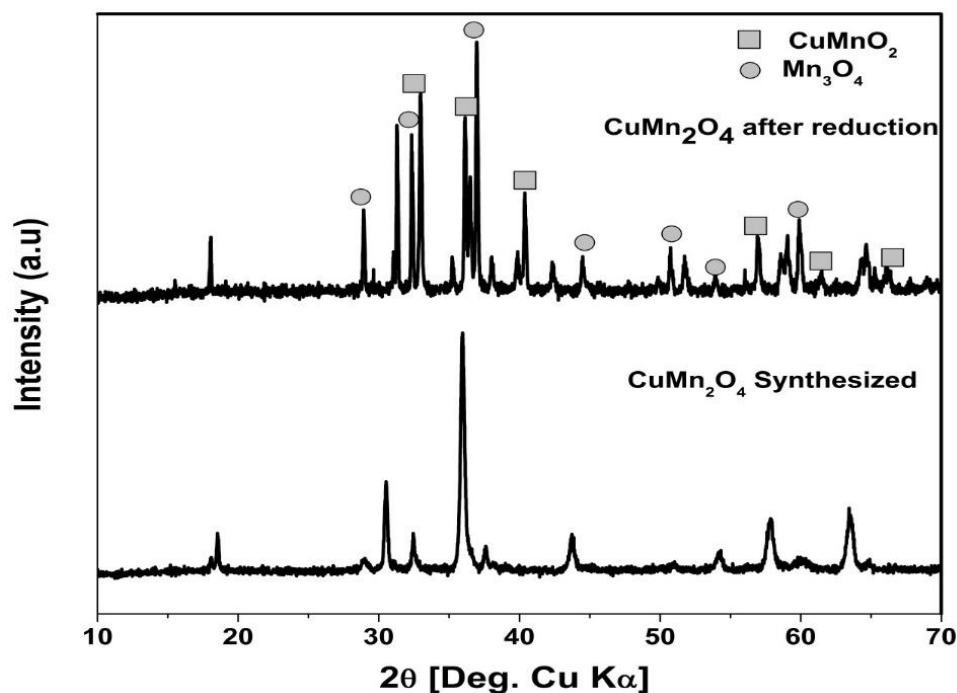


**Figure 5.6:** XRD pattern of the  $\text{CuMn}_2\text{O}_4$  reduction in argon at  $900\text{ }^\circ\text{C}$

In the presence of argon the phase  $\text{CuMnO}_2$ ,  $\text{Mn}_3\text{O}_4$  and  $\text{O}_2$  easily react to regenerate  $\text{CuMn}_2\text{O}_4$ , up-taking oxygen and recovering the initial weight. This was confirmed by XRD analysis of the sample submitted to the 5 redox cycles and cooled down in air flow, whose diffraction pattern is very similar to that of the initial sample, as it shows the presence of  $\text{CuMn}_2\text{O}_4$  as the main component, along with a minor contribution of  $\text{Mn}_3\text{O}_4$ . In fact, the excellent reversibility of the process is rather remarkable considering that complex solid state reactions taking place, and most likely are related to the high cationic mobility provided by the spinel structure.

The phase composition and structure of the  $\text{LiMn}_2\text{O}_4$  was characterized by XRD as shown in **Fig. 5.7**. The X-ray diffraction pattern is dominated by  $\text{LiMn}_2\text{O}_4$  crystal phase (JCPDS: 35-0782) which was identified as a single phase of cubic spinel with space group  $\text{Fd}\bar{3}\text{m}$ , although the presence of small impurities of  $\text{Mn}_3\text{O}_4$  can be observed from XRD pattern. These results



suggest that higher temperature ( $\geq 900\text{ }^{\circ}\text{C}$ ) and longer calcination times (more than 10 h) are required to obtain the spinel as a single phase.

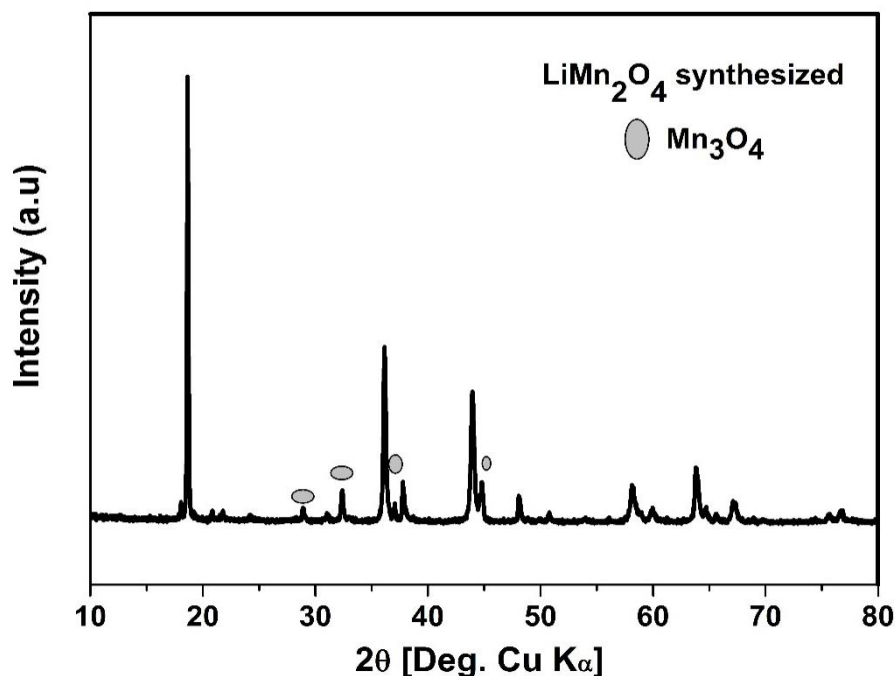


**Figure 5.7:** XRD patterns of the synthesized  $\text{LiMn}_2\text{O}_4$

As in the case of  $\text{CuMn}_2\text{O}_4$ , the redox behaviour of  $\text{LiMn}_2\text{O}_4$  was evaluated by performing successive cycles. **Fig 5.8** showed TGA results of the redox cycle performed by increasing the temperature up to  $900\text{ }^{\circ}\text{C}$  in argon, then cooling the sample down to  $700\text{ }^{\circ}\text{C}$ , and subsequently changing the gas flow to air while heating again the material. Under these conditions, the material experiences a fully reversible weight loss of 5.7 wt. %. Subsequently, certain mass uptake at around  $650\text{ }^{\circ}\text{C}$  is most likely related to the oxidation of  $\text{Mn}_3\text{O}_4$  to  $\text{Mn}_2\text{O}_3$ . Following that, a sharp decrease of weight, starting at around  $850\text{ }^{\circ}\text{C}$  and achieving 3.63 wt.% is observed,  $\text{LiMn}_2\text{O}_4$  revealed redox reversibility under this conditions as well as good stable redox cycles. The cyclability was completed over 5 charge-discharge cycles.

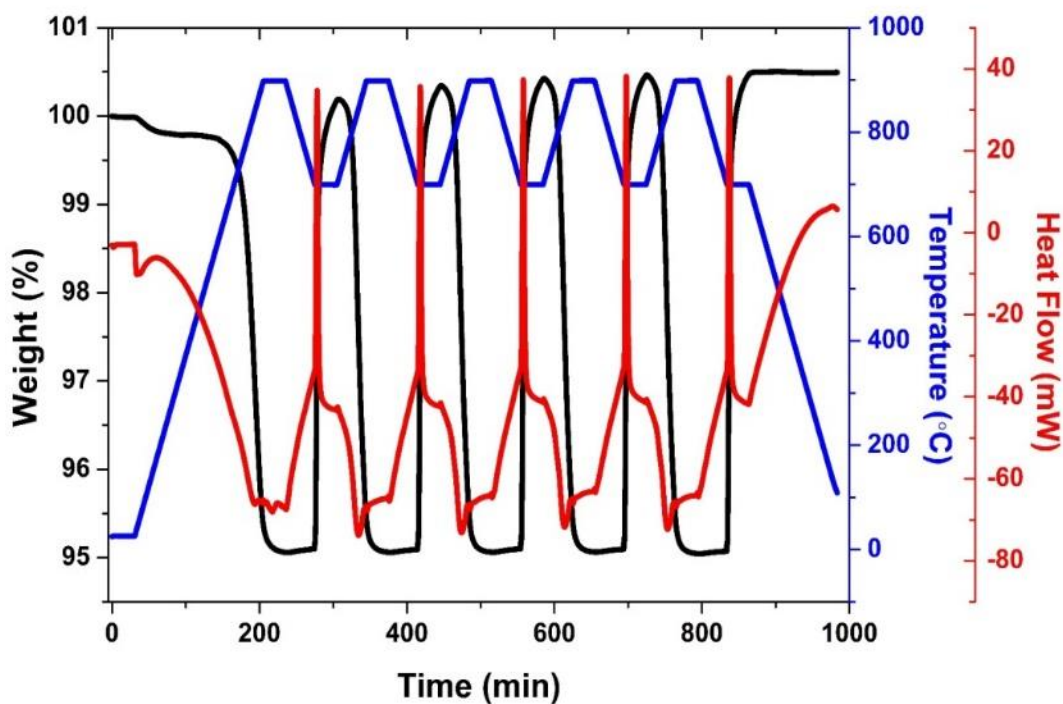
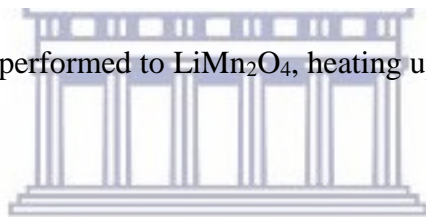


**Figure 5.8:** Five redox cycles performed to  $\text{LiMn}_2\text{O}_4$ , heating up to  $900\text{ }^\circ\text{C}$  and cooling down to  $700\text{ }^\circ\text{C}$  in Ar/air flow.



UNIVERSITY of the  
WESTERN CAPE

The enthalpy associated with DSC analysis was measured as discussed previously. **Fig 5.9** showed the enthalpy calculated from the area under the endothermic peak was  $209\text{ kJ kg}^{-1}$  and the exothermic peak obtained was  $186.8\text{ kJ kg}^{-1}$ . The measured heat storage and released values are higher than  $\text{CuMn}_2\text{O}_4$  and similar to those of pure Mn oxide, proving that  $\text{LiMn}_2\text{O}_4$  can be consisted for thermal energy storage material.

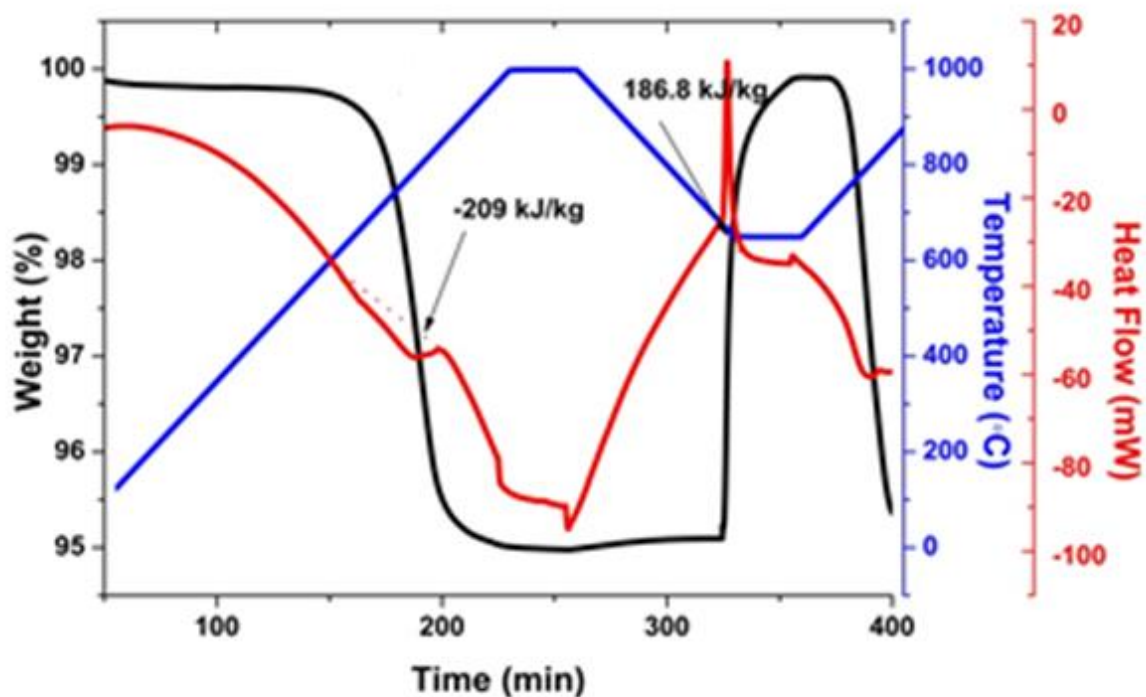


**Figure 5.9:** DSC analysis for the first cycle taken from **Figure 5.7**

**Fig 5.10** showed the XRD pattern of  $\text{LiMn}_2\text{O}_4$  after 5 cycles. XRD results revealed that only one main phase is present due to pure  $\text{LiMn}_2\text{O}_4$  without no further additional peaks of impurities after redox cycles. This suggest that the synthesis temperature was low or maybe  $\text{Mn}_3\text{O}_4$  was all transformed into  $\text{LiMn}_2\text{O}_4$  during thermal cycling, therefore forming a pure phase.

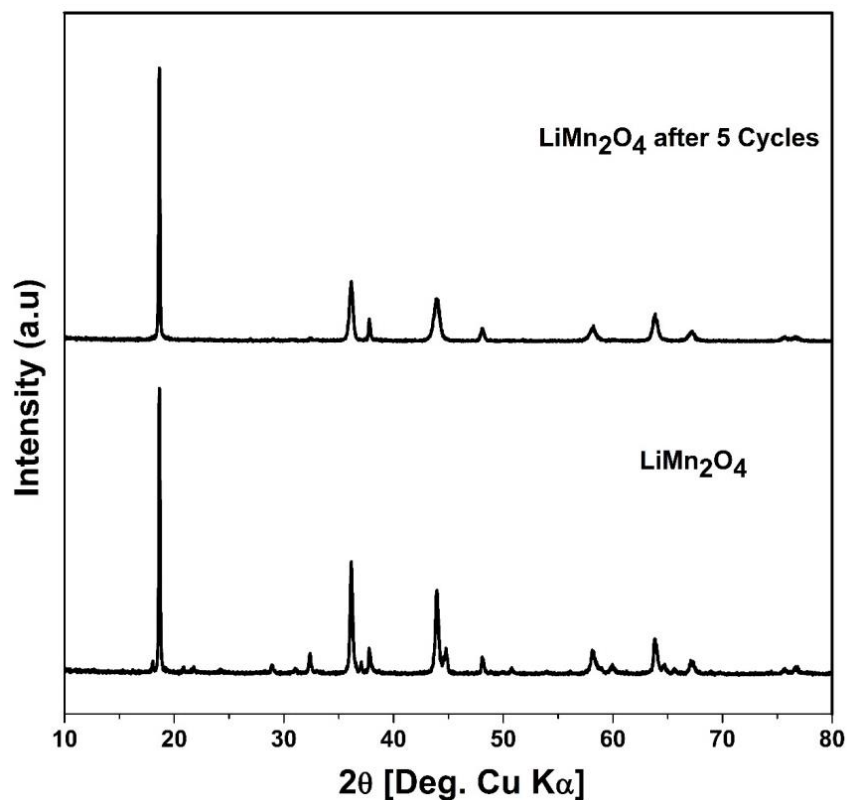


**Figure 5.10:** XRD pattern of LiMn<sub>2</sub>O<sub>4</sub> after five redox cycles.

SEM pictures depicted in **Fig 5.11** showed the morphology of LiMn<sub>2</sub>O<sub>4</sub> both as prepared and after 5 redox cycles. Before the high temperature treatment this material present particles with undefined shape and with a very broad size distribution in the range of 1 to 50  $\mu\text{m}$ . After redox cycles, this sample displayed high level of sintering, characterized by the formation of agglomerates of particles with polyhedral shapes, which appears denser than those of CuMn<sub>2</sub>O<sub>4</sub> following the same treatment. Nevertheless, sintering does not appear to affect the redox performance of the material, as the rate remains basically constant through the cycles.

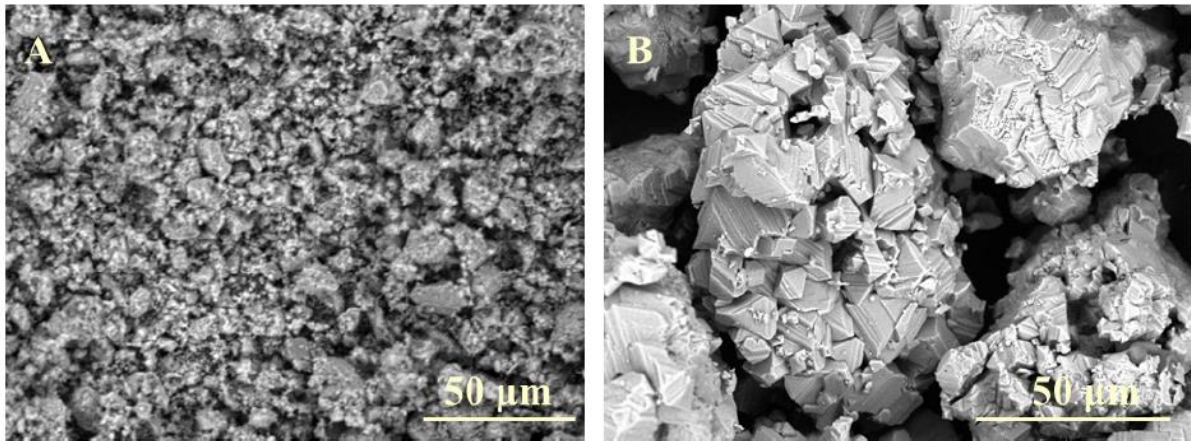


**Figure 5.11:** SEM images of synthesized  $\text{LiMn}_2\text{O}_4$ ; (A) as prepared material and (B) after 5 redox cycles.

**Fig 12** depicted the X-ray diffraction patterns of the  $\text{LiMn}_2\text{O}_4$  reduced in argon flow and stabilized by cooling down in an atmosphere of this inert gas.  $\text{LiMnO}_2$  phase is identified together with  $\text{Mn}_3\text{O}_4$  phase but, in contrast with the sample treated in air, reflections of  $\text{LiMn}_2\text{O}_4$  are not present. Such results confirm that the Li-spinel phase undergoes complete reduction during the redox cycle according to this process described by

Following equation:



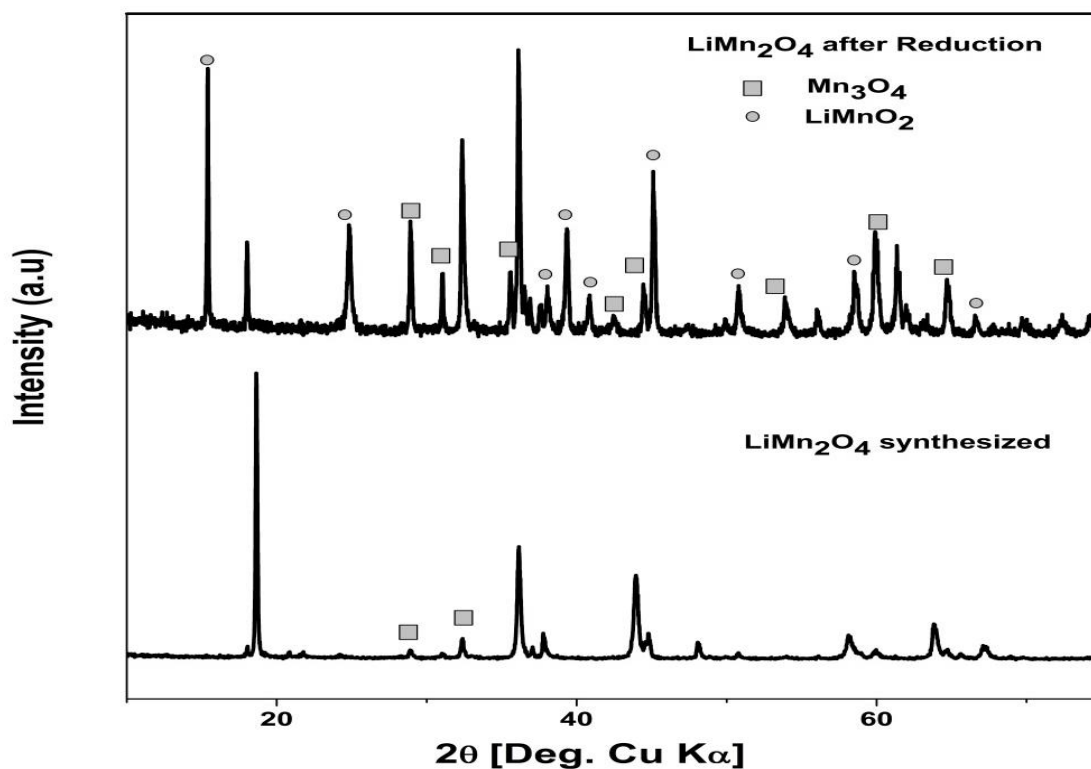
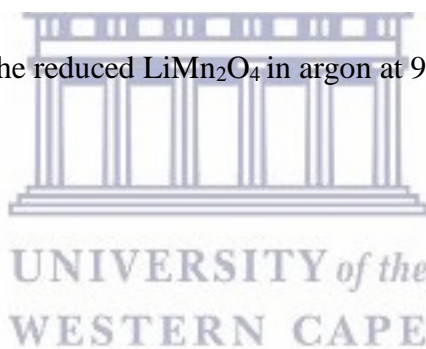


Figure 5.12: XRD pattern of the reduced  $\text{LiMn}_2\text{O}_4$  in argon at  $900\text{ }^\circ\text{C}$ .



## 5.4 Summary

In this work, the redox behaviour at high temperatures and different atmospheres of  $\text{LiMn}_2\text{O}_4$  and  $\text{CuMn}_2\text{O}_4$  materials has been investigated as to determine the feasibility of using these systems for thermochemical heat storage. Spinel lithium manganese oxides and copper manganese oxide were successfully synthesized by modified Pechini method, although the samples containing a small proportion of  $\text{Mn}_3\text{O}_4$  due to the incomplete reactions. Both materials showed to be redox reversible in the conditions applied and did not present any loss of cycle stability for the 5 redox cycles and it was evident from XRD with materials retaining their crystal phases. These spinel manganese-based materials could be explored where the cost is the limiting factor.  $\text{CuMn}_2\text{O}_4$  showed a reduction reaction temperature of  $910\text{ }^\circ\text{C}$  which is lower than that of pure manganese.  $\text{LiMn}_2\text{O}_4$  showed high reaction temperature with an

enthalpy of  $209 \text{ kJ kg}^{-1}$ . Both materials are of great interest for the storing solar heat. The key factor to be considered is developing metal co-doped manganese oxide by Li and Cu for thermochemical energy storage





## 5.5 References

- [1] T. Block, M. Schmu, Metal oxides for thermochemical energy storage : A comparison of several metal oxide systems, *Sol. Energy*. 126 (2016) 195–207.
- [2] C. Prieto, P. Cooper, A.I. Fernández, L.F. Cabeza, Review of technology : Thermochemical energy storage for concentrated solar power plants, *Renew. Sustain. Energy Rev.* 60 (2016) 909–929.
- [3] G. Alva, L. Liu, X. Huang, G. Fang, Thermal energy storage materials and systems for solar energy applications, *Renew. Sustain. Energy Rev.* 68 (2017) 693–706.
- [4] A.H. Abedin, M.A. Rosen, A Critical Review of Thermochemical Energy Storage Systems, *Open Renew. Energy J.* 4 (2011) 42–46.
- [5] J. Yan, C.Y. Zhao, First-principle study of CaO/Ca(OH)<sub>2</sub> thermochemical energy storage system by Li or Mg cation doping, *Chem. Eng. Sci.* 117 (2014) 293–300.
- [6] A.J. Carrillo, D.P. Serrano, P. Pizarro, J.M. Coronado, Manganese oxide-based thermochemical energy storage : Modulating temperatures of redox cycles by Fe – Cu co-doping, *J. Energy Storage*. (2016).
- [7] Y.A. Criado, M. Alonso, J.C. Abanades, Enhancement of a CaO/Ca(OH)<sub>2</sub> based material for thermochemical energy storage, *Sol. Energy*. 135 (2016) 800–809.
- [8] F. Varsano, C. Alvani, A. La Barbera, A. Masi, F. Padella, Lithium manganese oxides as high-temperature thermal energy storage system, *Thermochim. Acta.* 640 (2016) 26–35.
- [9] X. Fontanet, C. Barreneche, A.I. Ferna, A. Sole, I. Martorell, L.F. Cabeza, Requirements to consider when choosing a thermochemical material for solar energy storage, *Sol. Energy*. 97 (2013) 398–404.

- [10] A.J. Carrillo, D.P. Serrano, P. Pizarro, J.M. Coronado, Thermochemical heat storage based on the  $\text{Mn}_2\text{O}_3/\text{Mn}_3\text{O}_4$  redox couple: influence of the initial particle size on the morphological evolution and cyclability, *J. Mater. Chem. A*. 2 (2014) 19435–19443.
- [11] A.J. Carrillo, J. Moya, A. Bayón, P. Jana, V.A. De, P.O. Shea, M. Romero, J. Gonzalez-Aguilar, D. P. Serrano, P. Pizarro, J. M. Coronado, Thermochemical energy storage at high temperature via redox cycles of Mn and Co oxides : Pure oxides versus mixed ones, *Sol. Energy Mater. Sol. Cells*. 123 (2014) 47–57.
- [12] C. Agrafiotis, M. Roeb, M. Schmu, C. Sattler, Exploitation of thermochemical cycles based on solid oxide redox systems for thermochemical storage of solar heat . Part 1 : Testing of cobalt oxide-based powders, *Sol. Energy*. 102 (2014) 189–211.
- [13] C. Agrafiotis, S. Tescari, M. Roeb, M. Schmu, C. Sattler, Exploitation of thermochemical cycles based on solid oxide redox systems for thermochemical storage of solar heat . Part 3 : Cobalt oxide monolithic porous structures as integrated thermochemical reactors / heat exchangers, *Sol. Energy*. 114 (2015) 459–475.
- [14] C. Agrafiotis, M. Roeb, M. Schmu, C. Sattler, Exploitation of thermochemical cycles based on solid oxide redox systems for thermochemical storage of solar heat . Part 2 : Redox oxide-coated porous ceramic structures as integrated thermochemical reactors / heat exchangers, *Sol. Energy*. 114 (2015) 440–458.
- [15] M. Neises, S. Tescari, L. De Oliveira, M. Roeb, C. Sattler, B. Wong, Solar-heated rotary kiln for thermochemical energy storage, *Sol. Energy*. 86 (2012) 3040–3048.
- [16] J. Licurgo, E. Fuentealba, E. Alonso, C. Pe, C.A. Estrada, First experimental studies of solar redox reactions of copper oxides for thermochemical energy storage, *Sol. Energy*. 115 (2015) 297–305.
- [17] A.J. Schrader, A.P. Muroyama, P.G. Loutzenhiser, Solar electricity via an Air Brayton

- cycle with an integrated two-step thermochemical cycle for heat storage based on  $\text{Co}_3\text{O}_4/\text{CoO}$  redox reactions : Thermodynamic analysis, *Sol. Energy*. 118 (2015) 485–495.
- [18] A.J. Carrillo, D.P. Serrano, P. Pizarro, J.M. Coronado, Improving the thermochemical energy storage performance of the  $\text{Mn}_2\text{O}_3/\text{Mn}_3\text{O}_4$  redox couple by the incorporation of iron, *ChemSusChem*. 8 (2015) 1947–1954.
- [19] P. Ma, Q. Geng, X. Gao, S. Yang, G. Liu, Solution combustion of spinel  $\text{CuMn}_2\text{O}_4$  ceramic pigments for thickness sensitive spectrally selective ( TSSS ) paint coatings, *Ceram. Int.* 42 (2016) 11966–11973.
- [20] M. Enhessari, A. Salehabadi, K. Maarofian, S. Khanahmadzadeh, N. Branch, M. Branch, Synthesis and physicochemical properties of  $\text{CuMn}_2\text{O}_4$  nanoparticles; a potential semiconductor for photoelectric devices, *Int. J. Bio-Inorganic Hybrid Nanomater.* 5 (2016) 115–120.
- [21] P. Ma, Q. Geng, X. Gao, T. Zhou, S. Yang, G. Liu, Aqueous solution-derived  $\text{CuMn}_2\text{O}_4$  ceramic films for spectrally selective solar absorbers, *Ceram. Int.* 42 (2016) 19047–19057.
- [22] M. Zhao, B. Zhang, G. Huang, W. Dai, F. Wang, X. Song, Electrochemical performance of modified  $\text{LiMn}_2\text{O}_4$  used as cathode material for an aqueous rechargeable lithium battery, *energy & fuels*. 26 (2011) 1214–1219..
- [23] Q. Zhu, S. Zheng, X. Lu, Y. Wan, Q. Chen, J. Yang, Improved cycle performance of  $\text{LiMn}_2\text{O}_4$  cathode material for aqueous rechargeable lithium battery by  $\text{LaF}_3$  coating, *J. Alloys Compd.* 654 (2016) 384–391.
- [24] Y. Wang, L. Chen, Y. Wang, Y. Xia, Cycling stability of spinel  $\text{LiMn}_2\text{O}_4$  with different particle sizes in aqueous electrolyte, *Electrochim. Acta.* 173 (2015) 178–183.

- [25] I.M. Hung, Y.C. Yang, H.J. Su, J. Zhang, Influences of the surfactant on the performance of nano-LiMn<sub>2</sub>O<sub>4</sub> cathode material for lithium-ion battery, *Ceram. Int.* 41 (2015) S779–S786.
- [26] P. Jana, V.A. De La Peña O’Shea, J.M. Coronado, D.P. Serrano, Cobalt based catalysts prepared by Pechini method for CO<sub>2</sub>-free hydrogen production by methane decomposition, *Int. J. Hydrogen Energy.* 35 (2010) 10285–10294.
- [27] N.W. Hlongwa, D. Sastre, E. Iwuoha, A.J. Carrillo, C. Ikpo, D.P. Serrano, P. Pizarro, J. M. Coronado, Exploring the thermochemical heat storage capacity of AMn<sub>2</sub>O<sub>4</sub>(A = Li or Cu) spinels, *Solid State Ionics.* 320 (2018) 316–324. doi:10.1016/j.ssi.2018.03.019.



## CHAPTER SIX

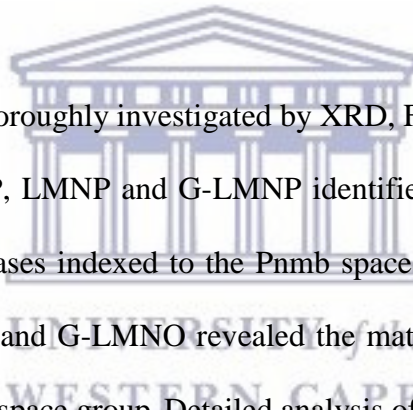
### 6 Conclusion and Recommendations



UNIVERSITY *of the*  
WESTERN CAPE

## 6.1 Conclusion

This research explored the properties of pristine and derivatised manganese-based electrode materials for electrochemical and thermochemical energy storage applications. The materials include  $\text{LiMnPO}_4$  (LMP);  $\text{LiMn}_2\text{O}_4$  (LMO); their nickel doped analogues consisting of LMNP and LMNO and the corresponding graphenised derivatives which comprise G-LMNP and G-LMNO; as well as  $\text{CuMn}_2\text{O}_4$ . The preparation of the materials for lithium ion capacitor studies involved solvothermal synthetic routes as well as Hummer's modification for the graphene-containing electrodes while employing a variant of the Pechini's method for the preparation of samples for thermochemical energy storage studies.



All the LICs materials were thoroughly investigated by XRD, FTIR and Raman spectroscopy. The XRD results for the LMP, LMNP and G-LMNP identified the as-prepared materials to have orthorhombic olivine phases indexed to the  $\text{Pnmb}$  space group whereas the diffraction patterns of the LMO, LMNO and G-LMNO revealed the materials to have the cubic spinel structure indexed to the  $\text{Fd}3\text{m}$  space group. Detailed analysis of the FTIR results for the LMP, LMNP and G-LMNP confirmed the presence of intramolecular vibrational bands typical of the  $\text{PO}_4^{3-}$  anion at  $650 - 530 \text{ cm}^{-1}$ . The C-C vibrational frequency occurring at  $1630 \text{ cm}^{-1}$  confirmed the presence of graphene in the G-LMNP. This was corroborated by the Raman results which revealed bands at  $1463$  and  $1526 \text{ cm}^{-1}$  representing the characteristic D and G bands of graphene along with the vibrational bands of  $\text{PO}_4^{3-}$  at  $980$  and  $1100 \text{ cm}^{-1}$ . Similarly, the FTIR spectra of LMO and the nickel doped graphene derivatives showed the vibrational stretching mode of  $\text{MnO}_6$  octahedra at  $510 - 620 \text{ cm}^{-1}$  which are responsible for the formation of  $\text{LiMn}_2\text{O}_4$  with the C-C symmetric stretching band at  $1580 \text{ cm}^{-1}$  for G-LMNO confirming the presence of

graphene in the nanocomposite material. Raman spectroscopic results also confirmed the D and G bands of graphene in the spinels.

Electrochemical studies conducted in 1 M Li<sub>2</sub>SO<sub>4</sub> aqueous electrolyte at a voltage window of 0 - 2 V showed the G-LMNO to have the highest capacitance at 80 F g<sup>-1</sup> and excellent cycle stability after 1000 cycling experiments with a capacitance retention of 70 %. It delivered a power density of 19.6 kW kg<sup>-1</sup> and energy density of 12.32 Wh kg<sup>-1</sup>. The improved electrochemical performance of the G-LMNO over the other electrodes could be attributed to the conductive graphene coating on the electrode surface. The same trend was also observed for the LMP series where the G-LMNP showed better cycling performance. The graphenised electrode derivatives present good properties that can be harnessed in the development of lithium ion capacitors for electrochemical energy storage. This level of electrochemical performance of the prepared LICs satisfies the demands of hybrid electric vehicles (HEV) applications. Additionally, the simplicity of the graphene nanosheets coating method, which uses electrostatic attraction between negatively charged graphene and positively charged LMO/LMP particles, will be applicable for various electrode materials.

Further studies in this work involved the interrogation of the thermochemical energy storage properties of LiMn<sub>2</sub>O<sub>4</sub> and CuMn<sub>2</sub>O<sub>4</sub>. The materials showed excellent redox cyclability in argon-air atmospheres without any apparent loss of performance for the five redox cycles performed. Considering the stability of these systems as well as the relatively high enthalpies and fast reaction oxidation kinetics, CuMn<sub>2</sub>O<sub>4</sub> and LiMn<sub>2</sub>O<sub>4</sub> can be said to be interesting alternatives to the standard Mn<sub>2</sub>O<sub>3</sub>/Mn<sub>3</sub>O<sub>4</sub> couple. The combination of these improvements, render such materials in an attractive option for thermal energy storage system used in concentrated solar power plants.



## 6.2 Recommendations

- It is important to further explore the properties of these materials by conducting X-ray photoelectron spectroscopic experiment to determine the elemental composition, chemical and electronic states of the elements present in the materials.
- Investigation of G-LMNO and G-LMNP using a full-cell symmetric device for comparisons with the asymmetric system.
- Explore the use of different electrolytic solutions such as ionic liquids, organic and non-neutral aqueous electrolytes for the development of lithium ion capacitors.
- Investigation of other methods of preparing the manganese-based materials such as microwave synthesis.
- Test the ability of all the fabricated Li-ion capacitors to power a light-emitting diode (LED).

